ABSTRACT

Title of dissertation: INVESTIGATION INTO THE AERODYNAMICS
OF SWASHPLATELESS ROTORS
USING CFD-CSD ANALYSIS

Arun I. Jose, Doctor of Philosophy, 2012

Dissertation directed by: Dr. James D. Baeder
Department of Aerospace Engineering

This study obtains a better understanding of the aerodynamics of integrated trailing edge flap (TEF) based swashplateless rotors. Both two dimensional (2D) and three dimensional (3D) analysis/simulations are performed to understand the behavior of TEF airfoils and integrated TEF based swashplateless rotors.

The 2D aerodynamics of TEF airfoils is explored in detail. A semi-empirical approach is developed for modeling drag for TEF airfoils in steady flows based on baseline airfoil drag data alone. Extensive 2D CFD simulations are performed for a wide range of flow conditions in order to better understand various aspects of the aerodynamics of TEF airfoils. The trends in the airloads (lift, drag, pitching moment, hinge moment) for TEF airfoils are obtained. Nonlinear phenomena such as flow separation, shocks and unsteady vortex shedding are investigated, and the flow conditions and trends associated with them are studied.

The effect of airfoil properties such as thickness and overhang are studied. Various approaches are used to model the effect of gaps at the leading edge of

the flap. An approximate "gap averaging" technique is developed, which provides good predictions of steady airloads at almost the same computational cost as a simulation where the gap is not modeled. Direct modeling of the gap is done by using a patched mesh in the gap region. To solve problems (such as poor grid quality/control and poor convergence) that are associated with the patched mesh simulations, an alternate approach using overlapping meshes is used. It is seen that for TEF airfoils, the presence of gaps adversely affects the effectiveness of the flap. The change in airloads is not negligible, especially at the relatively higher flap deflections associated with swashplateless TEF rotors.

Finally, uncoupled and coupled computational fluid/structural dynamics (CFD-CSD) simulations of conventional (baseline) and swashplateless TEF rotors is performed in hovering flight. The CFD-CSD code is validated against experiment and good agreement is observed. It is observed that the baseline UH-60 rotor performs better than the swashplateless UH-60 rotor. For an untwisted NACA0012 airfoil based rotor, the performance is similar for the baseline and swashplateless configurations. The effect of gaps on the performance of swashplateless TEF rotors is also investigated. It is seen that the presence of chordwise gaps significantly affects the effectiveness of the TEF to control the rotor. Spanwise gaps also affect the performance of swashplateless rotors but their effect is not as significant.

INVESTIGATION INTO THE AERODYNAMICS
OF SWASHPLATELESS ROTORS USING CFD-CSD ANALYSIS

by

Arun Isaac Jose

Dissertation submitted to the Faculty of the Graduate School of the
University of Maryland, College Park in partial fulfillment
of the requirements for the degree of
Doctor of Philosophy
2012

Advisory Committee:
Dr. James D. Baeder, Chair/Advisor
Dr. Inderjit Chopra
Dr. J. Gordon Leishman
Dr. Christopher Cadou
Dr. Ramani Duraiswami

Dedication

This dissertation is dedicated to my parents and my aunt

Sheela for all they have done for me.

Acknowledgments

I would like to express my deepest gratitude to my advisor, Dr. James Baeder, for guiding me through this long journey. Without his infinite patience, genuine concern and direct engagement in my research, this thesis would not have come to be. I have always been in awe of his intellectual astuteness, calmness, humility, patience and concern for his students. I have the highest regard for him as an advisor and as a human being, and consider myself extremely fortunate for having had the opportunity of working under him.

I would also like to thank Dr. Inderjit Chopra for his role as co-advisor during the early stages of my PhD. His leadership, vision and enthusiasm for research and innovation have greatly inspired me. I would also like to thank my other committee members for their guidance and interest in my research.

I would like to express my deep gratitude to my friends Vinod and Asitav, who have been with me from my undergrad years all the way through gradschool. Vinod's support and help at various stages of my research played a critical role in the completion of this work. Asitav has always been there for me with his unfailing help whenever I needed it most. Their support and encouragement has been a great source of comfort for me and carried me through some of the tough phases of my PhD.

I have also had the good fortune of receiving help from many senior graduate students and post-docs during the course of this work. In particular, I had the opportunity to work closely with Shreyas, whose support and expertise contributed

significantly to this thesis. I am thankful to Jaina and Karthik for their support, both academic and otherwise, during the early stages of my PhD. Jaye contributed to this work by helping me with the UMARC code.

I have been fortunate to have many good friends during my stint at the rotorcraft center. I would like to thank thank Mani, Sandeep, Jason, Abhishek, Anne, Moble, Nitin, Brandon, Vikram, Smita, Monica, Anand and Ria for making my years at the rotorcraft center so much fun. I will deeply cherish the wonderful times spent with them.

Lastly, this acknowledgment would be incomplete without a mention of my family, who, inspite of being far away, have indirectly contributed to the success of this work. My brother and sister have always been there for me with their companionship and love from my childhood days. Above all, I shall always remain indebted to my parents and my aunt Sheela for their love, support and care throughout my life. The foundation for all my successes in life have been laid by them. This thesis is dedicated to them.

Table of Contents

List of Tables

List of Figures

<center>Nomenclature</center>

a	(1) location of pitch axis measured from mid-chord and non-dimensionalized w.r.t. the semi-chord
	(2) speed of sound
a_i	i^{th} coefficient in drag formula
A	area of the rotor (πR^2)
A_n	coefficients of indicial response functions
b_n	exponents of indicial response functions
b	airfoil semi-chord
c	airfoil chord
C_c	chord force coefficient
C_d	drag coefficient
$C_{d_0}, C_{d_1}, C_{d_2}$	coefficients in drag modeling, $C_d = C_{d_0} + C_{d_1}\alpha_{\text{eff}} + C_{d_2}\alpha_{\text{eff}}^2$
C_{d_p}	pressure drag coefficient
C_{d_v}	contribution to drag from viscous terms $= C_d - C_{d_p}$
C_h	flap hinge moment coefficient
$C(k)$	Theodorsen function
C_l	lift force coefficient
C_m	pitching moment coefficient about 1/4-chord
C_n	normal force coefficient
C_p	pressure coefficient $= (p - p_\infty)/\frac{1}{2}\rho V^2$
C_Q	power/Torque coefficient $= P/(\rho \pi R^2 U_{\text{tip}}^3)$
C_T	thrust coefficient $= T/(\rho \pi R^2 U_{\text{tip}}^2)$
D	drag
e	internal energy per unit volume
E_t	internal energy per unit mass
$F(k)$	real part of the Theodorsen function
$G(k)$	imaginary part of the Theodorsen function
iblank	blanking array
J	Jacobian or cell volume
J_ν	Bessel functions of the first kind
j	index of grid-point in chord-wise direction
k	(1) reduced frequency $= \omega c/2V$
	(2) index of grid-point in normal direction (in 2D)
	(3) index of grid-point in spanwise direction (in 3D)
	(4) thermal conductivity
l	(1) index of grid-point in normal direction (in 3D)
	(2) flap hinge offset $= \hat{x}_h - \hat{x}_f = \xi(1 - \hat{x}_h) = 2(x_h - x_f) = 2\xi(1 - x_h)$
L	lift
M	Mach number
M_{tip}	tip Mach number
OH	flap overhang, $\xi = \frac{x_h - x_f}{1 - x_h} = \frac{\hat{x}_h - \hat{x}_f}{1 - \hat{x}_h}$
p	pressure
P	power

Pr	Prandtl number $= \frac{\mu C_p}{k} = 0.72$
q	non-conservative flow variable
Q	term containing the forcing functions for unsteady calculations
R	rotor radius
Re	Reynolds number
s	distance traveled by airfoil in semi-chords $= \frac{2Vt}{c}$
t	time
T	(1) thrust
	(2) temperature
T_i	i^{th} flap function
u	component of local velocity in the x-direction
U_z	inflow normalized by tip Mach number
U_{tip}	tip speed (ΩR)
v	component of local velocity in the y-direction
V	free-stream velocity
x	non-dimensional distance along the chord
x_f	flap location measured from leading edge and non-dimensionalized w.r.t. chord
$\hat{x}_f$	flap location measured from mid-chord and non-dimensionalized w.r.t. semi-chord $= 2x_f - 1$
x_h	flap hinge location measured from leading edge and non-dimensionalized w.r.t. chord
$\hat{x}_h$	flap hinge location measured from mid-chord and non-dimensionalized w.r.t. semi-chord $= 2x_h - 1$
Y_ν	Bessel functions of the second kind

Symbols

α	angle of attack
$\dot{\alpha}$	pitch rate
β	Glauert factor, $\beta = \sqrt{1 - M^2}$
δ	flap deflection (positive downwards)
ν_θ	rotating natural frequency for torsion mode
ψ, η, ζ	computational coordinates
γ	ratio of specific heats $= 1.4$
ξ	flap overhang, OH$= \frac{x_h - x_f}{1 - x_h} = \frac{\hat{x}_h - \hat{x}_f}{1 - \hat{x}_h}$
ϕ_W	Wagner function
σ	dummy time variable of integration
ρ	density
θ	blade deformation
μ	coefficient of dynamic viscosity
ω	angular frequency, rad/s
Ω	angular velocity of blade rotation, rad/s

Definitions

Index angle	angle of the blade root in the absence of torsional moments at the root
Hole points	points inside the mesh where the solution is not valid
Fringe points	points at the boundary of the hold where the solution is interpolated
Receiver point	points for which the values of the flow variables are obtained from another mesh through interpolation
Donor	cell (or grid-point represeneting the cell) from which the value of flow variables at a receiver point are interpolated
Baseline rotor	referring to rotor with swashplate

Abbreviations

2D	two dimensional
3D	three dimensional
CFD	computational fluid dynamics
CSD	computational structural dynamics
FM	figure of merit
IHC	implicit Hole Cutting
IGBP	inter-grid boundary point
LE	leading edge
OSV	opposite sense vortex
OVERTURNS	overset transonic unsteady rotor Navier-Stokes (CFD code)
RFA	rational function approximation
TE	trailing edge
TEF	trailing edge flap
TURNS	transonic unsteady rotor Navier-Stokes (CFD code)
UMARC	University of Maryland advanced rotorcraft code

Subscripts and Superscripts

0	initial value or zero perturbation value
∞	refers to free-stream
c	circulatory part
f	flap component
m	pitching moment component
l	lift force component
nc	noncirculatory part
α	angle of attack component
δ	flap deflection component

Chapter 1

Introduction

1.1   Background

Helicopters are one of man's most fascinating inventions. Although not as widely used as their fixed-wing counterparts, rotary-wing aircraft have an important role in air transportation for both civilian and military applications. Because of their unique ability to hover, helicopters can operate in a wide range of flight conditions where fixed-wing airplanes would be ineffective. Although fixed-wing aircraft are usually faster, aerodynamically simpler and more efficient, they require a high forward velocity to generate the aerodynamic forces required to sustain them in flight.

As a result, they cannot hover or remain airborne at very low speed. For this reason, many important missions like search-and-rescue simply cannot be performed with fixed-wing aircraft. Another advantage of the helicopter is that it does not require a runway to take off. This makes it possible to operate the helicopter in places that do not accommodate a large landing/takeoff area. This makes helicopters the preferred option for intra-city transportation, operations in rugged terrain, crowded cities, etc. Rotorcraft and fixed-wing aircraft, therefore, play complementary roles in catering to different air transportation requirements.

Today, helicopters play a critical role in a wide range of applications rang-

ing from military rescue operations to personal transportation. Advancement in rotorcraft technology is particularly important for maintaining superiority in the battlefield and is of strategic importance from a military perspective. While several decades have elapsed since the first helicopter, and billions of dollars of research has been invested in rotorcraft technology, the basic design of the helicopter has remained more or less unchanged.

1.1.1   Primary Control Using Swashplate

A helicopter consists of a main rotor with a tail rotor to balance the main rotor torque. And the main rotor is controlled using a swashplate in almost all helicopters. In the 1920's, Hafner (Ref. 1) became one of the first to use the swashplate in the form known today. Over the years, the swashplate became the default approach for producing cyclic pitch. The swashplate system consists of two plates, one fixed (below) and the other rotating (above) which are connected by a set of bearings between the two plates (see Fig. 1.1). The rotating plate rotates with the drive shaft and the rotor blades, and the control rods attached to it directly control blade pitch. The pitch inputs affect the control rods of the fixed plate. The vertical position and horizontal tilt of the fixed plate determine the blade collective and cyclic responses, respectively. Typically, the pitch collective and cyclic inputs are transmitted through hydraulic actuators in the fixed frame which move the fixed plate, forcing the rotating plate to move similarly. This system has been the predominant method for helicopter primary control without major alteration since the
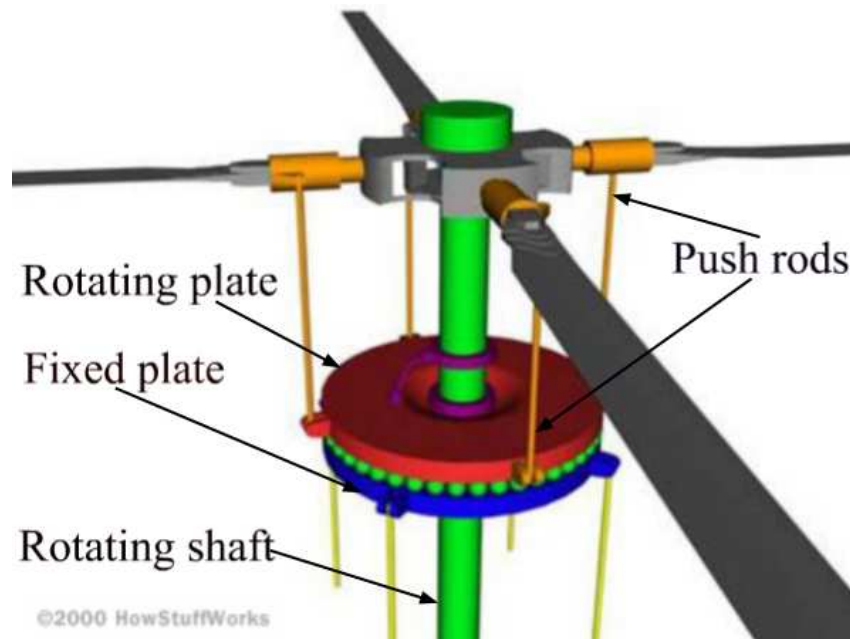
Figure 1.1: Schematic of swashplate (Source: www.howstuffworks.com)

inception of the first controllable helicopter.

However, despite its reliability, the swashplate system is not without drawbacks. Some of these are:

- The high part count, complexity and weight of the swashplate (see Fig. 1.2) lead to higher maintenance costs.

- The need for heavy and complex hydraulic systems to actuate the swashplate results in a significant weight and cost penalty.

- The rotor blade and hub attachments may account for up to 30–50% of the total parasitic drag on fully articulated designs (Refs. 2,3, 4).

Despite the widespread use of the swashplate concept, alternate (*swashplate-less*) approaches for helicopter primary control have been considered.

Figure 1.2: Example of swashplate with many parts (Source: www.fightercontrol.co.uk).

1.1.2 Swashplateless Rotor Concept

Swashplateless rotors typically use an external airfoil surface or an integrated trailing edge flap (TEF) to control the rotor instead of a swashplate. Figure 1.3 shows a rotor with an external airfoil control surface. In the integrated TEF approach, on the other hand, the flap is built into the body of the rotor (see Fig. 1.4), with the flap formed from the rear portion of the airfoil. Figure 1.5 shows a 2D schematic of the integrated TEF airfoil.

Because there is no pitch link to directly control the blade pitch, the blade pitch is controlled indirectly in a swashplateless rotor by adjusting the TEF (or external airfoil control surface). The TEF (or external airfoil control surface) can be used as a *lift flap* or *moment flap*. Although the following description of the swashplateless mechanism is provided for an integrated TEF, the same principle is

(a) Overall view of Kaman's K-MAX helicopter

(b) Closeup view of rotor blade

Figure 1.3: Kaman's rotor with external airfoil control surface for primary control (Source: airliners.net)
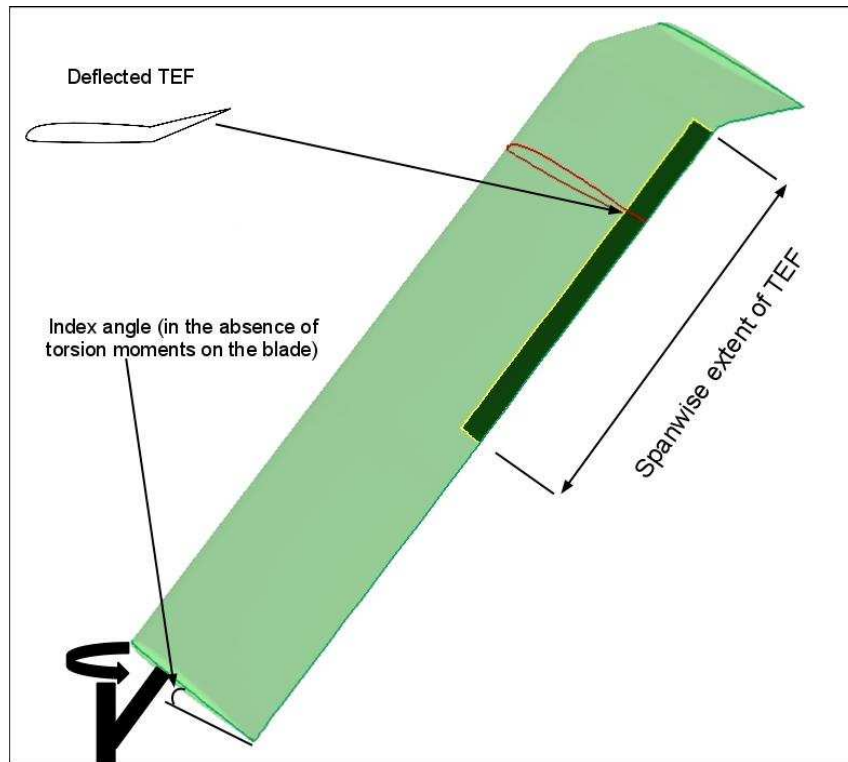
Figure 1.4: Swashplateless rotor.
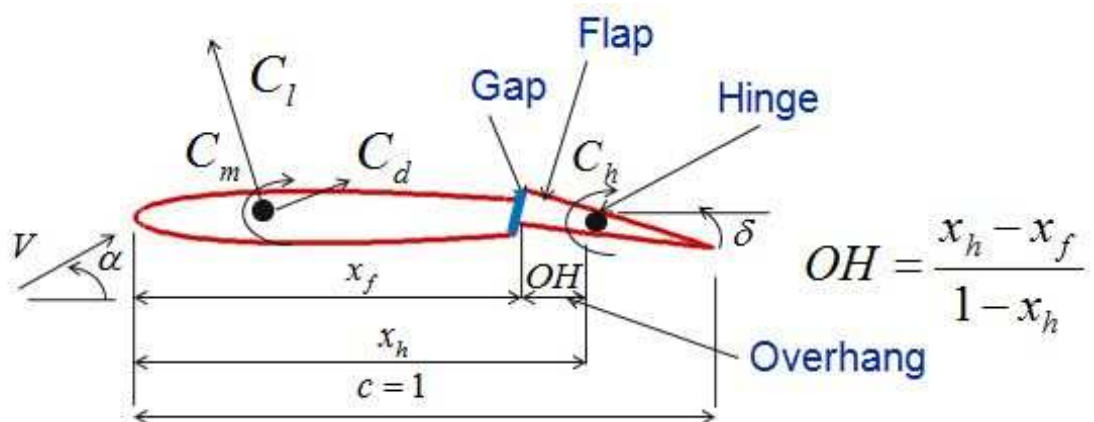
Figure 1.5: Schematic of integrated TEF airfoil.

valid for an external airfoil control surface as well. In a "lift flap," blade control is achieved by using the TEF to produce a change in lift, which in turn changes the blades flap response, thereby generating the forces required to control the rotor.

In the present work, the lift flap is not considered and only the "moment flap" is investigated.

In a moment flap, blade control is achieved by using the TEF to produce a pitching moment that torsionally deforms the blade to generate the forces required to control the rotor. The blade is allowed to deform about the *index angle*, which is defined as the angle of the blade root in the absence of torsional moments at the root (see Fig. 1.4). To produce the blade deformation required to control the rotor, the blade has to be torsionally soft. The rotating natural frequency for torsion mode (ν_θ) is much lower for a moment flap based swashplateless rotor than for a conventional (swashplate) rotor ($\nu_\theta \approx 2$ for swashplateless rotor as opposed to $\nu_\theta \approx$ 5–10 for a conventional rotor). Therefore, even a small change in pitching moment produced by deflecting the TEF is enough to deform the blade torsionally to produce the required change in effective blade pitch.
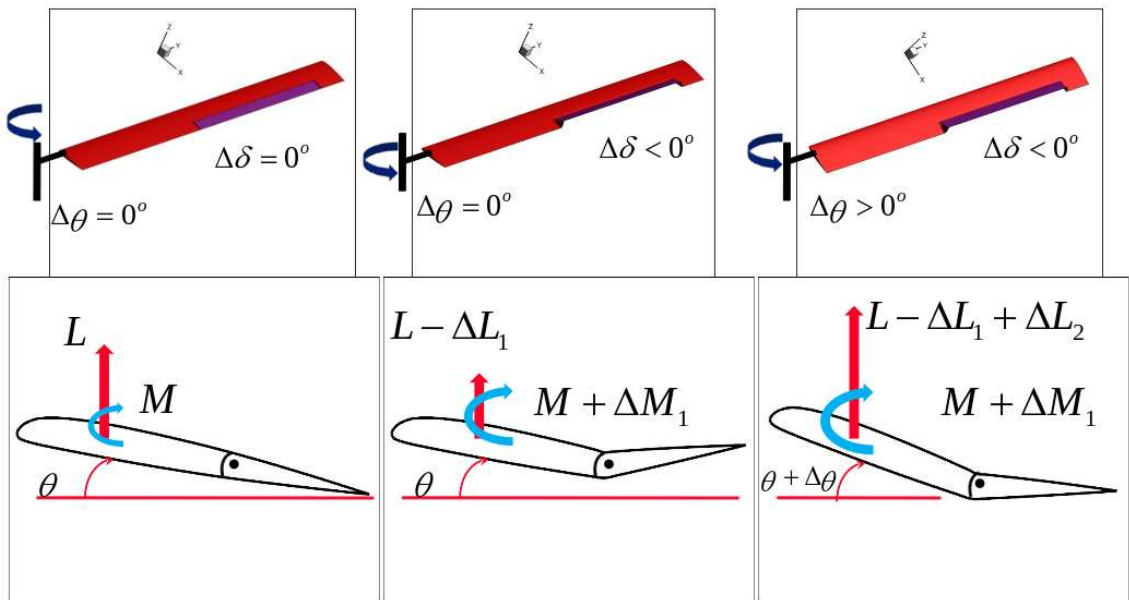
Figure 1.6: Mechanism of primary control using a moment flap.

Figure 1.6 illustrates in more detail the mechanism by which the moment flap operates. It shows a swashplateless TEF rotor with an undeflected TEF and the effect of deflecting the TEF upward. A positive TEF deflection angle (i.e., downward) produces a nose-down pitching moment at the quarter chord, while a negative TEF deflection angle (i.e., upward) produces a nose-up pitching moment. Using this principle, the blade can be deformed torsionally using the change in pitching moment produced by deflecting the TEF. The change in effective blade pitch in turn changes the overall lift distribution over the rotor. For example, to increase the lift produced by the rotor, the TEF is deflected upward. This causes an increase in the nose-up pitching moment and a decrease in the lift in the portion of the rotor where the flap is present (see Fig. 1.6). However, because of the torsionally soft nature of the swashplateless rotor, the increase in pitching moment causes the blade to twist elastically and increase the blade pitch. The increase in blade pitch results in a net increase in the lift. This means that although the immediate aerodynamic response of the blade to an upward deflection of the TEF is a decrease in lift, because of the blades structural response to the change in pitching moment, the final aerodynamic effect is an increase in total lift.

Although, swashplateless rotors are not common today, they have been considered from the earliest days of helicopter development. In 1930, Corradino d'Ascanio (Ref. 4) was among the first to come up with the idea of using trailing edge servo-tabs on the rotor blades. Kaman Aerospace started using the servo-flap mechanism on its helicopters (see Fig. 1.3) in the late 1940's and continue to use the concept even to this day. The servo-flap based swashplateless design had the following advantages

8

over the conventional swashplate design:

- The larger control arm between the blade feathering axis and the flap coupled with the fact that the blade is torsionally soft, means that the control forces required to twist the blade are small. The reduction in control forces eliminates or minimizes the need for hydraulic actuation, leading to significant weight and cost benefits.

- The absence of complex swashplate system leads to a cleaner hub, leading to significant reductions in drag and maintenance costs. Because the hub drag constitutes about 35% of the total parasitic drag of the helicopter (Ref. 4), this could potentially lead to significant performance benefits.

Although the external flap provides a greater moment arm, it involves exposed linkages and actuation mechanisms that incur a significant drag penalty. The power penalty incurred because of this is often unacceptable, especially for next generation rotorcraft. The use of integrated trailing edge flaps (TEF) is one possible solution to this problem. This retains the advantages of a swashplateless rotor while eliminating the high profile drags associated with external airfoil control surfaces.

The use of integrated TEFs also has its own challenges, particularly with regard to effectively actuating the TEFs. Some approaches for actuating the TEF are described in a later section. Although, the integrated TEF concept has recently received a lot of attention in the rotorcraft community as a mechanism for primary control, they have long been investigated for use on helicopter rotors for *active control.*

1.1.3 Active Controls

Active control methods supply optimally timed and phased aerodynamic inputs to the vehicle system to reduce one or more target loads. The two major types of active control methods for rotorcraft are *Higher Harmonic Control* (HHC) and *Individual Blade Control* (IBC). In HHC, small blade pitch inputs are added on top of the primary control inputs in the fixed frame. HHC uses frequencies higher than 1/rev and typically applies these using the existing swashplate. Studies have shown that HHC could increase the maximum forward flight speed by delaying the retreating blade stall limit (Refs. 5,6,7) as well as reduce the induced power (Ref. 8).

In IBC, the blade control mechanisms are located in the rotating frame and this leads to a reduction in weight as well as actuation power requirements. The ability to operate at different frequencies for different blades makes it possible to achieve several goals as well as operate with dissimilar blades. The different IBC methods can be classified into three broad categories: blade pitch, blade twist and active airfoils.

Active airfoil methods are typically known to have much lower actuation power than either pitch link or active twist based concepts. They involve the use of an active component in the airfoil that changes the aerodynamic environment and causes the blade to pitch indirectly. Examples include hinged TEFs, active camber control and conformable airfoils. In particular, the use of TEFs has received a lot of attention as a mechanism for vibration and noise reduction.

1.1.4 TEFs for Vibration and Noise Reduction

A detailed study of the flap concept was carried out in the 1970's when the Multicyclic Controllable Twist Rotor (MCTR) was designed, tested and analyzed in a joint Kaman Aerospace-US government project (Refs. 9,10,11,12). Although the study demonstrated a reduction in blade loads, the complexity and weight of the multi-control systems made the concept unattractive. However, with the advent of smart actuators with low power requirements and high bandwidth, the concept has received renewed interest. Because the actuators are now small enough to fit inside the blade profile, plain flaps become a practical alternative to servo-flaps, thereby leading to reductions in drag from the elimination of exposed linkages and gaps. The DARPA sponsored Smart Material Actuated Rotor Technology (SMART) program (Refs. 13, 14) lead to the development of smart actuators, experimental rotor tests and computational studies. This work showed that the flaps could produce the forces required for vibration reduction in forward flight. Preliminary reports also suggested that measured noise was reduced by up to 50%. The research into the use of TEFs for vibration control and noise reduction also lead to investigation of the TEF concept as a mechanism for primary control.

1.2 Motivation

In the present study, use of integrated TEFs is evaluated as a mechanism for primary control for realizing the swashplateless rotor concept. Analytical, CFD (Computational Fluid Dynamics) and coupled CFD-CSD analysis/simulations are

performed for studying the problem. This is necessary, because despite the potential advantages of using a TEF to control the rotor, additional aerodynamic and aeroelastic analysis is required to generate confidence in the TEF based swashplateless rotor concept and its potential performance benefits.

Some of the aerodynamic issues of interest that are associated with TEFs are: flow separation, transonic effects, stall and flap effectiveness. In addition the aeroelastic behavior of swashplateless rotors is different from that of conventional rotors. For an otherwise similar rotor blade at a given thrust setting, the blade pitch and deformations would be different for a conventional and swashplateless rotor. These in turn would affect the pressure distribution, performance and wake structure. Understanding these in more detail would be useful in designing better swashplateless rotor systems.

Trailing edge flaps (TEFs) used for primary must deflect more (by a factor of ≈ 3–4) than those used for vibration control and noise reduction. Higher amplitudes mean that the rotor airloads and wake flow-field are likely to be affected to a greater extent than in vibration and noise reduction applications. The discontinuities in lift and geometry that arise at the spanwise edges of the TEF be significant in a swashplateless rotor (because of the higher flap deflection amplitudes) and could lead to trailed vortices and induced drag. Therefore, is important to understand the extent to which the aforementioned factors would affect the wake and performance of the rotor.

An important aspect of the TEF design is the overhang (see Fig. 1.5), which is a measure of the offset of the flap hinge from the leading edge of the flap. An overhang

is used to reduce the hinge moment (Ref. 15) and hence the actuation power required to control the TEF. The protrusion of the flap leading edge because of overhang is likely to induce greater flow separation and possibly even shock formation (in transonic flows). Trailing edge flaps are also known to affect dynamic stall behavior (Refs. 16). Furthermore, although the presence of gaps (see Fig. 1.5) is not intended in the design, there is usually some flow leakage along the chordwise and spanwise edges of the TEF. Flow through these gaps could induce greater spanwise flow and flow separation that could degrade flap effectiveness – particularly in generating pitching moments. The presence of trailing edge flaps on the rotor for primary control could significantly affect the wake. Therefore, understanding these effects would prove useful both from a design as well as from a modeling perspective.

The swashplateless rotor concept has been studied using linear aerodynamics (Refs. 17, 18, 19). CFD has been used for studying vibration control (Ref. 20) and noise reduction (Ref. 21) for rotors with TEFs. However the use of CFD for studying swashplateless rotors with TEFs has not been done before. Also, it is important to correctly model the interaction between the aerodynamic and structural loads because the swashplateless rotor concept relies heavily on this coupling to control the rotor.

To address all the aforementioned concerns, it is important to perform a detailed study the aerodynamics of both 2D TEF airfoils and 3D swashplateless rotors.

1.3   Objectives

The objectives of the present work can be broadly classified into two categories:

1. Develop high fidelity tools able to study the detailed aerodynamics of TEF airfoils/rotors.

2. Apply these tools to understand the detailed aerodynamics and detailed flow field of TEF rotors along with their aerodynamic performance.

1.3.1   Tool Development/Implementation

A variety of tools are needed to understand the aerodynamics of TEF rotors:

2D Aerodynamics: The first step in understanding the aerodynamics of TEFs is to study the 2D aerodynamic behavior of airfoils with TEFs. Specifically, there is a need to:

1. Implement steady and unsteady aerodynamic models to predict the aerodynamics of TEF airfoils. This would prove useful in quick design calculations as well as for use in comprehensive rotor analysis codes.

2. Generate lookup tables for different airfoils that can be used in comprehensive rotor analysis codes for studying the behavior of swashplateless rotors.

3. Implement efficient and robust hole cutting strategies for overset grids for modeling the effect of gaps at the leading edge of a TEF. The present

work models the effect of the gap using both direct grid-based modeling of the flow through the gap as well as through approximate techniques.

3D Aerodynamics: So far CFD has not been used to study the aerodynamics of swashplateless rotors for primary control. The present work therefore aims to:

- Develop a framework for studying uncoupled CFD and coupled CFD-CSD simulations for swashplateless rotors by extending existing CFD-CSD coupling strategies available for conventional rotors.

- Model the effect of chordwise and spanwise gaps at the edges of the TEF.

1.3.2 Application

Once the tools for 2D and 3D analysis have been developed, they can be used to study specific aspects of the aerodynamics of TEF airfoils/rotors.

2D Simulations: The 2D aerodynamics of TEFs involves analyzing the effect of various blade properties as well as understanding the aerodynamic phenomena associated with TEFs.

1. Blade properties include flap size, airfoil thickness, overhang, gap, etc. These are varied for a range of flow conditions and their effect on the resulting TEF aerodynamics is studied.

2. Besides airfoil properties, it is also important to understand the various aerodynamic phenomena such as compressibility, flow separation and

vortex shedding associated with TEFs. These can be used as the basis for better decisions when designing swashplateless rotors.

3D Simulations: The present work investigates the following aspects of the swash-plateless rotor:

1. Compare the airloads and wake behavior of baseline and swashplateless rotors.

2. Compare the performance of baseline and swashplateless rotors for a range of thrusts.

3. Study the effect of gap on the performance of swashplateless rotors.

1.4 Previous Work

The present study on swashplateless rotor intersects with several earlier studies on various topics. This section looks into the previous work in some of the key areas that are investigated in this thesis.

1.4.1 Analytical Modeling

Analytical models can provide first order estimates of the steady and unsteady airloads for a TEF airfoil. The estimates of the lift, pitching moment and hinge moments can be obtained using thin airfoil theory as well as using linear aerodynamic modeling. Although analytical models do not take into account the nonlinear effects and are limited in their predictive capability, they are indispensable for design and

analysis because of their ability to provide immediate, first-order estimates of the behavior under a wide range of conditions. The aerodynamics of TEF airfoils can be split into steady and unsteady aerodynamics. Steady aerodynamics of TEFs can be obtained from thin airfoil theory. This is briefly described in Chapter 2.

Modeling the unsteady airloads is relatively more challenging (see Fig. 1.7). Such lower order models offer at least three or four orders of magnitude reduction in computational time over direct CFD solutions. The low computational cost them makes them highly suitable for use in routine rotor analysis, if their use can be properly justified. Over the years, several investigators have developed models for predicting the unsteady airloads on an airfoil operating in different modes of unsteady behavior such as variations in angle of attack, plunging motion, free-stream velocity, gusts, vortex, etc. The unsteady solutions can be obtained in the frequency domain or time domain. Frequency domain solutions assume periodic forcing and are particularly useful for obtaining a theoretical understanding of the behavior of a system. However, the unsteady environment of a helicopter is rarely periodic, often with no apriori knowledge of the unsteady motion of the system. For these cases, a time-domain representation of the unsteady problem is more useful. Here, the unsteady behavior is broken down into step (indicial) changes and the response of the system at any particular instant is obtained by convolution.

Exact solutions for a periodically oscillating or plunging airfoil (i.e., frequency domain solution) in a steady, incompressible free-stream flow was first obtained by Theodorsen (Ref. 22) while the corresponding time-domain solution was obtained by Wagner (Ref. 23). The problem of non-steady free-stream velocity fluctuations,
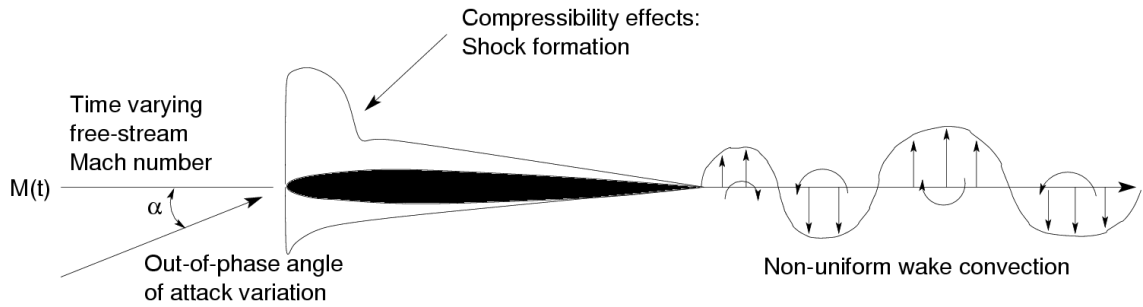
Figure 1.7: Airfoil in unsteady Flow.

such as those found at the blade element of a helicopter rotor, raises considerably the complexity of the problem. This is mainly because of the nonuniform convection velocity of the downstream wake. Nevertheless, solutions for the additional effects of unsteady free-stream were given by Greenberg (Ref. 24) and Kottapalli (Ref. 25). However, these theories make certain simplifying assumptions that restrict their range of validity to low free-stream velocity amplitudes. This is not useful for helicopter problems. A more comprehensive theory was given by Isaacs (Ref. 26). However, Isaacs model has certain practical limitations because the solution is expressed in the frequency domain. This makes it difficult to implement it for arbitrary types of forcing (angle of attack and Mach number). A time domain solution for arbitrary variations in pitch angle and free-stream velocity was developed by Van der Wall & Leishman (Ref. 27).

However, the aforementioned incompressible flow models would be ineffective at the higher subsonic Mach numbers encountered at the outboard sections of a helicopter rotor. For compressible flows, the pressure disturbances travel at a finite speed and there are greater lags in the aerodynamic response compared to incompressible flow. The issues of modeling compressibility effects on unsteady airfoil

18

behavior using linear indicial theory has been studied for many years, first by Mazelsky, Beddoes, Lomax and others (Refs. 28,29,30,31,32,33). and then by Leishman and co-workers (Refs. 34,35,36,37,38,39,40). Efficient mathematical models have been developed to determine the forces acting on an airfoil undergoing oscillations in angle of attack and plunge motion at constant Mach number.

An unsteady aerodynamic model for an airfoil with trailing edge flap in incompressible flow was developed in the frequency domain by Theodorsen (Ref. 41) and in the time domain for incompressible/compressible flows by Hariharan & Leishman (Ref. 36).

1.4.2 Trailing Edge Flaps and Swashplateless Rotors

Since swashplateless rotors with TEFs is the primary focus of this thesis, it is important to understand previous studies that have been done in this area.

1.4.2.1 Trailing Edge Flaps

Extensive experimental studies have been performed on NACA0009 airfoils with flap and tab by Ames (Ref. 42) and Street (Ref. 43) as early as the 1930's. These were performed primarily for steady low subsonic flows and were aimed at obtaining a fundamental understanding of the resulting pressure distributions and aerodynamic parameters for a flap-tab system. More recently, Hassan, Straub and Noonan (Ref. 15) performed extensive tests, both subsonic and transonic, for the flapped HH-06 and HH-09 airfoils. The study was performed in the context of

rotorcraft applications and provided data for TEFs with overhang.

The use of TEFs on rotors has been studied by several investigators particularly in the context of noise reduction and vibration control. Milgram and Chopra (Ref. 44, 45) modeled the TEF as a potential means of vibration reduction using comprehensive rotor analysis. Roget and Chopra (Ref. 46, 47) developed real time adaptive control schemes for helicopter hub vertical vibration reduction using on-blade trailing edge flaps.

Liu and Friedmann (Ref. 48) performed 2D unsteady CFD simulations as well as lower order aerodynamic modeling for an oscillating TEF. The TEF used in their study involved zero overhang. A gap was modeled at the leading edge of the TEF by using multiple grids. The simulations were carried out for a wide range of angles of attack, flap deflection amplitudes, reduced frequencies and Mach numbers.

1.4.2.2 Swashplateless Rotor

As mentioned previously, the use of TEFs as a mechanism for primary control of a helicopter rotor has received much attention in recent years. Several investigators have performed analytical studies based on linear aerodynamic theory and/or lookup tables to understand the behavior of the swashplateless rotors.

Ormiston (Ref. 17) conducted a feasibility study on the use of integrated TEFs for primary control. This study assumed rigid blades, quasi-steady thin airfoil theory and uniform inflow to perform its analysis. The study concluded that with respect to basic aeroelastic response characteristics, on-blade elevon (flap) control surfaces

20

have the potential to provide sufficient elevon collective and cyclic pitch control effectiveness to satisfy general requirements for primary flight control. The choice of an appropriate index angle for the swashplateless TEF rotor was shown to be important for making it possible to generate the range of pitch angles required to control the rotor. If an appropriate index angle is not chosen, the TEF amplitudes required to generate the required blade pitch amplitudes may be too high.

Shen and Chopra (Ref. 18) developed a comprehensive aeroelastic model to study primary control using TEFs for a typical bearingless rotor and an ultralight teetering rotor. The study identified the key parameters of the TEF system for primary control as blade pitch angle, torsional frequency, flap length and flap overhang length. The swashplateless TEF rotor was seen to achieve better rotor performance than the conventional configuration. The study also showed that TEFs are capable of trimming the rotor and simultaneously minimizing vibratory rotor hub loads. However, it must be noted that the aerodynamic model relied on thin airfoil theory and limited wind tunnel data and, therefore, the airloads predictions, especially drag, may not be accurate.

Falls and Chopra (Ref. 19,49,50) conducted experimental studies as well as comprehensive analysis of the trailing edge flap-tab concept as a mechanism for primary control. In the flap-tab concept, the flap itself is actuated indirectly by actuating a tab, which spans a portion of the flap (see Fig. 1.8). The study showed that a swashplateless rotor with flap-tab could be trimmed across a range of forward flight speeds. The study also showed significant reductions in parasitic drag and moderate reduction in the required power at hover and low forward speeds. Although
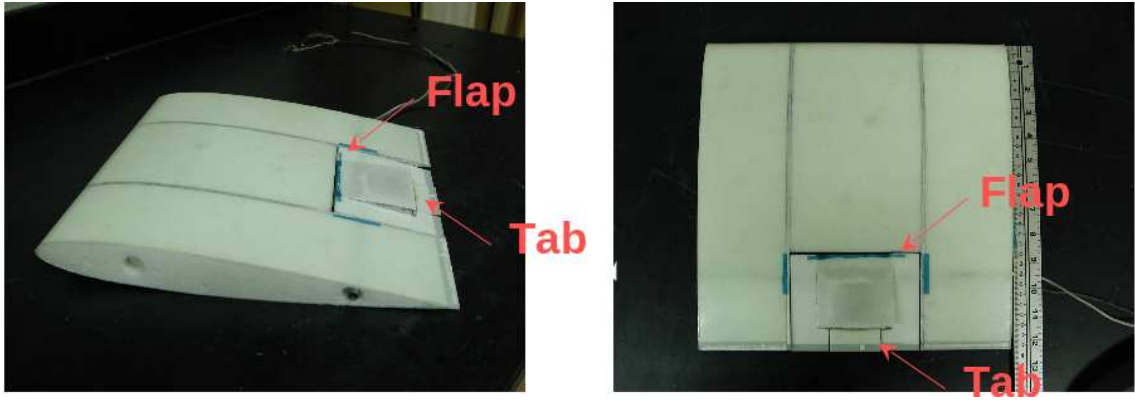
Figure 1.8: Flap-tab experimental setup by Falls, et al. (Ref. 50).

this study involved the use of more detailed lookup tables derived from steady CFD data, the predictive capability of an aerodynamic model based on a lookup table is limited and prone to error, especially when dealing with nonlinear phenomena such as flow separation, transonic effects and vortex interactions.

Sekula et al. (Ref. 51) performed an analytical study to examine the feasibility of a swashplateless rotor controlled using two TEFs, where the cyclic and collective controls are provided by separate TEFs. Based on an investigation of steady, forward and turning flight analyses, it was observed that a two-TEF swashplateless rotor where the outboard flap provides cyclic control and the inboard flap provides collective control can reduce TEF deflection requirements without a significant impact on power compared to a single flap system.

One important aspect of the swashplateless TEF rotor design is the actuation of the flaps. Actuation is particularly challenging for the integrated trailing edge flaps where the flap actuation mechanism has to be concealed within the rotor and must, therefore, be compact.

Shen and Chopra (Ref. 52) were among the first to perform detailed analysis of the actuation requirements for a swashplateless TEF rotor control system. A comprehensive rotorcraft analysis based on UMARC was developed for the swashplateless rotor configuration and the actuation requirements for primary control with TEFs was examined.

Fulton and Ormiston (Ref. 53) performed tests on a small-scale rotor with on-blade elevons. Their study looked into issues such as feasibility of using piezoceramic bimorph actuators, effects of low Reynolds numbers on elevon pitching moments, elevon reversal, etc.

More recently, Duling, Gandhi and Straub (Ref. 54) have studied the actuation requirements for a TEF based swashplateless rotor. The study looked at a swashplateless TEF rotor based on the baseline UH-60 rotor with a modified rotor torsion frequency of 2.1/rev. The results showed that the power penalty associated with TEF enabled primary control at high speeds is in the range of 6–7% (due to increased drag on the advancing side in the region of the TEFs and at the blade tips) and in the range of 2–4% at low and moderate speeds (from a drag increase over most of the azimuth in the region of the TEFs).

Over the years several actuation mechanisms have been considered for the swashplateless TEF rotor. The use of piezobimorph bender to actuate the TEF has been explored extensively by Chopra and co-workers (Ref. 55–59). Alternate mechanisms for actuating the TEFs on a swashplateless rotor have also been examined. For example Saxena and Chopra (Ref. 60) have explored the use of a compact brushless motor to actuate the flaps, Shaju et al. (Ref. 61) have looked into the use

of a piezohydraulic active pitch link while Furst and co-workers (Ref. 62, 63) have looked into the use of electro-mechanical actuators for swashplateless rotors.

1.4.3 Coupled CFD-CSD Simulations

Over the years computational tools to simulate the behavior of rotor systems have evolved greatly. The advent of comprehensive rotor analysis codes has helped greatly in predicting the behavior of rotors for different flight conditions. Most comprehensive rotor analysis codes rely on linear aerodynamic theory or lookup tables to provide an estimate of the rotor airloads during trim calculations. However, while these provide first order approximations, there are limitations because of their inability to capture 3D nonlinear effects encountered by the helicopter rotor. The mutual interaction of the structural and aerodynamic loads adds additional complexity to the problem.

Potentially, CFD has the capability for producing more accurate predictions of the airloads in the presence of 3D nonlinear phenomena. However, CFD is computationally several orders of magnitude more expensive than linear aerodynamic models. Therefore, using CFD airloads in the same manner as the linear aerodynamic models within the trim calculations is not necessarily practical. Also, CFD codes are usually developed independent of the rotor analysis codes and efficient strategies need to be developed to effectively couple the CFD and CSD (computational structural dynamics) components of the analysis. With the increasing availability of computational power over the past decade, coupling CFD with CSD has become feasible

and several investigators have modeled rotorcraft problems using this approach.

CFD-CSD coupling can be done in two ways for rotorcraft problems – *tight coupling* or *loose coupling*. In tight coupling, the airloads and blade deformations are exchanged between CFD and CSD codes at every time step. It is, therefore, the most accurate form of solution possible. However, it is computationally expensive and involves challenges in rotor trim, efficient process communication and maintaining time-wise accuracy between the CFD and CSD codes. In loose coupling, on the other hand, the structural and aerodynamic loads are exchanged only after atleast one rotor revolution and are assumed to be periodic. It is less rigorous than the tight coupling approach but is simpler to trim.

Altmikus (Ref. 64) compared the two coupling approaches and showed that both tight coupling and loose coupling produce the same airloads predictions for the same trim state. However, to reach the trim state, the tight coupling scheme required 2.5 times more computational cost compared to loose coupling. In the present work only the loose coupling strategy is used to study the swashplateless rotor problem.

The loose coupling strategy used in the present work uses the method proposed by Tung, et al. (Ref. 65). In the original study by Tung, the aerodynamic component involved the use of a 3D conservative formulation of the full potential equation. A 'split potential' formulation was used to incorporate known vorticity fields into the full-potential calculation to model the rotor-wake contributions.

Loose coupling using inviscid (Euler) codes was first performed by Servera (Ref. 66) and co-workers. They looked at the CFD-CSD modeling of flexible rotors

using the HOST (Helicopter Overall Simulation Tool) aerodynamic and WAVES (Without Artificial Viscosity Euler Solver) dynamics codes. The study showed improvements (over the simplified aerodynamics) in the pitching moment and torsion predictions but the integrated global parameters were not better predicted. Pahlke et al. (Ref. 67) were the first to perform loose coupling using a Navier-Stokes solver. Currently, CFD-CSD loose coupling based on Navier-Stokes solvers is a powerful tool used by several researchers for rotor analysis (Refs. 68, 69, 70, 71, 72).

1.4.4 Overset Structured Grids

The use of overset grids is very useful for treating problems involving relative motion between body components. Even where moving body components are not involved they are often the preferred approach when meshes with different topologies, refinement and/or alignment are used in the same computational region. They make it easier to model flows involving complex geometries or when there is a need to capture flow features in specific regions of the flow. The present work uses overset grids for 3D rotor simulations and for treating the TEF gaps in 2D flows.

The idea of using overset structured grids can be dated back to Steger, et al. (Ref. 73). Some of the traditional domain connectivity methods are listed in Ref. 74. Some of the well known structured grid connectivity codes are DCF3D (Domain Connectivity Functions in Three Dimensions; Ref. 75), Overture (Refs. 76, 77), PEGASUS (Ref. 78), BEGGAR (Ref. 79), ChalMesh (Ref. 80), Xcog (Ref. 81), DIRTLib (Donor Interpolation Receptor Transaction Library; Ref. 82), SUGGAR

(Structured Unstructured Generalized Overset Grid Assembler; Ref. 83), FASTRAN (Ref. 84), etc.

One common feature of the traditional methods is to use walls to cut "holes" in the overlapping meshes (see Chapter 2 for more details). Lee and Baeder (Ref. 85) were the first to develop an approach known as the Implicit Hole Cutting (IHC) method for establishing grid connectivity. This provided a more generic approach to grid connectivity that was both simple and effective in producing good hole cutting. More details about the traditional and IHC methods are provided in Chapter 2.

Lee's ideas have been further improved/extended by researchers from the University of Maryland, particularly by Lakshminarayan (Ref. 86) and Sitaraman (Ref. 87). More recently, Liao (Ref. 88) et al. have extended Lee's code to implement a parallel multigrid solver for overset grids within a hybrid multi-block framework. The present work adapts the implicit hole cutting (IHC) code developed by Lee and later modified by Lakshminarayan for handling body penetrating grids such as those encountered when modeling the gap at the leading edge of a trailing edge flap.

1.5   Outline of the Thesis

The material in this thesis is organized into four additional chapters. Chapter 2 talks about the analytical and computational approaches used to study the swash-plateless rotor problem. The steady and unsteady analytical models for predicting airloads on a TEF airfoil are first described. Because drag is an important aerody-namic parameter that cannot be analytically predicted, a semi-analytical approach

is described to estimate the steady drag for TEFs. Next, the various approaches used for modeling gaps for 2D flows are described. This includes a detailed description of the implicit hole cutting technique (IHC) used in the present work for establishing grid connectivity between overset grids. Lastly, the details of the 3D aerodynamic modeling of rotors, such as solver, mesh system, gap averaging, are outlined.

Chapter 3 discusses the 2D aerodynamics of TEFs. The 2D CFD code is first validated using experimental data for the HH-06 airfoil. The effect of airfoil parameters such as overhang and airfoil thickness are investigated. The effect of gaps at the leading edge of the flap is also studied. The effect of the gap is modeled using patched meshes, overset meshes and the gap averaging technique. The results obtained using the different approaches are compared and the merits and limitations of each are identified. Steady results are shown for a wide range of parameters such as angle of attack, flap deflection and Mach number. The flow phenomena associated with TEF airfoils is studied.

Chapter 4 looks at 3D aerodynamics of rotors in hover. Results are obtained for both uncoupled CFD as well as coupled CFD-CSD calculations. The code is validated using experimental data for the baseline (no TEF) UH-60 rotor in hover. Computational results are obtained for the baseline UH-60 rotor as well as for a swashplateless TEF rotor based on the UH-60 rotor. The airloads, wake and performance of these rotors is studied. Lastly, the effect of gaps on the performance of swashplateless TEF rotors is investigated.

Chapter 5 summarizes the work done in this thesis. The important conclusions

are outlined and possible areas for future work are identified.

Overall the thesis provides useful insights into the aerodynamics of trailing edge flap airfoils and rotors and expands the current understanding of swashplateless TEF rotors.

Chapter 2

Methodology

This chapter discusses the theory, algorithms and other implementation details associated with various aspects of this work. First, the 2D steady and unsteady thin airfoil theory based aerodynamic models are discussed. Next, the 2D CFD solver and grid generation details are described. This is followed by a detailed description of the treatment of overset grids, and particularly on the Implicit Hole Cutting (IHC) technique and its application for different problems encountered in this work. The 2D section is concluded with a description of several approaches for modeling the gap at the leading edge of the flap. In the 3D section the CFD solver specifications, rotor geometry and details of the mesh system are first explained. The structural dynamics solver (UMARC) is then described. Finally, the CFD-CSD coupling strategy is discussed and the details of its implementation for the present work are explained.

2.1   Analytical Model

The analytical model uses the assumptions of thin airfoil theory and is based primarily on the work of Theodorsen (Ref. 41). Figure 2.1 shows the schematic of the problem and highlights the parameters of interest (x_f, δ, etc.). The effect of the gap is not included in the analysis.
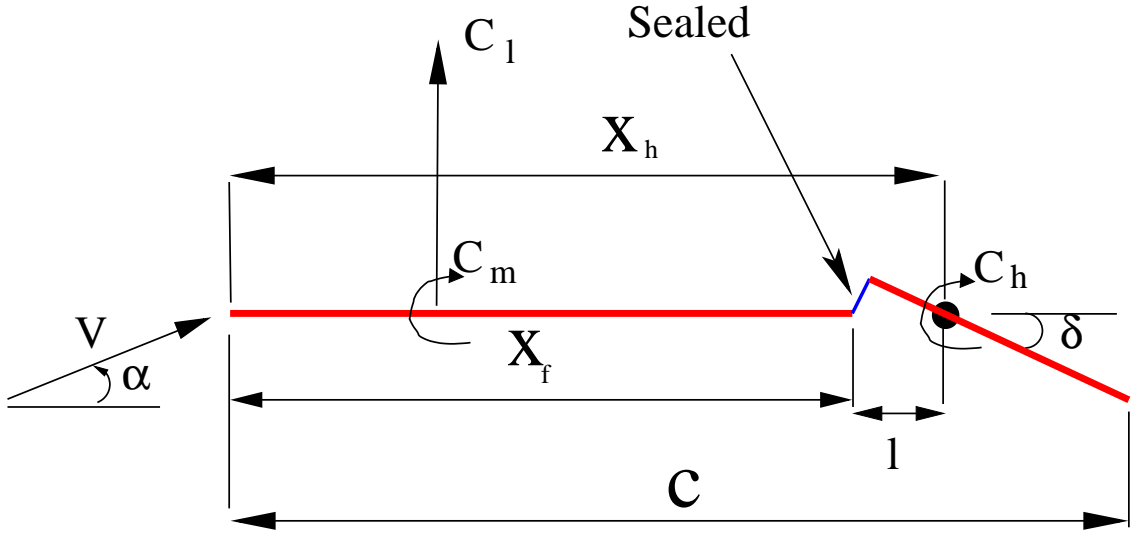
Figure 2.1: Schematic of the Trailing Edge Flap (TEF) problem.

2.1.1 Steady Thin-Airfoil Analysis

The parameters defining the steady trailing edge flap (TEF) problem are: the flap leading edge location (x_f), flap hinge location (x_h), the angle of attack (α) and flap deflections (δ). An important point to note is that, following the convention used in Ref. 41, the coordinate system in the analysis is taken to be at the mid-chord and the coordinates $(\hat{x}_f, \hat{x}_h, \text{etc.})$ are expressed in semi-chords (i.e., $\hat{x}_f = 2x_f - 1$). The primary aerodynamic quantities of interest for a TEF airfoil would be the lift, pitching moment and flap hinge moment. These can be written in the form:

$$C_l = C_{l0} + C_{l_\alpha}\alpha + C_{l_\delta}\delta \tag{2.1}$$

$$C_m = C_{m0} + C_{m_\alpha}\alpha + C_{m_\delta}\delta \tag{2.2}$$

$$C_h = C_{f0} + C_{h_\alpha}\alpha + C_{h_\delta}\delta \tag{2.3}$$

The aerodynamic parameters $(C_{l_u}, C_{m_u}$ and C_{h_u} where $u = \alpha, \delta)$ describe the aerodynamic characteristics of the airfoil under steady conditions and would be useful

31

for aeroelastic and design analysis. Within thin airfoil theory assumptions, it can be shown (Ref. 41) that for a zero-thickness airfoil (with no camber),

$$C_{l0} = 0 \tag{2.4}$$

$$C_{l_\alpha} = 2\pi \tag{2.5}$$

$$C_{l_\delta} = 2\left(T_{10}(\hat{x}_f) - lT_{21}(\hat{x}_f)\right) \tag{2.6}$$

$$C_{m0} = 0 \tag{2.7}$$

$$C_{m_\alpha} = \pi\left(a + \frac{1}{2}\right) \tag{2.8}$$

$$C_{m_\delta} = -\frac{1}{2}\left(T_{15}(\hat{x}_f) + lT_{22}(\hat{x}_f)\right) +$$
$$\left(a + \frac{1}{2}\right)\left(T_{10}(\hat{x}_f) - lT_{21}(\hat{x}_f)\right) \tag{2.9}$$

$$C_{h0} = 0 \tag{2.10}$$

$$C_{h_\alpha} = -\frac{1}{2}\left(T_{12}(\hat{x}_f) - 2lT_{20}(\hat{x}_f)\right) \tag{2.11}$$

$$C_{h_\delta} = -\frac{T_{18}(\hat{x}_f)}{2\pi} - \frac{1}{2\pi}\left(lT_{26}(\hat{x}_f) + l^2 T_{28}(\hat{x}_f)\right)$$
$$- \frac{1}{2\pi}\left(T_{12}(\hat{x}_f) - 2lT_{20}(\hat{x}_f)\right)\left(T_{10}(\hat{x}_f) - lT_{21}(\hat{x}_f)\right) \tag{2.12}$$

where $T_i(x)$ are the flap functions defined in Ref. 41 (see Appendix A); $l = \hat{x}_h - \hat{x}_f = \xi(1 - \hat{x}_h)$ is the offset of the flap hinge from the flap leading edge non-dimensionalized by semi-chord; a is the location of the pitch axis measured from mid-chord and normalized by semi-chord.

Figure 2.2 shows the variation of C_{l_δ} with flap location (x_f). It is seen that C_{l_δ} decreases monotonically from 2π (corresponding to lift curve slope for an airfoil) to zero (corresponding to zero flap size).

Figure 2.3 shows the variation of C_{m_δ} with flap location (for zero overhang).

$$C_{l_\delta} = 2(\sqrt{1 - \hat{x}^2} + \cos^{-1}\hat{x})$$

$$\hat{x} = \frac{2x}{c} - 1$$
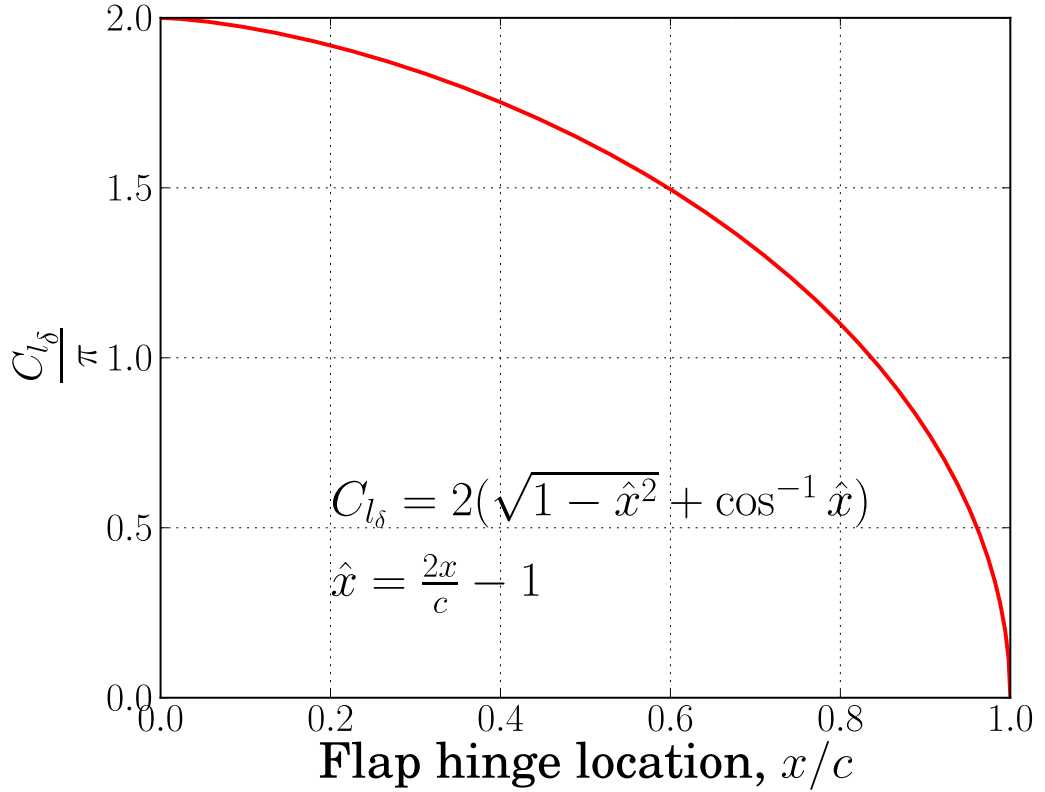
Figure 2.2: C_{l_δ} vs x_f (steady thin airfoil theory).

C_{m_δ} is negative for all flap locations. This means that a deflecting the flap downward will always produce a nose up pitching moment about the quarter-chord. Unlike the lift variation, the pitching moment about the quarter-chord first increases (in magnitude) up to $x_f = 0.75$ and then decreases rapidly. This means that for a "moment-flap" (i.e. blade control via pitching moment) pitching about the quarter-chord, the optimum flap location would be at the 3/4-chord point. However, C_{m_δ} varies only gradually in the vicinity of $x_f = 0.75$, (especially for $x_f < 0.75$). Therefore, for flap sizes varying from $0.15c$ to $0.4c$, the variation in C_{m_δ} is not too significant and other considerations may be used to determine the optimum flap size.

$$C_{m_\delta} = -\tfrac{1}{2}(1 + \hat{x})\sqrt{1 - \hat{x}^2}$$
$$\hat{x} = \tfrac{2x}{c} - 1$$
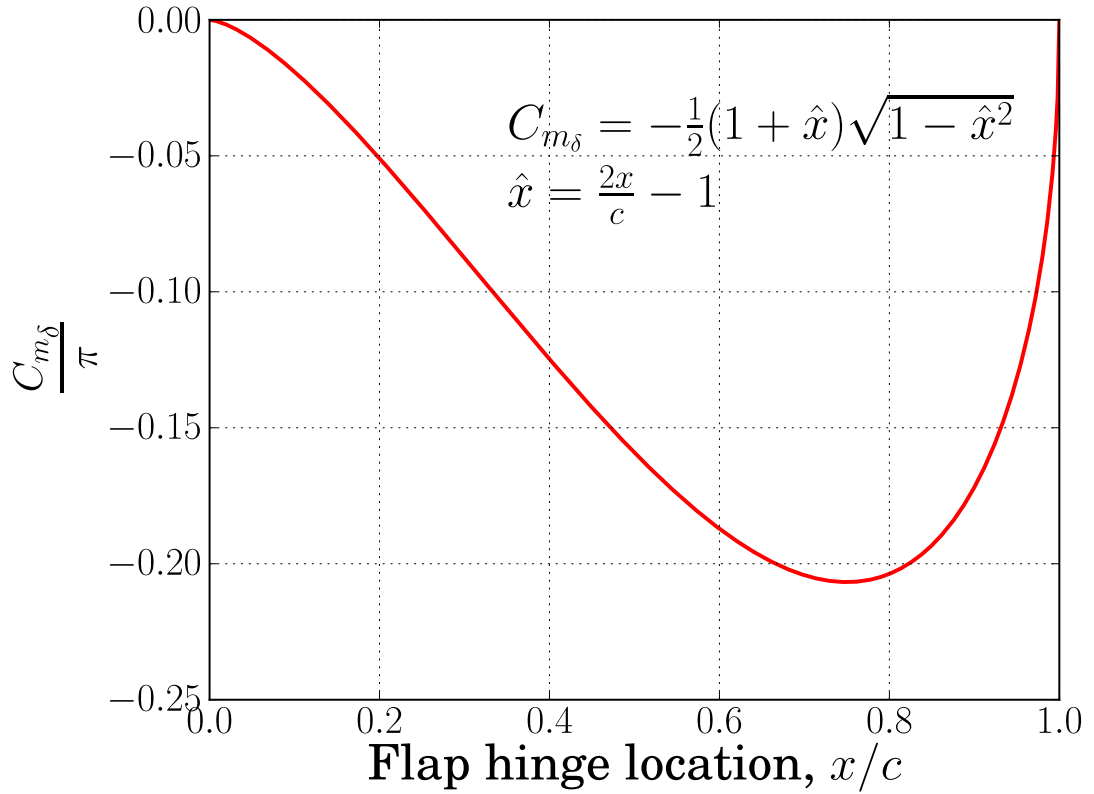
Figure 2.3: C_{m_δ} vs x_f (steady thin airfoil theory).

In a moment flap based swashplateless rotor, a positive TEF deflection (i.e., downward flap deflection) produces an *increase* in sectional lift in the portion of the blade spanned by the TEF, but also produces a nose down sectional pitching moment that tends to reduce the pitch angle at the blade root, thereby *decreasing* the overall lift across the entire blade span. Likewise, a negative TEF deflection (i.e., upward flap deflection) produces a *decrease* in lift in the portion of the blade spanned by the TEF, but also produces a nose up pitching moment that tends to increase the pitch angle at the blade root, thereby *increasing* the overall lift across the entire blade span. Therefore, for the swashplateless TEF rotor to perform effectively, it

is beneficial if this opposing interference lift produced locally (in the blade sections spanned by the TEF) is minimized. An understanding of the trends in C_{m_δ} and C_{h_δ} as shown in Figs. 2.2 and 2.3 can help in reducing this lift interference. If the variation in C_{l_δ} (Fig. 2.2) is compared with that of C_{m_δ} (Fig. 2.3) for $0.6 < x_f < 0.85$, it will be noted that the change in C_{l_δ} is much greater than that of C_{m_δ}. This means that by choosing a flap size of $0.15c$ instead of the optimum (from pitching moment perspective) of $0.25c$ would lead to only a small change in C_{m_δ} but results in a significant change in C_{l_δ} which would minimize the detrimental interference lift and improve the ability of the TEF to produce the forces needed to control the rotor. Another

Another important consideration while deciding flap size is the power required to actuate the TEFs, which is proportional to the hinge moment (C_h). From Figs. 2.4 and 2.5, it will be noted that both C_{h_α} and C_{h_δ} decrease with decreasing flap size and therefore, choosing a smaller flap size would offer benefits in the form of reduced actuation power. The fact that C_{h_α} is nearly the same as C_{h_δ} highlights the fact even if the flap is small, the actuation power may not be negligible because of the contribution of angle of attack (α) to the hinge moment.

Figures 2.4 and 2.5 show the variation of C_{h_α} and C_{h_δ} with flap location. As would be expected, the flap hinge moment, increases as the flap size increases. It is interesting to note that although C_{h_α} and C_{h_δ} have quite different mathematical expressions, they are nearly the same for all flap sizes. This implies that from a perspective of actuation power, a unit change in angle of attack and a unit change in flap deflection, will produce nearly the same change in flap hinge moment for all

$$C_{h_\alpha} = -\frac{1}{2}\left((2+\hat{x})\sqrt{1-\hat{x}^2} - (1+2\hat{x})\cos^{-1}\hat{x}\right)$$

$$\hat{x} = \frac{2x}{c} - 1$$
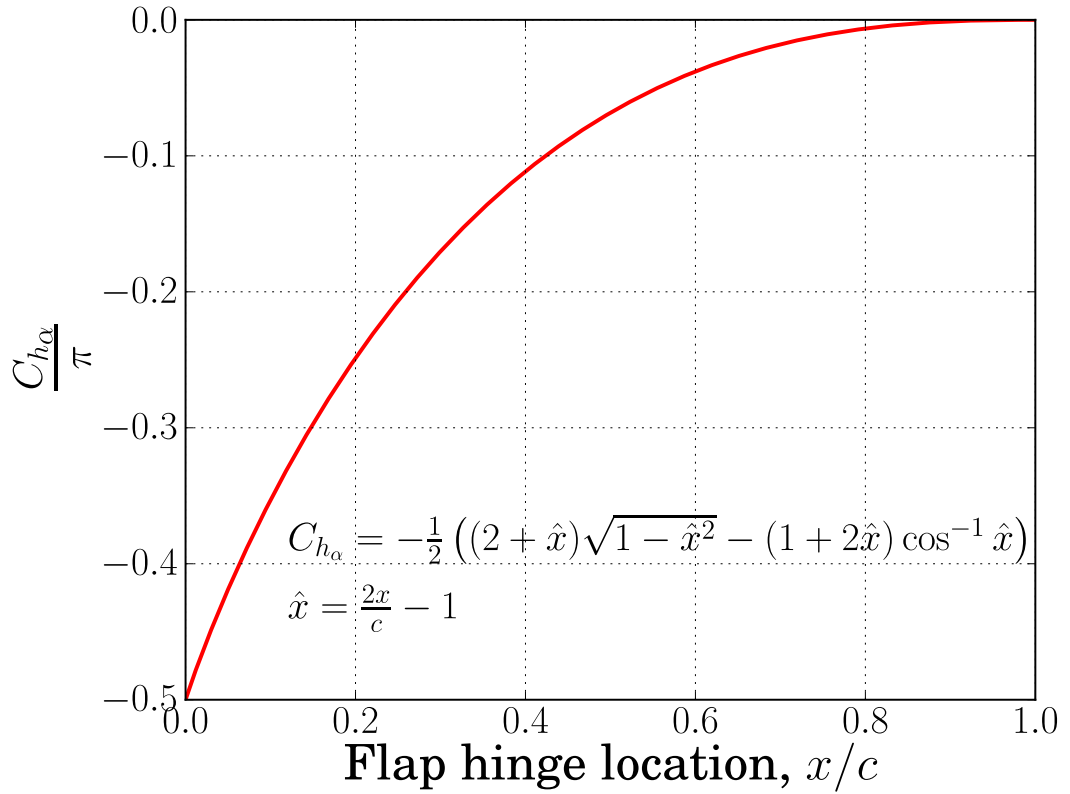
Figure 2.4: C_{h_α} vs x_f (steady thin airfoil theory).

flap sizes. Physically, this means that hinge moment depends almost wholly on the orientation of the flap with respect to the free-stream, regardless of whether this orientation is brought about through α or δ. The incompressible analysis presented above can be extended for steady compressible flows by scaling the results using the Glauert factor, $\beta = \sqrt{1-M^2}$.

2.1.2 Drag Modeling for TEF Airfoils in Steady Flow

While thin airfoil theory can be used to predict lift, pitching moment and hinge moment, there is no purely analytical model for predicting steady drag. Approaches
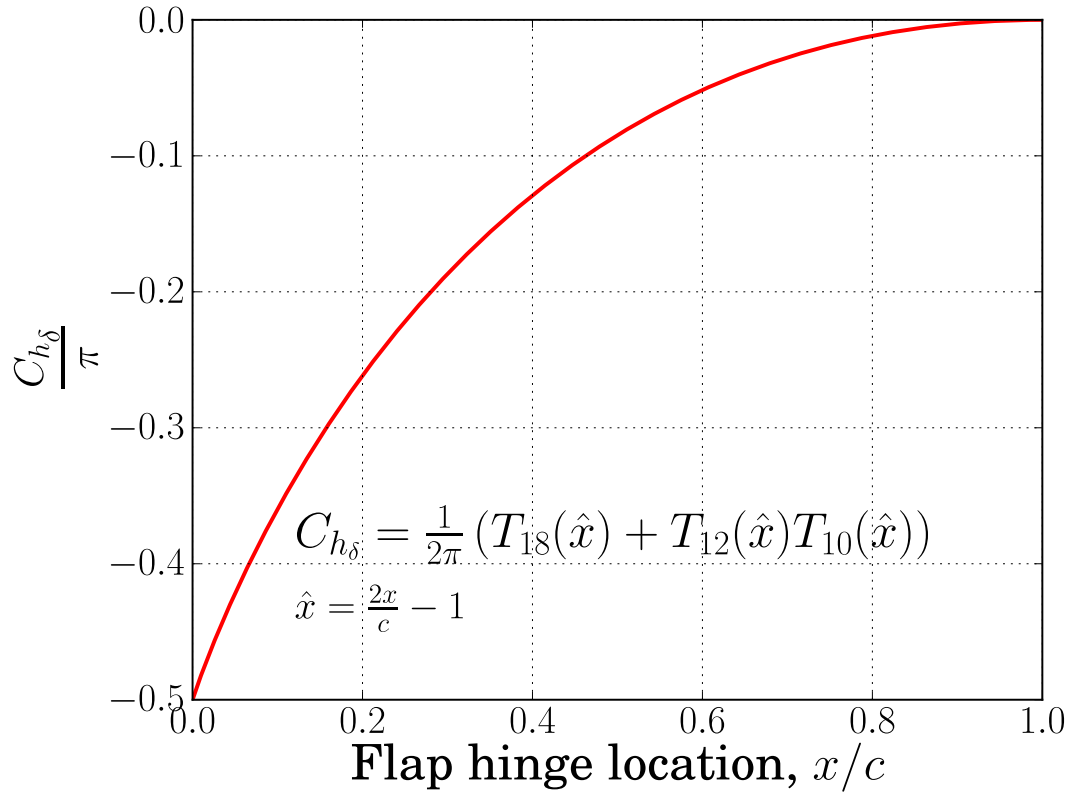
Figure 2.5: C_{h_δ} vs x_f (steady thin airfoil theory).

for modeling the drag using the concept of *recovery factor* has been investigated for steady and unsteady variations in angle of attack and flap deflection (Refs. 89, 90). However, even these approaches rely on experimental/CFD data for modeling the contribution to drag from viscous effects. Drag modeling is very important because it plays an important role in predicting the performance and efficiency of airplane/rotor systems. Generally, drag for a given airfoil is estimated based on experimental or CFD data. Such data is often available for some airfoils, although over a limited range of flow conditions. This data (CFD or experimental) can be used predict the airloads in design and analysis codes by using lookup tables.

However, although experimental or CFD drag data are available for different airfoils as a function of angle of attack, drag data for airfoils with TEFs is limited. Also, for TEF airfoils, data needs to be obtained for all possible combinations of α and δ within the flow regime of interest. This becomes a challenge for analysis of systems involving airfoils with TEFs where drag estimation is critical for the analysis. This is particularly so for the analysis of swashplateless rotors, which is the subject of the present work.

Developing good empirical and semi-empirical methods for drag estimation would therefore be very useful for a wide range of engineering applications. An attempt is made in this section to provide an approximate, semi-empirical model to estimate the drag for airfoils with TEF. To develop and verify the model, extensive drag data was obtained computationally for a wide range of conditions, from which a few results are presented here. All the drag data used in this section were obtained for integral TEFs with zero overhang. To provide data that is representative of commonly used rotor airfoils, the computations were performed on a NACA0012 airfoil using a 329×97 CFD grid. A Reynolds number of 3.41 million was used for all the runs.

Figure 2.6(a) shows the variation of drag as a function of flap deflection for a flap size of 25% chord. It is observed that drag exhibits a parabolic dependence on flap deflection. Drag can be split into pressure drag and viscous drag. Figures 2.6(b) and 2.6(c) show the variation of the pressure drag (C_{d_p}) and viscous drag (C_{d_v}) components as a function of flap deflection. It is seen that the pressure drag constitutes the major component of the drag and follows the same (parabolic) trend as the total

drag. The viscous drag is relatively almost constant with both angle of attack and flap deflection. An important point to note is that the pressure drag obtained from a Navier-Stokes solver may not be exactly the same as that obtained using an Euler solver because of cross-coupling between viscous and non-viscous terms.

It is observed that as the angle of attack increases, the magnitude of the flap deflection corresponding to minimum drag increases in magnitude but is opposite in sign to α. Another important point to note is that while the flap deflection corresponding to minimum drag changes with α, the minimum drag value itself is nearly the same for all three angles of attack. The camber introduced by deflecting the flap does affect the point of minimum drag, however the effect is not very significant, especially when the flap deflections are not too high. Based on these observations, a method to estimate the drag for a generic airfoil may be developed. In this regard, the following points may be noted:

- Drag has a parabolic dependence on both α and δ.

- The flap deflection corresponding to minimum drag corresponds approximately to zero lift (see Fig. 2.7).

- Airfoils of the same thickness but different camber (flap deflection has the effect of changing the camber of the airfoil) may be expected to have approximately the same drag at the same effective angle of attack. While this is not strictly true, it is still a reasonable assumption.

- Based on these considerations it would seem logical to model the drag for a trailing edge flap by using the concept of effective angle of attack.

39
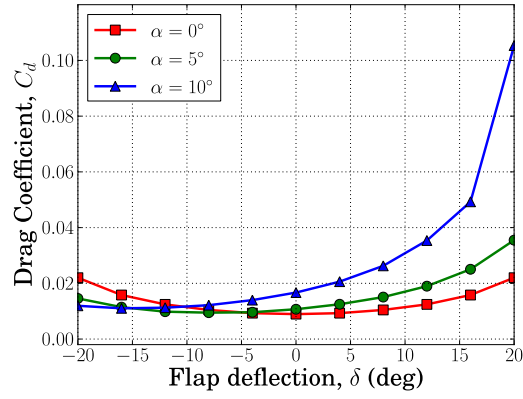
(a) C_d vs δ
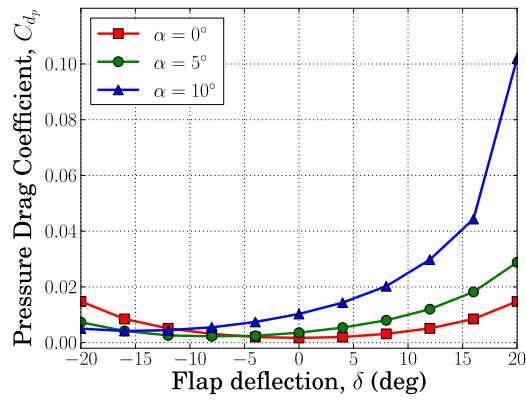
(b) C_{d_p} vs δ
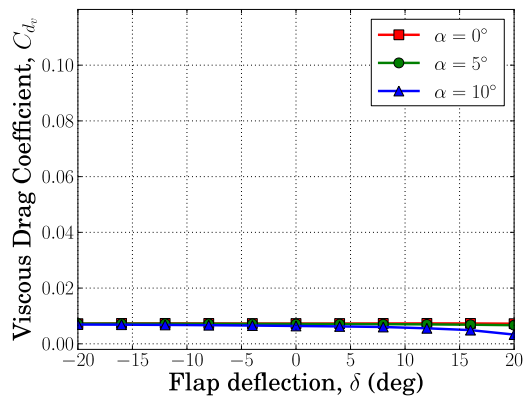
(c) C_{d_v} vs δ

Figure 2.6: Variation of drag as a function of flap deflection for a NACA0012 airfoil obtained using CFD, $M = 0.3$, $x_h = 0.75$, OH=0, $Re = 3.41$ million.
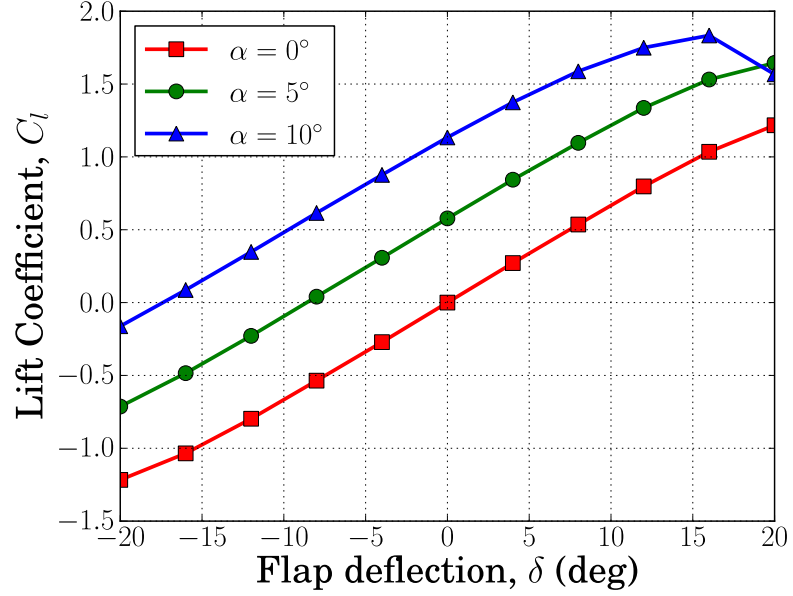
Figure 2.7: C_l vs δ for different angles of attack for a NACA0012 airfoil obtained using CFD, $M = 0.3$, $x_h = 0.75$, OH=0, $Re = 3.41$ million.

For symmetric airfoils, the effective angle of attack (α_{eff}) may be obtained as follows:

$$C_l = C_{l_\alpha}\alpha + C_{l_\delta}\delta \tag{2.13}$$

$$= C_{l_\alpha}\left(\alpha + \frac{C_{l_\delta}}{C_{l_\alpha}}\delta\right) \tag{2.14}$$

$$= C_{l_\alpha}\alpha_{\text{eff}} \tag{2.15}$$

$$\alpha_{\text{eff}} = \left(\alpha + \frac{C_{l_\delta}}{C_{l_\alpha}}\delta\right) \tag{2.16}$$

The values of C_{l_α} and C_{l_δ} can obtained from thin airfoil theory or from data obtained from CFD/experiment. If C_d vs α_{eff} is plotted (see Fig. 2.8(a)) it is observed that the curves corresponding to the three angles of attack fall on one curve (Note: The values of C_{l_α} and C_{l_δ} for this plot are taken from thin airfoil theory). Also, from Fig. 2.8(b) it is seen that the pressure drag, being the major component

41

of the total drag, follows the same trend. This means that the drag can be modeled using a single parameter (α_{eff}) instead of two parameters (α and δ). From a modeling perspective, this is a very useful conclusion because this means that by determining the relationship $C_d = C_d(\alpha)$ the relationship $C_d = C_d(\alpha, \delta, x_f)$ can be approximated. So if $C_d = f(\alpha)$ is known then $C_d = f(\alpha_{\text{eff}}) = f(\alpha_{\text{eff}}(\alpha, \delta, x_f))$ can be obtained. Because drag is known to have a parabolic dependence on α (Ref. 90), the relationship between drag and α_{eff} can also be written as:

$$C_d = C_{d_0} + C_{d_1}\alpha_{\text{eff}} + C_{d_2}\alpha_{\text{eff}}^2 \tag{2.17}$$

For a NACA0012 airfoil, $C_{d_0} = 0.008948$, $C_{d_1} = 0$, $C_{d_2} = 0.268$ rad^{-2} provides reasonably good estimates for C_d as a function of α and δ for the Reynolds number considered here. For this case $C_{d_1} = 0$ because drag is an even function of α for symmetric airfoils. Beyond $\alpha_{\text{eff}} = 15°$, the effect of boundary layer thickening and/or flow separation leads to a decrease in lift and a rapid increase in the drag. Drag modeling is valid only up to this angle of attack. It is to be noted that the above analysis was obtained for $M = 0.3$. Scaling the drag formula in Eq. 2.17 by the Glauert factor (β) would provide a reasonable approximation of compressibility effects up to the onset of super-critical flow. It must also be noted that as the Mach number increases, α_{stall} would be expected to decrease. For transonic flows or for flows involving massive flow separation/stall, the drag formula would not be expected to provide good estimates.

The drag model described in this section can be refined further to incorporate

42

(a) C_d vs α_{eff}
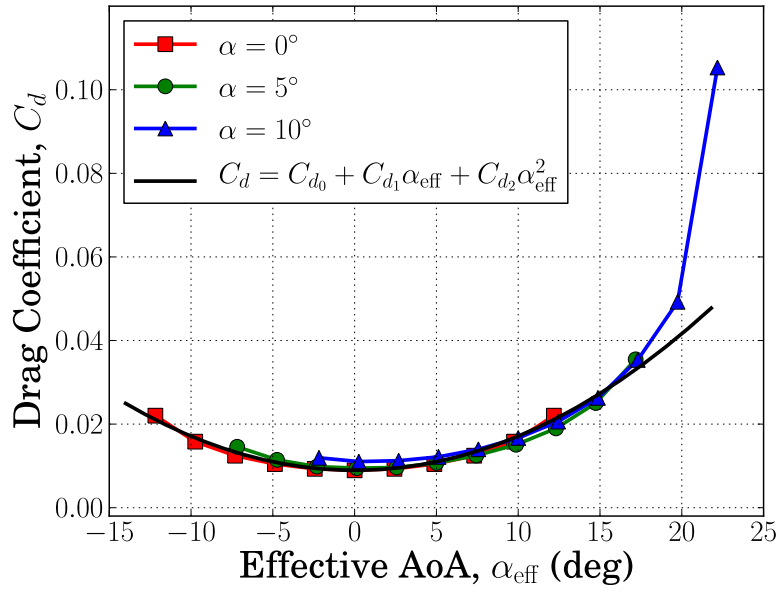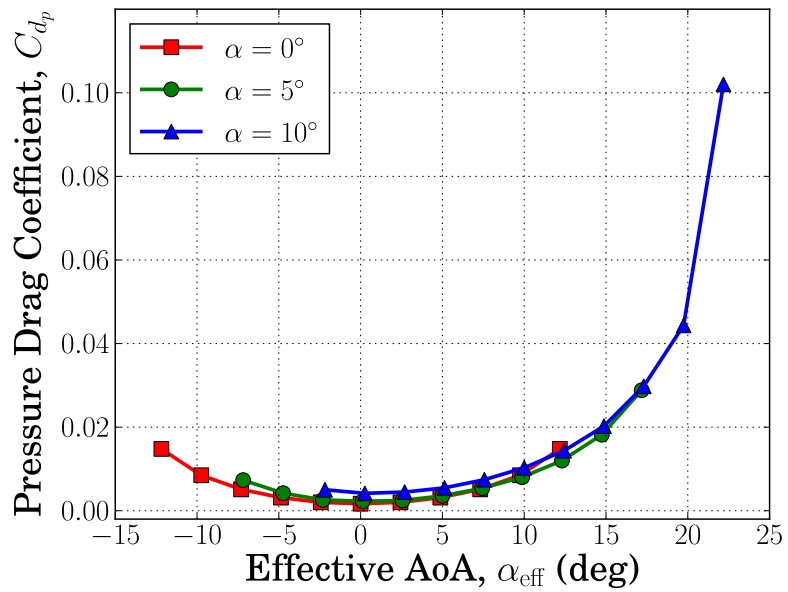
(b) C_{d_p} vs α_{eff}

Figure 2.8: Variation of drag as a function α_{eff} for a NACA0012 airfoil obtained using CFD, $M = 0.3$, $x_h = 0.75$, OH=0, $Re = 3.41$ million.

the effect of camber (i.e., different flap deflections) as well as for post-stall behavior. However, these are not described here. Some ideas for modeling the effect of camber and post-stall behavior are presented in Chapter 3 in the section on airloads and aerodynamic phenomena associated with TEFs.

2.1.3   Unsteady Thin-Airfoil Analysis

Although the steady analysis is very useful for understanding the aerodynamics of TEF airfoils, it cannot capture the effects caused by the unsteady flow field encountered by a helicopter rotor. The unsteady flow field can give rise to significant phase and magnitude differences between the actual and the quasi-steady airloads predictions. Appropriate modeling of the unsteady aerodynamics therefore becomes critical in effectively modeling the aerodynamics of helicopter rotors.

The unsteady solutions can be obtained in the *frequency domain* or *time domain*. Frequency domain solutions assume periodic forcing and are particularly useful in theoretical analysis of the behavior of a system. A time domain representation of the unsteady problem is more useful when the unsteady motion of the system is not known beforehand. Here, the unsteady motion is broken down into step changes. If the response of the system to a step change in forcing can be known (either from theory or CFD), then the unsteady airloads at any particular instant can be obtained by linearly summing the step (indicial) response of the system over all previous times up to the present time.

2.1.3.1 Frequency Domain Solution

In the frequency domain representation of the unsteady aerodynamics, the forcing function is assumed to be periodic and having a frequency which is typically expressed in terms of the reduced frequency k, i.e.

$$k = \frac{\omega c}{2V} \tag{2.18}$$

where ω is the angular frequency in rad/s; c is the airfoil chord, and V is the free-stream velocity.

The forcing functions may be represented as

$$\alpha(t) = \alpha_0 e^{i\omega t} \tag{2.19}$$

$$\delta(t) = \delta_0 e^{i\omega t} \tag{2.20}$$

The goal here is to determine $C_l(t)$, $C_m(t)$ and $C_h(t)$. Typically, the unsteady aerodynamic effects are split into circulatory and noncirculatory components. The circulatory terms include the effects due to the downwash induced on the airfoil by the vortices shed from the trailing edge. All other effects are included in the noncirculatory term. Accordingly, the airloads can be written as

$$C_l(t) = C_l^{\mathrm{nc}}(t) + C_l^c(t) \tag{2.21}$$

$$C_m(t) = C_m^{\mathrm{nc}}(t) + C_m^c(t) \tag{2.22}$$

$$C_h(t) = C_h^{\mathrm{nc}}(t) + C_h^c(t) \tag{2.23}$$

where, the "nc" superscript denotes the noncirculatory term, while the "c" super-script denotes the circulatory term. From Theodorsen's (Ref. 41) work, the circula-

tory and noncirculatory airloads are given by

$$C_l^c(t) = 2\pi C(k)Q \tag{2.24}$$

$$C_m^c(t) = \pi\left(a + \frac{1}{2}\right)C(k)Q \tag{2.25}$$

$$C_h^c(t) = -\frac{1}{2}T_{12}(\hat{x}_f)C(k)Q \tag{2.26}$$

$$C_l^{nc}(t) = \left(\pi\frac{\dot{\alpha}b}{V} - \pi a\frac{\ddot{\alpha}b^2}{V^2} - T_4(\hat{x}_f)\frac{\dot{\delta}b}{V} - T_1(\hat{x}_f)\frac{\ddot{\delta}b^2}{V^2}\right)$$
$$+ \frac{l}{V^2}\left(-2\sqrt{1-\hat{x}_f^2}Vb\dot{\delta} + T_4(\hat{x}_f)b^2\ddot{\delta}\right) \tag{2.27}$$

$$C_m^{nc}(t) = -\frac{1}{2}\left[\pi\left(\frac{1}{2}-a\right)\frac{\dot{\alpha}b}{V} + \pi\left(\frac{1}{8}+a^2\right)\frac{\ddot{\alpha}b^2}{V}\right.$$
$$\left. + T_{15}(\hat{x}_f)\delta + T_{16}(\hat{x}_f)\frac{\dot{\delta}b}{V} + 2T_{13}(\hat{x}_f)\frac{\ddot{\delta}b^2}{V^2}\right]$$
$$- \frac{l}{2V^2}\left(T_{22}(\hat{x}_f)V^2\delta + T_{23}(\hat{x}_f)V\dot{\delta}b + T_{24}(\hat{x}_f)\ddot{\delta}b^2\right) \tag{2.28}$$

$$C_h^{nc}(t) = -\frac{1}{2}\left(T_{17}(\hat{x}_f)\frac{\dot{\alpha}b}{V} + 2T_{13}(\hat{x}_f)\frac{\ddot{\alpha}b^2}{V^2}\right.$$
$$\left. + \frac{T_{18}(\hat{x}_f)}{\pi}\delta + \frac{T_{19}(\hat{x}_f)}{\pi}\frac{\dot{\delta}b}{V} - \frac{T_3(\hat{x}_f)}{\pi}\frac{\ddot{\delta}b^2}{V^2}\right)$$
$$- \frac{l}{2V^2}\left(T_{25}(\hat{x}_f)V\dot{\alpha}b + T_{24}(\hat{x}_f)\ddot{\alpha}b^2\right.$$
$$\left. + \frac{1}{\pi}T_{26}(\hat{x}_f)V^2\delta + \frac{1}{\pi}T_{27}(\hat{x}_f)V\dot{\delta}b + \frac{2}{\pi}T_2(\hat{x}_f)\ddot{\delta}b^2\right)$$
$$- \frac{l^2}{2V^2}\left(\frac{1}{\pi}T_{28}(\hat{x}_f)V^2\delta + \frac{1}{\pi}T_{29}(\hat{x}_f)V\dot{\delta}b - \frac{1}{\pi}T_5(\hat{x}_f)\ddot{\delta}b^2\right) \tag{2.29}$$

where, Q contains the forcing functions and is given by

$$Q = \alpha + \left(\frac{1}{2}-a\right)\frac{\dot{\alpha}b}{V} + \frac{T_{10}(\hat{x}_f) - lT_{21}(\hat{x}_f)}{\pi}\delta + \frac{T_{11}(\hat{x}_f) - 2lT_{10}(\hat{x}_f)}{2\pi}\frac{\dot{\delta}b}{V} \tag{2.30}$$

l is the offset of the flap hinge from the flap leading edge non-dimensionalized by semi-chord ($l = 2(x_h - x_f) = (\hat{x}_h - \hat{x}_f)$); $C(k)$ is the Theodorsen function (Ref. 22) given by

$$C(k) = F(k) + iG(k) \tag{2.31}$$

46

$$F(k) = \frac{J_1(J_1 + Y_0) + Y_1(Y_1 - J_0)}{(J_1 + Y_0)^2 + (J_0 - Y_1)^2} \tag{2.32}$$

$$G(k) = -\frac{Y_1 Y_0 + J_1 J_0}{(J_1 + Y_0)^2 + (J_0 - Y_1)^2} \tag{2.33}$$

with J_ν and Y_ν being Bessel functions of the first and second kind respectively. The Theodorsen function has the effect of introducing both a phase (because of the imaginary part) and a magnitude change with respect to the quasi-steady airloads.

2.1.3.2 Time Domain Solution

Once the frequency domain solution is derived, the time-domain solution can be obtained by extension. The time-domain solution is also split into circulatory and noncirculatory parts. The noncirculatory parts are identical for the frequency and time domain approaches. The circulatory terms are given by

$$C_l^c(t) = 2\pi \left(Q(t=0)\phi_W(s) + \int_0^s \frac{dQ}{d\sigma}(\sigma)\phi_W(s-\sigma)\,d\sigma \right) \tag{2.34}$$

$$C_m^c(t) = \pi \left(a + \frac{1}{2} \right) \left(Q(t=0)\phi_W(s) + \int_0^s \frac{dQ}{d\sigma}(\sigma)\phi_W(s-\sigma)\,d\sigma \right) \tag{2.35}$$

$$C_h^c(t) = -\frac{1}{2}\left(T_{12}(\hat{x}_f) - 2lT_{20}(\hat{x}_f) \right) \times$$
$$\left(Q(t=0)\phi_W(s) + \int_0^s \frac{dQ}{d\sigma}(\sigma)\phi_W(s-\sigma)\,d\sigma \right) \tag{2.36}$$

where $\phi_W(s)$ is the Wagner function (Ref. 23) and s is the the distance traveled by the airfoil in semi-chords.

$$s = \frac{2Vt}{c} \tag{2.37}$$

Notice that in the time-domain solution, the Theodorsen function is replaced by a Duhamel integral and the Wagner function. The Wagner function, $\phi_W(s)$, is known exactly but is usually represented approximately in exponential form. One

approximation to the Wagner function for $s = 0+$ (see Fig. 2.9), which is attributed to R. T. Jones (Ref. 91), is written as a two-term exponential series with four coefficients, i.e.,

$$\phi_W(s) \; = \; 1 - A_1 e^{-b_1 s} - A_2 e^{-b_2 s} \tag{2.38}$$

$$= \; 1 - 0.165 e^{-0.0455s} - 0.335 e^{-0.3s} \tag{2.39}$$

The exponential representation is not only simple, but makes it possible to solve the equation at a much lower computational cost. This is because, for a problem involving N time-steps, the direct evaluation of the Duhamel integral in Eqs. 2.34–2.36 for every time-step is an $O(N^2)$ process. However, by representing the Wagner function as an exponential series, an $O(N)$ recurrence algorithm (Ref. 28) can be used to solve the problem. This greatly enhances the efficiency of the indicial method, especially when repeated evaluations are involved, as in a comprehensive rotor analysis code. Figure 2.9 shows the Wagner function compared with CFD. The CFD solution to the Wagner function was obtained from the response to a step (indicial) change in the angle of attack.

2.1.3.3 Compressible Thin Airfoil Theory

The analysis presented so far, is valid only for incompressible flows. However, helicopter rotors encounter higher subsonic and transonic Mach numbers in the outboard regions of the blade. There are no exact analytical solutions for compressible flows. This is because, for subsonic flows, the governing equation is the hyperbolic wave equation whereas for incompressible flows, the governing equation is Laplace's

$$\phi_W(s) \approx 1 - A_1 e^{-b_1 s} - A_2 e^{-b_2 s}$$

$$= 1 - 0.165 e^{-0.0455 s} - 0.335 e^{-0.3 s}$$
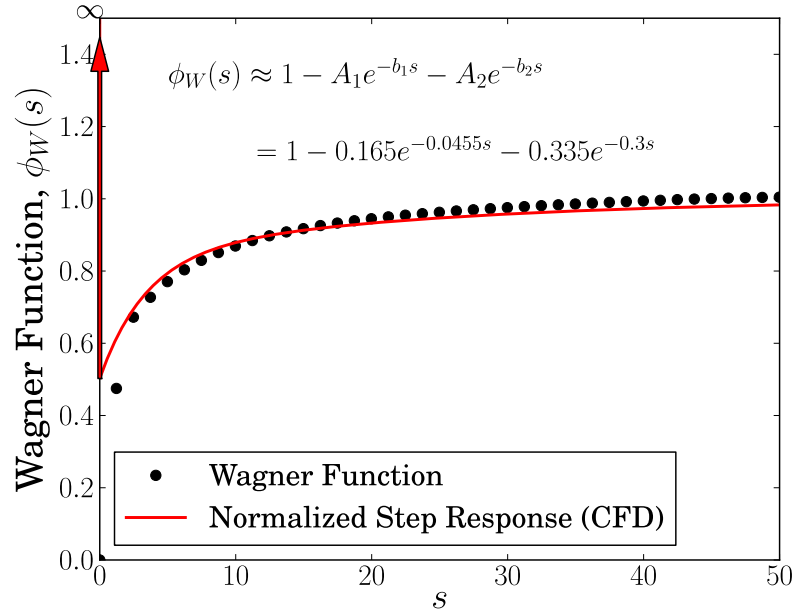
Figure 2.9: Wagner function

equation. Therefore, unlike incompressible flows for which the speed of sound is infinite, for compressible flows, the disturbances travel at a finite speed. Consequently, even the noncirculatory forces have a time history associated with them. The initial pressure loading on the airfoil surface can be obtained using linear piston theory (Ref. 33) while the transient behavior has been evaluated exactly for limited values of time by Lomax et al. (Ref. 92). For a more detailed discussion on unsteady aerodynamics for compressible flows see Ref. 90.

For TEF airfoils in compressible flow, expressions for the circulatory and noncirculatory forces have been obtained in the time-domain by Hariharan and Leishman (Ref. 93). These were obtained using reciprocal or reverse flow theorems (Ref. 94), which provide a means to solve various indicial problems (such as the traveling gust problem or TEF problem) based on already known solutions for
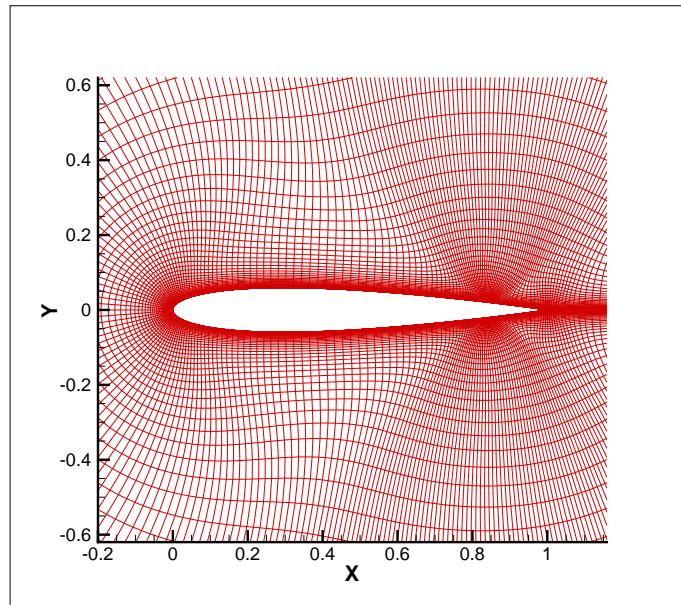
Figure 2.10: C-grid used for CFD computations on the NACA0006 airfoil.

airfoil flows and thereby obviate the need to solve each new problem from first prin-
ciples. For a more detailed discussion of the solution procedure for TEF airfoils in
compressible flow, see Ref. 93 and Ref. 90.

2.2 2D CFD Solver – TURNS

All CFD calculations were made using an extension of the **T**ransonic **U**nsteady
Rotor **N**avier-**S**tokes (TURNS) code (Ref. 95). This is a single block Navier-Stokes
solver that has been used to study a variety of steady/unsteady airfoil and rotor
flow problems. Most of the the calculations were performed in the viscous mode on
a structured C-grid (see Fig. 2.2). A finite difference upwind numerical algorithm
was used to solve the governing equations, with the evaluation of the inviscid fluxes
being based on Roe's upwind-biased flux-difference scheme.

2.2.1 The Governing Equations

The Conservative form of the Navier-Stokes equations can be written as :

$$\frac{\partial Q}{\partial t} + \frac{\partial (E - E_v)}{\partial x} + \frac{\partial (F - F_v)}{\partial y} = 0 \tag{2.40}$$

$$Q = \begin{bmatrix} \rho \\ \rho u \\ \rho v \\ \rho E_t \end{bmatrix} \tag{2.41}$$

$$E = \begin{bmatrix} \rho u \\ \rho u^2 + p \\ \rho uv \\ (\rho E_t + p)u \end{bmatrix}, \ F = \begin{bmatrix} \rho v \\ \rho vu \\ \rho v^2 + p \\ (\rho E_t + p)v \end{bmatrix} \tag{2.42}$$

$$E_v = \begin{bmatrix} 0 \\ \tau_{xx} \\ \tau_{xy} \\ u\tau_{xx} + v\tau_{xy} - q_x \end{bmatrix}, \ F_v = \begin{bmatrix} 0 \\ \tau_{xy} \\ \tau_{yy} \\ u\tau_{xy} + v\tau_{yy} - q_y \end{bmatrix} \tag{2.43}$$

where

$$E_t = C_v T + \frac{1}{2}\left(u^2 + v^2\right) \tag{2.44}$$

$$q_x = -k\frac{\partial T}{\partial x} \tag{2.45}$$

$$\tau_{xx} = \frac{2}{3}\mu\left(2\frac{\partial u}{\partial x} - \frac{\partial v}{\partial y}\right) \tag{2.46}$$

$$\tau_{xy} = \mu\left(\frac{\partial u}{\partial y} + \frac{\partial v}{\partial x}\right) \tag{2.47}$$

51

To have well conditioned matrices during the solution process, the equations need to be normalized. For the above equations, the various flow parameters are non-dimensionalized using reference parameters in the following manner

$$x^* = \frac{x}{L}, \quad y^* = \frac{y}{L}, \quad t^* = \frac{ta_\infty}{L}, \quad \rho^* = \frac{\rho}{\rho_\infty},$$

$$u^* = \frac{u}{a_\infty}, \quad v^* = \frac{v}{a_\infty}, \quad T^* = \frac{T}{T_\infty}, \quad p^* = \frac{p}{\rho a_\infty^2},$$

$$E_t^* = \frac{E_t}{a_\infty^2}, \quad \mu^* = \frac{\mu}{\mu_\infty}$$

and

$$\tau_{xx}^* = \frac{2\mu^*}{3Re_L}\left(2\frac{\partial u^*}{\partial x^*} - \frac{\partial v^*}{\partial y^*}\right) \quad q_x^* = \frac{-\mu^*}{(\gamma-1)M_\infty^2 Re_L Pr}\frac{\partial T^*}{\partial x^*}$$

where L is taken as the chord length, a_∞ is the velocity of sound far away from the airfoil, ρ_∞ is taken to be the density of the free-stream. The Reynolds number and Prandtl number are given by

$$Re_L = \frac{\rho_\infty a_\infty L}{\mu_\infty}, \quad Pr = \frac{\mu C_p}{k}$$

2.2.2 Transformation from the Physical Domain to the Computational Domain

The physical domain is mapped on to a computational domain where the grid lines are orthogonal and equal-spaced. The governing equations can then be solved on the computational domain by determining the metrics of the transformation. The transformed equations can be written as

$$\frac{\partial \overline{Q}}{\partial t} + \frac{\partial \overline{E}}{\partial \xi} + \frac{\partial \overline{F}}{\partial \eta} = \frac{\partial \overline{E}_v}{\partial \xi} + \frac{\partial \overline{F}_v}{\partial \eta} \tag{2.48}$$

Where the barred vectors are the vectors in the transformed $(\xi - \eta)$ coordinate

system. These can be expressed in terms of the Cartesian vectors as follows:

$$\overline{Q} = \frac{1}{J}[Q] \tag{2.49}$$

$$\overline{E} = \frac{1}{J}[\xi_x E + \xi_y F] \tag{2.50}$$

$$\overline{F} = \frac{1}{J}[\eta_x E + \eta_y F] \tag{2.51}$$

$$\overline{E_v} = \frac{1}{J}[\xi_x E_v + \xi_y F_v] \tag{2.52}$$

$$\overline{F_v} = \frac{1}{J}[\eta_x E_v + \eta_y F_v] \tag{2.53}$$

where J is the Jacobian of the inverse coordinate transformation (i.e., $J = \det\left(\frac{\partial(x,y)}{\partial(\epsilon,\eta)}\right)$).

2.3   2D Grid Generation

For all the 2D simulations, a C-grid is used to simulate the flow around the airfoil. Typically, a grid resolution of about 329×97 is used. Figure 2.11 shows a typical CFD grid for a TEF airfoil with overhang. The grid is refined near the leading edge of the flap so that the high gradients are well captured. For TEF airfoils the grid is first generated for an airfoil with undeflected flap and then deformed in the region of the flap by using appropriate smoothing parameters. The deformation for points away from the airfoil are obtained by using appropriate decay parameters. Depending on the requirements of the problem, the grid density is increased. For example, for the gap modeling simulations, the grid density is increased in the gap region because the airfoil grid has to exchange information with a highly refined gap mesh.
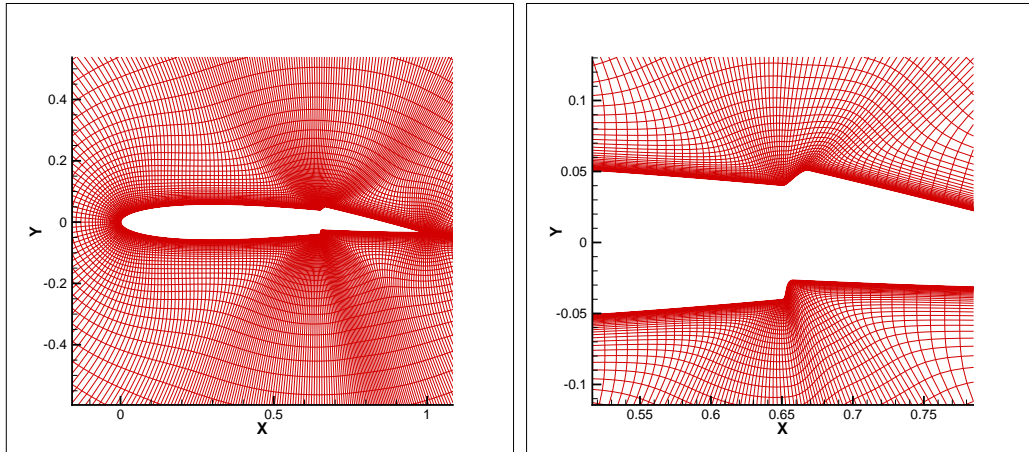
(a) Airfoil mesh with overhang   (b) Airfoil mesh with overhang (close up)

Figure 2.11: Flap and grid configuration for overhang for NACA0012 airfoil.

2.3.1   Overlapping Meshes and Grid Connectivity

One of the important challenges in CFD simulations is to generate good meshes to accurately solve the airloads and flow phenomena associated with the problem. CFD meshes can be classified as structured or unstructured meshes. In a structured mesh, each grid point has the same number of adjacent grid points (4 for 2D problems and 6 for 3D problems) to which it is connected, whereas in an unstructured mesh, the number of adjacent points to which a grid point is connected is not fixed. Generally, structured meshes involve less computational storage, are computationally faster and can handle wall boundary layers better . However, one of the major drawbacks of structured meshes lies in the treatment of complex geometries and particularly when there are multiple bodies in the flowfield.

The use of multiple meshes that fit one-on-one with each other leads to significant constraints on the mesh generation process. For example, the constraint that one grid should match another grid in a particular region imposes restrictions on

either grid which could give rise to difficulties in grid generation because each mesh has to have the same grid density and positioning as the other. This is particularly troublesome when we are dealing with complex geometries. The compromises that have to be made in grid quality to satisfy the constraints could give rise to poor convergence, very small time-step requirements, loss of flexibility and reduced robustness. While unstructured meshes are commonly used for complex geometries they have cells that have rigidly water-tight connections. Because of this, unstructured grids are not as flexible when components move relative to each other and re-gridding becomes necessary.

One alternative is to use multiple structured grids that overlap with each other (overset grids) and establish efficient methods to transfer information between the meshes. Overset structured grids may be viewed as unstructured globally but structured locally. They possess the global geometric flexibility of unstructured meshes while retaining the benefits associated with structuredness. The idea here is that rather than using a single mesh, a set of overlapping meshes are used which span the computational domain. In the regions where the meshes overlap, the solution is computed on one mesh and interpolated onto the other. Some of the potential advantages of the overset grids approach are :

- Because the two meshes are independent of each other, the grid resolution of one can be much higher than that of the other, thereby making it possible to increase the grid density in regions where special flow features need to be captured while maintaining a coarser grid in other regions.

- Because the alignment and geometry of the overlapping grids need not strictly correspond with each other, the grid generation process is easier and there is greater flexibility.

- Because overlapping meshes have fewer constraints, it is easier to have good quality meshes, thereby improving convergence and robustness.

2.3.2 Traditional Hole Cutting Method

Traditionally, overset grids have been treated by using what is known as "hole-cutting". Figure 2.12 shows a schematic describing the various terms involved in the overset grids connectivity process. For this particular example, two meshes are used. The first mesh is referred to as the *background mesh*, spreading over most of the computational domain (this grid is usually coarse) and the second mesh is referred to as the *body mesh* (close to the body), which is usually fine.

The important terms that are needed to explain the overset grid method are described below:

Hole : This is a region cut out from the *body mesh*. All *background mesh* points in this region (i.e., *iblank* points) are ignored (i.e., the governing equation is not solved at these points).

Hole points : These are points of the *background mesh* which lie inside the hole. The governing equations are not solved at these points.

Inter-grid Boundary Point (IGBP): These are points on the boundary of the

body mesh which also lie in the *background mesh*. For each *IBP*, the corresponding *donor* cell of the *background mesh* is determined and the values of the flow variables at the corners of the *donor* cell are interpolated to obtain the value at the *IBP*.

Hole Fringe Points (HFP): These are points of the *background mesh* which lie outside the hole but inside the *body mesh*. For each *HFP*, the corresponding *donor* cell of the *body mesh* is determined and the values of the flow variables at the corners of the *donor* cell are interpolated to obtain the value at the *HFP*.

Receiver point : These are points for which the values of the flow variables are obtained from another mesh through interpolation by identifying the *donor* cell in which it lies. Both *Hole fringe points* and *Inter-grid Boundary Points* act as *receiver* points.

Donor (Cell): This is a cell (in the *background mesh* or *body mesh*) which is used to compute the value at a *receiver* point. The location of the *receiver* point in the cell is used to compute the weightage for each corner point of the *donor* cell. The *donor* cell is indexed by the index of its lower, left corner point.

Traditionally, establishing connectivity between the overlapping meshes typically involves the following steps:

1. First, for each mesh involved, an initial region (hole) is cut out, inside which the points are blanked out by using an *iblank* array. This hole typically contains
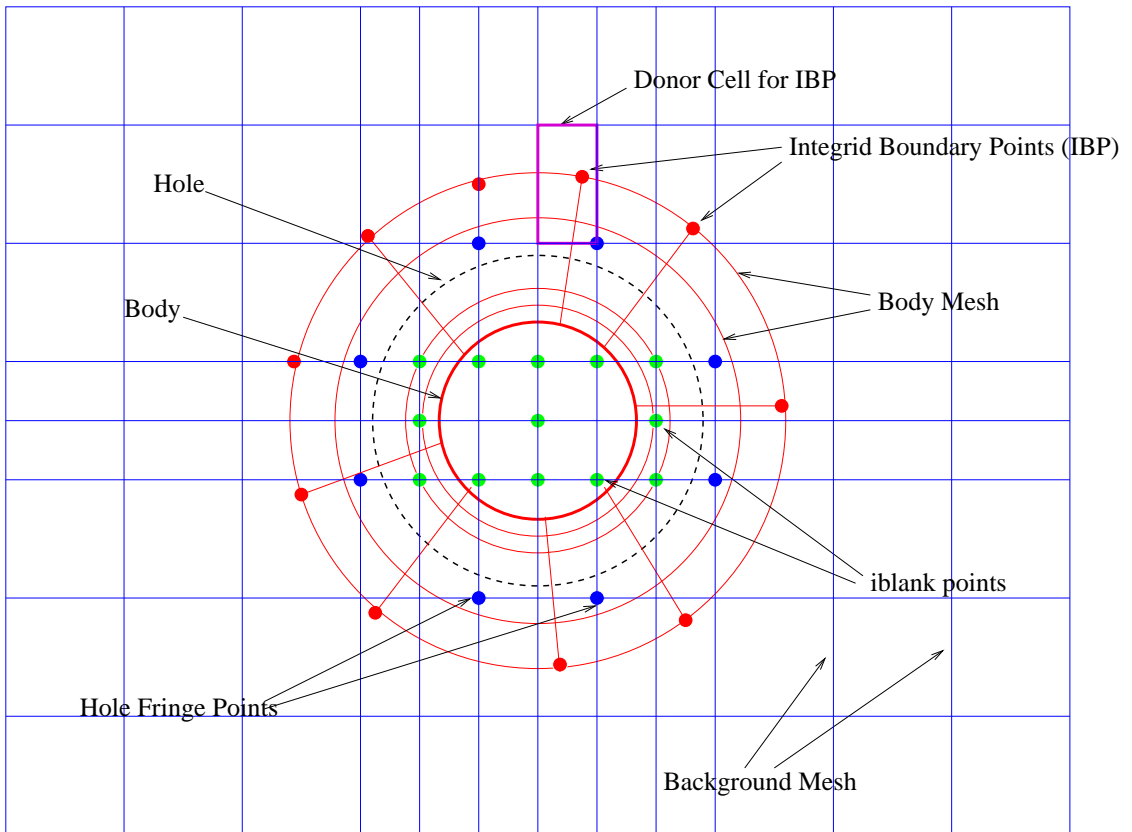
Figure 2.12: Schematic describing the terms involved in the traditional hole cutting problem.

the complete solid body which is contained in the mesh.

2. The hole is then resized so that good overlap is achieved between the meshes involved.

3. The fringe points at the edge of the hole which require information from other grids to serve as boundary conditions are identified.

4. The fringe points and the hole boundary points constitute the Inter-Grid Boundary Point (IGBP) list. For each point in this list, the j, k, l indices as well as the x-y-z coordinates are stored.

5. For each point in the IGBP list, an optimum donor cell is determined from all possible grids. Ideally, the finest grid should contain the donor cell.

At the end of the overset grid algorithm the following information is obtained and organized into appropriate data structures :

- A list of boundary and fringe points – both indices and grid numbers.

- A list of corresponding donor cells – indices of a corner point, grid numbers, grid numbers and locations of the points in the cells.

- An *iblank* array which has a value of 0 at hole points, -1 at boundary and fringe points and 1 at all other points.

During the solution process, the interior grid points that are not blanked out are treated normally. The values at the receiver points (boundary interpolation points and fringe points) are interpolated from their donor cells in other meshes. At

the hole points, the solution is not calculated. However, although the receiver points are blanked out, they need to be treated with special care during the implicit update and flux calculations. If the receiver points are not blanked out they can cause errors during the implicit time update. However, they need to be used for accurate flux calculations. This problem can be resolved by setting appropriate iblank values (0, -1 and 1) such that the fringe points are blanked out during the implicit inversion but included in the flux calculations (see Lakshminarayan (Ref. 86)).

Despite its advantages there are many challenges with using traditional overset grid techniques. Some of these are listed below:

- Creating the hole is not a straightforward process. This is particularly so because the hole is determined by marching away from the body surface. For complex geometries and those having imperfections, this can lead to problems in hole generation.

- The hole that is generated often has disparities in the cell sizes in the fringe region.

- Hole cutting for wall-less refinement grids and those with bodies have to be handled differently.

- The process is not automatic and issues such as setting grid priority, optimization, etc. may require tweaking by the user.

2.3.3 Implicit Hole Cutting Method

A simpler and more compact approach to handle overset grids is known as the Implicit Hole Cutting (IHC) technique which was first developed by Lee (Ref. 85) and further modified during the course of the present work by Lakshminarayan (Ref. 86). In this technique, grid connectivity is established without explicitly knowing, cutting and expanding the hole. The basic idea behind the IHC method that in any given region, the solution is computed at the point associated with the smallest cell size and interpolated at the other points. The method parses through every point in each grid to chooses the best cell in multiple overlapped regions, leaving the rest as receiver points. Hole cutting is a byproduct of this process of cell selection.

Since cell size is a parameter required by the solver as well, no additional computation is required separately for the connectivity process. Also, since cell size is the criterion for deciding which points are solved and which points are interpolated, the method automatically generates an optimum hole that minimizes the discontinuity in cell sizes across the inter-grid boundary. The IHC method senses the presence of the wall because of the progressively decreasing cell sizes as the wall/body-surface is approached and the hole is automatically cut around the body at the optimum location. The original IHC method developed by Lee (Ref. 85) was later modified by Lakshminarayan (Ref. 86) to incorporate more generic boundary conditions and donor search methods. The following section describes the details of the new IHC algorithm.

61

2.3.3.1 Overall Algorithm

The basic steps of the IHC algorithm as developed by Lee (Ref. 85) and later modified by Lakshminarayan (Ref. 86) are described in this section. The algorithm is described for the 2D problem. The 3D algorithm follows the same steps with the addition of an extra dimension. The IHC code is provided with the grid coordinates (x and y arrays) and IHC boundary conditions as input. The code then generates a list of receiver points and donor cells for each mesh along with data structures which link the receivers points to their donors.

Figure 2.13 shows the various subroutines involved in the IHC system. The basic inputs to the IHC system are : `ngrids` (number of grids) `x1, y1` (x and y coordinates), and IHC boundary conditions (specified in an input file). The IHC code generates a list of receiver points (`imesh` array) and donor cells (`idonor` array) for each mesh along with fractions (`frac` array) describing the location of each fringe point within its donor. A global list of the interpolation variables (conservative flow variables q and turbulence viscosity ν) of the donor cells in each mesh is maintained. The values at the receiver points within each donor cell is computed by using a simple bi-linear interpolation scheme.

The original IHC method (developed by Lee) made use of grid topology information to determine boundary interpolation points and interior receiver points. However, the use of grid topology information makes the process less generic, often requiring different approaches for establishing connectivity between meshes. In the modified IHC method (developed by Lakshminarayan) the concept of IHC bound-
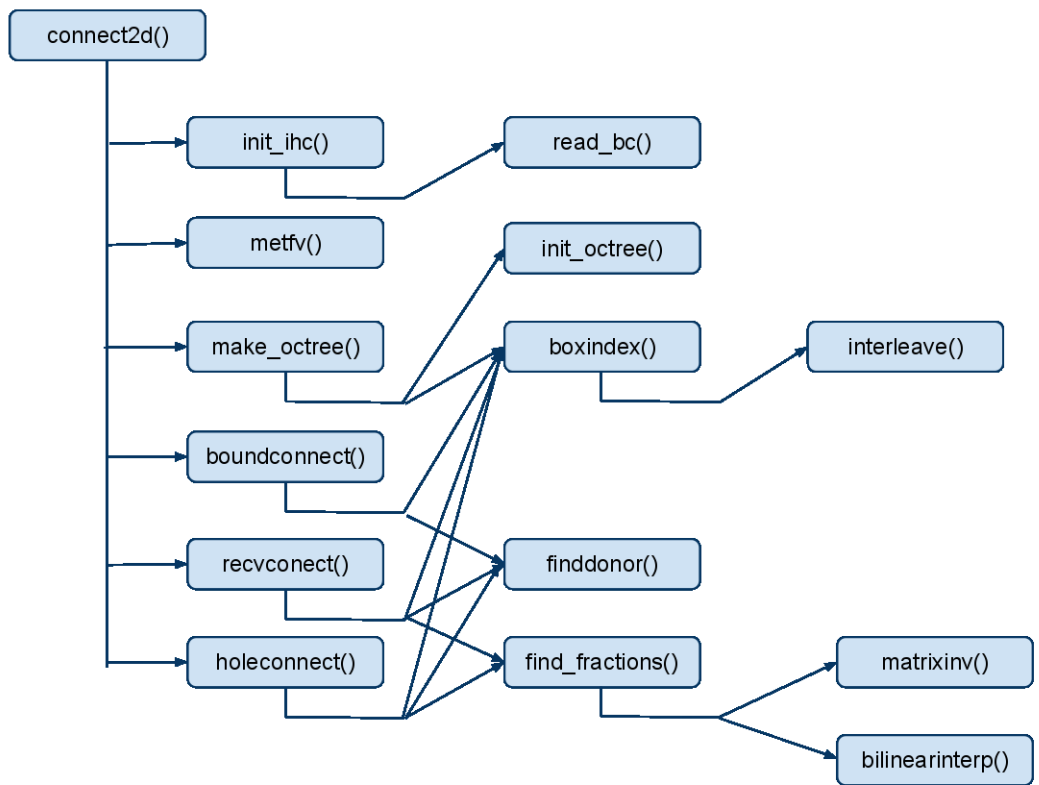
Figure 2.13: Relationship between various subroutines involved in the IHC system.

ary conditions is used, which makes the code more generic and provides a better interface and control of the IHC process. Only the new approach is described below:

1. The first step is to determine whether any pair of grids in the overset system overlap with each other. A knowledge of this can save a lot of time in the subsequent donor search algorithm since grids that do not overlap with each other need not be searched for donors. This is accomplished in the `boundconnect()` subroutine by parsing through the boundaries of all the meshes and determining whether any given pair of meshes overlap with each other.

2. The next step is to find the donors for "forced" receiver points (`recvconnect()` subroutine). These are grid points which *must* receive information from another grid. Usually, these are points on the boundary of grids embedded within another grid.

3. Finally, the donor-receiver information is obtained for all the remaining grid points in each mesh (`holeconnect()` subroutine). For any given grid point, its cell size is compared with those of cells in other grids which contain it. In the absence of any other constraint, the cell having the smallest size becomes the donor cell. If a grid point does not have a suitable donor in another mesh its iblank values is set to 1 and it is used in the solution process. If a suitable donor is found, then the value of *iblank* for that grid point is set to −1 and it is treated appropriately in the solution process (for more details on solution process, see Lakshminarayan (Ref. 86)). If a grid point is determined to be inside a body it's iblank is set to 0 and it is not considered in the solution

process.

As seen in Fig. 2.13, the boundary connectivity process merely establishes the overlap relationships and therefore does not create any donors/receivers. The forced-receiver connectivity subroutine and the hole connectivity are where the donor and receiver lists are generated.

2.3.3.2   Donor Search Algorithm

The main component in each of the three main subroutines (`boundconnect()`, `recvconnect()` and `holeconnect()`) is the donor search process. The efficiency and robustness of the donor search algorithm is important for the effectiveness of the IHC algorithm. The donor search is carried out by performing a stencil walk through the cells of the donor mesh.

In the stencil walk process, the dot product, $\vec{n} \cdot \vec{r}$, is computed for each face of the cell; where, $\vec{n} = \vec{p} \times \vec{q}$ is the inward normal to the face (see Fig. 2.14) and $\vec{r}$ represents the position of receiver point. For a point lying inside the cell, all six dot products should be positive. If a point does not lie inside the cell, the next cell in the stencil walk is indicated by the faces with negative dot products. It should be noted that for this approach to work, the three axis in the computational space should follow the directions of the right hand rule. The original IHC algorithm developed by Lee (Ref.85) consisted of two key steps :

1. Guessing the initial cell for the donor search. The initial cell for first grid point in the receiver mesh is arbitrary. For all subsequent receiver nodes, the initial
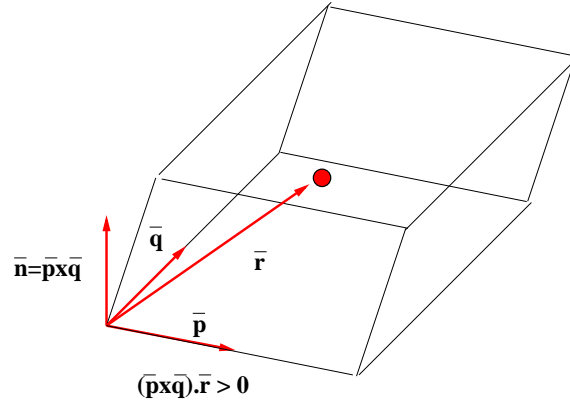
Figure 2.14: Test for inside/outside status of a point during stencil walk.

guess is taken to be the donor for the previous grid point. This is consistent with the fact that adjacent receiver points are likely to have identical or close by donor cells.

2. A stencil walk continues until a donor is found or until a fixed number of steps ($n_{\mathrm{maxsearch}}$) is exceeded. If a donor is not found in $n_{\mathrm{maxsearch}}$ timesteps, it is assumed that there is no valid donor. The donor search is also abandoned if the stencil walk enters into a repetitive loop where the same sequence of cells are traversed again and again. Also, appropriate modifications are made to the stencil walk process depending on the mesh topology.

While this approach works for a large number of cases, it is not very robust. Some of the drawbacks of this approach are :

- If $n_{\mathrm{maxsearch}}$ is too small, the search may be abandoned even though a valid donor may be present. If $n_{\mathrm{maxsearch}}$ is too large, the efficiency of the IHC method is degraded because a large number of searches are performed for

every point that does not have a donor, thereby increasing the computational cost.

- Since there is only one initial guess, the stencil walk follows only one path. If this path does not lead to the donor within the stipulated number of steps, it is assumed that no donor is available even though a different initial guess might actually yield a path to a donor. This is particularly so when the original path encounters walls, wake cuts, odd geometries, etc.

- The stencil walk is further complicated by the fact that different mesh topologies (e.g., C-grid, CH-grid, O-grid, etc.) require slightly different treatments. The makes the process less generic and more complicated.

In order to address these concerns, the new/modified IHC algorithm developed by Lakshminarayan (Ref. 86) adopts an octree based donor search algorithm. While the new algorithm does not necessarily significantly reduce the computational cost, it makes it more robust at nearly the same computational cost. Also, while the new approach involves the same two steps (i.e., initial guess followed by stencil walk) it involves better and (if necessary) multiple initial guesses and stencil walks before concluding that the receiver point does not have a donor. The new approach is independent of mesh topology and is therefore more generic. The following section describes the octree system donor search algorithm.

2.3.3.3 The Octree System

One of the improvements in the new IHC method is to use an octree based search technique (Ref. 96, 97) that makes the search process more robust. The purpose of using an octree system is twofold:

1. To provide better initial guesses for the stencil walk so that the stencil walk is shortened.

2. To provide multiple alternate initial guesses to initiate different stencil walk paths if the first path does not yield a donor. This makes the IHC method more robust and independent of mesh topology.

In this technique (Ref. 96, 97) , the donor mesh is scaled in both coordinate directions and is enclosed in a unit square box. This box is further subdivided into $2^2 = 4$ ($2^3 = 8$ for 3D) equal sized boxes to form level 1. Each box in level 1 is further subdivided into four boxes to form level 2 consisting of a total of $4 \times 4 = 16$ boxes. This process can be continued for as many levels as required (see Fig. 2.15). Level l would have 2^{dl} boxes (where $d = 2$ for 2D and 3 for 3D). At each level, the boxes are numbered according to the convention shown in Fig. 2.16. Figure 2.17 shows numbered boxes for levels 2 and 3. Numbering the boxes in this manner is important because it makes it possible to identify the box containing a given grid point very quickly and efficiently using bit-shift operators. Given the coordinates of a point in the computational domain, the number of the box containing the point at level l can be determined as follows:
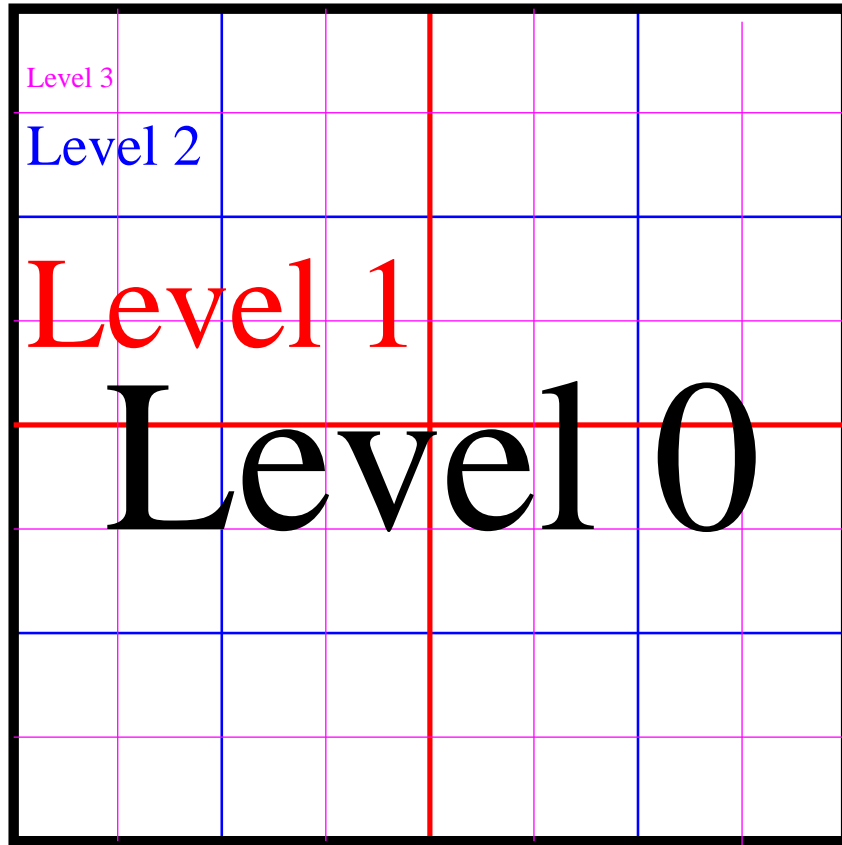
Figure 2.15: Levels in the octree system.
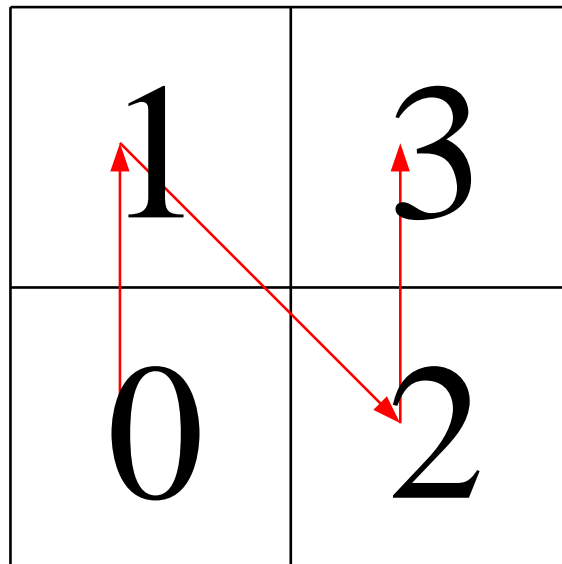
Figure 2.16: Numbering convention for the octree method.

5	7	13	15
4	6	12	14
1	3	9	11
0	2	8	10

21	23	29	31	53	55	61	63
20	22	28	30	52	54	60	62
17	19	25	27	49	51	57	59
16	18	24	26	48	50	56	58
5	7	13	15	37	39	45	47
4	6	12	14	36	38	44	46
1	3	9	11	33	35	41	43
0	2	8	10	32	34	40	42

(a) Box numbering for level 2   (b) Box numbering for level 3

Figure 2.17: Examples of how boxes are numbered for different levels in the octree method.

1. The coordinates of the point are normalized by the same values that are used to scale the computational domain into the unit square box.

$$x_1 = x/L_x \tag{2.54}$$

$$x_2 = y/L_y \tag{2.55}$$

where x, y are the coordinates of the point and $x_{1,2}$ are the normalized coordinates. Typically, $L_x = x_{\max} - x_{\min}$ and $L_y = y_{\max} - y_{\min}$.

2. Perform bit interleaving of x_1 and x_2 to obtain X (see Fig. 2.18 for details of how this is done).

3. Multiply X by 2^{dl} and ignore the numbers after the decimal point. A computationally efficient way to implement this is to perform a bit shift operation on X, since multiplying by 2^{dl} is equivalent to shifting the decimal point by $d \times l$

places in binary representation. It will be seen that the number so obtained is the box number at level l containing the grid point.

Once the boxes are generated and numbered at each level, the first and last ordered grid point of the donor mesh in each box (grid points being ordered first in the j and then k directions) is determined. This involves determining the box number at each level for every grid point in the donor mesh. While this requires some computational expense, the use of bit shift operators described earlier can significantly reduce the computational cost. Figure 2.19 shows the first and last ordered point for each box at level 2. Once this is done, the octree system is ready for use in the donor search algorithm. The donor search algorithm, developed by Lakshminarayan (Ref. 86) based on the octree system involves the following steps:

1. Taking the initial donor guess to be the donor for the previous receiver point, perform a quick stencil walk for $n_{\text{quicksearch}}$ steps. For most grid points, this is often adequate since the adjacent receiver points would be expected to have identical or adjacent donor cells.

2. For l varying from l_{max} to l_{min}, perform the following steps.

3. At level l, find the number of the box containing the receiver point.

4. Set the initial guess for the donor to be the first ordered point in the box and perform a stencil walk for $n_{\text{maxsearch}}$ steps (Note: $n_{\text{maxsearch}}$ is typically larger than $n_{\text{quicksearch}}$). This provides an alternate search path based on a good initial guess. If a donor is found, exit the loop. If no donor is found and

71

Steps involved in determining box containing the point (0.45,0.35) at level 3

Step 1 :

$x = 0.45_{10} = 0 . |0|1|1|1|0|0|1|1|0|0|1|1|0|0|1|1|\ldots$

$y = 0.35_{10} = 0 . |0|1|0|1|1|0|0|1|1|0|0|1|1|0|0|1|\ldots$

Step 2 :

$X = 0 . |0|0|1|1|0|1|1|0|1|0|0|1|0|1|1|0|1|0|0|1|0|1|1|0|1|0|0|1|0|1|1|\ldots$

shift decimal point by 2x3=6 places

Step 3 :

$[2^{dl} . X] = [2^{2x3} . X] = 1\ 1\ 1\ 0_2 = 14_{10}$

(0.0,1.0)							(1.0,1.0)
21	23	29	31	53	55	61	63
20	22	28	30	52	54	60	62
17	19	25	27	49	51	57	59
16	18	24	26	48	50	56	58
5	7	13	15	37	39	45	47
4	6	12	14	36	38	44	46
1	3	9	11	33	35	41	43
0	2	8	10	32	34	40	42

(0.0,0.35)

(0.0,0.0)   (0.45,0.0)   (1.0,0.0)
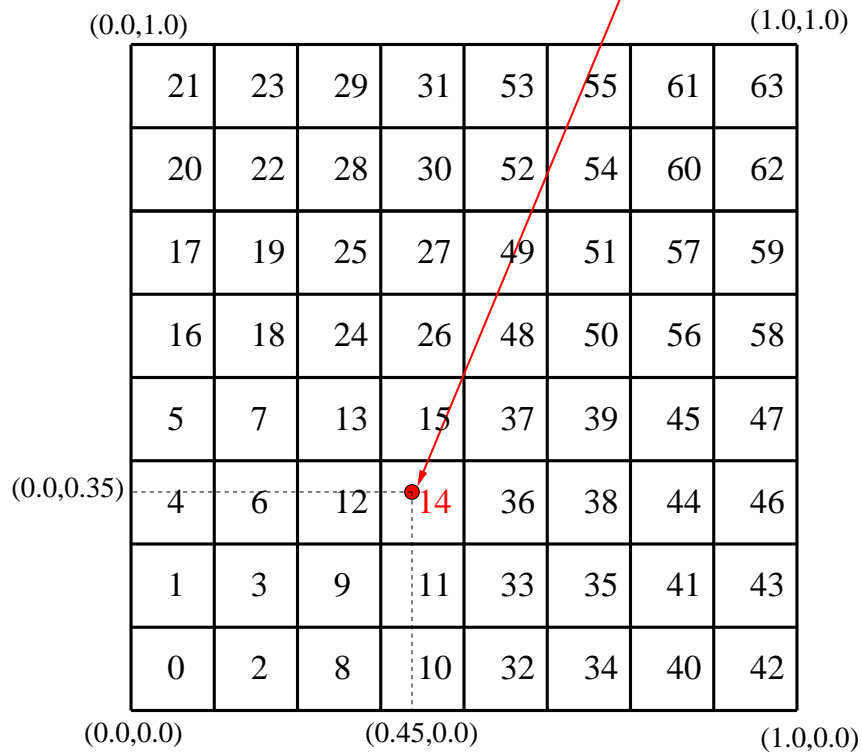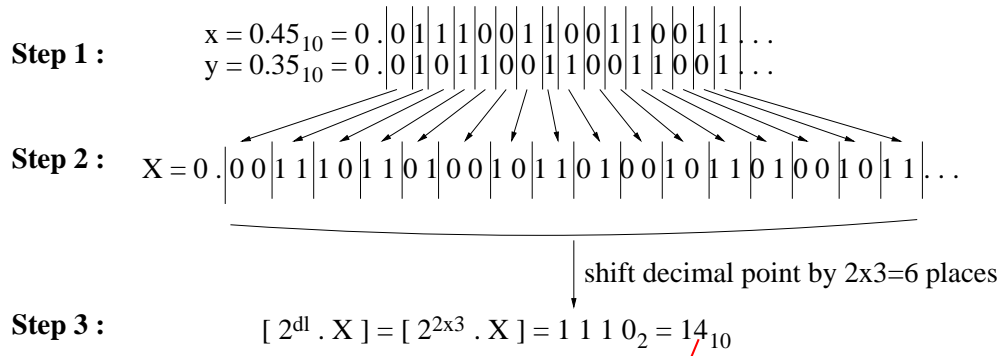
Figure 2.18: Schematic describing process of determining the box containing a point at a given level in the octree system.
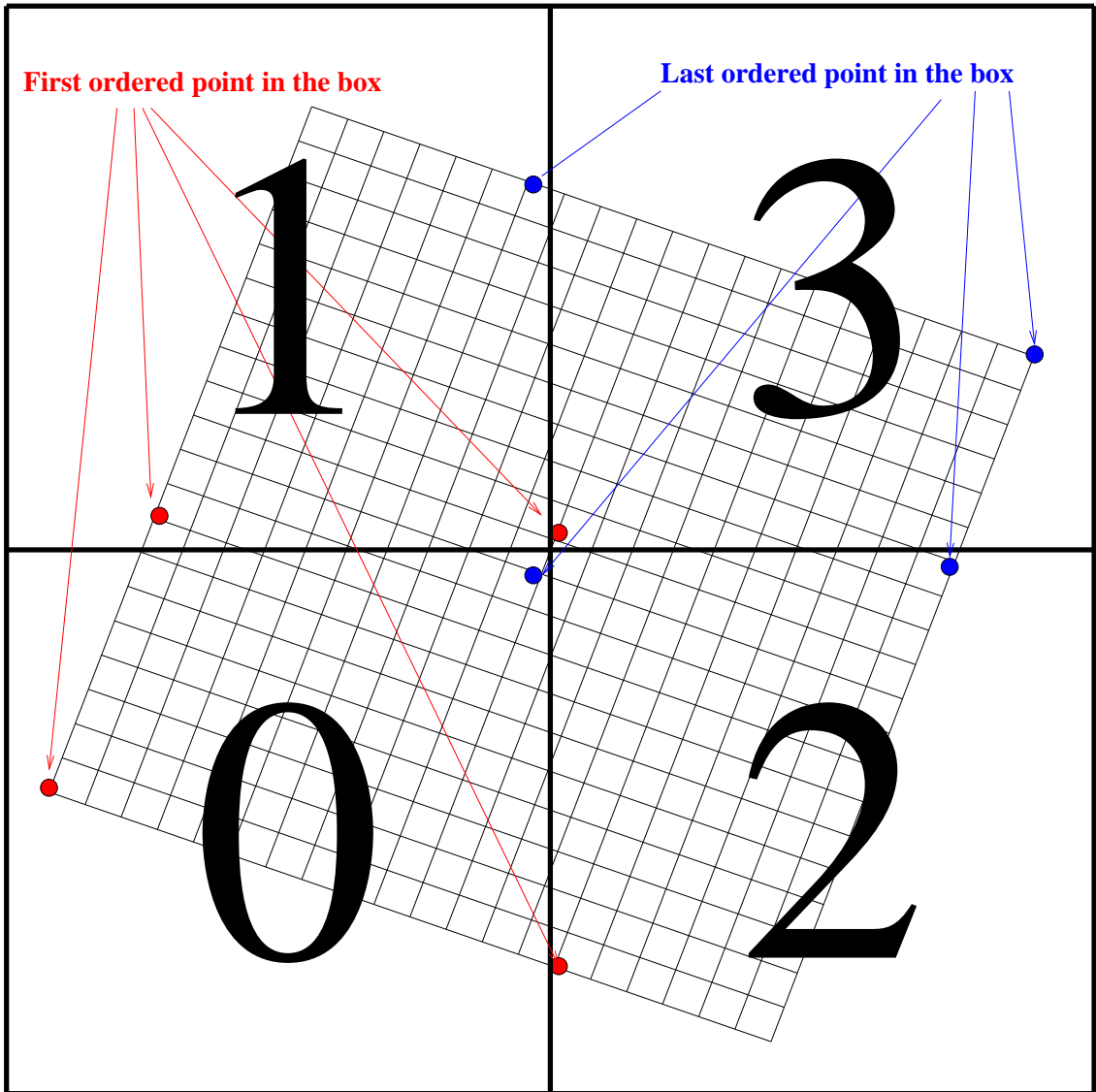
Figure 2.19: First and last ordered points/cells in each box at level 1 in the octree system.

the search terminates at a wall, increment $n_{\text{bodycross}}$ by 1.

5. If no donor is found, set the new initial guess for the donor to be the *last* ordered point in the box and repeat the stencil walk for $n_{\text{maxsearch}}$ steps. If a donor is found, exit the loop. If no donor is found and the search terminates at a wall, increment $n_{\text{bodycross}}$ by 1.

6. If no donor is found, decrease l by 1, go to step 3 and repeat the process at the next level. Repeating the stencil walk with different initial donor guesses at different levels makes the donor search process more robust. Also, since the stencil walk is performed from several starting points, the algorithm is independent of mesh topology.

7. If no donor is still found after traversing all levels, assume that the there is no valid donor. If the donor search terminated at the wall at all levels, then assume the grid point to be inside the wall (i.e., iblank=0).

2.4 Gap Modeling

The ability of the TEF to adjust the airloads, particularly the pitching moment, is critical for its performance in a swashplateless rotor. One important factor that could affect the effectiveness of the TEF is the presence of gaps at the leading edge of the TEF. Although the presence of gaps is not intended in the design, usually there are some flow leakages along the chordwise and spanwise edges of the TEF. Flow through these gaps could induce flow across the airfoil and affect the

flap effectiveness. It would therefore be useful to understand the extent to which gap flow affects the airloads of a TEF airfoil and ultimately the performance of a swashplateless rotor. In the present work, the effect of gap is modeled in 2D using different techniques :

1. Gap averaging technique.

2. Gap modeling using patched meshes.

3. Gap modeling using overlapping meshes.

Each of these are explained in the following sections.

2.4.1 Gap Averaging Technique

This method simulates a "pseudo-gap" by averaging the flow variables over upper and lower surfaces of the airfoil in the region across the gap (see Fig. 2.20). The flow variables at corresponding grid points that lie immediately adjacent to the airfoil on the lower and upper surfaces of the airfoil are averaged and the values so obtained are then set to the corresponding grid points on the airfoil surface.

$$q_l(j, k = 1) = q_u(j, k = 1) = \frac{1}{2} \left(q_l(j, k = 2) + q_u(j, k = 2) \right) \qquad (2.56)$$

where, q denotes the non-conservative flow variables (ρ, u, v, p); the subscripts l and u refer to lower and upper surfaces respectively; j denotes a grid point in the chordwise direction; $k = 1$ denotes a grid point on the surface of the airfoil (marked green in Fig. 2.20) while $k = 2$ denotes a grid point that is immediately above the
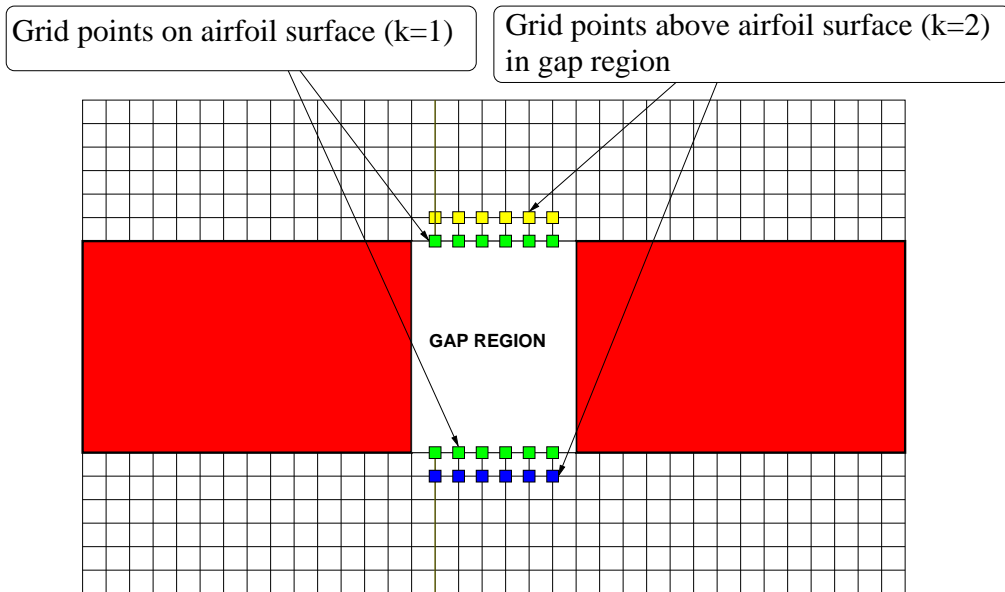
Figure 2.20: Schematic explaining the gap averaging technique.

surface (marked yellow and blue in Fig. 2.20). The non-conservative flow variables on the surface are then used to determine the conservative variables on the surface of the airfoil.

This approach has the effect of equalizing the density, pressure and velocities on the upper and lower surfaces of the gap. Although, in reality there would be a small pressure gradient across the gap, assuming the pressures to be equal provides a very useful approximation that significantly simplifies the gap treatment without any computational penalties. Since the actual flow in the gap is not directly modeled, this approach uses only a single airfoil mesh which may be identical to one used in the "no gap" simulation.

2.4.2 Gap Modeling Using Patched Mesh

This problem is relatively more involved because the treatment of the gap requires the use of two meshes and care needs to be taken to appropriately transfer information between meshes and apply boundary conditions. In this approach, a patched mesh is used to model the effect of the gap at the flap leading edge. The patched mesh overlaps the main airfoil mesh over 10 grid lines (see Fig. 2.21). Because a patched mesh is used, the number of grid points along the chordwise direction in the airfoil mesh should match those in the patched mesh. In the present work, the number of points along the thickness of the gap was taken to be 5 times the number of points across the gap in the chordwise direction. Since the gap is small and requires a large number of grid points in the chordwise direction in order to capture the boundary layer, the main airfoil mesh has to be strongly clustered in the vicinity of the gap. However, clustering the grid in the vicinity of the flap followed by grid deformation could affect the grid quality and often leads to convergence issues. Also, the time-step sizes required for this problem need to be small and this imposes penalties with regard to computational time.

2.4.3 Gap Modeling Using Overlapping Meshes

Another approach to model the gap is to use overlapping grids. The present work uses the IHC code described earlier and adapts it for solving the TEF with gap problem. Because of the assumptions made by the earlier IHC approach, the treatment of the gap problem using the same main airfoil mesh as the "no gap"
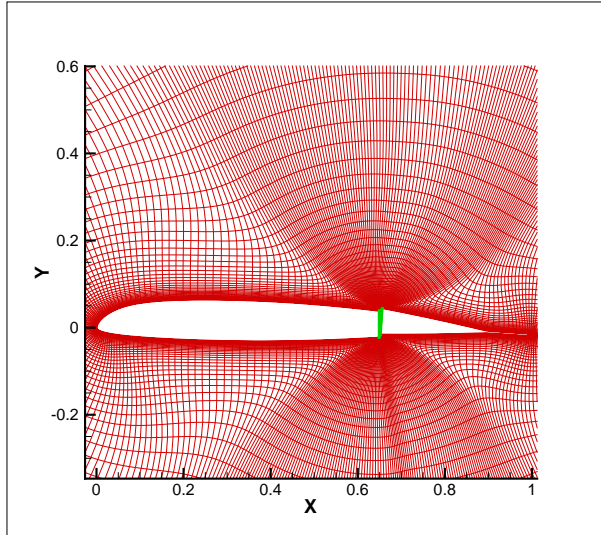
(a) Zoomed out view
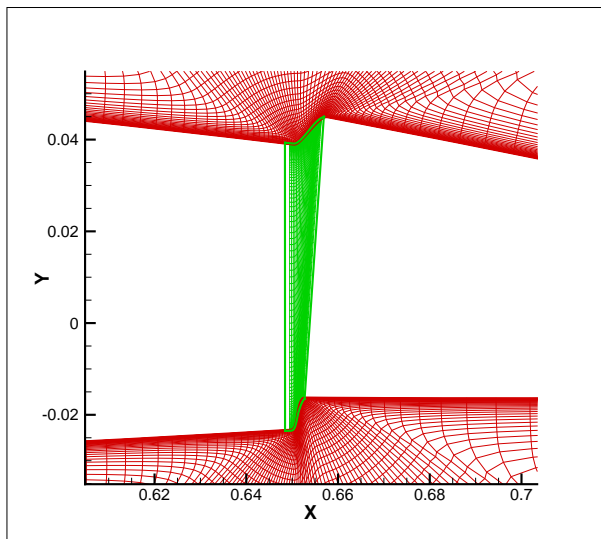
(b) Close up of gap

Figure 2.21: Patched grid used for direct simulation of gap at flap leading edge.

78

(a) $\delta = 0°$ (b) $\delta = 4°$
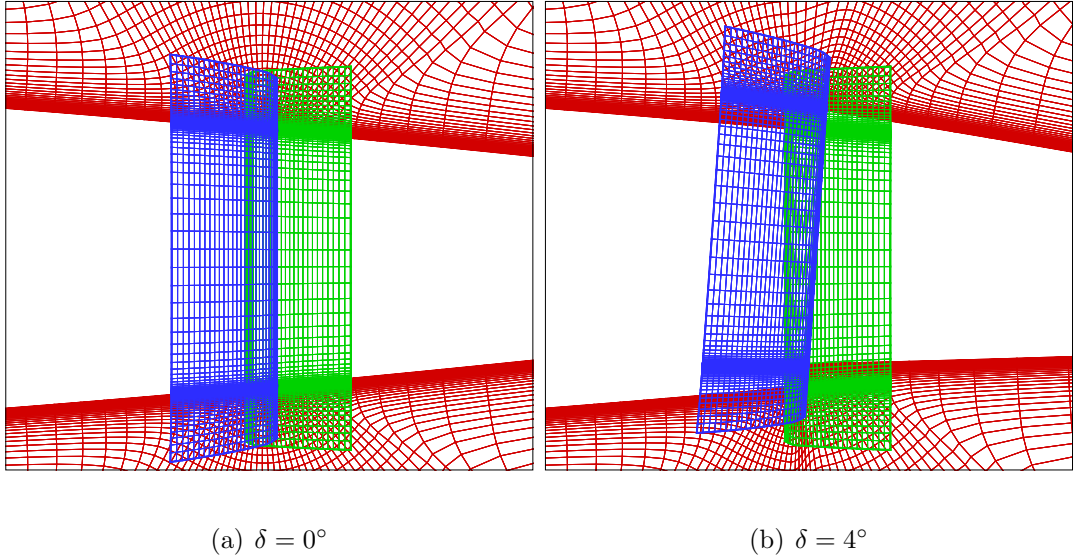
Figure 2.22: Grid layout in the gap region without iblanking for a NACA0012 airfoil with 1% gap, OH=40%.

problem requires some adjustments. The direct approach to model the gap would be to generate separate meshes around the main element of the airfoil and trailing edge flap and allow the IHC code to automatically determine the connectivity of the meshes in the gap region. Grid points from either mesh which fall inside the solid body of the other mesh would be blanked out in the process. While this approach is straightforward from the perspective of the IHC code, it involves adjustments in the main grid generation and solver codes with which the IHC code interacts. This means that for identical geometries with and without the gap, the mesh system and solver procedure would have to undergo significant restructuring. Therefore, rather than modify the solver/grid-generation system, the existing IHC code was extended so that it could use the same grid from a "no gap simulation" and simulate a cut/gap so that flow may now pass through the body.

In the present study, the gap was modeled by using two gap grids, one attached

79
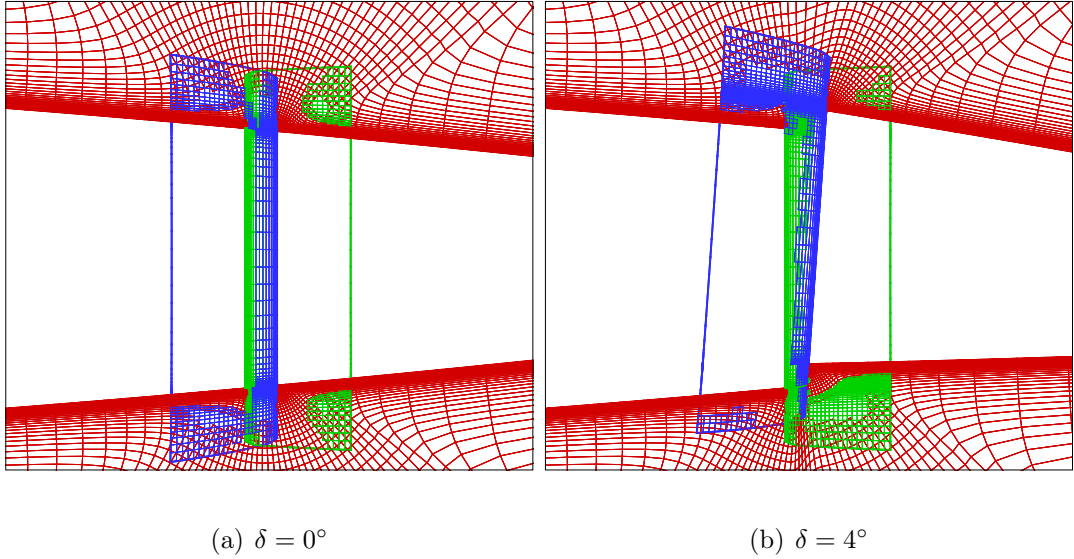
Figure 2.23: Grid layout in the gap region with iblanking for a NACA0012 airfoil with 1% gap, OH=40%.

to the wall of the main airfoil element and the other attached to the wall of the flap leading edge. Figure 2.22(a) shows the grid system with the flap undeflected. When the flap deflects, the grid attached to the flap is rotated by the same angle as the flap deflection, while the grid attached to the main airfoil element is kept stationary. The fact that the gap grid is rotated instead of deformed, ensures that the grid cells do not become skewed and the convergence issues associated with the earlier patched mesh approach are eliminated. Figure 2.22(b) shows the grid system when the flap is deflected. Each gap grid is extended well beyond the wall of the opposing gap grid so that even when the grids are rotated, they have a region of overlap. This also facilitates better information transfer with the main airfoil mesh.

Once the grid is deformed, the IHC code is used to establish the connectivity. For all grids, a fixed number of grid lines (say 15–20) from the wall are immunized, i.e., their values are not interpolated from another grid. However, for main airfoil

grid points (including wall points) which lie within the gap grids *and* between the grid lines containing the gap walls the rules are reversed, i.e., the immunized grid points (including the wall points) are forced to become receiver points whose values are interpolated from the gap grids.

One challenge with treating gap meshes using the existing IHC code was that gap mesh points inside the main airfoil body are treated as inside body points. In order to overcome this problem, some modifications were introduced in the IHC code. A "wallcut" array is specified, which establishes a relationship between the grids involved in the overset grid system so that certain meshes are allowed to cut through the wall of other meshes without being treated as inside body points. Also, special care must be taken to ensure that the corner points of the gap are not iblanked and that immunized grid points of either gap mesh do not intersect each other.

(a) Top   (b) Bottom
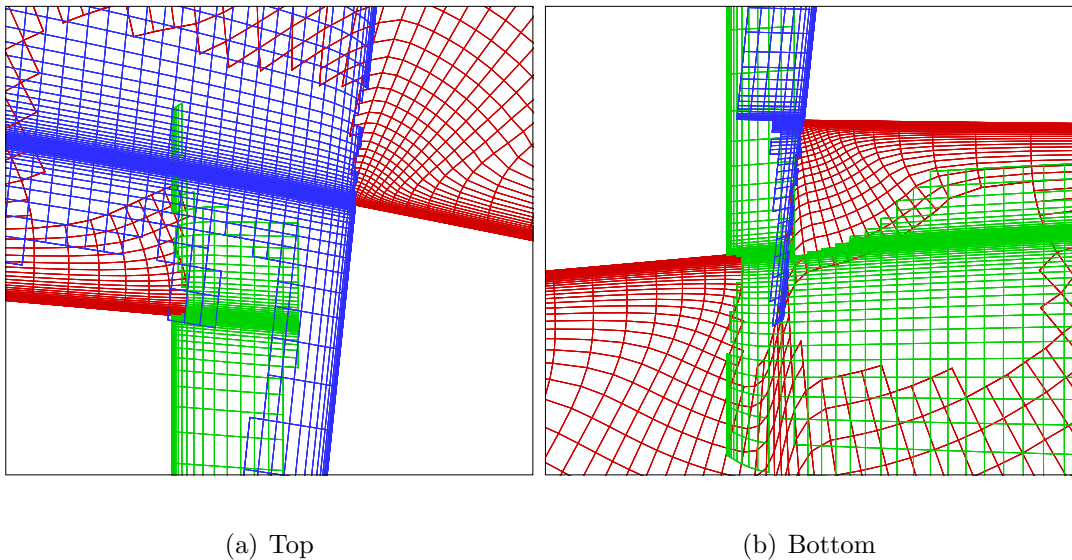
Figure 2.24: Zoomed view of top and bottom of the gap for a NACA0012 airfoil with 1% gap, $\delta = 6°$, OH=40%.

Figures 2.23(a) and 2.23(b) show the grid system after the implicit hole cutting procedure is carried out. As can be seen from the figures, the IHC approach does not create a single hole but rather, treats the smallest cell at a given point as the donor cell. Notice also that a fixed number of grid-lines near the wall are immunized irrespective of their size. Another important point to note is that the last three layers of non-wall-boundary grid-cells of any grid are not allowed to be donors. This ensures that there is sufficient overlap between two grids at their boundary interface.

Figure 2.24 shows a zoomed view of the top and bottom regions of the gap for a flap deflection of $6°$. As seen in the figures, the gap grids slide past each other and therefore do not get skewed when the flap is deflected. It is also seen that cells having the smallest volume is chosen at any given region (unless overruled by the wall or boundary immunization criteria) thereby leading to an optimum grid connectivity. Another point to note is that the grid spacing at the gap walls can be refined independent of the main airfoil mesh. All these features illustrate the advantages of the IHC method.

2.5   3D CFD Simulations

The 3D CFD simulations involve a full-fledged rotor blade. For all the simulations performed in the present work, a four bladed rotor is modeled. Since the present work only considers hover simulations, the CFD computations need to be performed only on one blade. Simulations are performed for baseline (conventional) and swashplateless TEF rotors.

2.5.1 3D CFD Solver – OVERTURNS

The computations are performed using the overset structured mesh solver OVERTURNS (Ref. 98). All the computations are performed in a time-accurate manner in the inertial frame of reference. The code solves the compressible RANS equations using the diagonalized approximate factorization framework, described by Buelow et al. (Ref. 99) and Pandya et al. (Ref. 100). The diagonal form of implicit approximate factorization method was originally developed by Pulliam and Chaussee (Ref. 101). The inviscid terms are computed using a third order MUSCL scheme utilizing Koren's limiter with Roe's flux difference splitting and the viscous terms are computed using second order central differencing.

2.5.2 Mesh System

For the baseline rotor simulations, the mesh system consists of a $133 \times 130 \times 61$ C-O blade mesh and a $67 \times 174 \times 112$ cylindrical background mesh (see Fig. 2.25). For the swashplateless rotor simulations the number of points in the chordwise direction is increased from 133 to 161 in order to capture the gradients at the flap leading edge/gap. The background mesh extends $4.5R$ below the rotor, $3R$ above the rotor and $4R$ in the radial direction. Appropriate clustering is used in regions with high gradients. This mesh is used for the thrust sweep and performance calculations. For some cases, a finer mesh with a $265 \times 259 \times 61$ blade mesh and a $67 \times 347 \times 223$ background mesh is used. For the fine mesh simulations, the grid spacing was set to ≈ 0.025-chord in the regions (tip, root, TEF edges) where vortices are expected

to be present. For the swashplateless rotor, the juncture of the TEF is treated by a gradual change in the flap deflection (see Fig. 2.26). Although this might involve some approximation in the geometry at the TEF juncture, the resultant inaccuracies in airloads would not be significant. The implicit hole-cutting technique (Ref. 85) is used to find the connectivity information between overset meshes (see Fig. 2.25(d)).
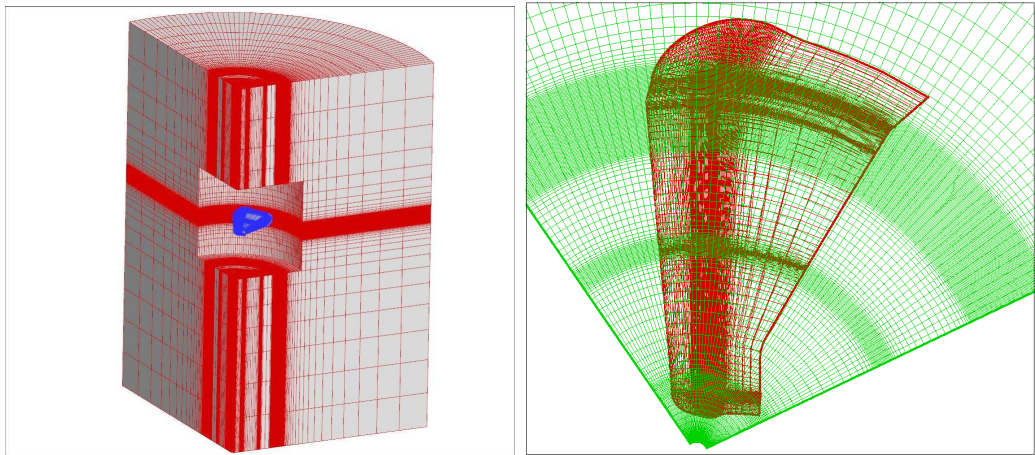
(a) 3D view of background mesh

(b) Top view of blade and background mesh
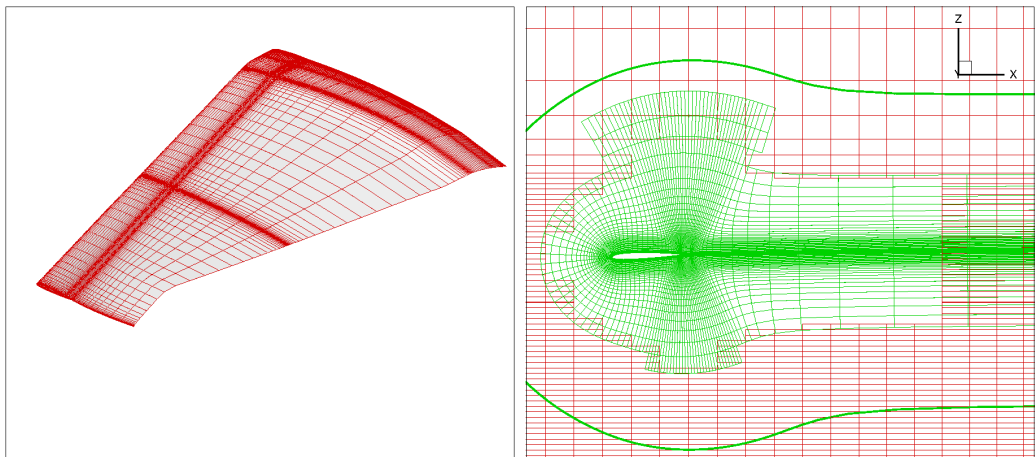
(c) Blade surface grid

(d) Blade cross section with IHC

Figure 2.25: Mesh system
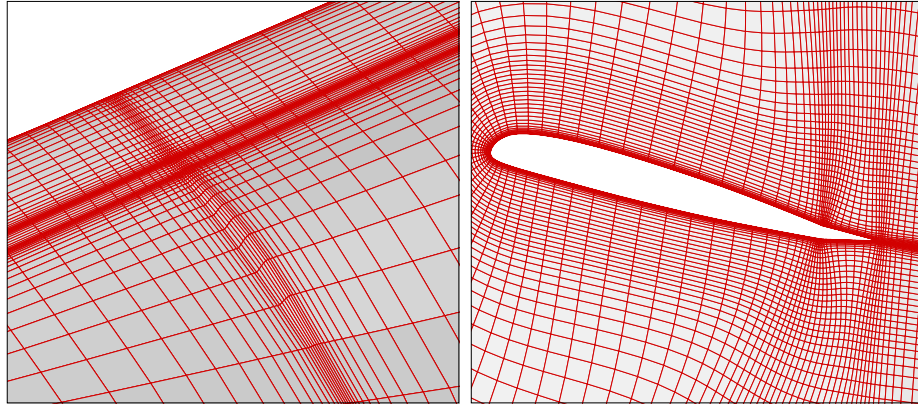
(a) TEF grid fairing   (b) TEF Cross section

Figure 2.26: TEF grid

2.5.3 Structural Dynamics Solver – UMARC

The blade deformations for a given C_T/σ (or TEF deflection) are obtained from the University of Maryland Advanced Rotorcraft Code (UMARC) (Ref. 102). The rotor blades are modeled as second-order nonlinear isotropic Euler-Bernoulli beams. The blades undergo coupled flap, lag, torsion and axial degrees of motion. A lifting line model is used to obtain the airloads. The sectional blade lift, drag and pitching moment coefficients are obtained using table look up for most cases. The table lookup data is largely obtained from 2D CFD simulations. A Weissinger-L near wake model (Ref. 103) is used along with Leishman-Beddoes 2D unsteady aerodynamic model (Ref. 104). In the present work, a uniform inflow model (rather than a free-wake model) is used in UMARC so as to achieve better convergence within UMARC.

2.5.4   CFD-CSD Coupling

CFD-CSD coupling for a rotor can be modeled using loose coupling or tight coupling. In the loose coupling approach, the airloads and blade deformations are exchanged between the structural and CFD solver codes only at the end of one (or more) rotor revolutions. In the tight coupling approach (Ref. 105, 106), the information is exchanged between the codes at every time-step. The loose coupling approach is limited to steady, periodic flight conditions. The tight coupling approach is more accurate and can handle more complicated flight conditions such as maneuvers. However, the computational cost for tight coupling is much higher. Since the present work focuses only on hover, the loose coupling approach is adequate.

The present work uses a python based coupling library to establish communication between the CFD and CSD codes (see Fig. 2.27). Loose coupling is implemented using the delta method proposed by Tung et al. (Ref. 65) and is described in Fig. 2.28. Note that, in the Fig. 2.28, F/M refers to forces or moments; the subscript i refers to the ith coupling cycle; the superscript LL refers to results obtained using lifting line theory, which is used in the comprehensive rotor analysis code to estimate the airloads. The approach involves the following steps :

1. The structural dynamics code (UMARC) is first used to obtain an estimate of the blade deformations, trim control angles and sectional airloads (forces, F_0^{LL} and moments, M_0^{LL}) using a lifting line approach (with lookup tables) for calculating the aerodynamic loads.

2. The structural deformations and trim specifications provided by CSD are used
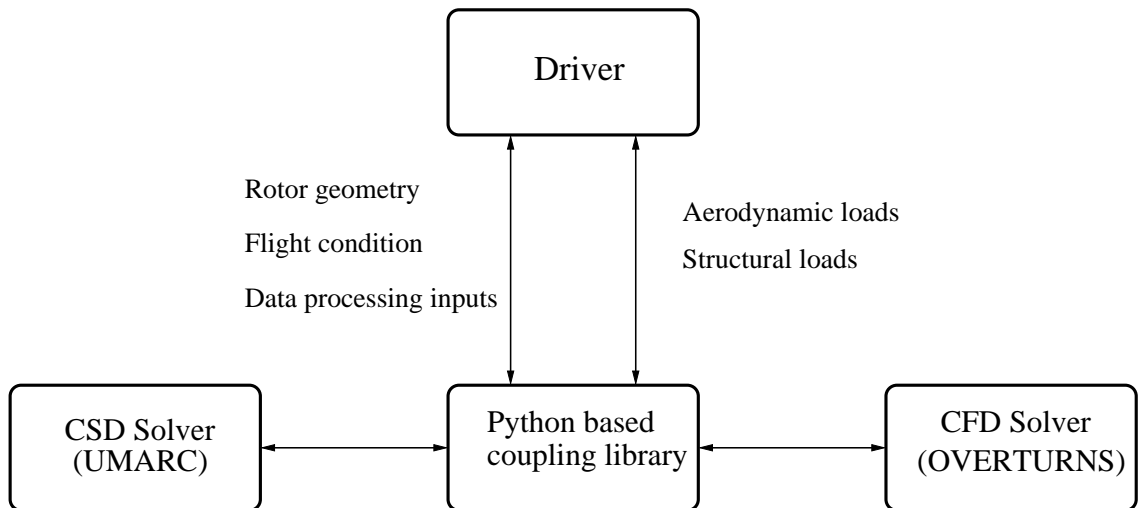
Figure 2.27: CFD-CSD code

by the CFD solver to predict the blade airloads.

3. The difference between the airloads obtained by the CFD and CSD modules are the "delta" airloads. These delta airloads are used to correct the lifting line airloads in the next UMARC trim calculations. The new trim state and blade deformations obtained from the improved airloads are then provided as inputs to the CFD solver for the next cycle.

4. This process of deformation/trim or airloads exchange between the CSD and CFD modules is repeated till satisfactory convergence of the control angles is observed, at which point the airloads prediction by the CFD and CSD modules are nearly identical.
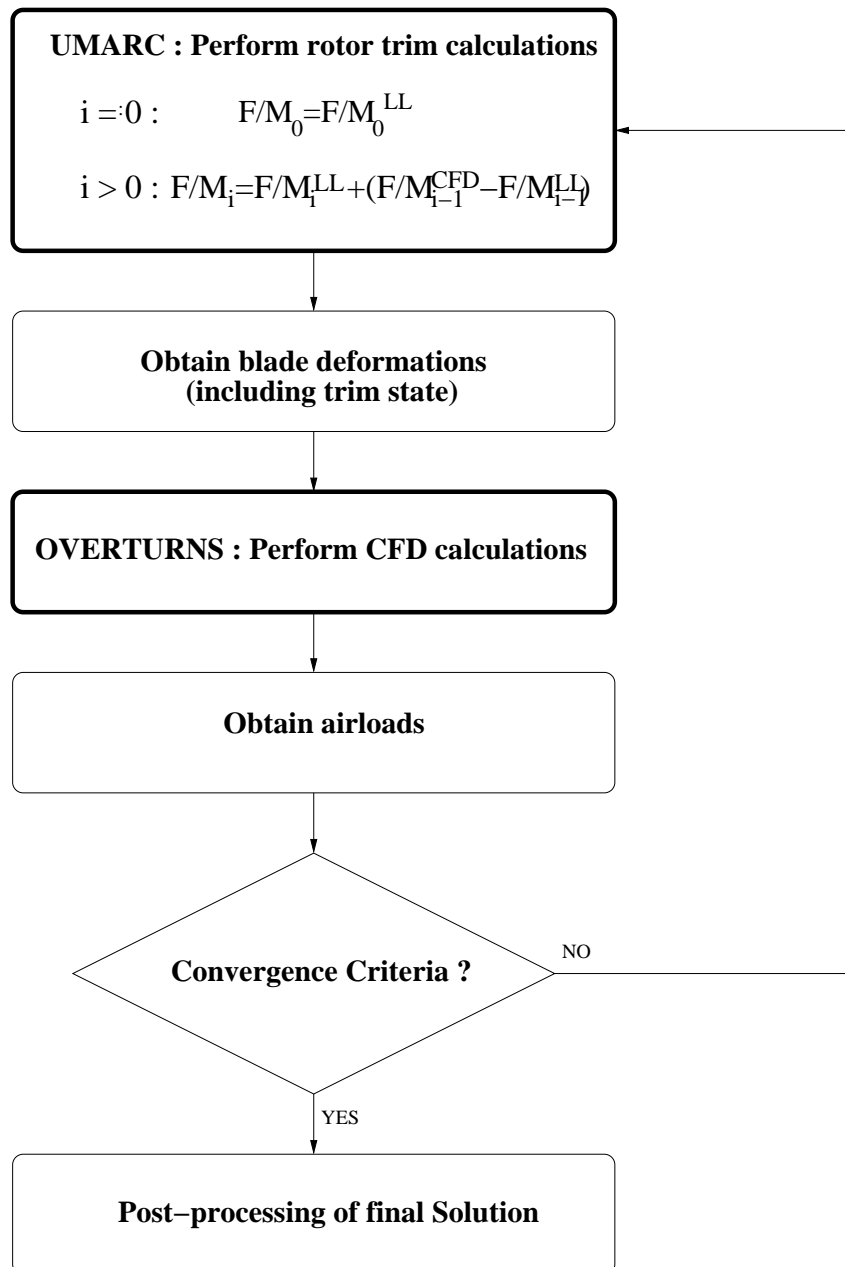
Figure 2.28: CFD-CSD coupling algorithm.

2.5.5 Gap Averaging

The 3D gap averaging technique is identical to the 2D gap averaging technique with the addition of an extra dimension. In 3D, the gap averaging is done in spanwise and chordwise directions. For most of the runs, a chordwise gap of 1% chord and a

spanwise gap of 1% radius is used. Figure 2.29 shows the regions where gap averaging is applied on the surface of a swashplateless UH-60 rotor. The blue (spanwise gaps) and red (chordwise gaps) regions marked on the blade surface indicates the grid points at which gap averaging is applied for $0.01c$ chordwise and $0.01R$ spanwise gaps.
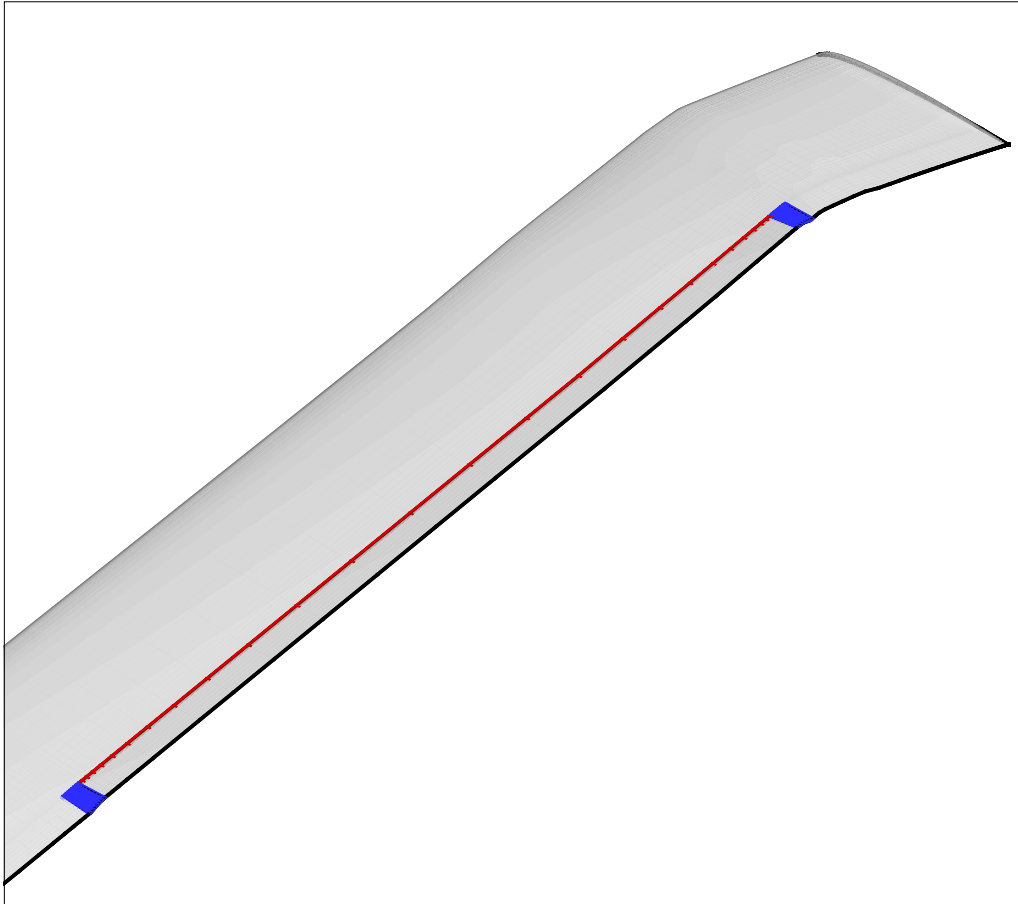
(a) Spanwise and chordwise gaps (full view)
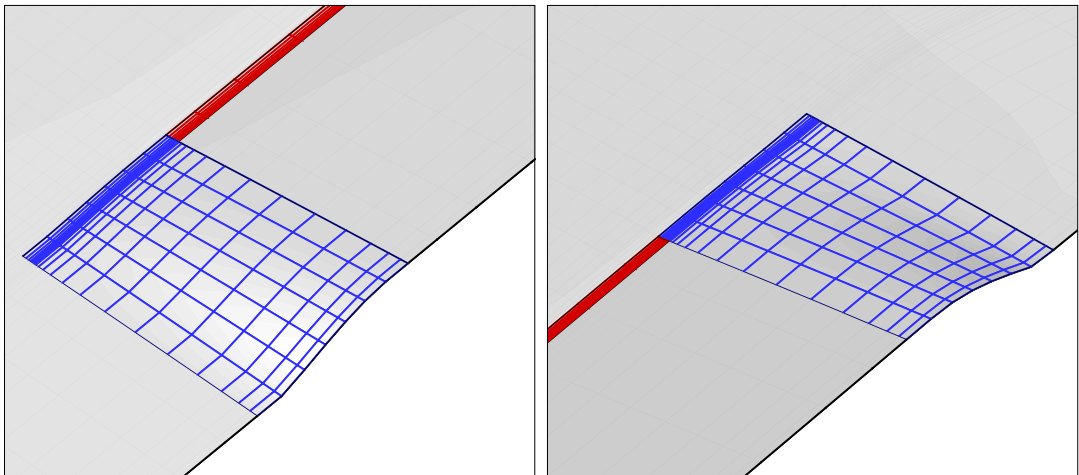
(b) Inboard spanwise gap (zoomed view)

(c) Outboard spanwise gap (zoomed view)

Figure 2.29: Zoomed view of inboard and outboard spanwise gaps for the swash-plateless UH-60 rotor.

Chapter 3

2D TEF Aerodynamics

This chapter looks into the aerodynamics of a 2D trailing edge flap (TEF) airfoil. The effect of different airfoil design parameters (airfoil thickness, overhang, gap, etc.) and the aerodynamic phenomena associated with TEF airfoils are studied. Firstly, the 2D CFD code is validated for steady, unsteady and overset grid problems. Then, the effect of TEF airfoil design features like overhang, airfoil thickness, etc. are studied. Next, the effect of aerodynamic phenomena such as compressibility, flow separation and vortex shedding on the airloads is studied for TEF airfoils by performing simulations over a wide range of flow conditions.

The 2D analysis provides valuable insights which can be considered while designing swashplateless TEF rotors. Also, the data obtained through 2D CFD simulations can be used for generating lookup tables which can be used in 3D comprehensive rotor analysis codes.

3.1 Code Verification/Validation

Validation is important for the establishing the reliability of a code. This section shows the validation studies performed for the different 2D aerodynamics problems considered in the present work. First, the CFD results are verified by comparing them with the unsteady linear aerodynamic model. The 2D steady CFD

model for the trailing edge flap with overhang is then validated with experimental data. Finally, different strategies for modeling the effect of gaps in a TEF airfoil are compared with experimental results and their relatives merits are evaluated.

3.1.1   2D Unsteady Aerodynamic Model

In the present work, unsteady aerodynamic models have been formulated for looking into unsteady airloads for a TEF airfoil. As noted in Chapter 2, the unsteady aerodynamic model can be represented in frequency and time domain form. The frequency domain solution was developed by Theodorsen (Ref. 41). The time domain solution is based on the frequency domain solution but treats the variation in the forcing (in this case, flap deflection, δ) as a series of indicial (step) changes. The time domain solution is implemented using the Duhamel integral and uses an exponential representation of the Wagner function for computational efficiency.

The unsteady CFD calculations are performed by deforming the grid in the region close to the flap. Appropriate decay parameters are used so that, at grid points far away from the flap there is little or no movement. All the unsteady CFD simulations are performed for the NACA0006 airfoil. To remove the initial transients, the CFD and lower-order time-domain simulations are performed for 5 cycles of oscillation and the final cycle is compared with the results obtained from the frequency domain solution. A reduced frequency of 0.2 was used for all unsteady cases (unless stated otherwise). All the results shown in this section were obtained for a $M = 0.3$. Therefore, compressibility effects do not manifest in the

flow. Compressibility effects for TEF airfoils may be modeled using compressible indicial models such as those described in Hariharan et al. (Ref. 93), but are not treated in the present work.

Figures 3.1 and 3.2 show the variation of the lift coefficient (C_l) for flap deflection amplitudes of 8° and 20° respectively. These are computed by running the solver in inviscid (Euler) mode for a flap size of 40% chord and a Mach number of 0.3. It is seen that there is excellent agreement between the CFD and the unsteady aerodynamic theories, even for flap deflection amplitudes as high as 20°. Once the initial transients are removed (in about 5 oscillation cycles), the frequency and time-domain solutions are mathematically equivalent and any differences would be because of the inaccuracies in the exponential representation of the Wagner function as given by Eq. 2.39. Because the frequency (Theodorsen) and time-domain (indicial) solutions are seen to be virtually identical, the time-domain solution is omitted for subsequent plots.

Figures 3.3 and 3.4 show the variation of pitching moment for $\delta = 8° \sin \omega t$ and $\delta = 20° \sin \omega t$ respectively. It is seen that pitching moment predictions also show excellent agreement with CFD. It is interesting to note that even at high flap deflection amplitudes of 20°, when thin airfoil theory predictions of steady airloads fail due to small perturbation assumptions of the theory and/or flow separation, the unsteady linear aerodynamic model provides such good predictions of the unsteady airloads. One reason for this excellent agreement is because of the inviscid nature of the CFD simulation eliminates some of the nonlinearities associated with a full Navier-Stokes solver. Another contributing reason for this behavior could be that
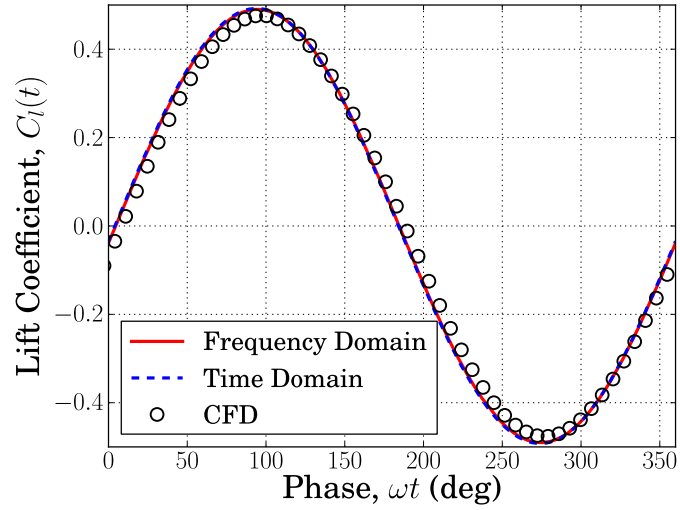
Figure 3.1: C_l vs ωt for $\alpha = 0°$, $\delta = 8° \sin \omega t$ and $x_f = 0.6$, NACA0006 airfoil (inviscid CFD calculations).
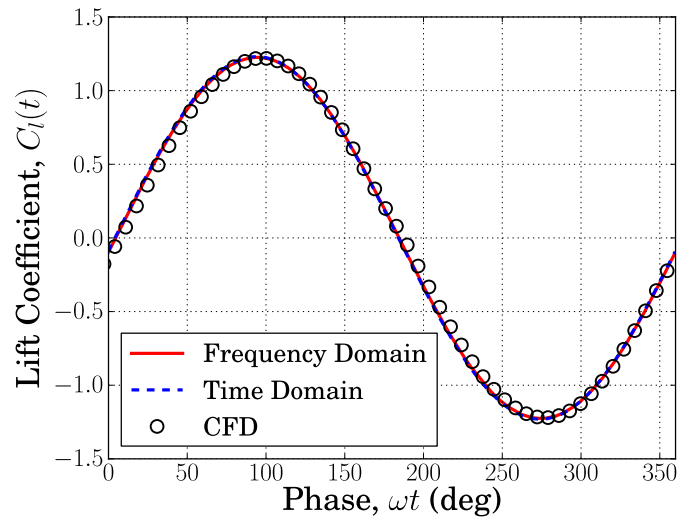
Figure 3.2: C_l vs ωt for $\alpha = 0°$, $\delta = 20° \sin \omega t$ and $x_f = 0.6$, NACA0006 airfoil (inviscid CFD calculations).

because of the high reduced frequency, even before the nonlinear phenomena have time to develop, the magnitude of flap deflection decreases quickly and returns to the

94

linear regime. Figures 3.5 and 3.6 show the hinge moments for the same conditions as for the lift and pitching moment. Although there is good agreement with CFD, the hinge moment predictions are not as good as the lift and pitching moment predictions.
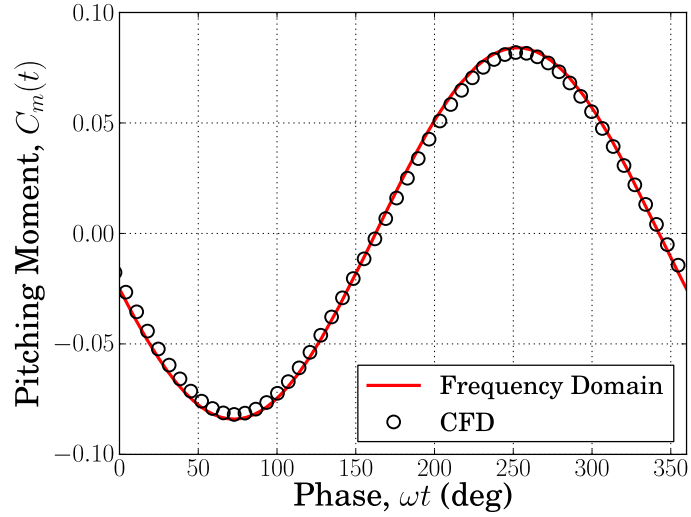
Figure 3.3: C_m vs ωt for $\alpha = 0°$, $\delta = 8° \sin \omega t$ and $x_f = 0.6$, NACA0006 airfoil (inviscid CFD calculations).

Figures 3.7 and 3.8 show the C_l variation for a viscous ($Re = 4.8 \times 10^6$, $M = 0.3$) computation for a flap size of 20% and flap amplitude of 2°. It is noted that for the Reynolds number and flap size considered here, the viscosity and flap location do not significantly affect the accuracy of the lift predictions using the unsteady aerodynamic theories (i.e., the results are similar to the inviscid computations). However, it must be noted that the amplitude of flap deflection for this viscous case is low and therefore strong nonlinear effects such as flow separation are not encountered.
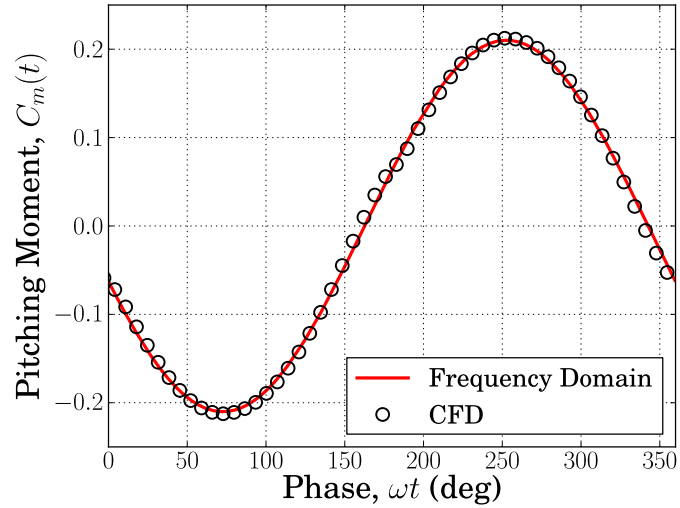
Figure 3.4: C_m vs ωt for $\alpha = 0°$, $\delta = 20° \sin \omega t$ and $x_f = 0.6$, NACA0006 airfoil (inviscid CFD calculations).
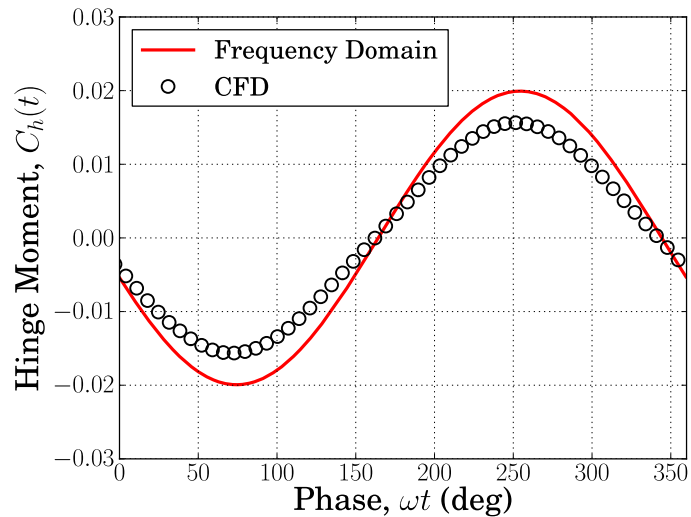
Figure 3.5: C_f vs ωt for $\alpha = 0°$, $\delta = 8° \sin \omega t$ and $x_f = 0.6$, NACA0006 airfoil (inviscid CFD calculations).

Overall, it is seen that for the cases considered, there is very good agreement between CFD and the linear aerodynamic models. However, at the same time,
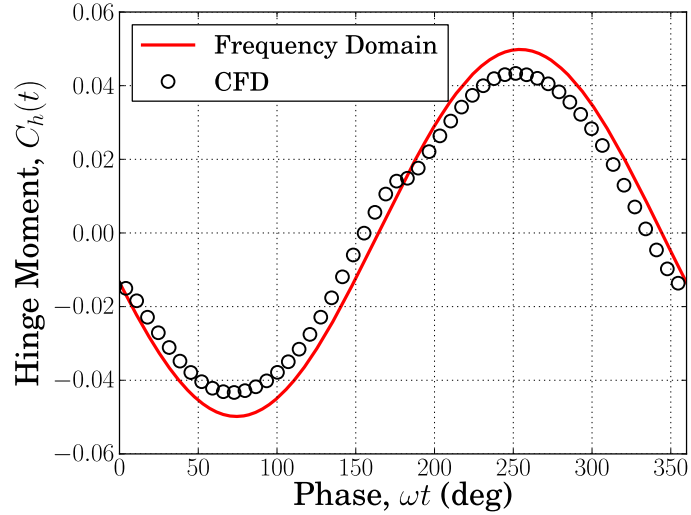
Figure 3.6: C_f vs ωt for $\alpha = 0°$, $\delta = 20° \sin \omega t$ and $x_f = 0.6$, NACA0006 airfoil (inviscid CFD calculations).

it must be noted that these results were obtained in the linear flow regime (i.e., low Mach number and angles of attack). Therefore, for the simulations considered here, nonlinear phenomena such as shocks, flow separation, etc. are not encountered. In the presence of strong nonlinear effects, the assumptions underlying the linear aerodynamic models would breakdown and they would fail to provide accurate predictions of the airloads. Thus, in the absence of any nonlinear phenomena, this study shows that the aerodynamic models provide very good predictions of the unsteady airloads at a computational cost that is about four orders of magnitude smaller than that of CFD. For example, a CFD simulation that would take about an hour to complete would take only a fraction of a second with the linear aerodynamic models.
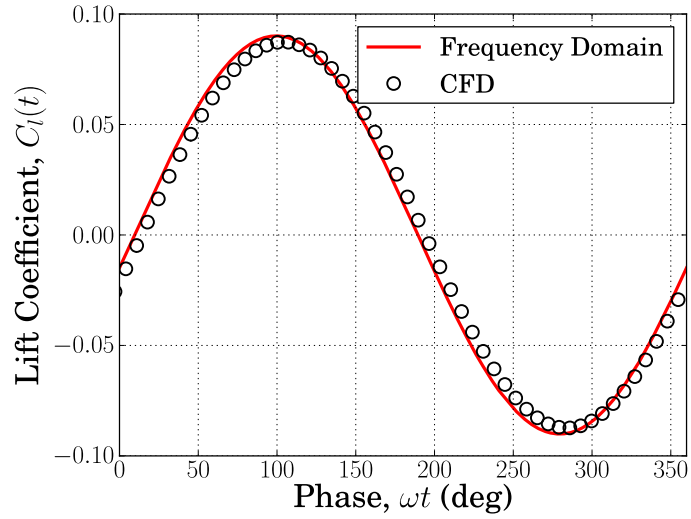
Figure 3.7: C_l vs ωt for $\alpha = 0°$, $\delta = 2° \sin \omega t$ and $x_f = 0.8$ ($Re = 4.8 \times 10^6$), NACA0006 airfoil.
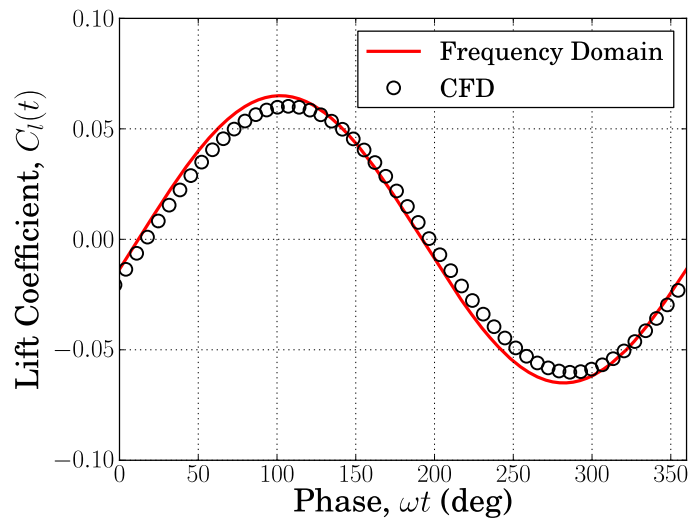
Figure 3.8: C_l vs ωt for $\alpha = 0°$, $\delta = 2° \sin \omega t$ and $x_f = 0.9$ ($Re = 4.8 \times 10^6$), NACA0006 airfoil.

3.1.2 2D TEF Airfoil with Overhang in Steady Flow

In the present work, a large number of 2D steady runs have been performed both for understanding the aerodynamics of TEF airfoils as well as for generat-

ing data for lookup tables to be used in 3D comprehensive rotor analysis codes. Therefore, validation is necessary to ensure that the code captures the flowfield and airloads accurately for TEF airfoils. The steady validation cases considered are obtained for a TEF airfoil with non-zero overhang. The definition of overhang (OH or ξ) as used in the present work is given by:

$$\xi = \frac{x_h - x_f}{1 - x_h} \tag{3.1}$$

where, x_h and x_f are the locations of the flap hinge and flap leading edge respectively, measured from the airfoil leading edge and normalized by airfoil chord. Experimental results for an integrated TEF with overhang have been obtained by Hassan et al. (Ref. 15). These are used to validate the CFD results. Results are obtained at moderate and transonic Mach numbers. Most of the tests are performed on the HH-06 airfoil which has 9.5% thickness. These two-dimensional wind tunnel tests were conducted in the NASA Langley 0.3-m Transonic Cryogenic Tunnel (TCT). For all the cases considered in this validation study, the flap hinge is located at 75% chord location. Airfoil and flap "inserts" were used interchangeably to yield flap overhang nose balance values of 35%, 40% and 45%. Note that changing the overhang changes the flap size (distance from flap LE to TE). Figure 3.9 illustrates the use of flap inserts to achieve the desired overhang in the experiments. Fifty one pressure ports were located along the main airfoil and trailing edge flap to determine the pressure distributions. For the primary airfoil (i.e., the front portion not constituting the flap), 22 ports were placed on the upper surface and 17 ports
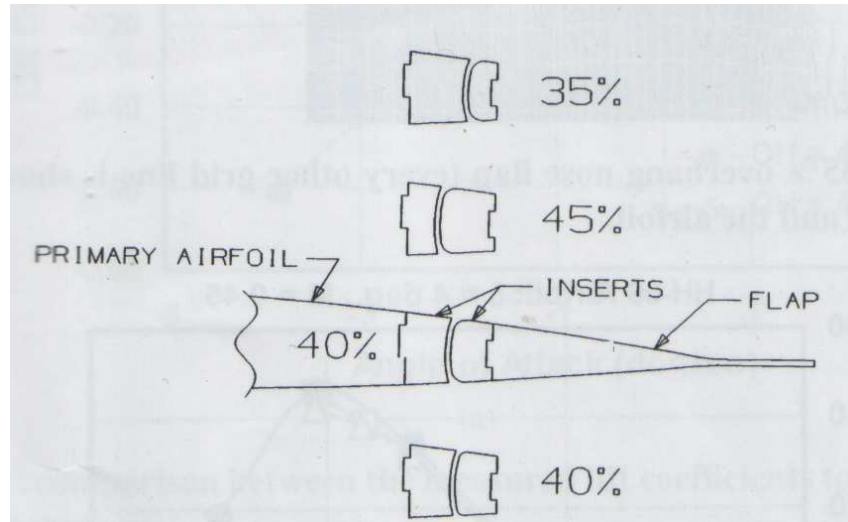
Figure 3.9: Schematic of airfoil/flap inserts used to adjust the percent flap nose overhang (Ref. 15).

were placed on the lower surface. On the flaps, 6 ports were used on the upper surface and 6 ports on the lower surface. Airfoil sectional drag values (C_d) were derived from a knowledge of the total pressure loss across the wake of the model. Moments, C_m and C_h were obtained from the integration of the surface pressures about the airfoil's quarter chord point and flap hinge respectively.

The experimental integrated airloads results are first compared with the CFD simulations without any gap treatment. Figures 3.10, 3.11 and 3.12 show the CFD validation of the experimental results for the HH-06 airfoil. It is seen that there is excellent agreement in the lift predictions for both subsonic and transonic Mach numbers (see Fig. 3.10). The predictions of the flap hinge moment are good but some deviations are observed. It should be noted that the experimental data for C_h is based on only 6 pressure ports on the top and bottom of the flap. This is inadequate to capture the strong pressure gradients near the flap leading edge
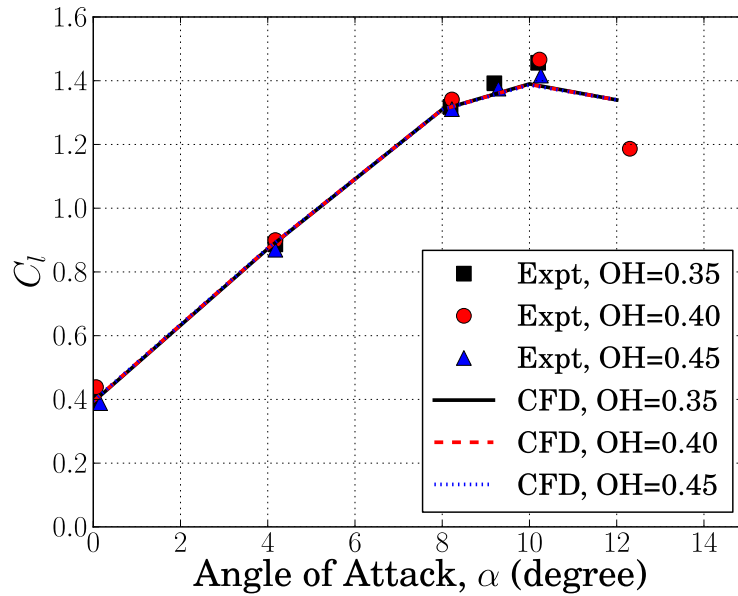
(a) C_l vs α, $M = 0.45$, $\delta = 4°$, $Re = 2.7$ million
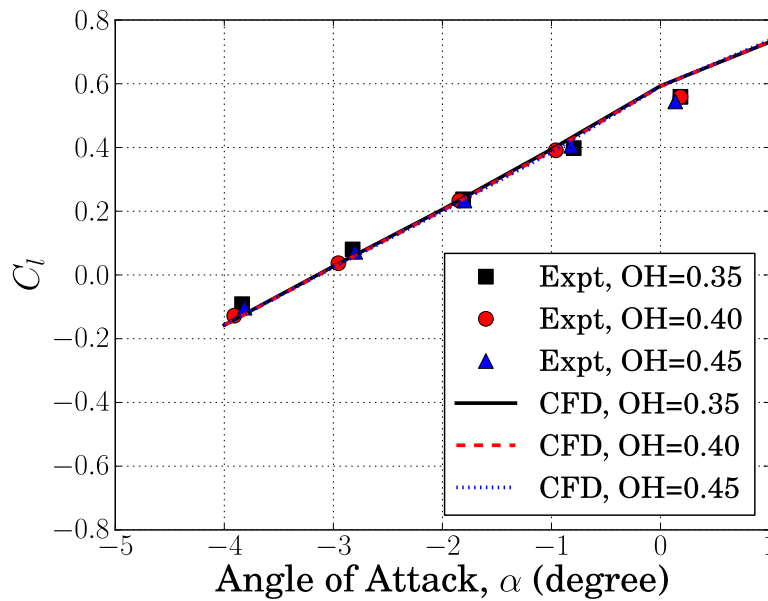
(b) C_l vs α, $M = 0.75$, $\delta = 4°$, $Re = 5.0$ million

Figure 3.10: C_l vs α using CFD and experiment for HH-06 airfoil.
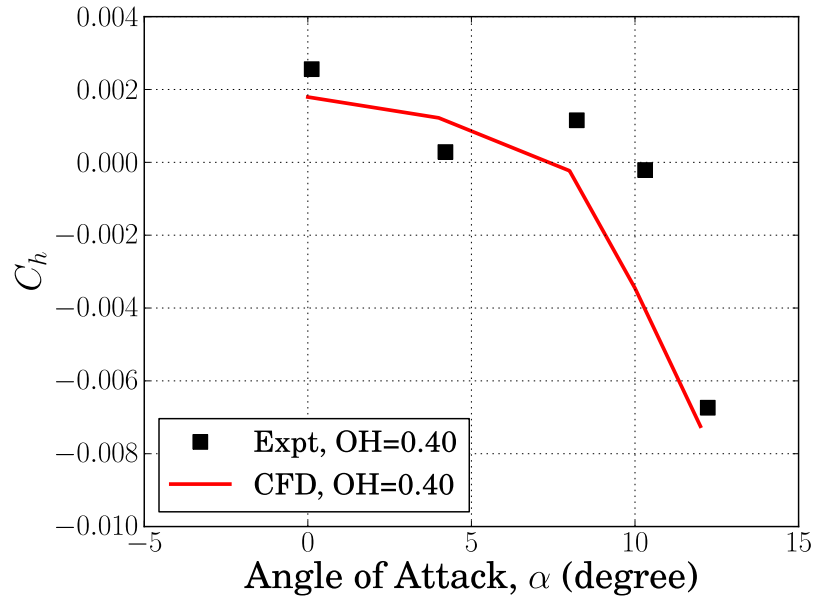
Figure 3.11: C_h vs α using CFD and experiment for HH-06 airfoil, $M = 0.45$, $\delta = 4°$, $Re = 2.7$ million.
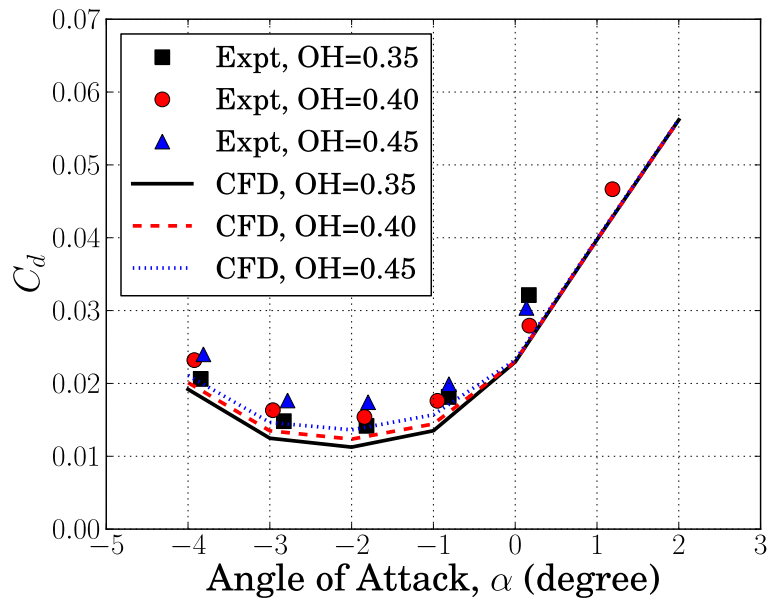
Figure 3.12: C_d vs α using CFD and experiment for HH-06 airfoil, $M = 0.75$, $\delta = 4°$, $Re = 5.0$ million.

and the errors in the results so obtained may not be negligible. The fact that the CFD and experimental results for C_h show slight deviations is therefore not surprising. Also, the finer details of the airfoil geometry at the flap leading edge for the experiment are not known exactly (although there is a small gap as mentioned later) and may influence the pressure distribution in that region. The CFD and experimental drag predictions are also seen to be in good agreement with each other. It is seen that drag increases with overhang. This is to be expected, since the increased protrusion of the flap leading edge due to overhang would be expected to offer more resistance to the flow (and possibly even induce flow separation) thereby leading to an increase in drag.

3.1.3 Gap Modeling

The different approaches to model the gap were discussed in an earlier chapter. These are :

1. The gap averaging approach.

2. Direct gap modeling using patched meshes.

3. Direct gap modeling using overset meshes.

Figure 3.13 shows the corresponding C_p profile obtained using CFD and experiment for flow over a HH-06 airfoil with 0.5% gap at $M = 0.758$, $\alpha = -4.03°$, $\delta = 4°$, $x_h = 0.75$, OH=40% and $Re = 5$ million. The experimental data is based on Hassan et. al. (Ref. 15) and the CFD results are obtained using different approaches

(i.e., no gap treatment, gap treatment using patched meshes, gap treatment using overset meshes and gap treatment using gap averaging technique). From the pressure profile, it can be seen that there are two shocks – one at the leading edge of the TEF and the other around $x/c = 0.2$ on the lower surface of the airfoil.

When the gap is not modeled, there are clear deviations in the pressure profile both near the shock and over the surface of the TEF. All the gap modeling approaches (gap averaging, patched meshes and overset meshes) show excellent agreement with experiment and are very similar to each other. The overset mesh approach differs slightly from the other two approaches on the location of the shock on the lower surface of the airfoil.

Figure 3.14 shows the Mach contours and streamlines obtained near the overhang and gap regions using the different CFD approaches for the aforementioned case. Among the direct gap modeling approaches, only the flow field for the patched mesh approach is shown. It is observed that a strong shock is formed on the lower surface of the airfoil and a small shock is formed at the leading edge of the upper flap surface. Because of the complex nature of the flow, the flow-field would be expected to be sensitive to the presence of the gap, particularly over the flap surface which lies downstream of the gap. It is seen that gap averaging has the effect of inducing an apparent flow across the airfoil even though there is no actual flow simulation inside the gap. Flow occurs from top to bottom for this case, as seen by the streamlines going into and out of the airfoil in the gap region. The gap averaging approach generates a flow field that is closer to that obtained using actual gap treatment using additional CFD meshes than when the gap is not modeled at all. Without
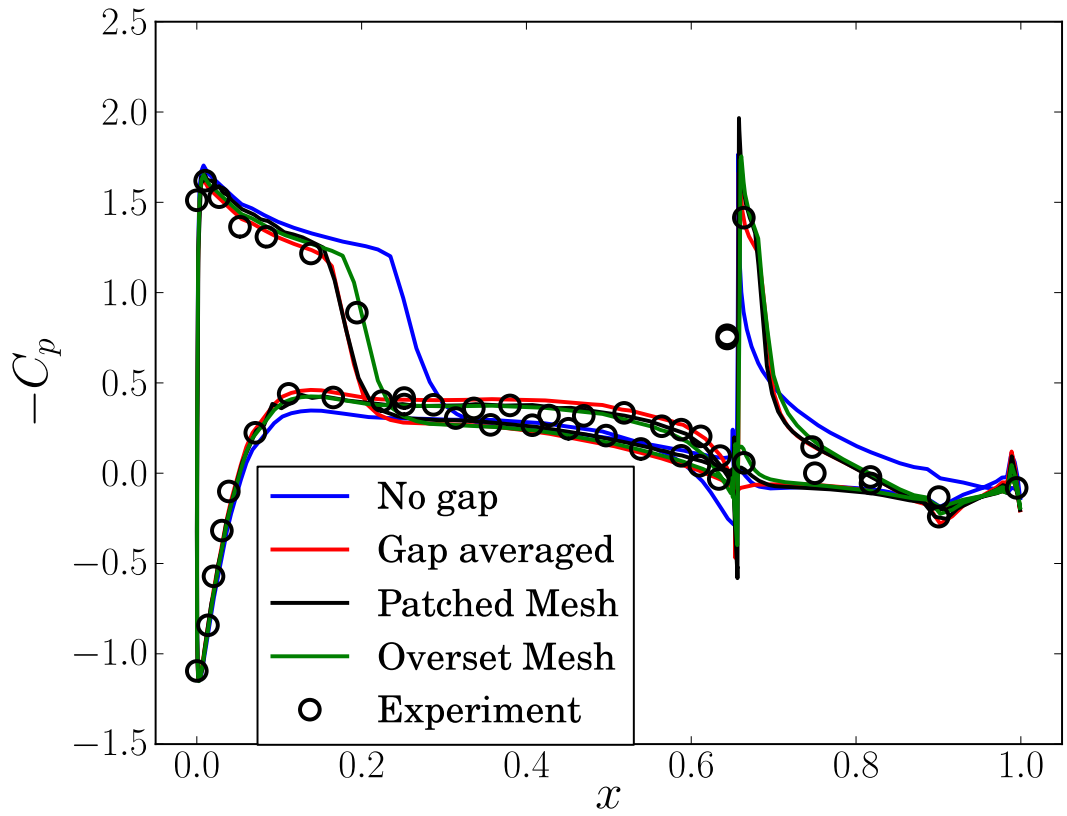
Figure 3.13: Comparison of C_p for a HH-06 airfoil using different approaches, $M = 0.758$, $\alpha = -4°$, $\delta = 4°$, $x_h = 0.75$, $Re = 5$ million.

any gap modeling, the protrusion of the flap leading edge causes a thickening of the boundary layer on the upper surface of the flap. Also, the shock formed at the flap leading edge is seen to be weak. When the gap is modeled (using gap averaging or patched/overset meshes), there is no boundary layer thickening over the upper flap surface and the shock formed is similar for the direct and approximate gap modeling approaches. The effect of the gap flow on the shock and flow separation over the flap is responsible for the differences in the pressure distribution over the upper flap surface with and without gap modeling.

The fact that the gap averaging approach gives almost the same flow field and pressure distribution as the patched mesh approach at the same computational cost as the approach that does not treat the gap, makes it very useful for handling gap problems. However, it must also be noted that the gap averaging method is an approximate method, and does not necessarily capture the actual physics for more complicated flow conditions. In particular, it does not capture the flow structures inside the gap, the effect of gap geometry or the viscous losses inside the gap. It is often seen to transfer too much momentum across the gap and thereby eliminate the recirculating flow at the flap leading edge at the bottom surface (see Fig. 3.14). Also, the simple averaging of flow variables is non-physical and may cause too much or too less of momentum transfer across the gap. Nevertheless, the gap averaging approach does offer a simple and computationally inexpensive alternative to full fledged gap modeling, and for a general problem it may certainly be expected to perform better than not treating the gap at all.
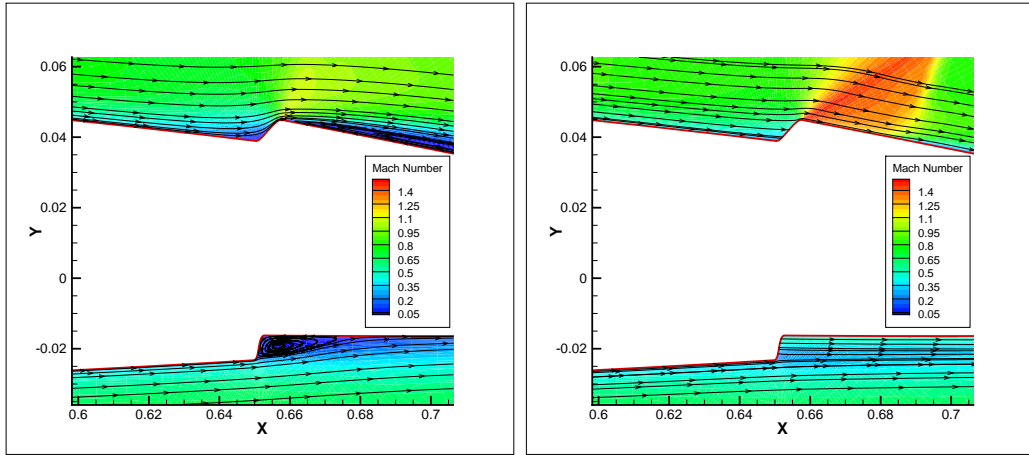
(a) No gap treatment

(b) Gap averaging
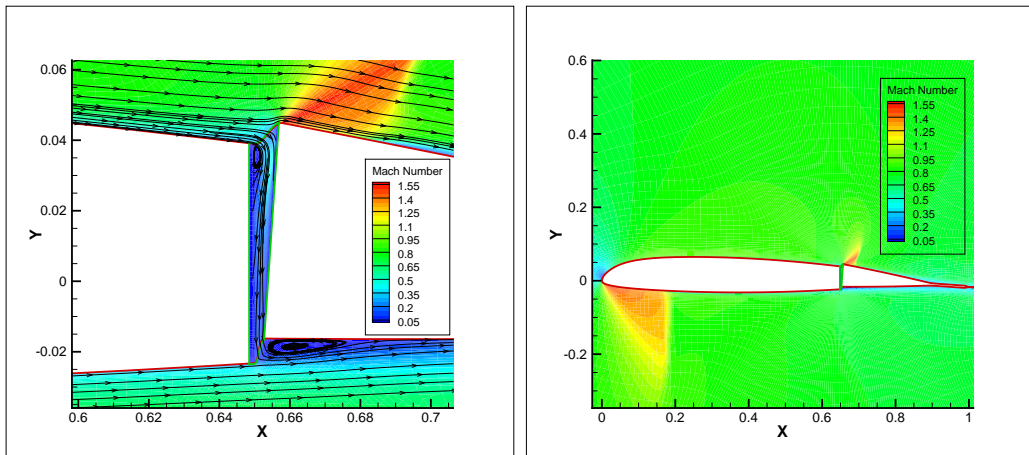
(c) Patched mesh

(d) Patched mesh (zoomed out)

Figure 3.14: Comparison of streamlines in the gap region using different approaches for a HH-06 airfoil with 0.5% gap, $M = 0.758$, $\alpha = -4.03°$, $\delta = 4°$, $x_h = 0.75$, OH=0.4, $Re = 5.0$ million.

Having established the validity of the different 2D codes (analytical and CFD), the following sections describe the application of these codes towards understanding the behavior of TEF airfoils.

3.2   Effect of Airfoil Properties

An understanding of the effect of various airfoil properties is very important for coming up with a good design. The design process requires many decisions, such as the choice of airfoil type, thickness, flap size, etc. Also, for TEF airfoils used in helicopter applications, it would be useful to understand the effect of gaps at the leading edge of the TEF. The effect of some of these airfoil properties on the behavior of TEF airfoils is discussed in this section.

3.2.1   Effect of Thickness

The thickness of an airfoil section depends on its application. Since the results obtained using thin airfoil theory are derived for a zero thickness airfoils, it would be useful to look into the effect of thickness on the steady airloads for a TEF airfoil. Figure 3.15 shows the variation of C_l, C_d, C_m and C_h with thickness for the NACA00XX family of airfoils using CFD. The results shown are obtained for $M = 0.3$, $\alpha = 0°$, $Re = 4.8$ million, $\delta = 6°$ and $x_f = x_h = 0.6$ & 0.75 (zero overhang). It is observed that for low lift conditions, C_l is not significantly affected by thickness (see Fig. 3.15(a)). Thickness would be expected to affect the lift more significantly in the nonlinear (stall, transonic) regime. However, this is not investigated in detail

in the present work. Drag on the other hand is seen to increase with thickness (see Fig. 3.15(b)). This is to be expected, since greater thickness implies greater opposition to the flow and hence more drag. A roughly linear variation of drag with thickness is observed at this low Mach number.

(a) C_l

(b) C_d

(c) C_m

(d) C_h
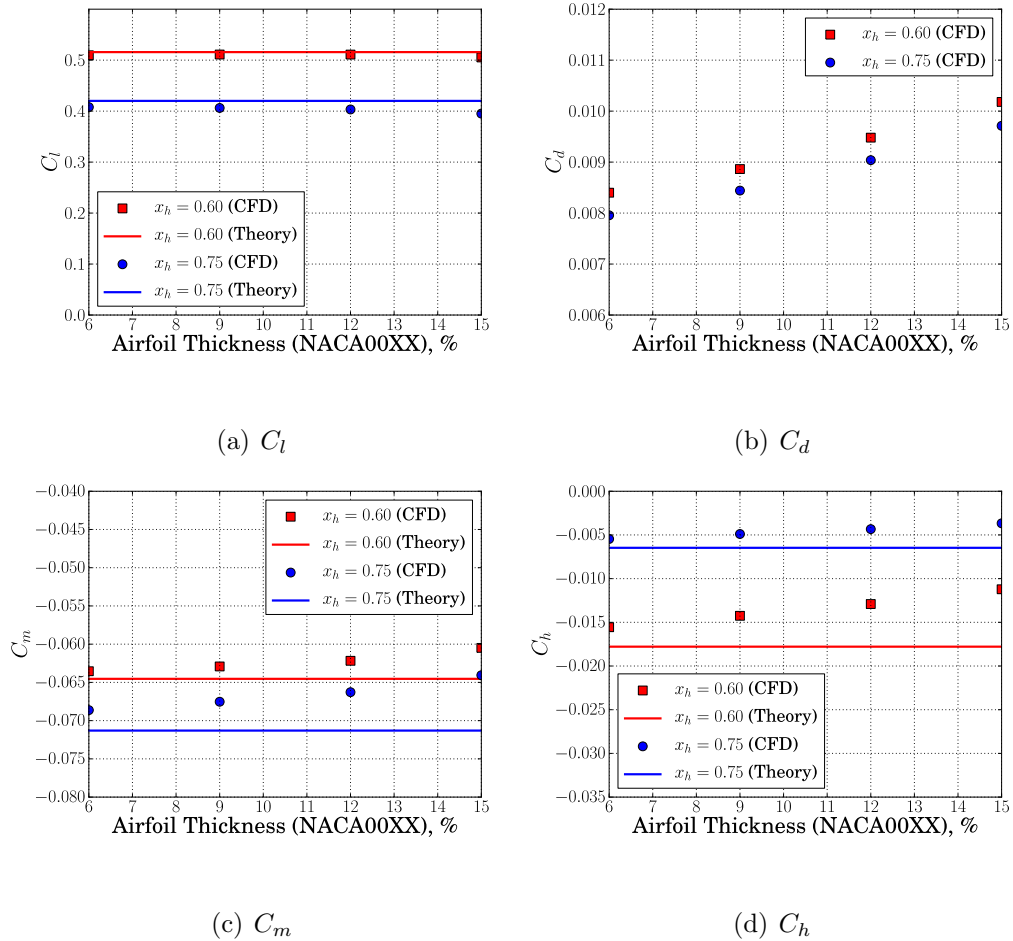
Figure 3.15: Effect of airfoil thickness airloads for the NACA00XX airfoils, $M = 0.3$, $\alpha = 0°$, $x_h = 0.60$ & 0.75, zero overhang, Re=4.8 million.

For pitching moment, a gradual decrease in magnitude is observed with increasing airfoil thickness (see Fig. 3.15(c)). A roughly linear variation is observed. The magnitude of the hinge moment on the other hand decreases linearly with airfoil thickness with the slope being roughly proportional to the magnitude of the thin

airfoil theory hinge moment. As the airfoil thickness varies from 6% (NACA0006) to 15% (NACA0015), the reduction in the magnitude of hinge moment is as high as 20% (see Fig. 3.15(d)). Figure 3.16 shows the pressure profile for different airfoil thicknesses. It is observed that as the thickness increases, the pressure variation near the airfoil leading edge becomes more rounded. Also, as the thickness increases, there is a downward movement of the pressure curve near the airfoil trailing edge. Since the form of the pressure distribution on the upper and lower surface of the airfoil changes markedly with thickness, it is difficult to attribute the trends observed in the pitching and hinge moments to a particular aerodynamic phenomenon.

3.2.2   Effect of Overhang

Figures 3.17–3.19 show the effect of overhang (OH=ξ) on the airloads (C_l, C_d, C_m and C_h) for the NACA0006 airfoil with integral trailing edge flap. The results are obtained for $M = 0.3$, $\alpha = 0°$ and $Re = 6$ million. It is observed (see Figs. 3.17 and 3.18) that the lift and pitching moment are not significantly affected by flap overhang and both CFD and theory show nearly constant values. Although Eqs. 2.6 and 2.9 show that overhang (l) affects the lift and pitching moment, it is observed that the contribution of the additional terms to the lift and pitching moment is not significant. The magnitude of the lift and pitching moment obtained using CFD is slightly lower than that obtained from theory.
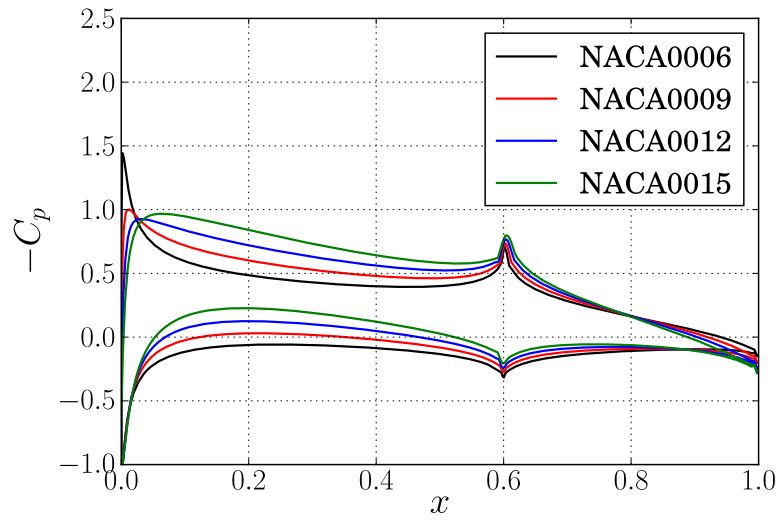
(a) $x_h = 0.60$
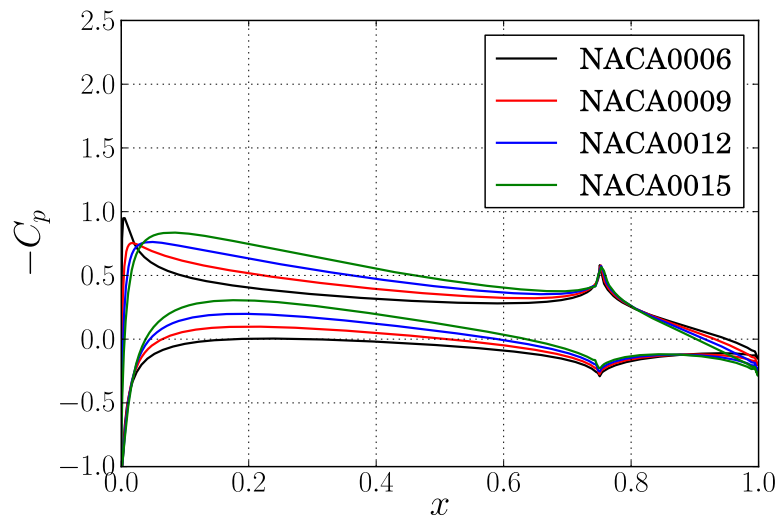
(b) $x_h = 0.75$

Figure 3.16: C_p vs x NACA0006 airfoil, $M = 0.3$, $\alpha = 0°$, $\delta = 6°$, $x_h = 0.60$ & 0.75, Re=4.8 million.
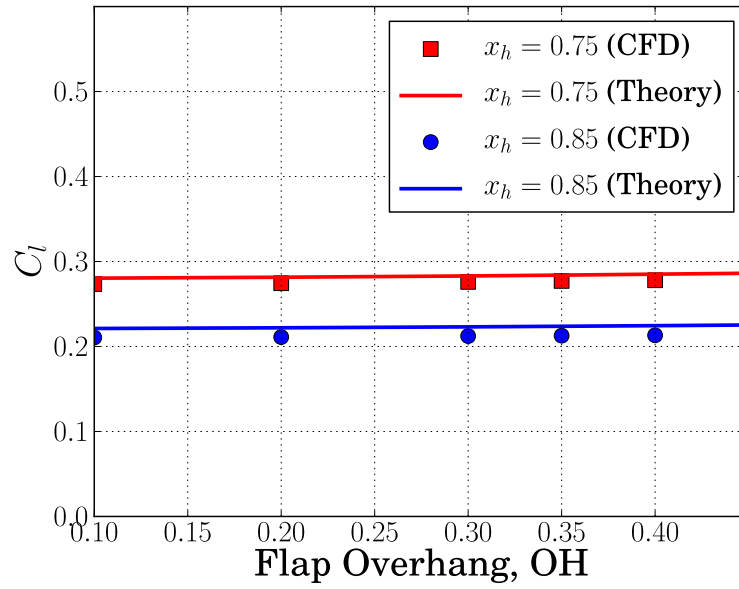
(a) $\delta = 4°$
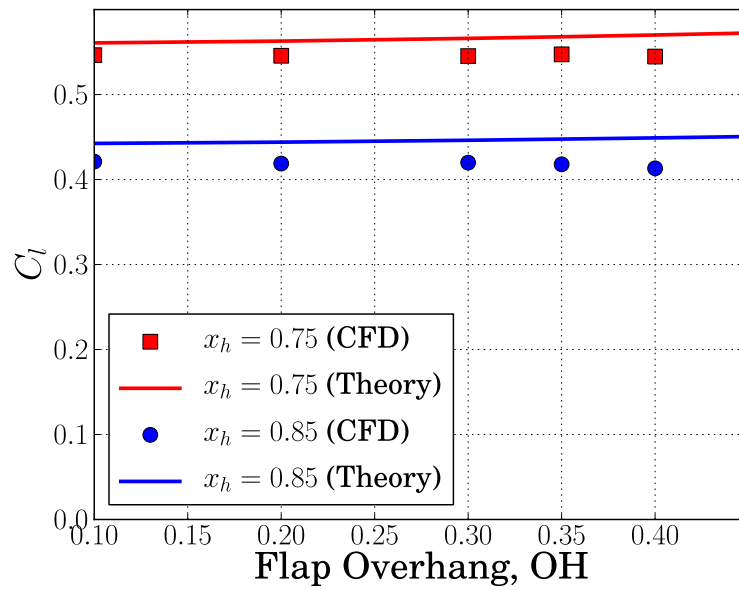
(b) $\delta = 8°$

Figure 3.17: C_l vs Overhang (OH) using CFD and theory for the NACA0006 airfoil, $M = 0.3$, $\alpha = 0°$, $x_h = 0.75$ & 0.85, Re=6 million.
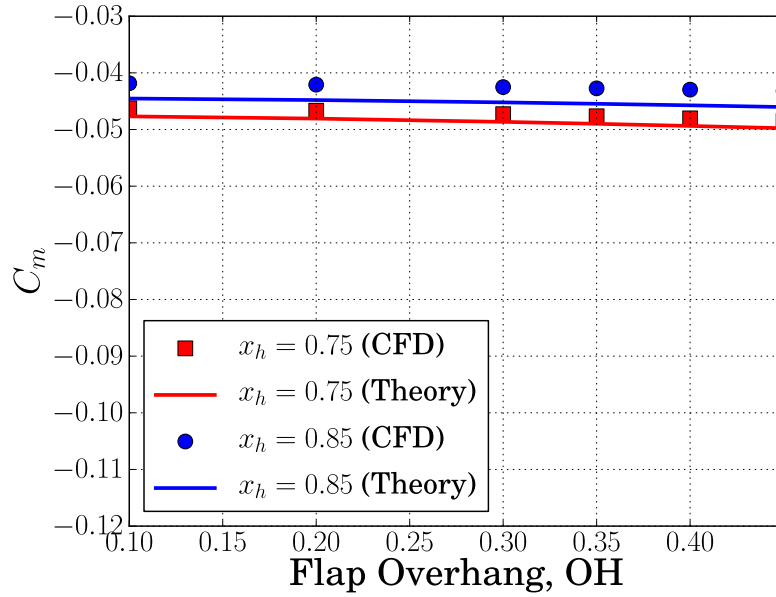
(a) $\delta = 4°$
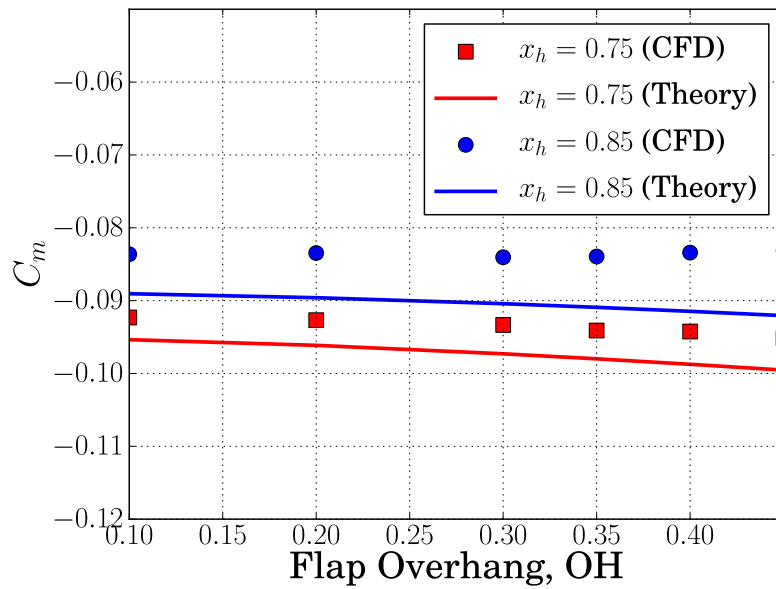
(b) $\delta = 8°$

Figure 3.18: C_m vs Overhang (OH) using CFD and theory for the NACA0006 airfoil, $M = 0.3$, $\alpha = 0°$, $x_h = 0.75$ & 0.85, Re=6 million.

The flap hinge moment (Fig. 3.19) on the other hand is very sensitive to over-

113

hang. Although an offset is observed between the CFD and theoretical results, the general trend is well captured. In particular, it is observed for this case that at a flap overhang of around 40% the flap hinge moment goes to zero. This means that by choosing a suitable flap overhang, the hinge moments and hence the actuation power can be significantly reduced without significantly affecting the lift and pitching moment characteristics. However, it should also be noted that too large an overhang could lead to a positive value of C_{h_δ} which can cause static divergence. This is because a positive flap deflection would then generate a positive hinge moment leading to a further positive deflection of the flap, and so on until divergence. Therefore, from a design perspective the overhang should be sufficiently smaller than the overhang corresponding to zero flap hinge moment. Also, for the flap sizes considered, the hinge moment does not change significantly with flap size. This is to be expected because the C_{h_α} and C_{h_δ} curves are nearly flat around $x_h \approx 0.8$ (see Figs. 2.4 and 2.5). The offset observed between CFD and theory is typical for hinge moment predictions, as will be seen in later sections.

Figure 3.20 shows the variation of drag with overhang. It is seen that for a flap deflection of 4°, the drag penalty is not too significant whereas for $\delta = 8°$, the effect of overhang on drag is more pronounced. This is to be expected because a higher flap deflection causes more protrusion of the flap leading edge on the upper airfoil surface thereby offering more resistance to the flow, while at the same time increasing the possibility of a boundary layer thickening or flow separation.
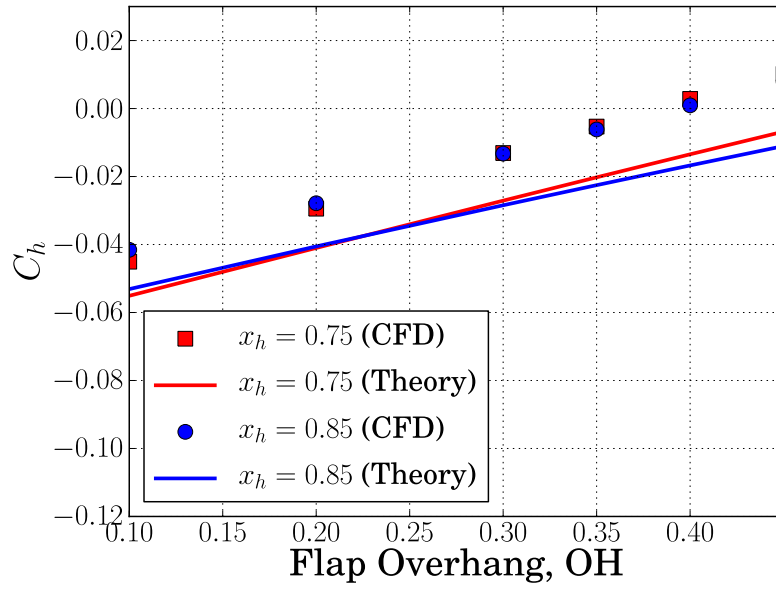
(a) $\delta = 4°$
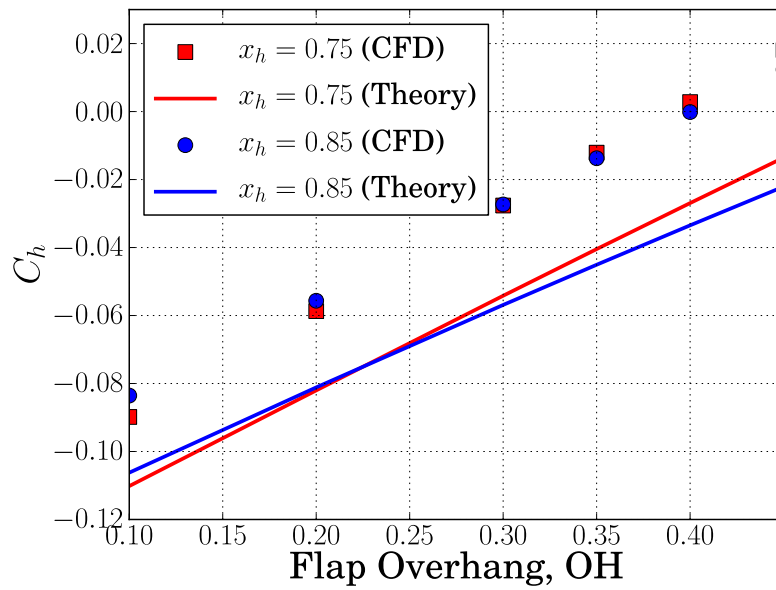
(b) $\delta = 8°$

Figure 3.19: C_h vs Overhang (OH) using CFD and theory for the NACA0006 airfoil, $M = 0.3$, $\alpha = 0°$, $x_h = 0.75$ & 0.85, Re=6 million.
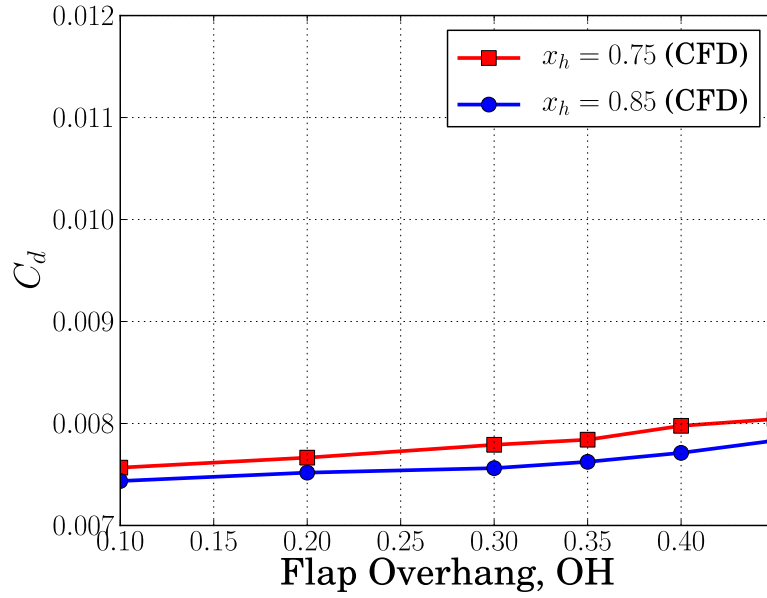
(a) $\delta = 4°$
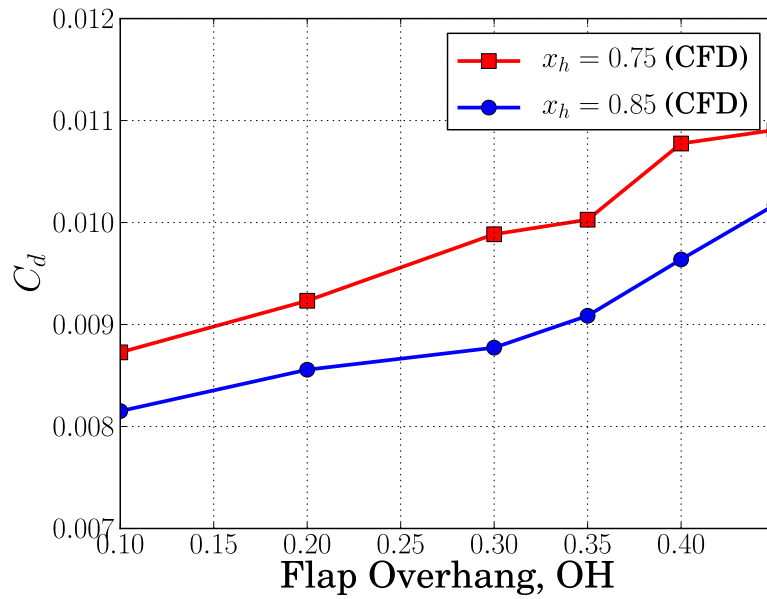
(b) $\delta = 8°$

Figure 3.20: C_d vs Overhang (OH) using CFD and theory for the NACA0006 airfoil, $M = 0.3$, $\alpha = 0°$, $x_h = 0.75$ & 0.85, Re=6 million.

3.2.3 Effect of Gap

Figure 3.21 shows the various aerodynamic quantities (C_l, C_d, C_m, C_h) as a function of flap deflection (δ) for the NACA0012 airfoil with 1% gap, OH=0.40 and $\alpha = 0°$. The results are obtained for using CFD meshes in the gap region as well as using the approximate gap averaging technique and are compared with the no-gap simulation. It is observed that for a positive flap deflection (i.e., flap down) the overall effect of the gap flow is to decrease lift and pitching moment, while increasing drag and flap hinge moment. The results indicate that for $\delta = 0°$ and $4°$ the effect of the gap is not significant. However, for $\delta = 8°$ the deviations in the aerodynamic quantities are no longer negligible. Figure 3.22 shows the same results for $\alpha = 5°$. Here it is seen that for all non-zero flap deflections, the effect of the gap is 10% or greater. The drag in particular, seems to be significantly affected by the presence of the gap. For all the cases shown in Figs. 3.21 and 3.22, the gap averaging technique gives close agreement with the direct approach using CFD meshes inside the gap. When the gap is not modeled, the deviations in the integrated aerodynamic quantities are not negligible for higher angles of attack and/or flap deflections.

Figure 3.23 shows the C_p distribution over the airfoil for the cases considered in Figs. 3.21 and 3.22. For all the cases, the results obtained using gap averaging are clearly better than those without gap treatment when compared with actual gap treatment using the patched mesh. It is seen from the pressure profiles shown in Figs. 3.23(d), 3.23(e) and 3.23(f) that the effect of gap modeling is relatively more pronounced for these cases, particularly over the flap surface. This is because

(a) C_l
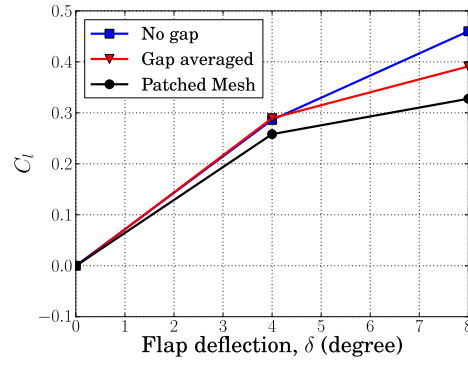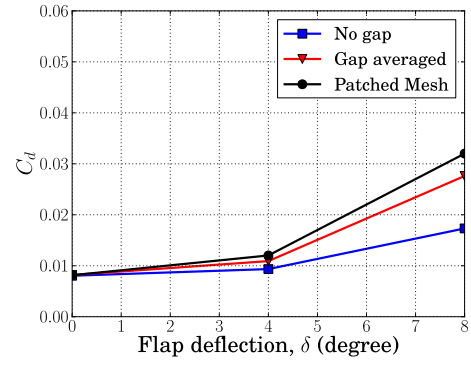
(b) C_d
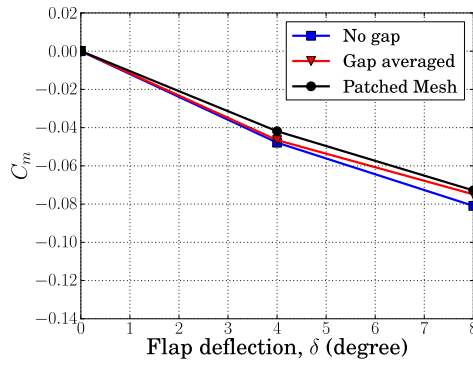
(c) C_m
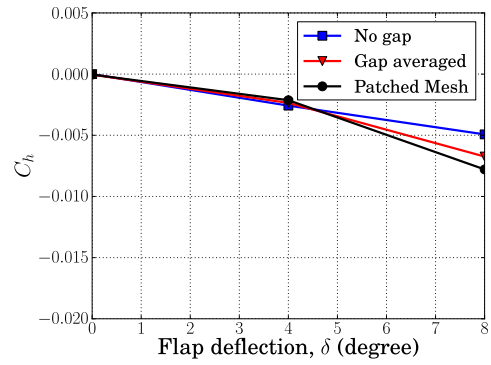
(d) C_h

Figure 3.21: C_l, C_d, C_m, C_h vs δ for the NACA0012 airfoil with 1% gap, $\alpha = 0°$, $M = 0.45$, OH= 0.4, $x_h = 0.75$, Re=5 million.

(a) C_l
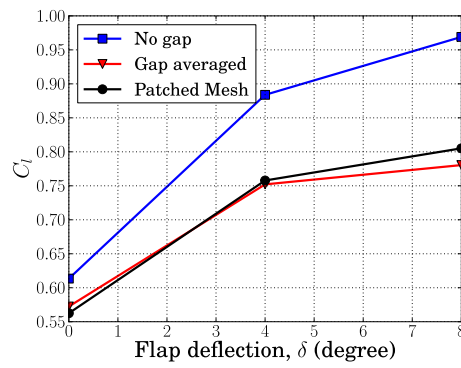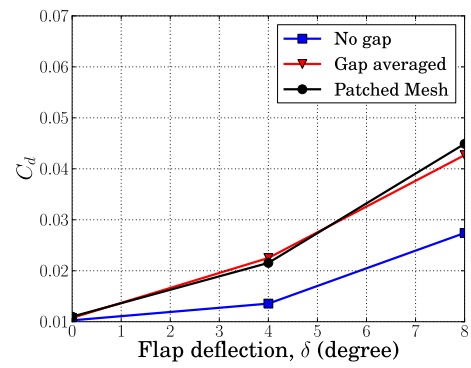
(b) C_d
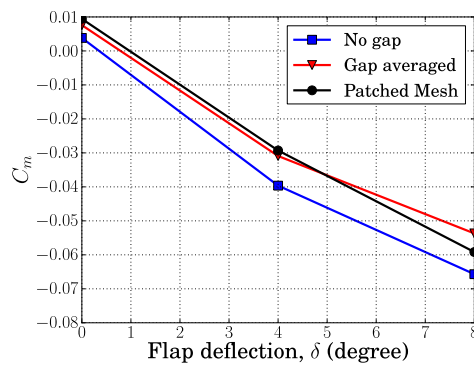
(c) C_m
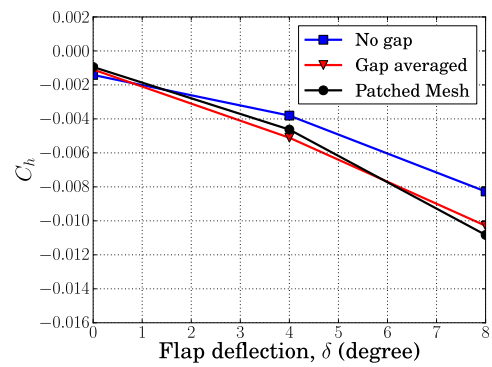
(d) C_h

Figure 3.22: C_l, C_d, C_m, C_h vs δ for the NACA0012 airfoil with 1% gap, $\alpha = 5°$, $M = 0.45$, OH= 0.4, $x_h = 0.75$, Re=5 million.

for these cases, the pressure difference between the upper and lower surfaces of the airfoil are greater and consequently the flow "induced" through the gap would also be larger. In other words the extent to which the C_p curve needs to be re-adjusted in order to equalize the pressures on the upper and lower surfaces in the gap region would be greater at these higher AoA and/or flap deflections. It is also observed that differences between the pressure profiles obtained with and without gap modeling are more pronounced for points downstream of the flap leading edge. This, as will be seen later, is because of flow separation over the flap and the effect of gap flow on the flow separation. For $\alpha = 5°$ and $\delta = 4°$, $8°$ clear differences are observed in the pressure distributions upstream of the gap as well.

Figures 3.24, 3.25 and 3.26 show the Mach contours and streamlines using the three approaches for the cases where the differences between the results obtained with and without gap treatment is not negligible. It is seen from the patched mesh contours that a re-circulation zone is formed on the lower surface of the flap leading edge. This is true for most cases with positive flap deflections. The re-circulation zone is also present when the gap is not modeled but not necessarily captured with gap averaging. This is because the gap averaging technique appears to transfer more momentum from the upper surface of the airfoil to the lower surface than the patched mesh approach. This energizes the boundary layer on the lower surface and prevents the formation of the re-circulation zone. However, although there is no flow separation on the lower surface, the lack of re-circulation zone does not affect the airloads significantly and gap averaging does not lead to any significant deviations from the patched mesh results.
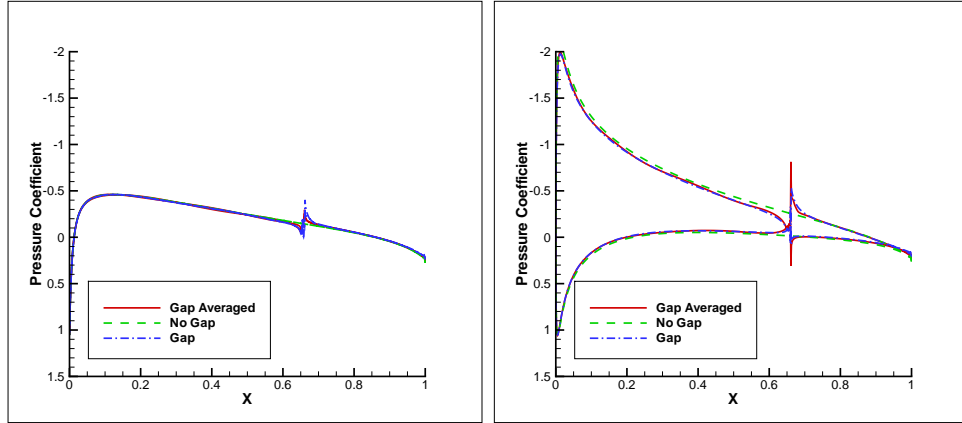
(a) $\alpha = 0°$, $\delta = 0°$

(b) $\alpha = 5°$, $\delta = 0°$
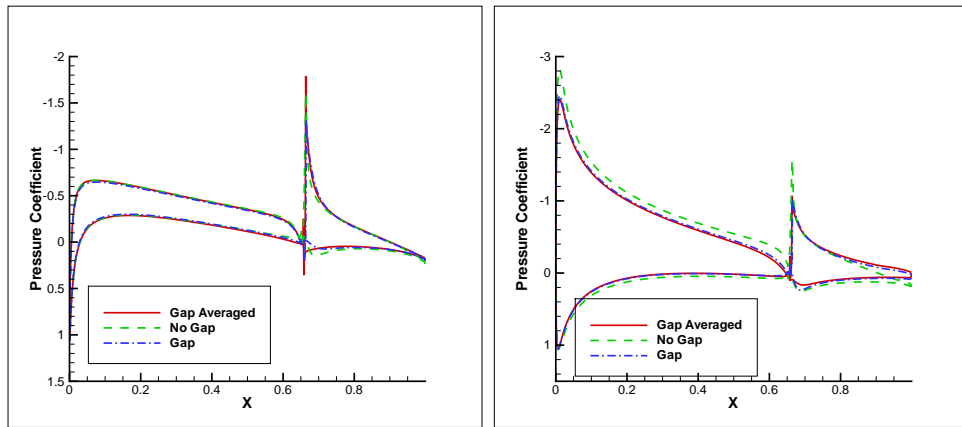
(c) $\alpha = 0°$, $\delta = 4°$

(d) $\alpha = 5°$, $\delta = 4°$
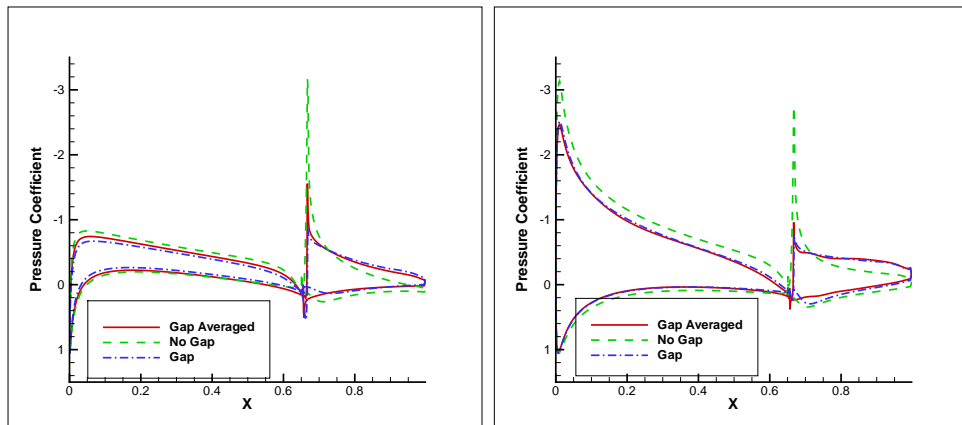
(e) $\alpha = 0°$, $\delta = 8°$

(f) $\alpha = 5°$, $\delta = 8°$

Figure 3.23: Comparison of C_p profiles using the three approaches for the NACA0012 airfoil with 1% gap, $M = 0.45$, OH$= 0.4$, $x_h = 0.75$, Re=5 million.
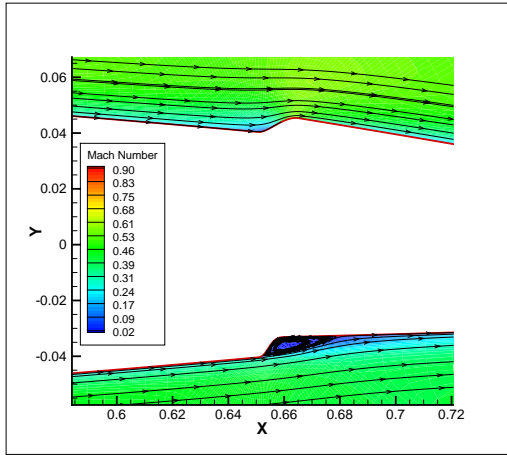
(a) No gap treatment
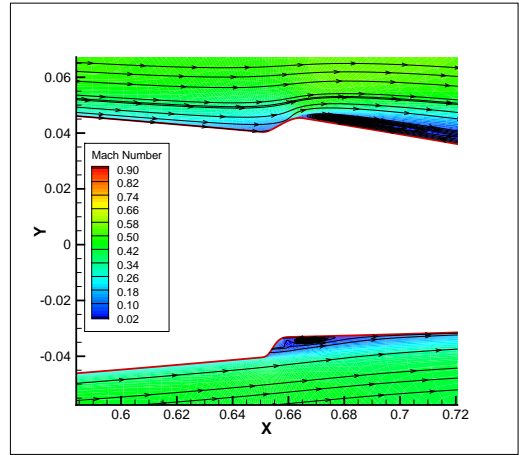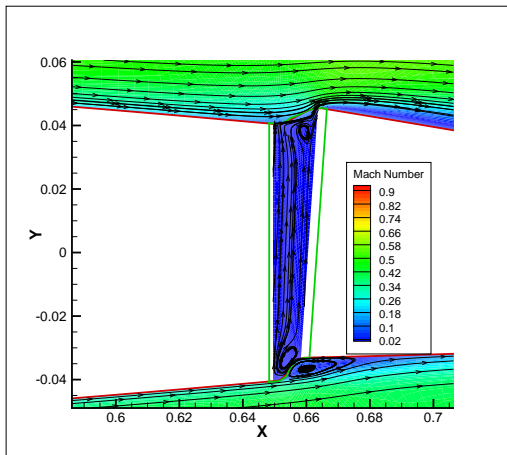
(b) Gap averaging
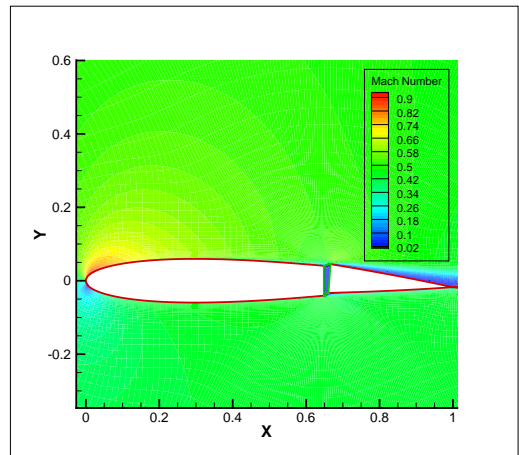
(c) Patched mesh

(d) Patched mesh (zoomed out)

Figure 3.24: Comparison of streamlines in the gap region using different approaches for the NACA0012 airfoil with 1% gap, $M = 0.45$, $\alpha = 5°$, $\delta = 4°$, $x_h = 0.75$, OH=0.4, $Re = 5.0$ million.
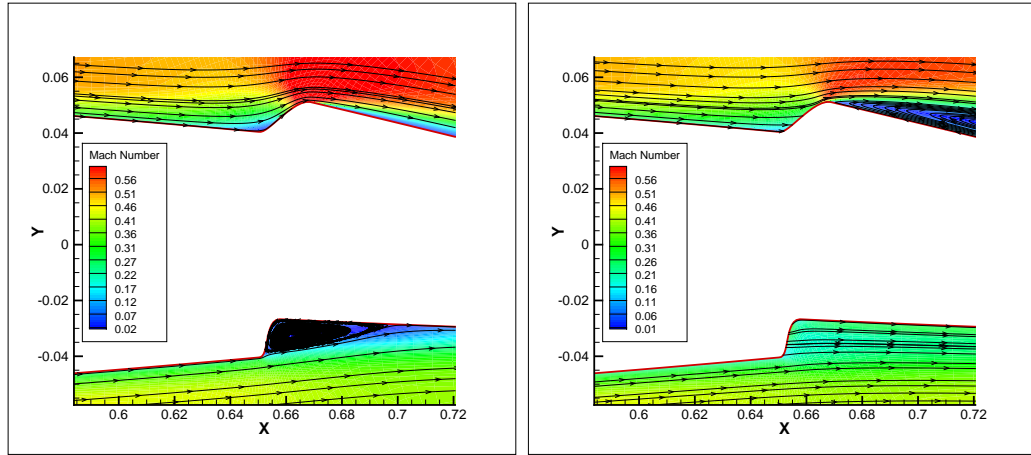
(a) No gap treatment
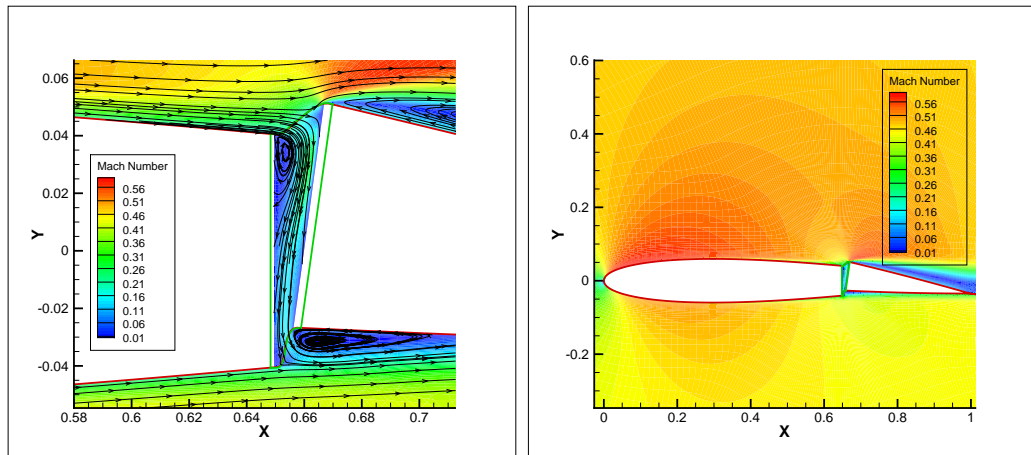
(b) Gap averaging

(c) Patched mesh

(d) Patched mesh (zoomed out)

Figure 3.25: Comparison of streamlines in the gap region using different approaches for the NACA0012 airfoil with 1% gap, $M = 0.45$, $\alpha = 0°$, $\delta = 8°$, $x_h = 0.75$, OH=0.4, $Re = 5.0$ million.
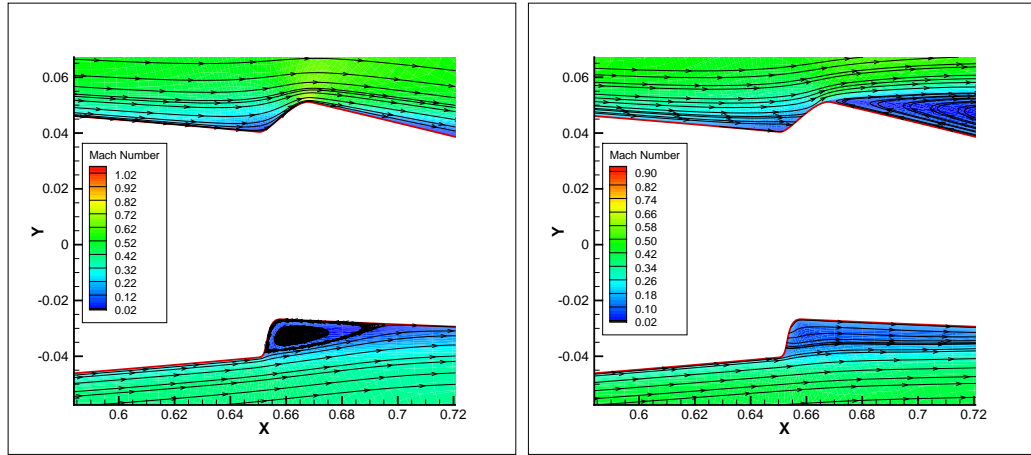
(a) No gap treatment

(b) Gap averaging
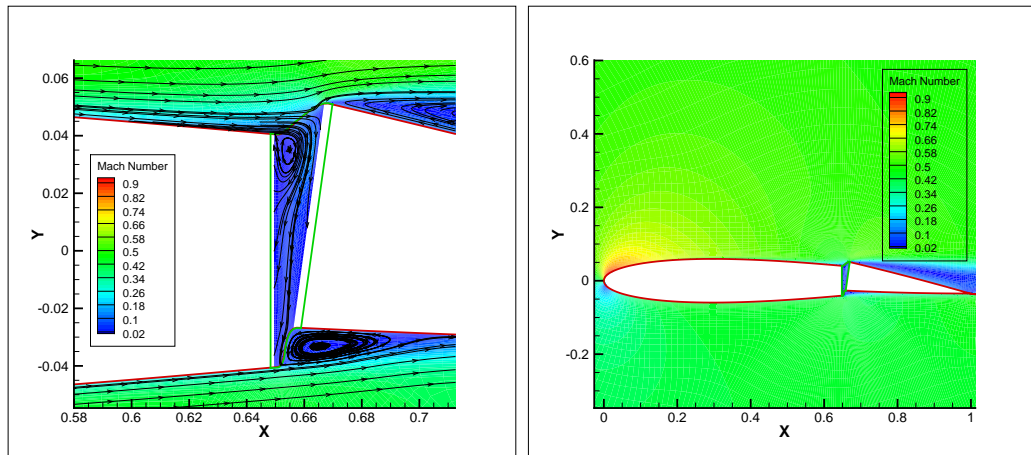
(c) Patched mesh

(d) Patched mesh (zoomed out)

Figure 3.26: Comparison of streamlines in the gap region using different approaches for the NACA0012 airfoil with 1% gap, $M = 0.45$, $\alpha = 5°$, $\delta = 8°$, $x_h = 0.75$, OH=0.4, $Re = 5.0$ million.

On the upper surface, the loss of momentum makes the flap more prone to flow separation or boundary layer thickening. It is clearly seen that for those cases where the integrated quantities (C_l, C_d, etc.) show significant deviations, gap modeling (using either approach) tends to induce flow separation over the upper flap surface. This tendency towards flow separation is not captured when the gap is not treated. Because flow separation strongly influences the pressure distribution over the flap, the effect of gap modeling on the airloads for these cases is not negligible. The effect of gap flow on the extent of flow separation over the flap is the primary reason behind the deviations in the pressure distributions observed downstream of the flap leading edge. Also, since flow separation has significant affect on the drag, C_d is strongly affected by the presence of the gap (as was seen in Figs. 3.21 and 3.22). Because the range of angles of attack and flap deflections encountered by helicopter rotors are similar to those considered here, gap modeling would be necessary for obtaining good predictions of the aerodynamic loads on the rotors.

For all the cases seen so far, part of the difficulty in accurately predicting the airloads and flow field using the gap averaging technique is because of overhang. Overhang causes the leading edge of the TEF to protrude into the flow and the resultant flow field is more prone to flow separation and is sensitive to small changes in geometry and boundary conditions. Figures 3.27 and 3.28 show the airloads for zero overhang for $M = 0.45$, $\alpha = 0°$ & $5°$, OH=0, Re=5 million, $x_h = 0.65$. Since overhang is zero, the gap location, which now coincides with the hinge location, is the same as in the earlier simulations with nonzero overhang ($x_h = 0.75$, OH=0.40). the hinge location now coincides with the earlier gap location. For these cases, it

is seen that the gap averaging technique provides very good approximations of the airloads and is very close to the results obtained using actual CFD meshes inside the gap. The pressure distributions shown in Fig. 3.29 further confirm this fact.

The differences between the simulations with and without gap are all the more pronounced for the zero overhang cases because for $OH = 0.40$, the pressure difference across the airfoil in the gap region was relatively small for the "no gap" simulations. As a result, the need for modeling the gap, which has the effect of eliminating the pressure difference across the gap, was not clearly demonstrated in the pressure profile plots (see Fig. 3.23). For the zero overhang cases on the other hand, the pressure difference across the airfoil in the gap region is not small for the "no gap" simulation and the differences in the pressure profile (and airloads) when the gap is modeled, is more clearly visible. Also, as noted earlier, when the overhang is zero, there is no protrusion of the flap leading edge. This makes the flow field simpler and less sensitive to small changes in geometry. As a result, the gap averaging approach yields very similar results, both in airloads and pressure distributions, to those obtained using overset meshes.

Figure 3.30 and 3.31 show the steady airloads for gap sizes of $0.005c$, $0.01c$, $0.02c$ and $0.03c$ for a NACA0009 airfoil for $M = 0.3$, $x_h = 0.65$, OH=0, $\delta = 4°$. It is observed that for all the airloads, the mere presence of the gap results in a significant offset in the airloads. This may be attributed to the equalization of pressure across the airfoil in the gap region and the resultant effect on the pressure distribution over the entire airfoil. This is illustrated in Figure 3.32, which shows the pressure profiles for various gap sizes. When the gap is not modeled, there is a significant

(a) C_l
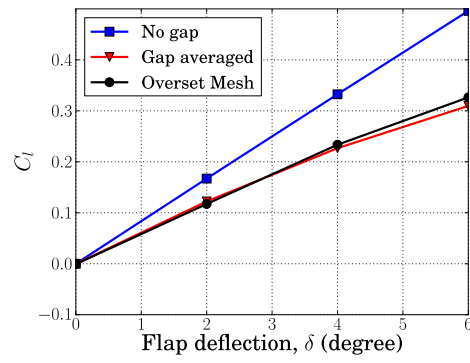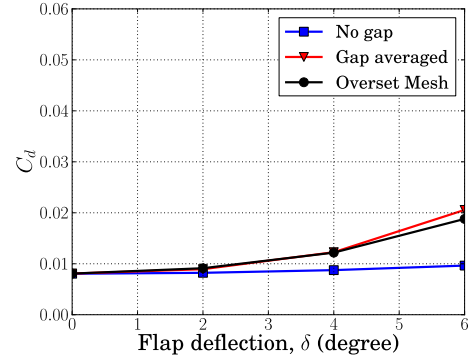
(b) C_d
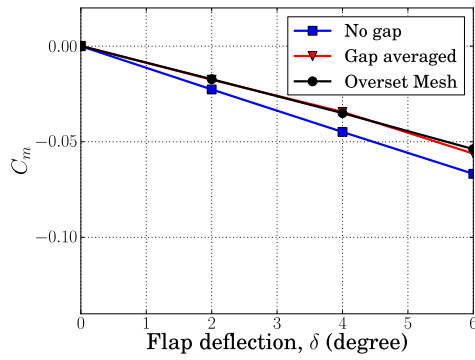
(c) C_m
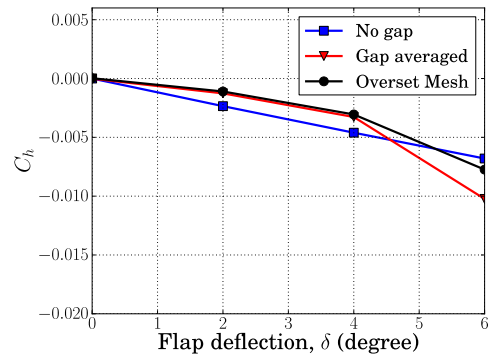
(d) C_h

Figure 3.27: C_l, C_d, C_m, C_h vs δ for the NACA0012 airfoil with 1% gap, $\alpha = 0°$, $M = 0.45$, OH= 0, $x_h = 0.65$, Re=5 million.

127

(a) C_l
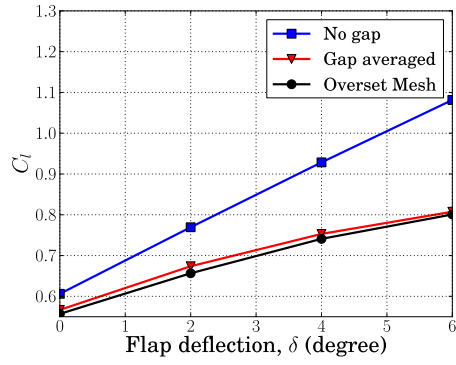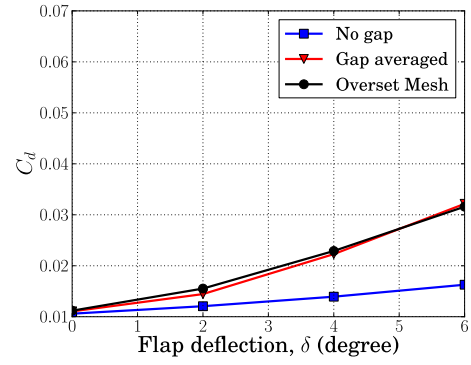
(b) C_d
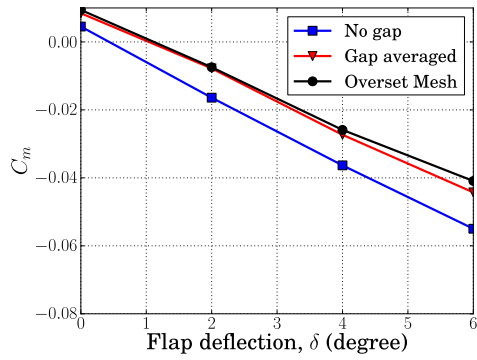
(c) C_m
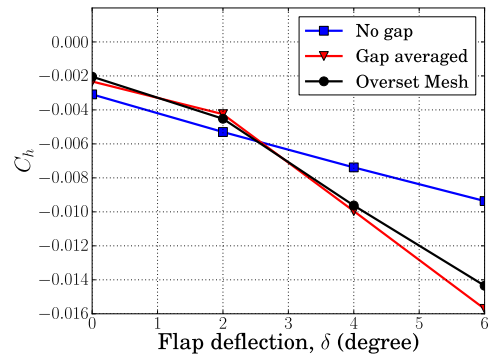
(d) C_h

Figure 3.28: C_l, C_d, C_m, C_h vs δ for the NACA0012 airfoil with 1% gap, $\alpha = 5°$, $M = 0.45$, OH= 0, $x_h = 0.65$, Re=5 million.

(a) $\alpha = 0°$, $\delta = 0°$

(b) $\alpha = 5°$, $\delta = 0°$

(c) $\alpha = 0°$, $\delta = 4°$

(d) $\alpha = 5°$, $\delta = 4°$

(e) $\alpha = 0°$, $\delta = 6°$

(f) $\alpha = 5°$, $\delta = 6°$
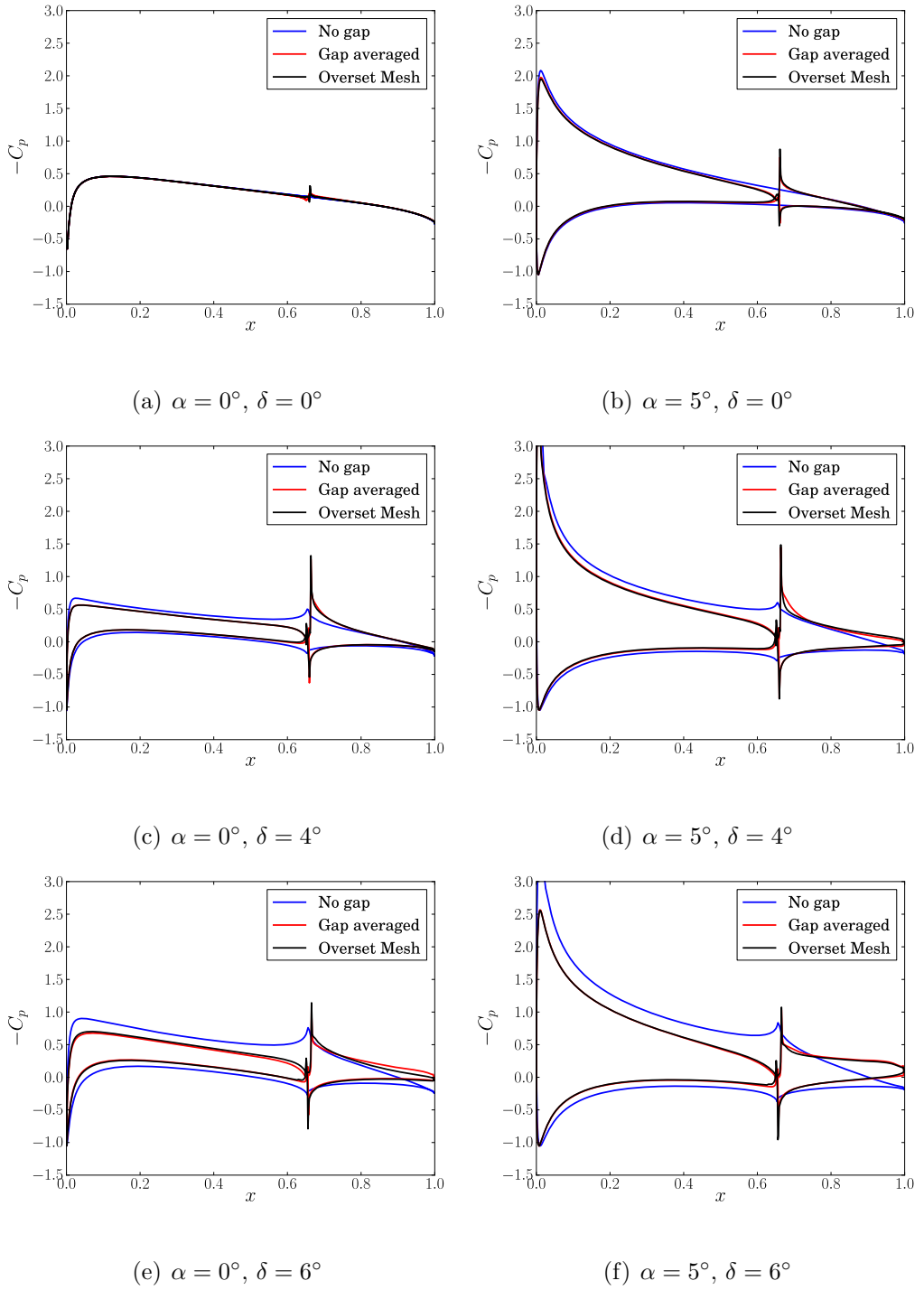
Figure 3.29: Comparison of C_p profiles using the three approaches for the NACA0012 airfoil with 1% gap, $M = 0.45$, OH= 0, $x_h = 0.65$, Re=5 million.

difference in the pressure across the gap. When the gap is modeled (using actual meshes or gap averaging), the pressure difference across the gap becomes zero and this leads to a change in pressure distribution both upstream and downstream of the gap. This is responsible for the offset in the airloads regardless of gap size.

(a) C_l

(b) C_d

(c) C_m

(d) C_h
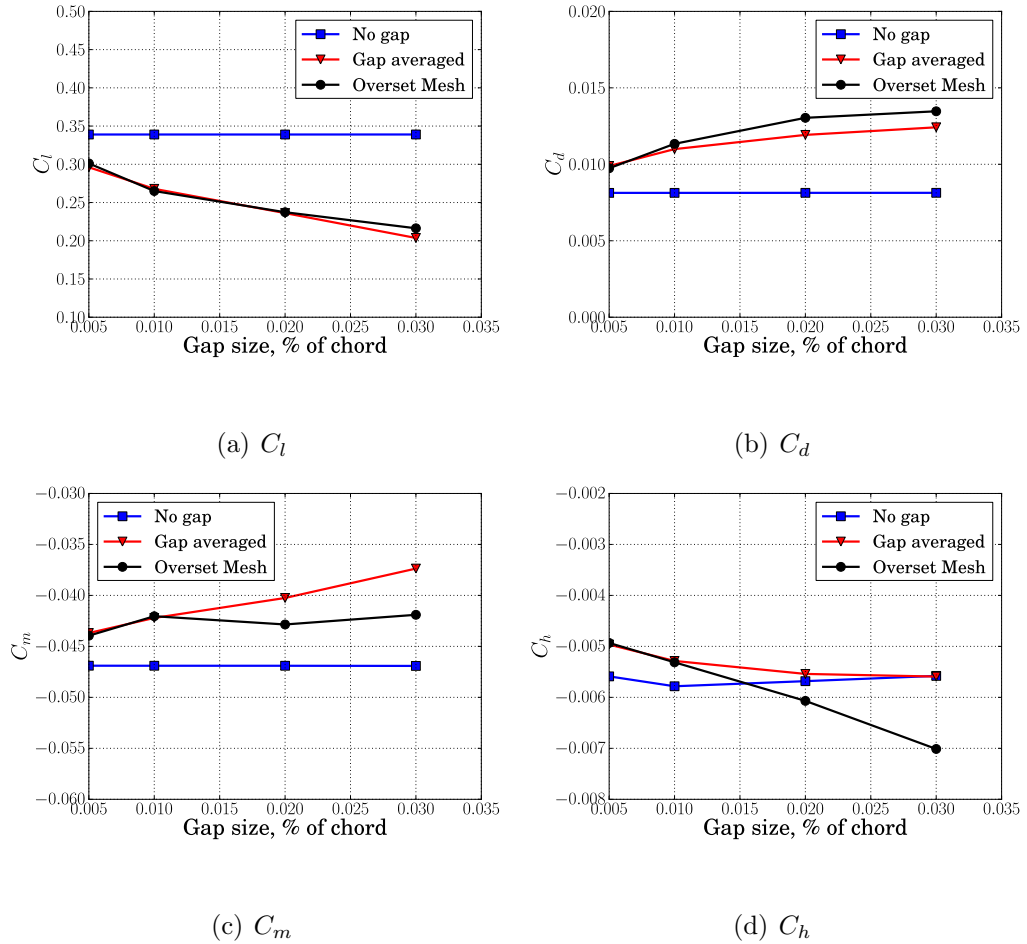
Figure 3.30: C_l, C_d, C_m, C_h vs gap size for the NACA0009 airfoil, $\alpha = 0°$, $\delta = 4°$, $M = 0.45$, OH= 0, $x_h = 0.65$, Re=5 million.

As may be expected, increasing the gap size decreases the effectiveness of the flap. Lift is seen to decrease with increasing gap size while drag increases. The loss in lift may be attributed to the fact that pressure is equalized over a larger portion of the airfoil chord, which in turn affects the pressure upstream and downstream

(a) C_l
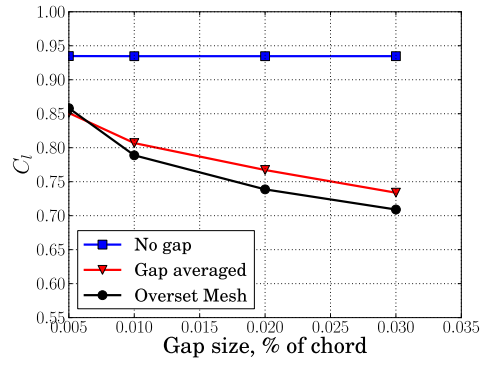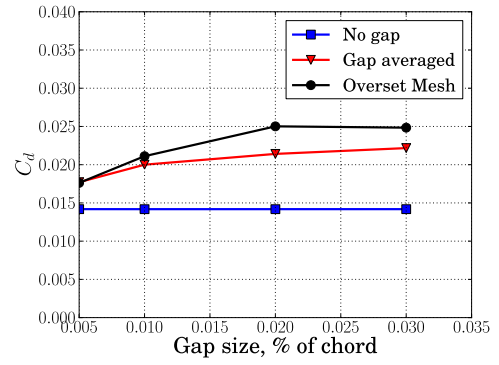
(b) C_d
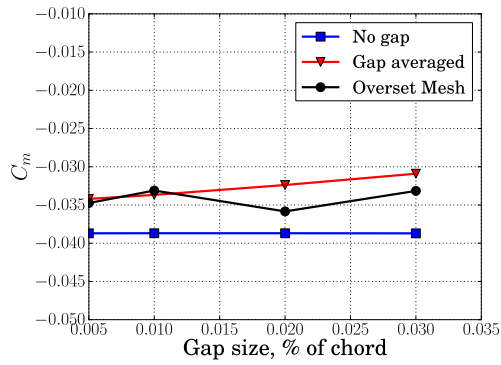
(c) C_m
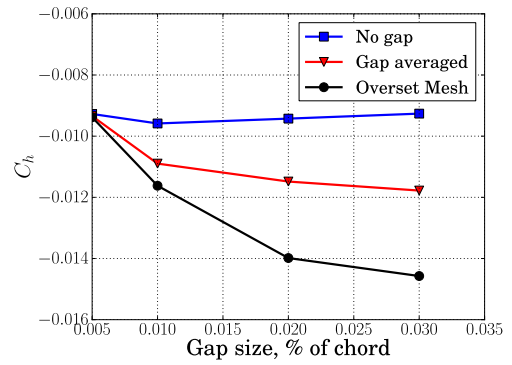
(d) C_h

Figure 3.31: C_l, C_d, C_m, C_h vs gap size for the NACA0009 airfoil, $\alpha = 5°$, $\delta = 4°$, $M = 0.45$, OH= 0, $x_h = 0.65$, Re=5 million.

131

(a) $\alpha = 0°$, 0.5% gap

(b) $\alpha = 5°$, 0.5% gap

(c) $\alpha = 0°$, 1% gap

(d) $\alpha = 5°$, 1% gap

(e) $\alpha = 0°$, 2% gap

(f) $\alpha = 5°$, 2% gap
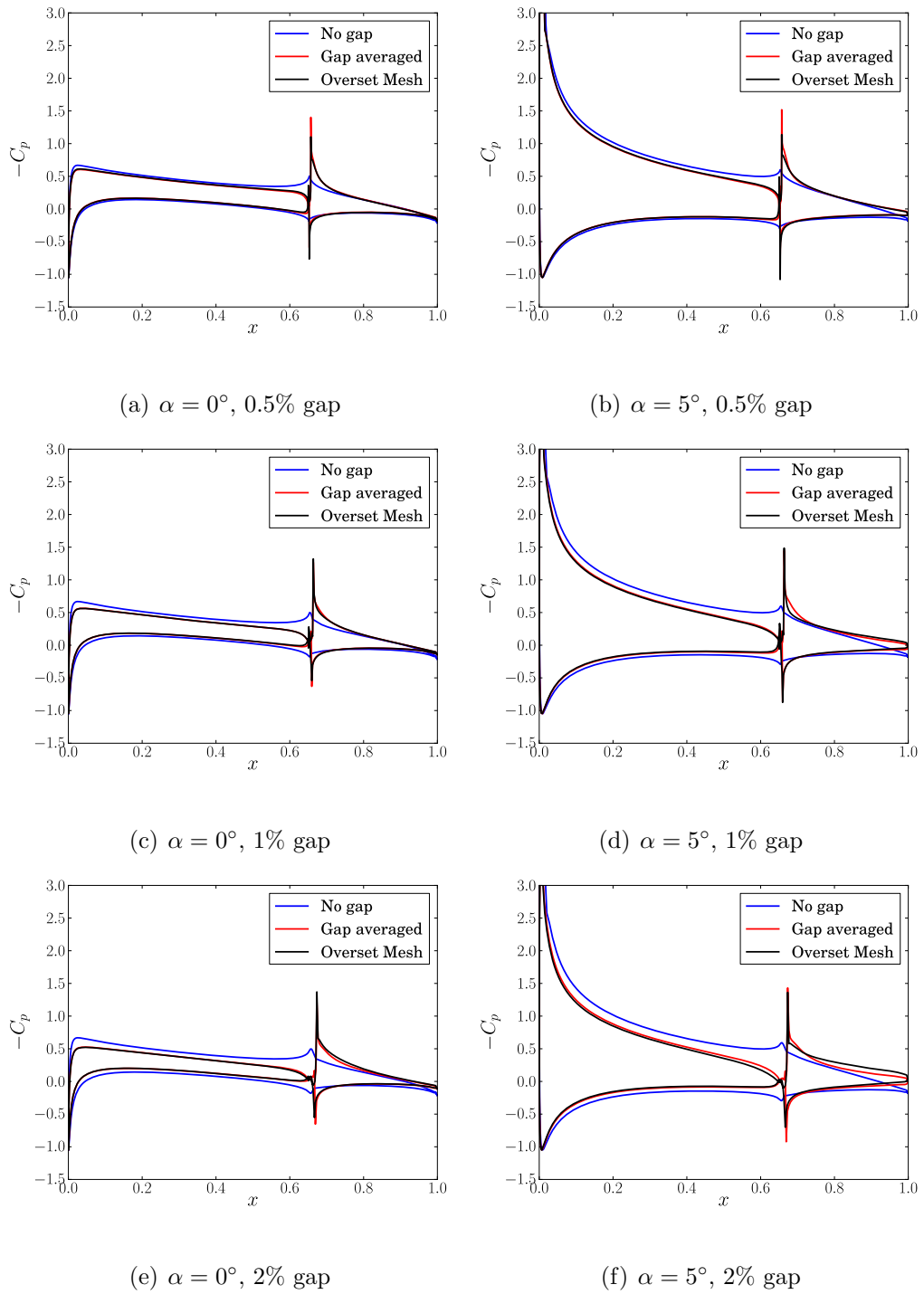
Figure 3.32: Comparison of C_p profiles using the three approaches for the NACA0009 airfoil with different gap sizes gap, at $\delta = 4°$, $M = 0.45$, OH= 0, $x_h = 0.65$, Re=5 million.

(a) $\alpha = 0°$

(b) $\alpha = 5°$

(c) $\alpha = 0°$ (zoomed)

(d) $\alpha = 5°$ (zoomed)
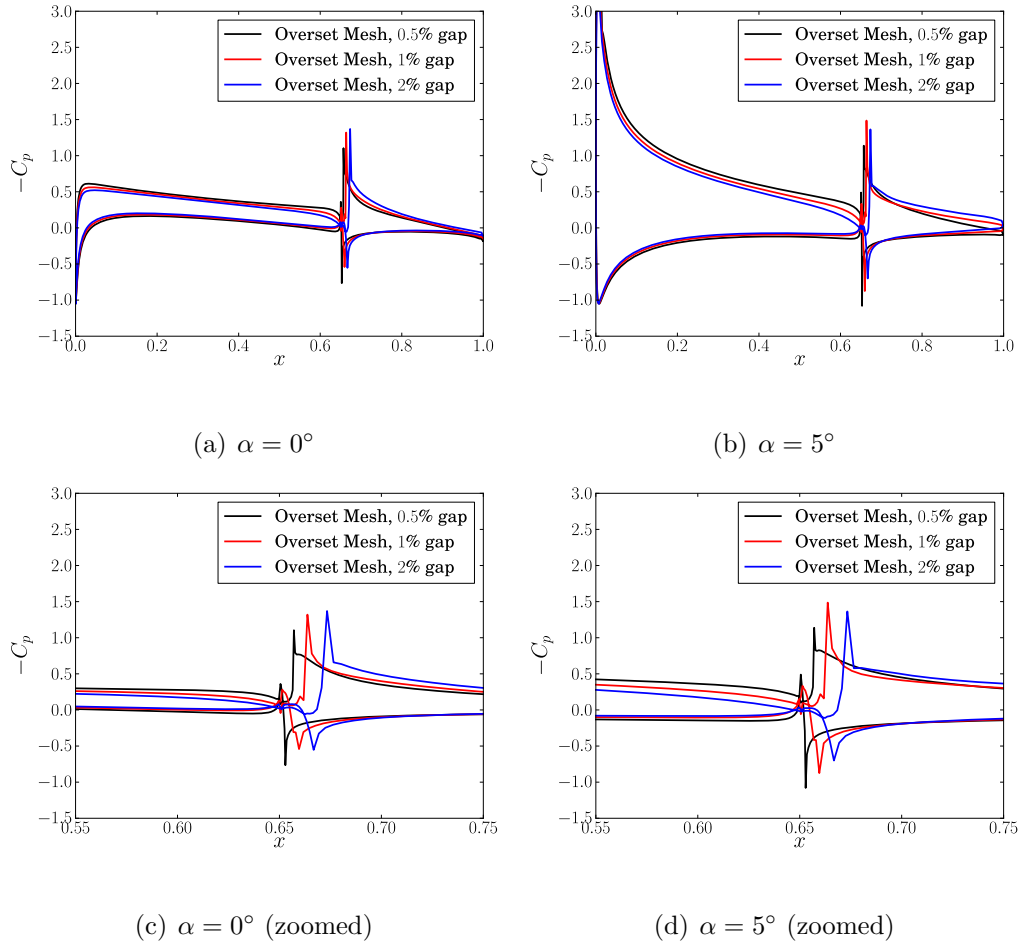
Figure 3.33: Comparison of C_p profiles using the overset mesh approach for the NACA0009 airfoil with different gap sizes gap, at $\delta = 4°$, $M = 0.45$, OH= 0, $x_h = 0.65$, Re=5 million.

of the gap. Also, as gap size increases, the position of the suction peak at the leading edge of the TEF is moved to the right (see Fig. 3.33). Flow separation and/or boundary layer thickening over the TEF can also happen due to increased gap size (see Fig. 3.32 and 3.33). Flow separation and boundary layer thickening is responsible for the increase in drag. Pitching moment is not as significantly affected by increasing the gap size. The hinge moment on the other hand is more strongly affected by gap size. Again, the change in pressure distribution over the flap due to flow separation and/or boundary layer thickening could contribute to the significant changes observed in hinge moment due to changes in gap size.

The gap averaging technique does a good job of predicting the pressure distribution for the various gap sizes. Deviations between gap averaging and the overset mesh approach are more pronounced for higher gap sizes but nearly always much better than the predictions made when the gap is not modeled at all.

3.3   Airloads and Aerodynamic Phenomena Associated with TEF airfoils

So far, the effect of various airfoil properties on the airloads associated with TEFs has been studied as shown for some representative cases. However, away from the surface of the airfoil itself, the flowfield surrounding it also has many interesting features that need to be better understood. For the successful deployment of TEFs on rotors it is important to understand these flow phenomena and how they can be controlled/affected by changing the flow variables (α, δ, M, etc.).

Flow Variable	Range of Values
Mach Number (M)	0.3, 0.4, 0.5, 0.6, 0.65, 0.7, 0.75, 0.8
Angle of Attack (α)	0.0° to 20.0° in steps in 2.5°
Flap Deflection (δ)	−10.0° to 10.0° in steps of 2.5°

Table 3.1: Range of flow parameters at which the 2D simulations are run.

In order to study the aerodynamic phenomena associated with TEFs, a large number of runs are performed over a wide range of flow conditions. The data obtained from these runs are post-processed to obtain the integrated airloads, (C_l, C_d, C_m and C_h) pressure profiles, Mach/vorticity contour plots, etc. to obtain an understanding of the behavior of TEF airfoils.

3.3.1 Details of Runs

The 2D TEF CFD runs are performed using the 2D TURNS code. Table 3.1 shows the range of Mach numbers, AoAs and flap deflections for which the runs are performed. The simulations are performed for each combination of the above values of Mach number, angle of attack and flap deflection for the NACA0012 and SC1095R8 airfoils with 15% chord flap size. Typically, a 329×97 C-grid was used for most of the computations. For all the cases considered here, a zero overhang is used.

Since airloads data is thus available for various combinations of angle of attack and flap deflection, it would be useful to represent the data in a way that would be

compact while at the same time providing a useful way to compare the results for different combinations of AoA and flap deflection. One approach to accomplish this would be to use the concept of effective angle of attack (α_{eff}) based on thin airfoil theory that was seen earlier in the section on drag modeling in Chapter 2. The idea behind using the effective angle of attack is that it provides a way to merge C_l and C_d curves for different flap deflections. This makes it easier to visualize and compare the data. The fact that the use of α_{eff} collapses the lift curves for different flap deflections into a single line can be shown from linear thin airfoil theory. A similar behavior for drag is not as evident but was seen to be approximately true in the section on drag modeling. This representation is useful only for lift and drag, since the pitching moment (C_m) and hinge moment (C_h) do not follow the same trend.

3.3.2   Lift Coefficient

Figure 3.34 shows the variation of lift coefficient (C_l) as a function of α_{eff} for the NACA0012 airfoil at $M = 0.3$. It is seen that, as predicted by thin airfoil theory, the different lift curves fall on the same line until the onset of stall. It is seen that despite the strong camber introduced by flap deflections (varying from $-10°$ to $+10°$), the different flap deflection curves fall nearly on the same line. There is some deviation from theory as the flap deflection changes, but the differences are not significant. At $M = 0.3$, the lift curve is linear for all flap deflections up to $\alpha_{\text{eff}} \approx 10°$. Beyond this, static stall occurs one by one for the various flap deflections,

with the $\delta = +10°$ case (i.e., a 10° downward flap deflection) experiencing stall last. This behavior is consistent with the stall behavior expected from cambered airfoils since flap deflection can be seen as a form of camber. This means that using a positive flap deflection can delay the onset of stall as compared to an airfoil with no flap deflection. From a design perspective, this could mean that choosing the index angle for a swashplateless TEF rotor such that the TEF is deflected downward during most of its flight envelop could lead to benefits in the form of delayed stall. However, a more detailed analysis of the other factors influencing the behavior/performance of swashplateless TEF rotors will have to be considered before drawing such conclusions. Also, although a positive flap deflection also implies earlier stall onset at negative angles of attack, in the regions of the blade span where the TEF is typically deployed, it would predominantly experience only positive angles of attack.

Notice that this particular choice of flap size and spacing of α and δ exhibits certain patterns of behavior. By noting the starting point of each flap deflection curve (i.e., corresponding to $\alpha = 0$) it can be deduced that a change in flap deflection of 5° produces nearly the same change in lift as an angle of attack change of 2.5°. This is indicated by the fact that $\alpha = 2.5°$, $\delta = -10°$ has nearly the same lift as $\alpha = 0°$, $\delta = -5°$; $\alpha = 2.5°$, $\delta = -5°$ has nearly the same lift as $\alpha = 2.5°$, $\delta = 0°$, and so on. This can be explained by looking at the relationship between $C_{l\alpha}$ and $C_{l\delta}$. Using Eqs. 2.5 and 2.6 it can be shown that for a flap flap size of 15% the ratio $C_{l\alpha}/C_{l\delta} = 2.0812 \approx 2$. This means that from the perspective of the lift coefficient (which is proportional to α_{eff}) a 1° change in angle of attack is
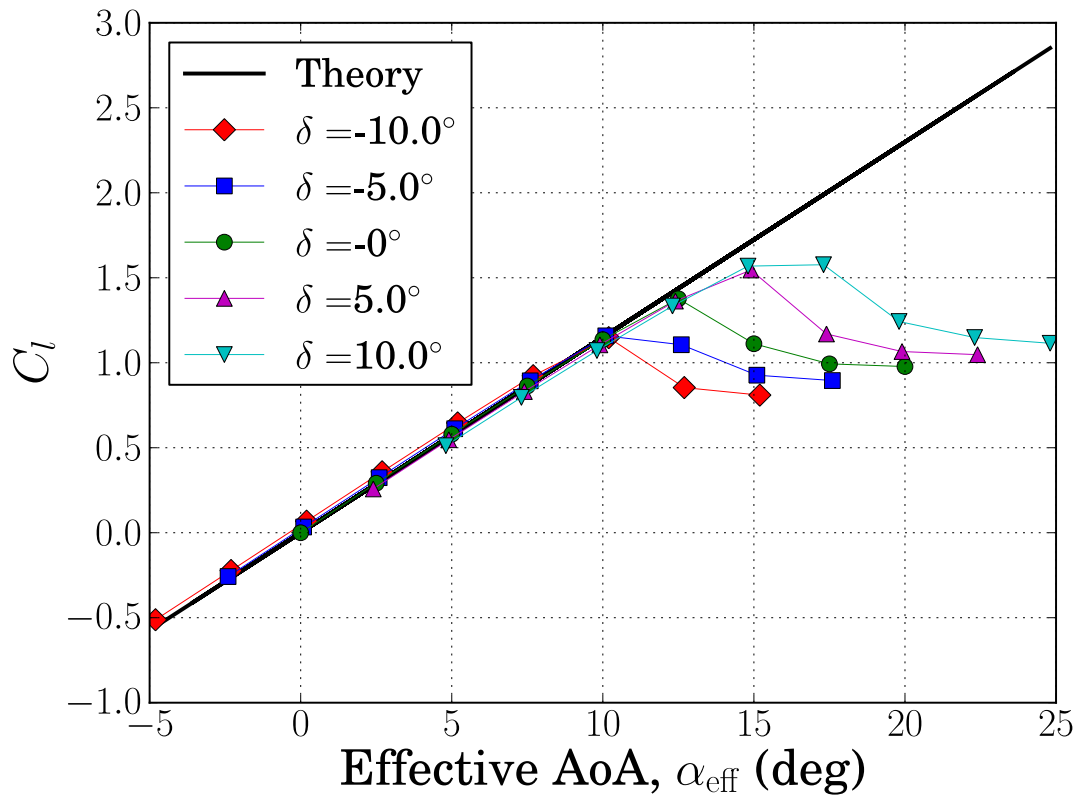
Figure 3.34: C_l vs α_{eff} for the NACA0012 airfoil, $M = 0.3$, 15% chord flap, $Re = 4.8$ million.

approximately equivalent to a 2° change in flap deflection for such a flap.

Figure 3.35 shows the Mach contours and streamlines for different the combinations of angles of attack and flap deflections at $M = 0.3$. The contour plots help to identify the occurrence and extent of nonlinear phenomena such as boundary layer thickening, flow separation (indicated by the blue, low Mach number region) and transonic effects (indicated by the red, high Mach number region). The angle of attack (α) increases from 7.5° to 17.5° from left to right while the flap deflection (δ) varies from $-5°$ to $+5°$ from top to bottom. Mach contour plot arrays for the complete range of AoA and flap deflection at all Mach numbers is provided in Appendix B. For the matrix of plots in Fig. 3.35, the implication of the earlier observation about the relationship between α and δ and their contribution to α_{eff} (i.e., 2.5° change in α is equivalent to 5° change in δ) means that two plots with equivalent α_{eff} can be obtained by moving either one place to the right and two places above or one place to the left and two places below in the matrix. If the plots are observed with this in mind, it is observed that plots with equivalent angles of attack do not necessarily have the same flow features. This is because, the kind of pressure distribution produced over the airfoil surface by a change in angle of attack is not the same as the kind of pressure distribution produced by a change in flap deflection. Although, the concept of effective angle of attack provides a means of interchanging α and δ in the integrated quantities (lift and drag), their effects cannot be likewise interchanged in the local pressure distributions. This is clearly illustrated in Fig. 3.36 which shows the $-C_p$ vs x plots for cases contained in Fig. 3.35. For example, it is seen that the plot corresponding to $\alpha = 7.5°$ and

$\delta = 5°$ and that corresponding to $\alpha = 10°$ and $\delta = 0°$ do not have similar pressure distributions, despite having nearly the same effective angle of attack. Figure 3.37 looks at four cases which have nearly the same effective angle of attack (α_{eff} and compares their pressure profiles. It is seen that although each of these cases have $\alpha_{\text{eff}} \approx 2.5°$, they have different pressure distributions. Angle of attack (α) affects lift primarily by changing the pressure distribution near the leading edge of the airfoil whereas flap deflection affects lift primarily by modifying the pressure distribution near the flap. This means that when nonlinear phenomena (such as supersonic effects or flow separation) begin to manifest, they will manifest differently for two configurations with the same α_{eff}. For example, flow separation, which is caused by adverse pressure gradients can be controlled to some extent by redistributing the pressure along the airfoil and thereby producing a higher lift without inducing stall.

A change in α produces a pressure profile where the lift is produced primarily near the leading edge. A change in δ on the other hand involves a suction peak near the leading edge of the TEF and a more uniform pressure distribution over the airfoil. This means that aerodynamic effects such as flow separation that are triggered by adverse pressure gradients will be affected differently by equivalent (from the perspective of α_{eff}) changes in α and δ.

This can be seen in the Mach contour plots contained in Appendix B, where it is observed that full scale flow separation is dependent more on the angle of attack rather than on flap deflection. Flap deflection does affect flow separation but mostly only locally/partially. This provides the possibility of delaying the onset of stall by using a positive flap deflection (instead of a higher angle of attack) as noted earlier.
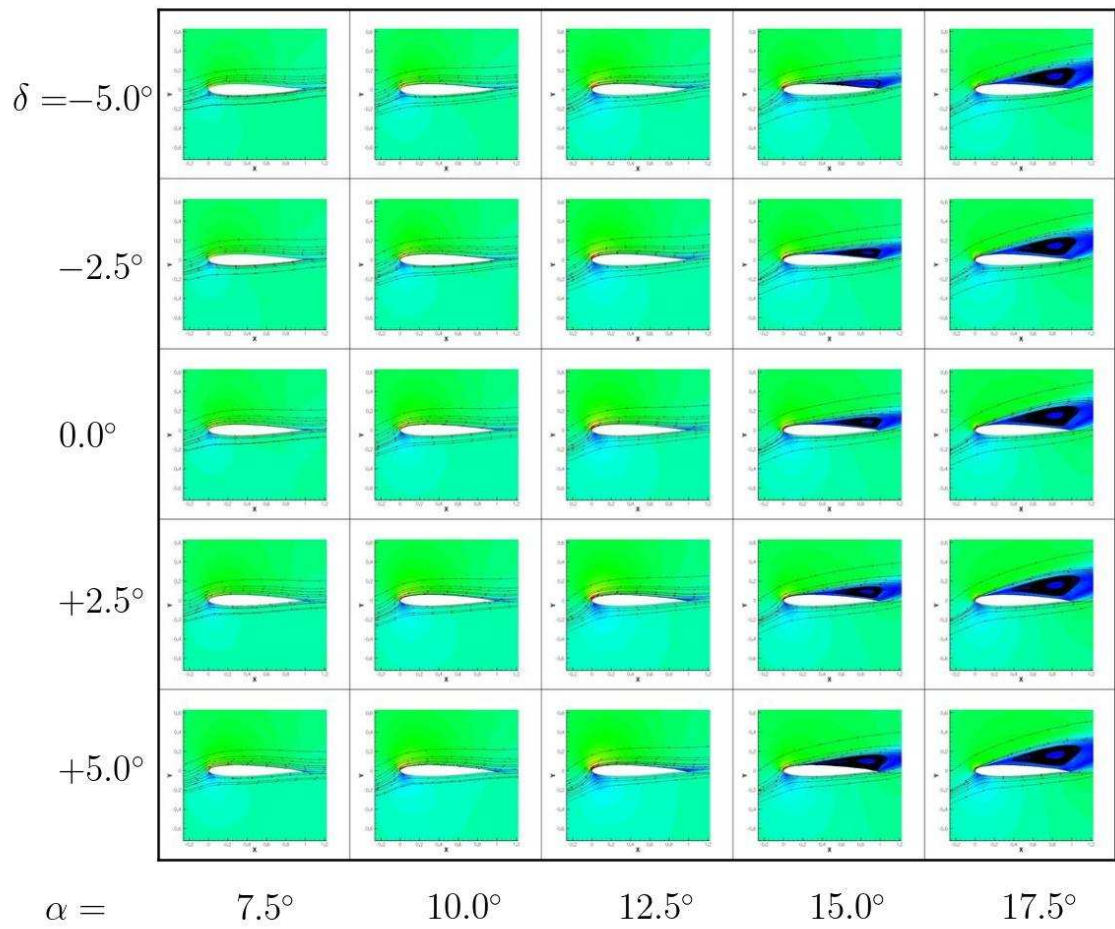
Figure 3.35: Mach contours for different α and δ for the NACA0012 airfoil, $M = 0.3$, 15% chord flap, $Re = 4.8$ million.
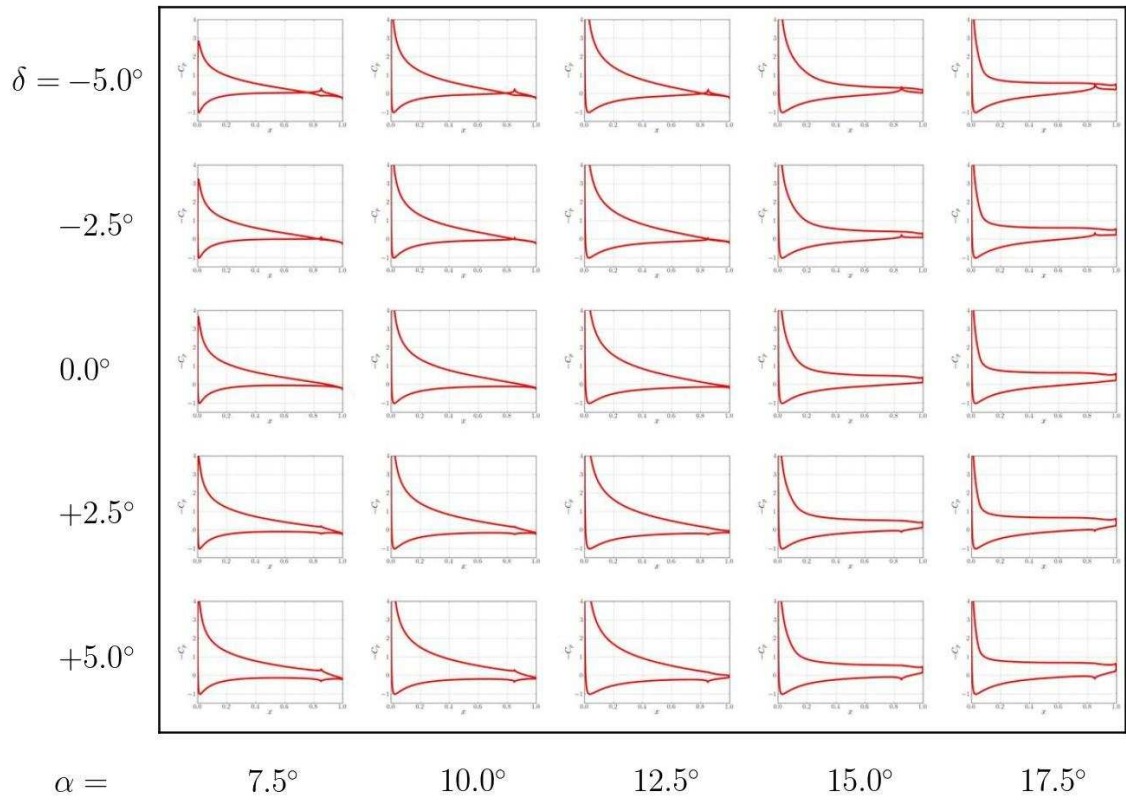
Figure 3.36: $-C_p$ vs x for different α and δ for the NACA0012 airfoil, $M = 0.3$, 15% chord flap, $Re = 4.8$ million.

(a) $\alpha = 0.0°$, $\delta = 5°$

(b) $\alpha = 2.5°$, $\delta = 0°$

(c) $\alpha = 5.0°$, $\delta = -5°$

(d) $\alpha = 7.5°$, $\delta = -10°$
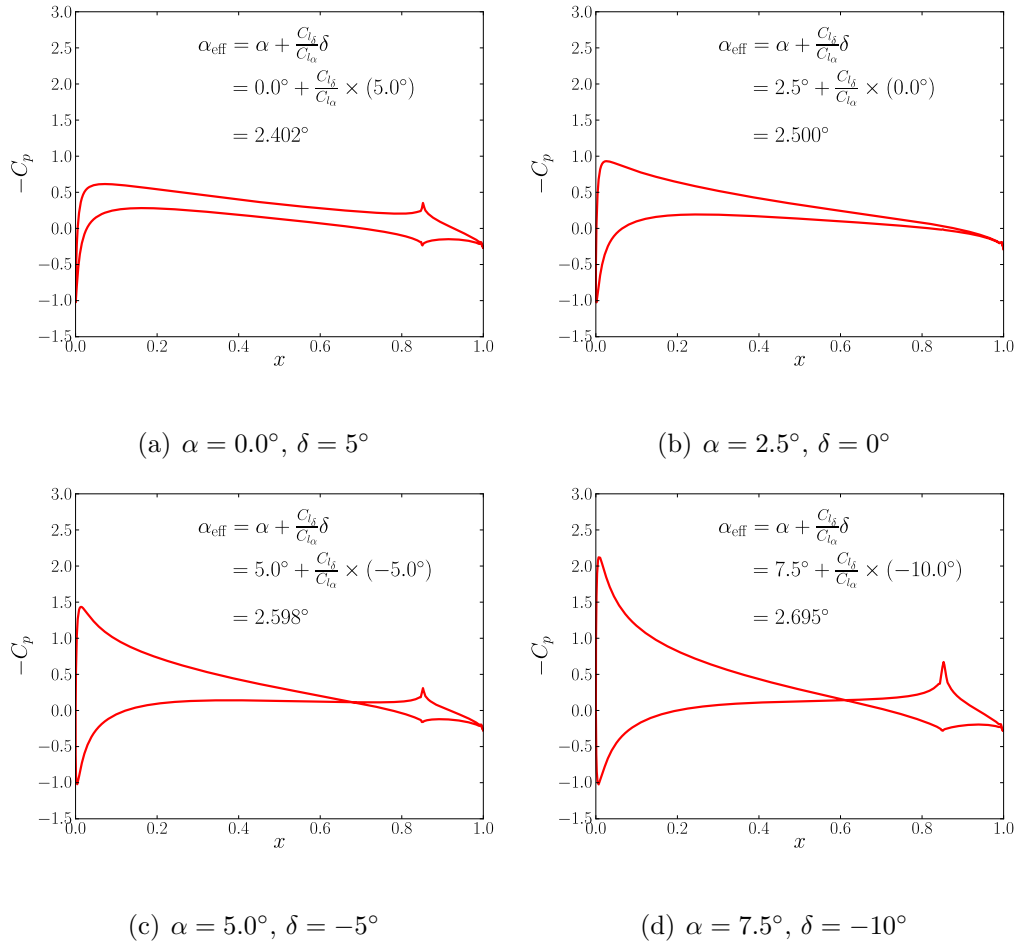
Figure 3.37: Comparison of pressure profiles for cases with nearly the same α_{eff} for the NACA0012 airfoil, $M = 0.3$, $x_h = 0.85$, OH=0, $Re = 4.8$ million.

Typically, stall occurs in three ways:

1. Leading edge stall.

2. Trailing edge stall.

3. Thin airfoil stall.

For a more detailed description of the each kind of stall behavior, see Ref. 107. From the Mach contour plots in Appendix B, it is seen that the NACA0012 airfoil experiences *trailing edge stall*, where the flow separates in the trailing edge region of the airfoil and gradually moves toward the leading edge. Since trailing edge stall is a gradual process, it is not possible to identify a precise point where stall occurs. Generally, trailing edge stall has been found to be less sensitive to airfoil shape than leading edge or thin airfoil stall and is common in airfoils with higher t/c ratios and camber lines.

Figure 3.38 shows the C_l vs α_{eff} plot for a transonic Mach number of 0.6. The lift coefficient shows the same trends, with the exception that stall occurs much earlier. Figures.3.39 and 3.40 show the Mach contours and pressure distributions respectively for the this Mach number. It is seen that stall occurs earlier because flow separation is hastened by transonic effects on the upper surface of the airfoil. Flow separation can be identified by the flat pressure profiles in the region of separation. It also has the effect of eliminating the suction peak at the leading edge of the flap, thereby reducing the effectiveness of the flap.

At lower angles of attack, a supersonic pocket is formed on the upper surface of the airfoil near the leading edge. The supersonic pocket can be seen in the C_p

144

plots in the form of a region of constant pressure terminating in an abrupt change in pressure (i.e., a shock). As the angle of attack increases, the supersonic pocket grows and becomes an oblique shock at the airfoil leading edge, behind which flow is seen to be fully separated. An interesting phenomena that is observed before and sometimes after the formation of the oblique shock, is that of shock induced vortex shedding. This is indicated by the presence of wavy patterns in some of the pressure distribution plots (see Fig. 3.40). At $M = 0.6$, this phenomenon is seen for the NACA0012 airfoil at $\alpha = 7.5°$ and $10°$. Vortex shedding takes place at the base of the shock and occurs for all flap deflections. Since vortex shedding would be unsteady, it is undesirable and could cause unsteadiness in the airloads. Beyond a certain angle of attack, shock induced vortex shedding does not occur for the NACA0012 airfoil and the flow is fully separated over the upper surface of the airfoil.

Figure 3.41 summarizes the C_l vs α_{eff} plots for all the remaining Mach numbers. The corresponding Mach contour plots and pressure distribution plots are provided in Appendix B for completeness. The same general trends are seen for all the Mach numbers and are summarized below:

- The flow is initially linear at low effective angle of attack and then enters into stall as the angle of attack increases.

- The effective angle of attack at which stall occurs becomes smaller as the Mach number increases. Stall occurs earlier at higher Mach numbers because of flow separation induced by the strong pressure gradients generated by the
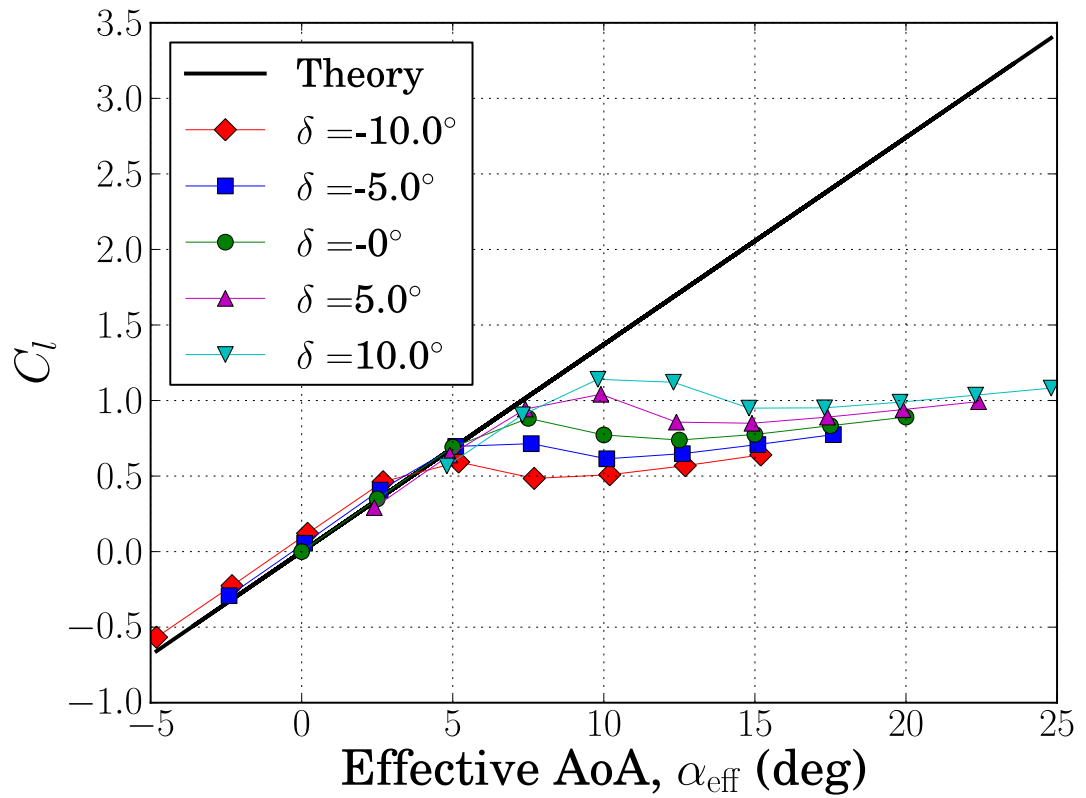
Figure 3.38: C_l vs α_{eff} for the NACA0012 airfoil, $M = 0.6$, 15% chord flap, $Re = 4.8$ million.
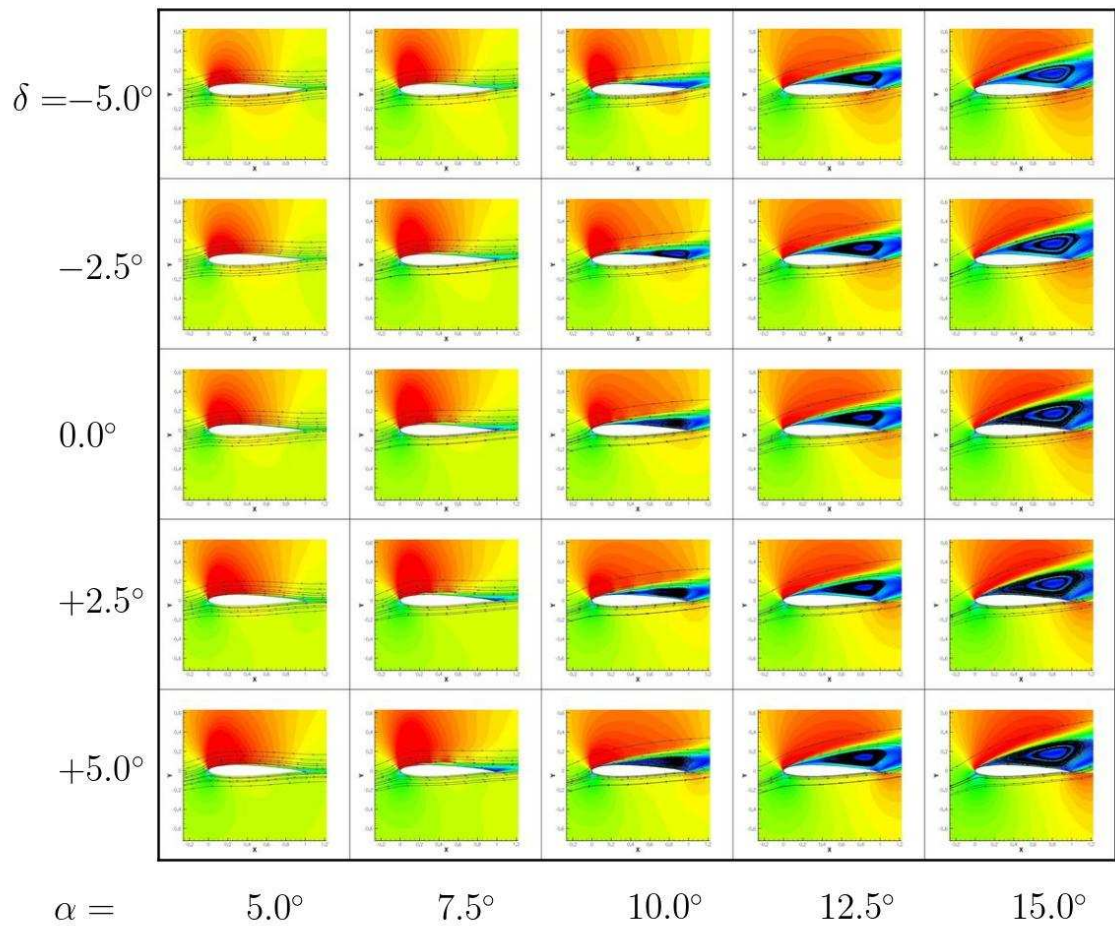
Figure 3.39: Mach contours for different α and δ for the NACA0012 airfoil, $M = 0.6$, 15% chord flap, $Re = 4.8$ million.
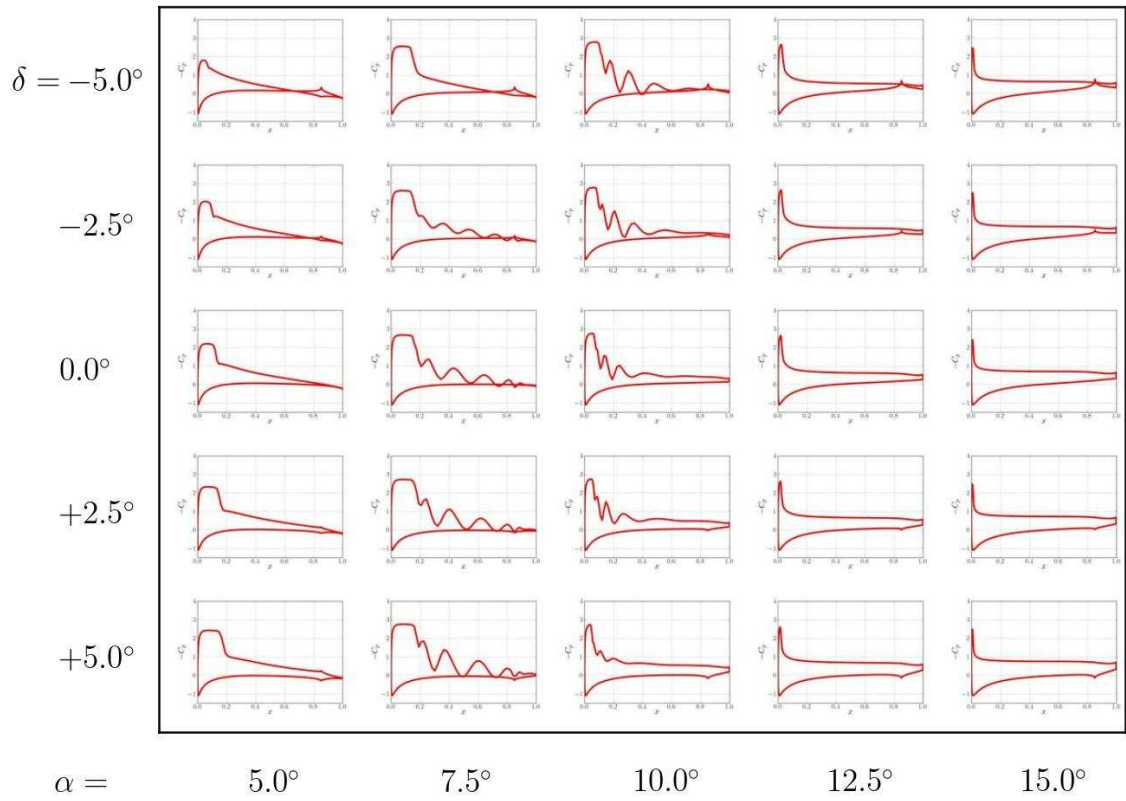
Figure 3.40: $-C_p$ vs x for different α and δ for the NACA0012 airfoil, $M = 0.6$, 15% chord flap, $Re = 4.8$ million.

formation of shocks.

- For the same effective angle of attack, a negative flap deflection (when α is positive) has a slightly higher lift.

- Full-scale flow separation occurs at higher angles of attack and is seen to be predominantly affected by angle of attack rather than by flap deflection.

- For the higher subsonic Mach numbers, a supersonic pocket is formed at the leading edge of the airfoil. This supersonic pocket grows as the angle of attack increases until an oblique shock is formed over the airfoil surface.

- The formation of the oblique shock is often accompanied by the phenomenon of shock induced vortex shedding. As the α increases further, the oblique shock is fully formed over the complete airfoil, with a region of fully separated flow behind it.

Based on Figs. 3.41 and the corresponding Mach-streamline and pressure profile plots, a stall boundary can be generated for the NACA0012 airfoil at this flap size. For each flap deflection, the AoA at which stall occurs can be approximately determined from the aforementioned plots. This data would prove very useful both from a design and modeling perspective. From a design perspective, it can help to identify the limits beyond which performance losses may be expected. From a modeling perspective, it would be useful to identify boundaries beyond which the modeling parameters for lift, drag, pitching moment, etc. can be adjusted to model the behavior consistent with stall.
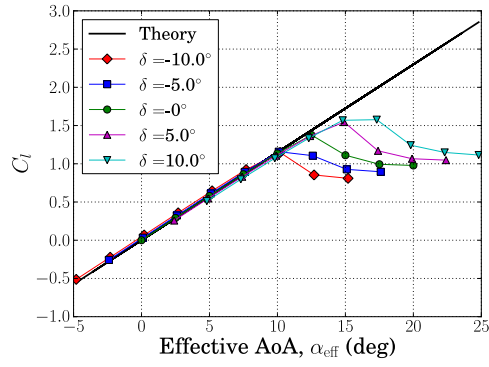
(a) $M = 0.3$
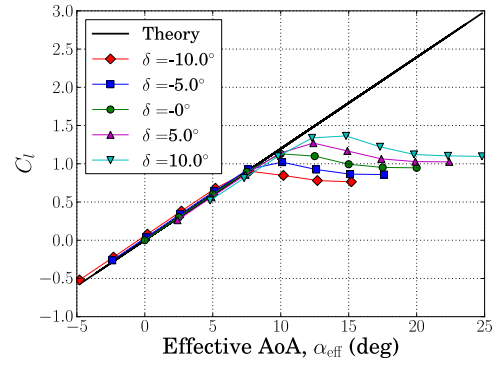
(b) $M = 0.4$
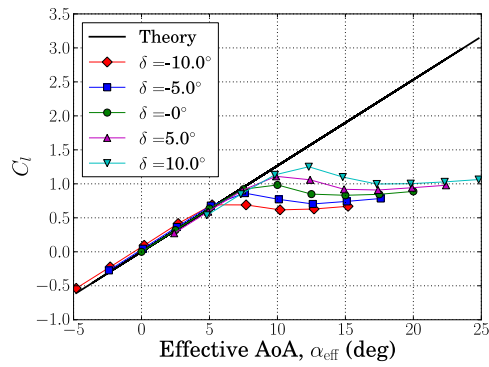
(c) $M = 0.5$
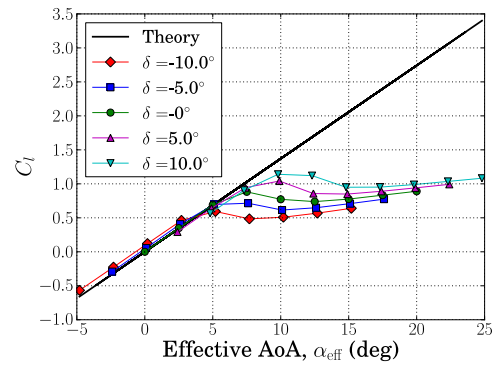
(d) $M = 0.6$
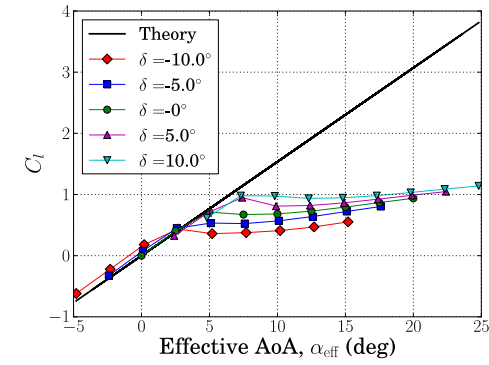
(e) $M = 0.7$
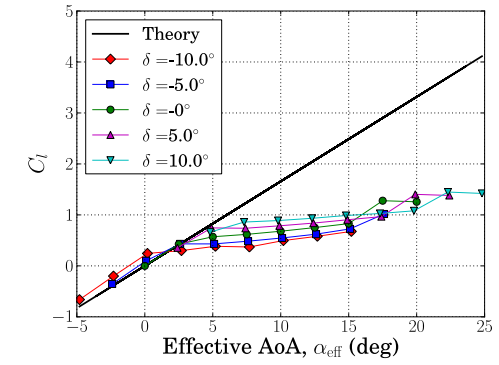
(f) $M = 0.75$

Figure 3.41: C_l vs α_{eff} for different Mach numbers for a NACA0012 airfoil, 15% chord flap, $Re = 4.8$ million.
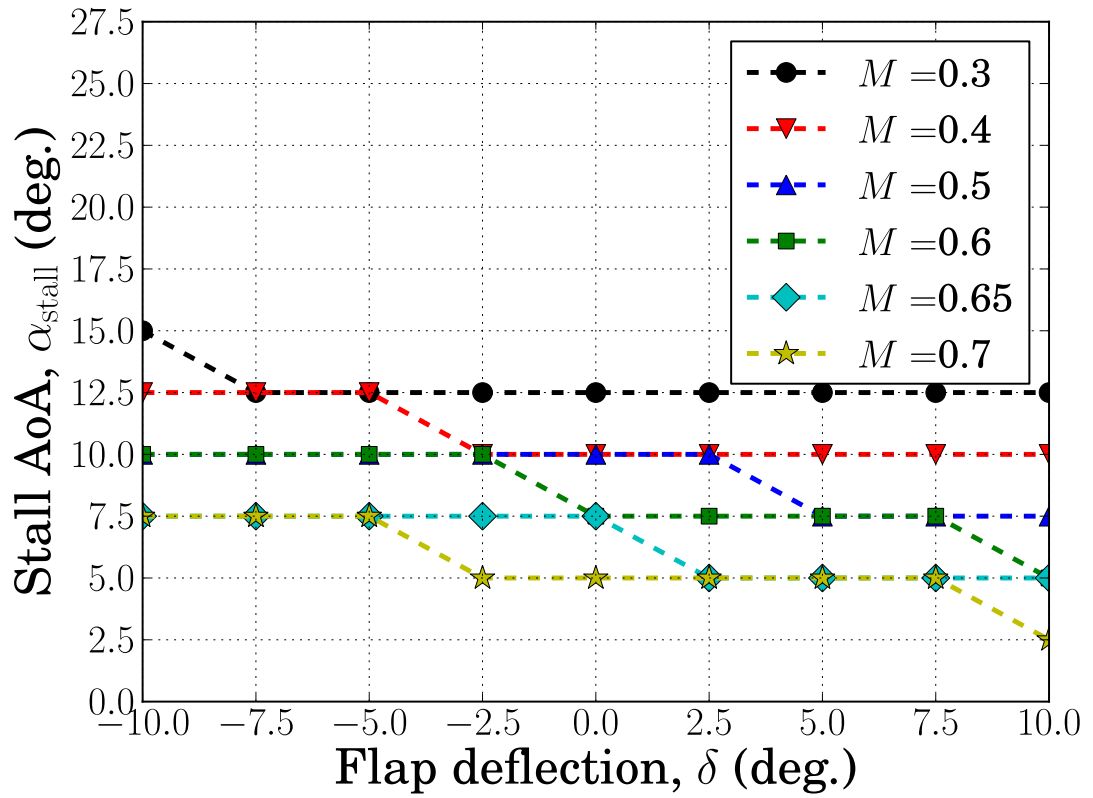
Figure 3.42: Stall boundary (α_{stall}) for different flap deflections (δ) for the NACA0012 airfoil, 15% chord flap, $Re = 4.8$ million.

Figure 3.42 shows the stall boundaries for different flap deflections for the NACA0012 airfoil with 15% flap size for different Mach numbers. Because, the NACA0012 airfoil experiences trailing edge stall, the stall process occurs gradually and the exact point of stall is more difficult to identify from the Mach contour plots. The angle of attack corresponding to stall (α_{stall}) is taken to be the AoA corresponding to maximum lift for the given flap deflection. Also, it must be noted that because of the discrete nature of the data points ($2.5°$ α intervals), the actual stall may occur in between two neighboring points considered in the present simulations. In order to have a conservative estimate, for flap deflections for which there is some ambiguity because the two adjacent α values in the stall region have nearly the same lift, the lower α value is taken to be the stall point. It is important to note that the stall boundary shown in Fig. 3.42 is obtained for a flap size of 15% and a Reynolds number of 4.8 million. However, since flap size for rotor applications are generally close to 15% and generally speaking, angle of attack is the dominant factor (rather than flap deflection) in determining stall, it may be assumed that other NACA0012 airfoils with slightly different flap sizes would have similar if not identical stall limits.

3.3.3 Drag Coefficient

Figure 3.43 shows the variation of the drag coefficient for $M = 0.3$. Again, for reasons of compactness and ease of representation, the drag data is also plotted against α_{eff}. This representation was chosen based on the observations made in the section on drag modeling, where it was seen that the drag can be conveniently

152

represented as a function of α_{eff}. It is seen that drag has a parabolic dependence on α_{eff} until stall. Figure 3.43(b) shows the variation of drag in the unstalled range of α_{eff}. The parabolic dependence on α_{eff} is more clearly seen here. It is also observed that for the range of flap deflections considered ($\delta = -10$ to $+10$), there is some deviation from the baseline parabolic behavior. This shows that a difference in camber does affect the drag more than lift, although the it is not very significant for small flap deflections. For nearly the same positive AoA, a positive flap deflection is seen to have slightly lower drag than negative flap deflections. It is also seen that as δ varies from -10 to $+10$, the dependence of drag on δ (i.e., camber), for nearly the same α_{eff}, also follows a parabolic trend. This can be used to further refine the drag modeling approach described earlier. However, this would require further simulations for the given airfoil for different TEF deflections and therefore cannot rely purely on AoA data usually available for an airfoil.

From Fig. 3.43(a) it is seen that beyond stall, drag has a nearly linear dependence on α_{eff}. It is also observed that the slope of the drag curve beyond stall is nearly the same for all the TEF deflections. This is another useful observation from the perspective of drag modeling. Once the slope of the post-stall drag curve is obtained from AoA data for the given airfoil, this can be used to predict the drag beyond stall even for cases involving TEF deflections. Figures 3.44 and 3.45 shows the drag vs α_{eff} plots for higher Mach numbers. The same general trends are observed for all the Mach numbers and are summarized below:

1. The drag exhibits a parabolic dependence on α_{eff} until stall.
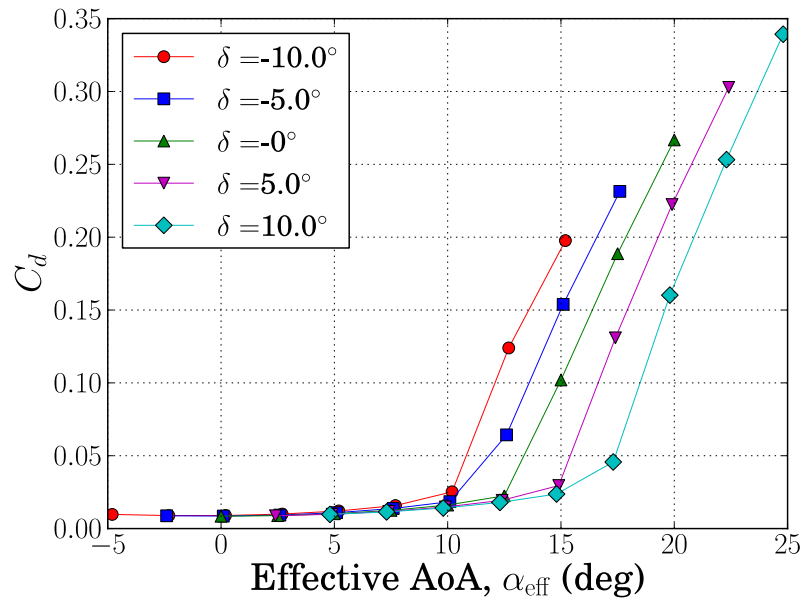
(a) Full Range
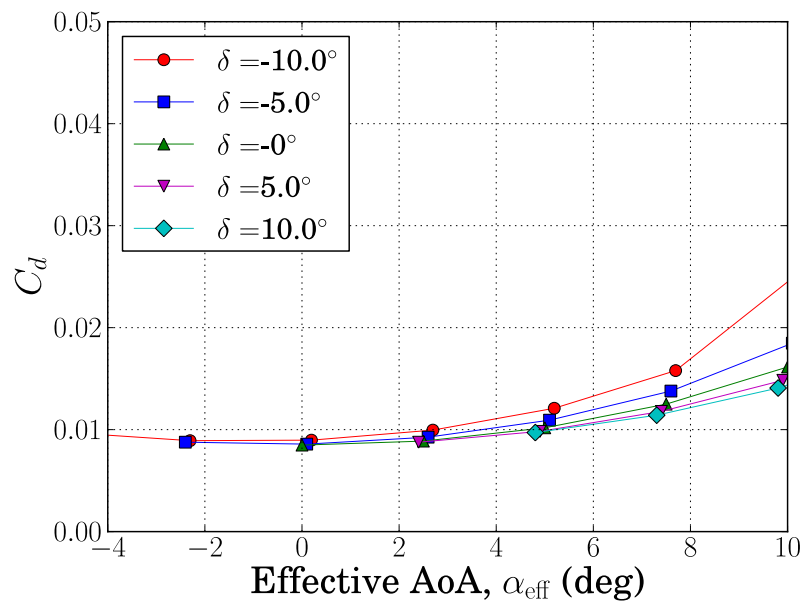
(b) Unstalled Range

Figure 3.43: C_d vs α_{eff} for the NACA0012 airfoil, $M = 0.3$, 15% chord flap, $Re = 4.8$ million.
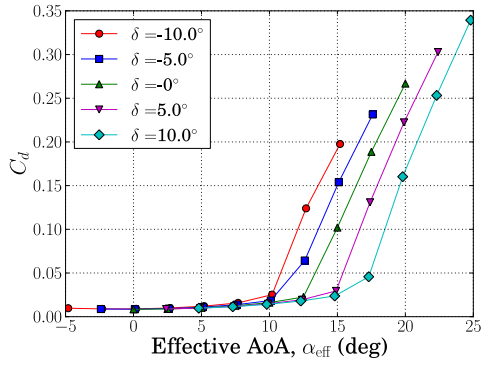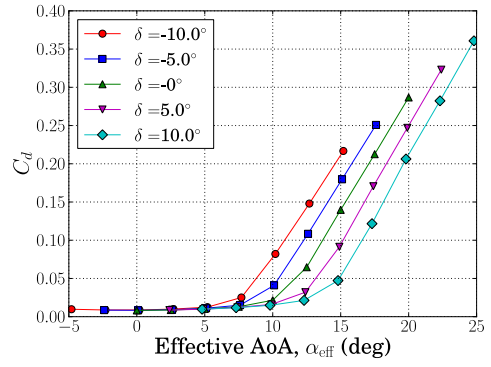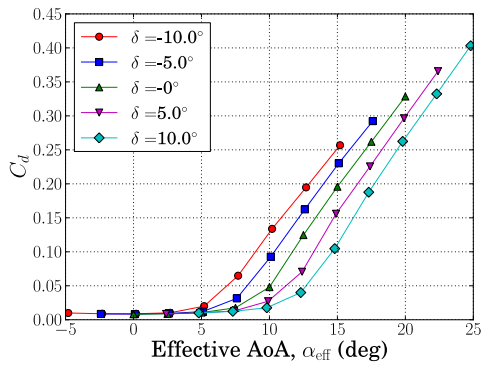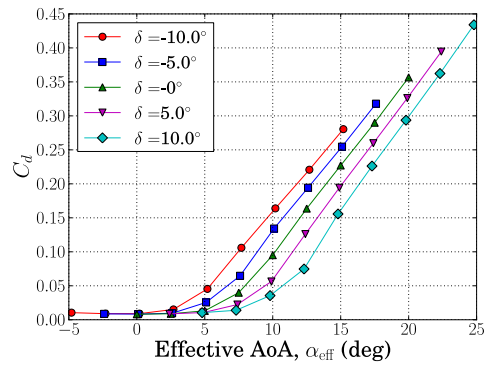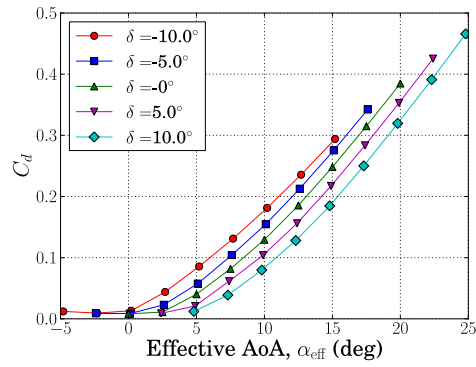
(a) $M = 0.3$
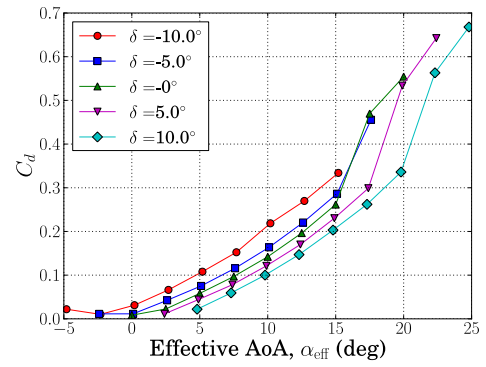
(b) $M = 0.4$

(c) $M = 0.5$

(d) $M = 0.6$

(e) $M = 0.7$

(f) $M = 0.75$

Figure 3.44: C_d vs α_{eff} for different Mach numbers for a NACA0012 airfoil, 15% chord flap, $Re = 4.8$ million.

155
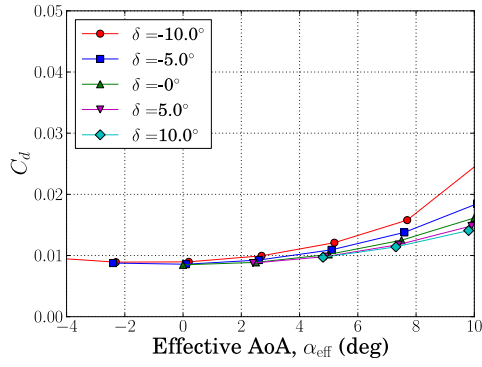
(a) $M = 0.3$
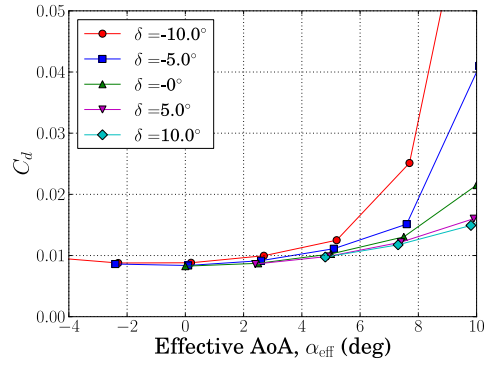
(b) $M = 0.4$
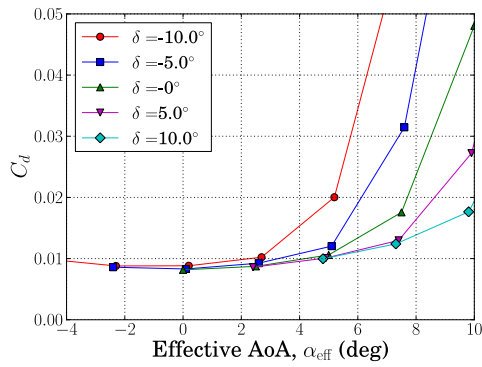
(c) $M = 0.5$
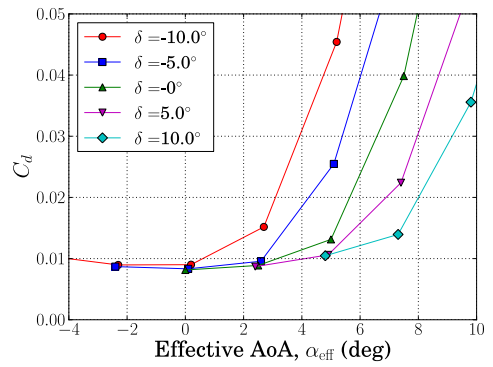
(d) $M = 0.6$
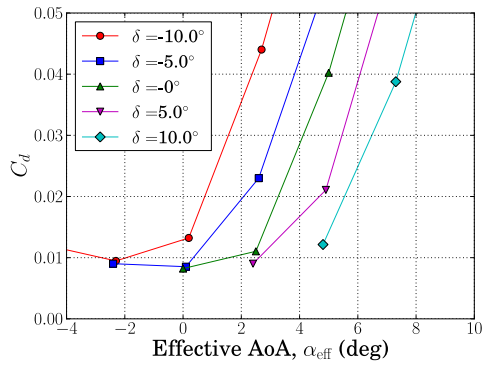
(e) $M = 0.7$
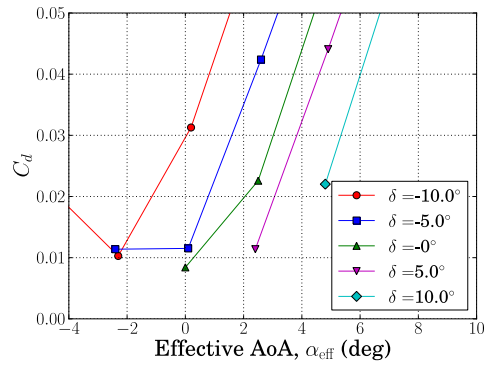
(f) $M = 0.75$

Figure 3.45: C_d vs α_{eff} for different Mach numbers for a NACA0012 airfoil, 15% chord flap, $Re = 4.8$ million.

2. Camber is seen to have a small (but not negligible) effect on drag, with positive (downward) flap deflections having slightly lower drag than negative flap deflections for nearly the same positive α_{eff}.

3. Beyond stall, drag varies linearly with α_{eff}. The slope of the drag curve is nearly the same for all flap deflections (and nearly the same for all Mach numbers).

3.3.4 Pitching Moment and Hinge Moment

Figure 3.46 shows the variation of pitching moment (C_m) as a function of the flap deflection for different angles of attack at $M = 0.3$. From Eq. 2.8 it will be recalled that $C_{m\alpha} = 0$ according to thin airfoil theory (for zero camber). Therefore, within the assumptions of the analytical model C_m is purely a function of δ. From Fig. 3.46 it is seen that the CFD results are similar to the theoretical values at small angles of attack. There are some deviations from theory, but the differences are not very significant. Once stall occurs at higher angles of attack, the offset between CFD and theory is significant. However, while there is a significant offset between CFD and theory at the higher angles of attack, pitching moment still varies linearly with δ. It is also observed that as α increases, the slope of the C_m vs δ curve decreases slightly. This is because, once flow separation occurs on the upper surface of the airfoil, the pressure profile over the upper surface becomes flat and the effectiveness of the flap is reduced. Flow is however, usually attached on the lower surface as indicated by the existence of suction peaks at the leading edge of the flap on the

lower surface for the stalled cases. Thus, while stall reduces the effectiveness of the flap, it can still be used to control the pitching moment. This fact holds particular importance in the context of swashplateless TEF rotors where the blade is controlled by changing the pitching moment by deflecting the TEF. Also, since there are significant enough deviations between theory and CFD for the pitching moment, it is important to use preferably a full-fledged CFD-CSD coupling model or atleast a lookup table based aerodynamic model to predict the pitching moments within the trim code. This is all the more important because swashplateless TEF rotors rely on effective adjustment of pitching moments to control the rotor. The low torsional stiffness of the swashplateless TEF rotor makes it extremely sensitive to small differences in the prediction of the pitching moment. Figure 3.47 shows the trends in pitching moment results for the remaining Mach numbers and is summarized below:

- Pitching moment behaves linearly with flap deflection. The CFD predictions fall in the same ballpark as theory for lower angles of attack while the higher angles of attack show significant offsets.

- The magnitude of the pitching moment at zero flap deflection first increases with angle of attack and then, once α exceeds α_{stall} there is a drastic fall in $C_m(\delta = 0)$.

- The C_m vs δ curve is linear before and after stall but with different slopes. This is because after stall, the pressure distribution on the upper surface is flattened while that on the lower surface is still attached, thereby making the TEF only partially effective. This also means that, a knowledge of $C_m(\alpha, M)$

158

and $\alpha_{\text{stall}}(M)$ for a given airfoil without flap (either from CFD or experiment) can be used to predict the pitching moment behavior of the airfoil with TEF to an reasonable level of accuracy even for nonlinear flow conditions.
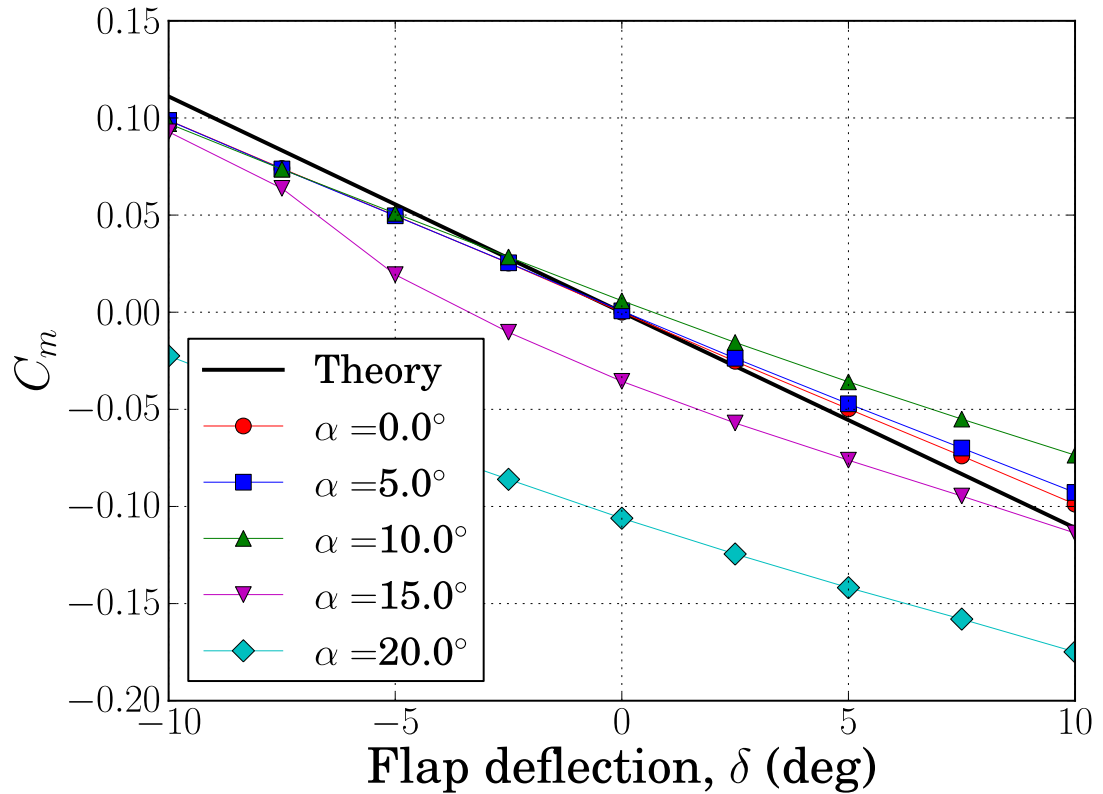
Figure 3.46: C_m vs δ for different angles of attack for the NACA0012 airfoil, $M = 0.3$, 15% chord flap, $Re = 4.8$ million.

Figure 3.48 shows the variation of the flap hinge moment as a function of δ for different Mach numbers. Unlike pitching moment, the theoretical hinge moment is dependent on both α and δ (i.e., $C_{h\alpha} \neq 0$). It is also seen that there are significant deviations between CFD and theory both in the offset as well as in the slope of the C_h vs δ curve. This means that like the pitching moment, it is important to rely on
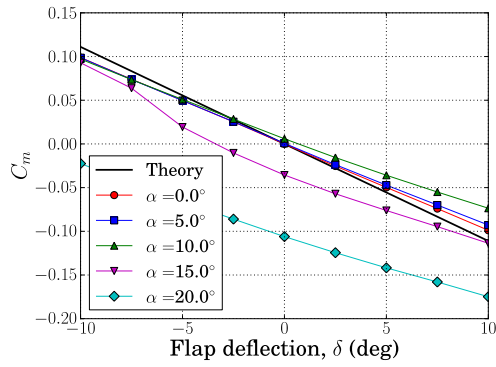
(a) $M = 0.3$ (b) $M = 0.4$
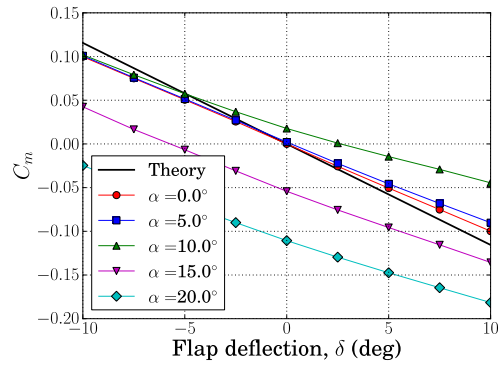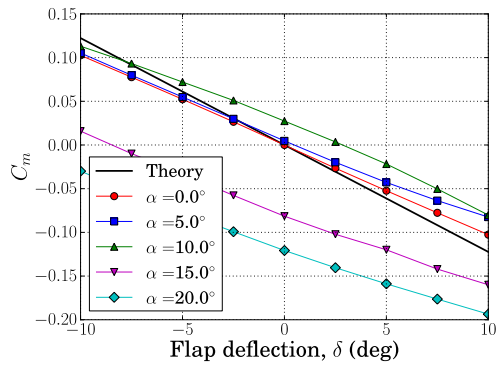
(c) $M = 0.5$ (d) $M = 0.6$
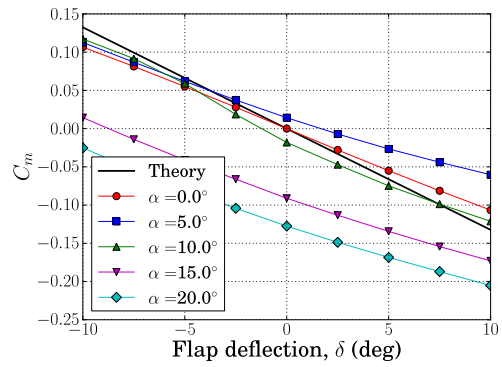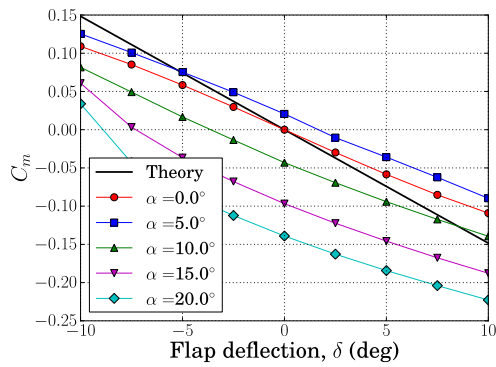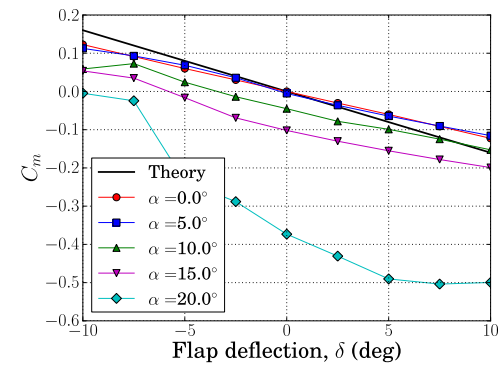
(e) $M = 0.7$ (f) $M = 0.75$

Figure 3.47: C_m vs δ at different Mach numbers for a NACA0012 airfoil, 15% chord flap, $Re = 4.8$ million.

CFD data (either through CFD simulations coupled with the trim code or through lookup tables) to obtain good estimates of the hinge moment predictions. Accurately predicting the hinge moments is necessary for estimating TEF actuation power and is therefore important from a design perspective. However, unlike the pitching moment, the hinge moment predictions do not directly affect the trimming of the rotor and are therefore not as critical in simulating the behavior of swashplateless TEF rotors.

3.3.5 Comparison of NACA0012 and SC1095R8 Airfoils

Besides the simulations on the NACA0012 airfoil, simulations were also performed for the SC1095R8 airfoil. Figure 3.49 compares the airfoil profiles for the NACA0012 and SC1095R8 airfoils. The airloads, Mach streamline and C_p plots for the SC1095R8 are included in Appendix C. The trends in airloads and aerodynamic behavior of the SC1095R8 airfoil are similar to that of the NACA0012 airfoil. Some of the noteworthy features are summarized below :

- Since the SC1095R8 is not a symmetric airfoil, the lift curve predicted by thin airfoil theory has an offset with respect to the actual data. However, the slope and general trends are similar.

- Like the NACA0012 airfoil, the SC1095R8 airfoil also exhibits trailing edge stall for a Reynolds number of 4.8 million.

- A comparison of the stall boundary (compare Figs. 3.42 and 3.50) shows that the SC1095R8 airfoil experiences delayed stall at lower subsonic Mach numbers
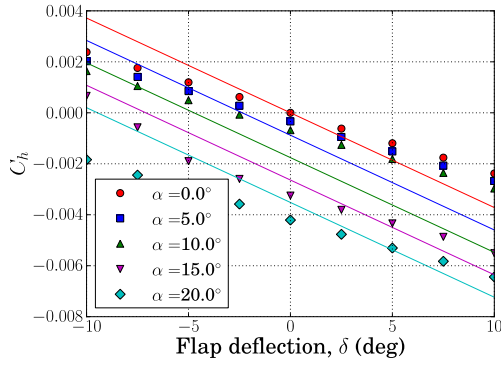
(a) $M = 0.3$
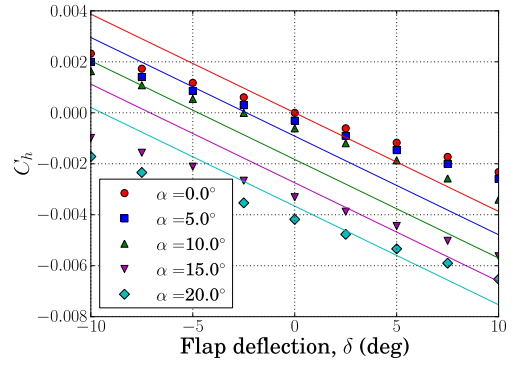
(b) $M = 0.4$
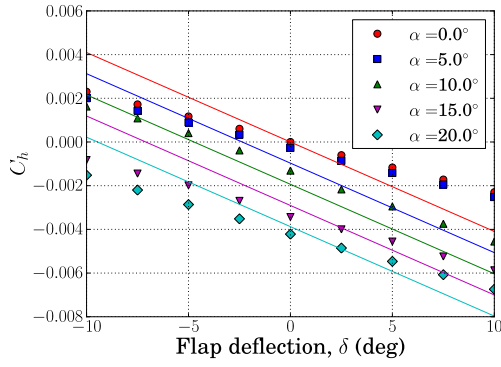
(c) $M = 0.5$
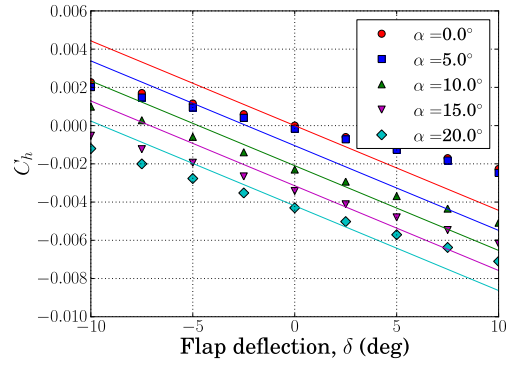
(d) $M = 0.6$
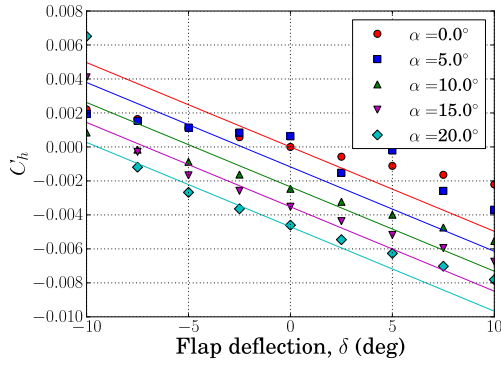
(e) $M = 0.7$
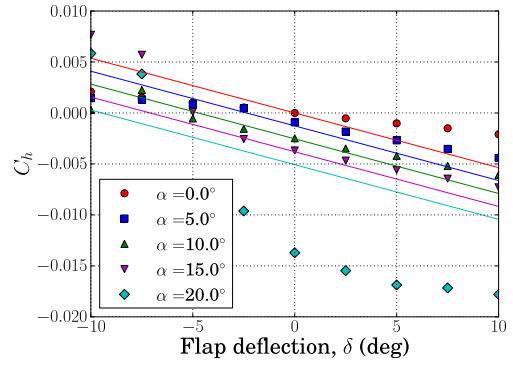
(f) $M = 0.75$

Figure 3.48: C_h vs δ at different Mach numbers for a NACA0012 airfoil, 15% chord flap, $Re = 4.8$ million.

162
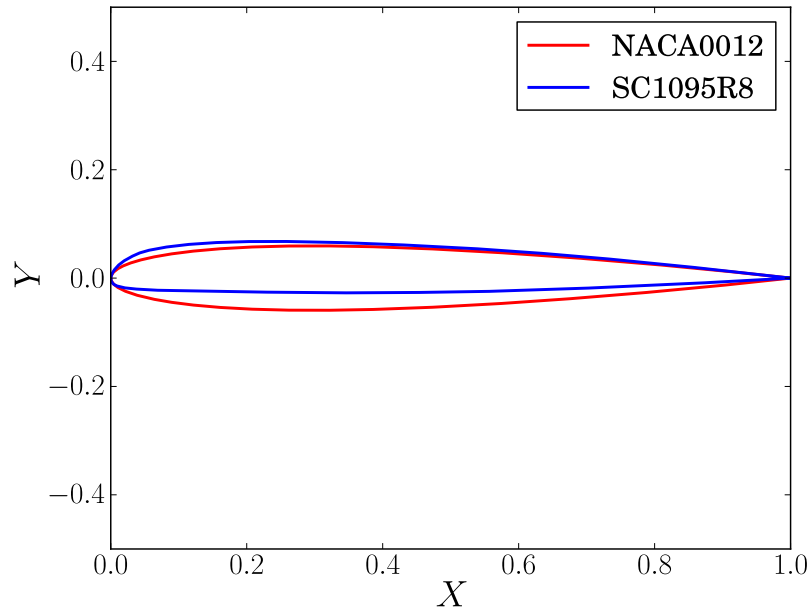
Figure 3.49: Airfoil profiles for the NACA0012 and SC1095R8 airfoils.

as compared to the NACA0012 airfoil. At higher subsonic and transonic Mach numbers, however, it experiences stall earlier than the NACA0012 airfoil.

- One notable difference in the behavior of the two airfoils can be seen at the higher subsonic and transonic Mach numbers. It is seen that the SC1095R8 airfoil experiences shock induced vortex shedding for most of the higher angles of attack at transonic Mach numbers. While the NACA0012 airfoil experiences vortex shedding primarily during the transition from the supersonic pocket to the oblique shock, the SC1095R8 airfoil experiences vortex shedding even after the oblique shock is formed over the airfoil. This is most evident from Figs. 3.51 and 3.52 which compare the vorticity contours for the two airfoils at $M = 0.7$. The implications of this behavior in transonic flow on the performance of the rotor are not obvious, especially because the actual behavior of

the rotor in an unsteady and 3D flowfield is hard to predict based on purely 2D simulations. Systematic 3D wing/rotor simulations are necessary to understand the consequences of these differences in transonic behavior on the performance of the rotor.
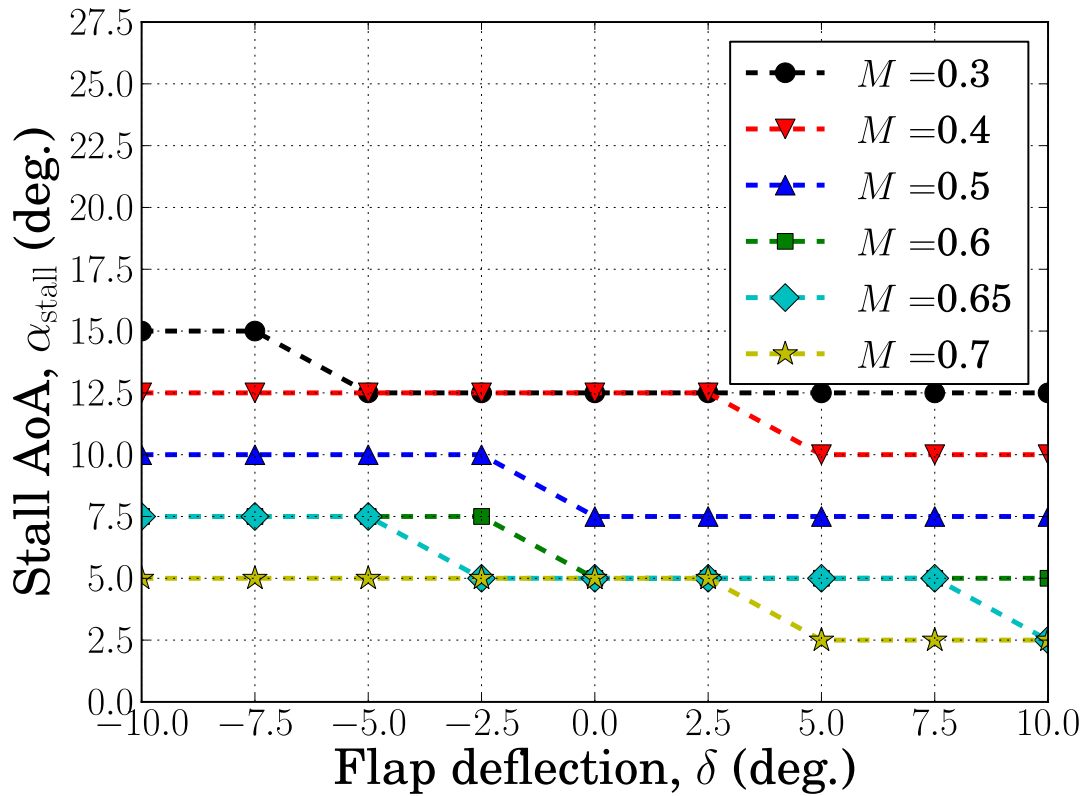
Figure 3.50: Stall boundary (α_stall) for different flap deflections (δ) for the SC1095R8 airfoil, 15% chord flap, $Re = 4.8$ million.

3.4   Summary and Notable Conclusions

This Chapter has looked at various aspects the aerodynamics of trailing edge flaps for 2D flows. These are summarized below :
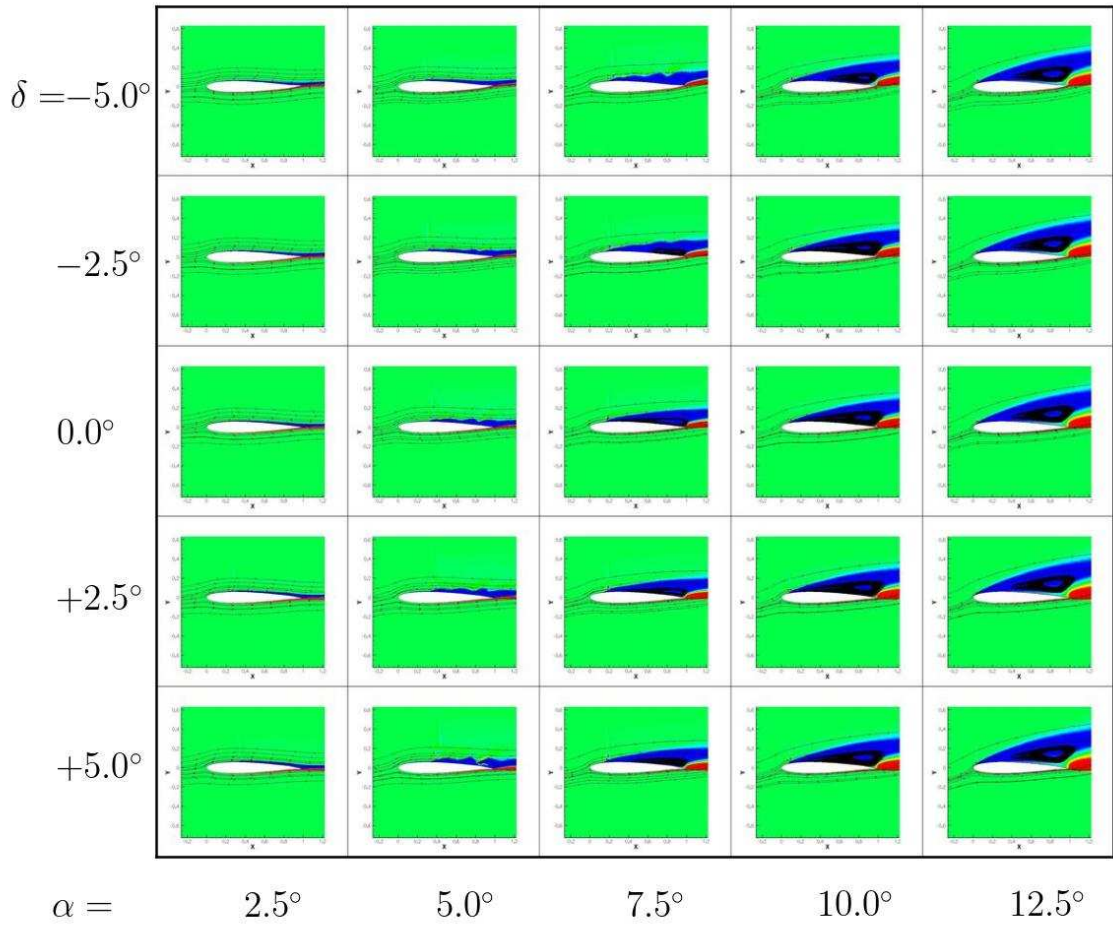
Figure 3.51: Vorticity contours for different α and δ for the NACA0012 airfoil, $M = 0.7$, 15% chord flap, $Re = 4.8$ million.
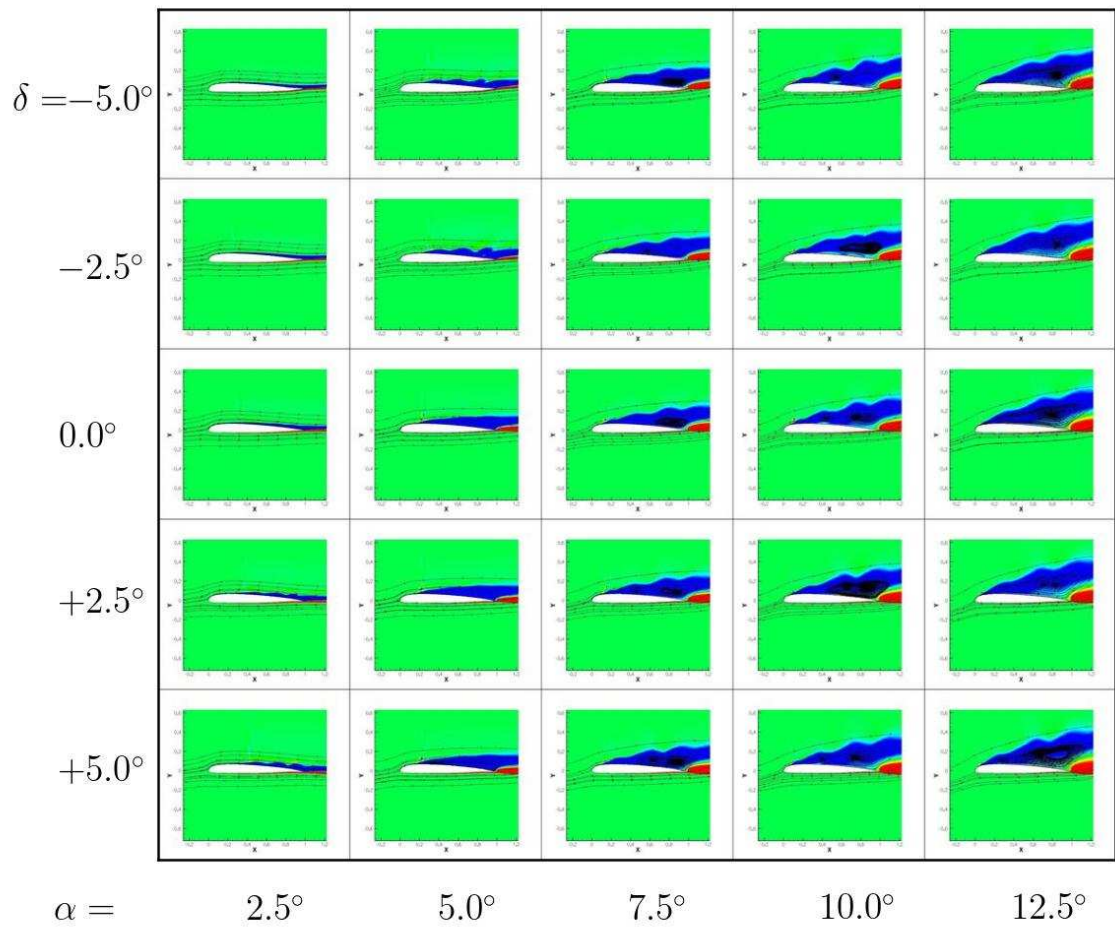
Figure 3.52: Vorticity contours for different α and δ for the SC1095R8 airfoil, $M = 0.7$, 15% chord flap, $Re = 4.8$ million.

1. Different 2D aerodynamic codes were validated against experiment.

2. Unsteady aerodynamic model was verified by comparing it with results obtained using CFD.

   - Good agreement was observed for the lift and drag predictions of the steady CFD simulations for TEF airfoil with overhang. Hinge moment was found to have be in the same ball park as the experimental results.

   - The gap code was validated and was seen to provide improved predictions of the pressure distribution.

3. The effect of various airfoil properties on the airloads of a TEF airfoil was studied.

   - In low lift conditions, airfoil thickness was found to have a negligible effect on lift. Drag was seen to increase linearly with airfoil thickness.

   - Pitching moment was seen to decrease gradually (in magnitude) with as the airfoil thickness increases. Hinge moment was significantly affected by thickness and was seen to vary linearly with thickness.

   - The effect of overhang on lift and pitching moment was not significant, while the flap hinge moment was seen to vary linearly with overhang. Drag penalty is greater when the flap deflection is more.

   - The effect of gaps at the leading edge of the TEF was studied using different modeling approaches. Gaps were modeled using CFD meshes as well as using the approximate "gap averaging" technique. The studies

showed that the effect of gaps is not negligible, particularly at the higher

flap deflections possible for swashplateless TEF rotors, and has an adverse

effect on the performance of airfoils with TEFs.

- The greater the pressure difference at the flap leading edge without a gap, the greater will be the effect of introducing a gap on the steady airloads.

- For a positive flap deflection, increasing the gap size was seen to decrease lift and increase drag. The decrease in lift is primarily due to equalization of pressure across the gap over a larger area and the resultant effect on the pressure distribution upstream and downstream of the gap. The increase in drag may be attributed to flow separation and/or thickening of the boundary layer due to increased gap size.

- Pitching moment was not as drastically affected by increasing gap size. Hinge moment was strongly affected by increasing the gap size, primarily because of flow separation, which often accompanies increased gap size.

- The gap averaging approach was seen to provide airloads and pressure distribution predictions that are very similar to those obtained using additional CFD meshes (patched or overset) at the same computational cost as the approach where the gap is not modeled.

- The gap averaging technique was found to be most effective for small gap sizes ($< 2\%$ chord) and zero overhang. The presence of large overhang or gap sizes results in larger deviations in the airloads obtained using gap averaging and overset/patched mesh approaches, but is nevertheless

better than those obtained when the gap is not modeled at all.

4. Next, the airloads and aerodynamic phenomena associated with TEFs was studied extensively for the NACA0012 and SC1095R8 airfoils.

- The relationship between α, δ and their effect on the integrated airloads was investigated. The concept of effective angle of attack (α_{eff} was found to be useful in studying and modeling integrated lift and drag. Maintaining the TEF with positive flap deflection was seen to offer benefits in the form of delayed stall.

- The stall limits for the airfoils were identified for combinations of α and δ. The stall limits were seen to be predominantly influenced by angle of attack rather than flap deflection.

- Approaches to model the behavior before and after stall were suggested for lift and drag. Drag was seen to exhibit a parabolic dependence on α_{eff} before stall. After stall, drag follows a linear dependence on α_{eff} with a constant slope for all flap deflections.

- Nonlinear flow phenomena such as shocks, flow separation and shock induced vortex shedding were studied and their effect on the integrated airloads was observed.

- The NACA0012 and SC1095R8 airfoils were seen to experience trailing edge stall at the flap size and Reynolds numbers considered in the present simulations.

169

- The phenomenon of shock induced vortex shedding was observed at higher subsonic/transonic Mach numbers as the flow transitioned from a supersonic pocket in the front portion of the airfoil to an oblique shock.

- The occurrence of shock induced vortex shedding was seen to be different for the NACA0012 and SC1095R8 airfoils. For the NACA0012 airfoil, there was a rapid transition from shock induced vortex shedding to fully separated flow behind the oblique shock, whereas for the SC1095R8 airfoil, the phenomenon of shock induced vortex shedding persisted for higher angles of attack.

- Pitching moment and hinge moments were observed to vary linearly with flap deflection for subsonic and transonic Mach numbers.

- Significant offsets were observed for the pitching moment vs δ curve at higher angles of attack. This indicates the need for using direct CFD or lookup tables to accurately predict the pitching moments in comprehensive rotor analysis codes. This is especially true for swashplateless TEF rotors which are controlled by adjusting the pitching moment and are extremely sensitive to small differences in pitching moment prediction.

- Differences in offset and slope was observed for the hinge moment vs δ curves obtained using CFD and theory, again highlighting the need to use lookup tables in comprehensive analysis.

Overall, the studies described in this chapter provided useful insights and tools for understanding the behavior of TEF airfoils. Some of the tools developed for 2D

analysis can be extended for 3D rotor simulations as well. Extensive data obtained

for the NACA0012 and SC1095R8 airfoils has been used to develop lookup tables

to support 3D rotor analysis in the following chapter.

Chapter 4

3D Aerodynamics

This chapter discusses uncoupled CFD as well as coupled CFD-CSD simulations of conventional (baseline) and swashplateless TEF rotors in hover. The objective is to obtain an understanding of the performance and airloads of the swashplateless TEF rotor and compare it with that of a conventional rotor in hover. Simulations are also carried out to study the wake structure and the effect of gaps on the performance/airloads for a swashplateless TEF rotor.

The present study is useful because until now, studies on the swashplateless TEF rotor have relied primarily on lookup tables (or linear thin airfoil theory based aerodynamic models) to estimate the airloads within the comprehensive rotor analysis codes. The conclusions based on these approximate aerodynamic models cannot be fully relied upon. This is particularly so for swashplateless TEF rotor analysis because of the very strong coupling between the aerodynamic and structural loads. Unlike the conventional rotor, the key controlling mechanism of a moment-flap based swashplateless TEF rotor relies on the coupling between structural and aerodynamic loads and is, therefore, very sensitive to small perturbations in the either the airloads or blade configuration. In the present work, the use of CFD ensures that the trim calculations in the comprehensive rotor analysis code is well supported by high fidelity airloads provided by CFD. At the same time, the regular exchange of data

between the CFD and CSD codes for several coupling cycles ensures that the rotor configuration (blade collective, deformations, etc.) and the airloads correspond well with each other. Before looking at the fully coupled CFD-CSD simulations, it would be useful to understand the basic airloads and wake behavior for the baseline and swashplateless rotors using uncoupled CFD simulations.

4.1 Uncoupled CFD Simulations (Prescribed Deformation/Collective)

In the uncoupled CFD simulations, the blade deformations and collective are first computed by trimming the rotor for a given thrust using the comprehensive rotor analysis code (UMARC). The blade collective and deformations so obtained are then provided to the CFD code (OVERTURNS) which then maintains the same blade configuration throughout the simulation. Thus, the blade configuration is only passed once from the CSD code to the CFD code and there is no subsequent exchange of information between the CFD and CSD codes (hence the name, uncoupled CFD simulation). Because the CSD code uses a linear aerodynamic model (or lookup tables) in the aerodynamic calculations involved in trimming the rotor, the blade deformations so obtained would not be as accurate as those obtained with the support of 3D CFD simulations. However, for simulations performed for understanding the wake (involving highly refined grids) the uncoupled CFD simulation serves the purpose, without making the computational cost prohibitively expensive.

The swashplateless UH-60 rotor used in the simulations was obtained by modifying the baseline UH-60 rotor. The following modifications were made to the

173

baseline UH-60 rotor in order to make it a swashplateless TEF rotor:

1. A 15% chord integrated TEF (with zero overhang) is added from $r/R = 0.545$ to $r/R = 0.925$. At the chordwise and spanwise edges of the TEF, the grids are faired, with no effective flow through the gaps, unless otherwise stated.

2. The pitchlink stiffness is changed to about $1/45^\text{th}$ the stiffness of the baseline rotor.

3. For the uncoupled simulations, an index angle of $15°$ was used. As defined earlier, the index angle is defined as the angle of the blade root in the absence of torsional moments at the root; effectively it is a pre-pitch of the blade.

The uncoupled CFD simulations were performed on a fine mesh system ($265 \times 259 \times 61$ blade mesh and $67 \times 347 \times 223$ background mesh) for the baseline and swashplateless UH-60 rotors at a prescribed C_T/σ of 0.084. The blade deformations and trim settings are obtained from an initial run using UMARC for the aforementioned thrust. The blade deformations are then kept fixed throughout the CFD simulation. A typical CFD simulation involves about 6 rotor revolutions so as to eliminate the initial starting vortex and also allow the wake to develop below the rotor. Since the CFD and CSD codes are uncoupled, the CFD simulation may result in a different thrust value, and the spanwise distribution of forces will not be identical with those from the UMARC run.
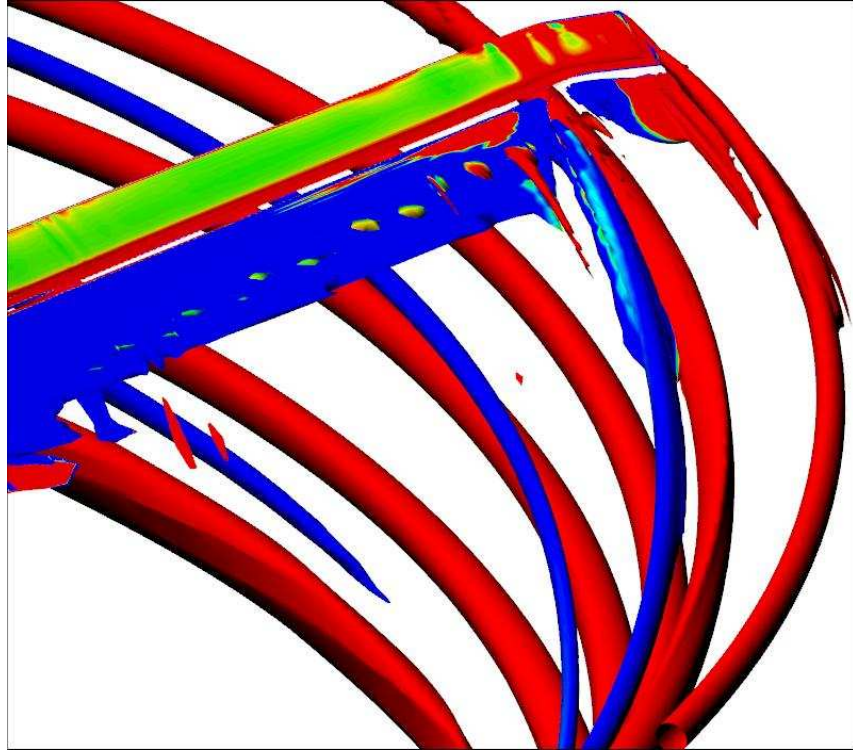
Figure 4.1: Iso-surfaces of q-criterion for baseline rotor at $C_T/\sigma = 0.084$ (prescribed) on a fine mesh for prescribed deformations.

4.1.0.1 Airloads and Blade Deformation

Figure 4.1 shows the wake structure for a baseline UH-60 rotor at $C_T/\sigma = 0.084$ (prescribed). The wake is captured by plotting the iso-surfaces of q-criterion. The fine mesh captures the wake well below the rotor. It is seen that at the point of interaction between the first returning vortex with the blade, a vortex having an opposite sense of rotation to that of the tip vortex is formed (as indicated by the blue vortex tube in Fig. 4.1). The opposite sense vortex (OSV) will be discussed in greater detail in the next section.

Figure 4.2 shows the spanwise distribution of airloads and blade deforma-

(a) Normal force

(b) Pitching moment

(c) Chord force

(d) Blade deformation
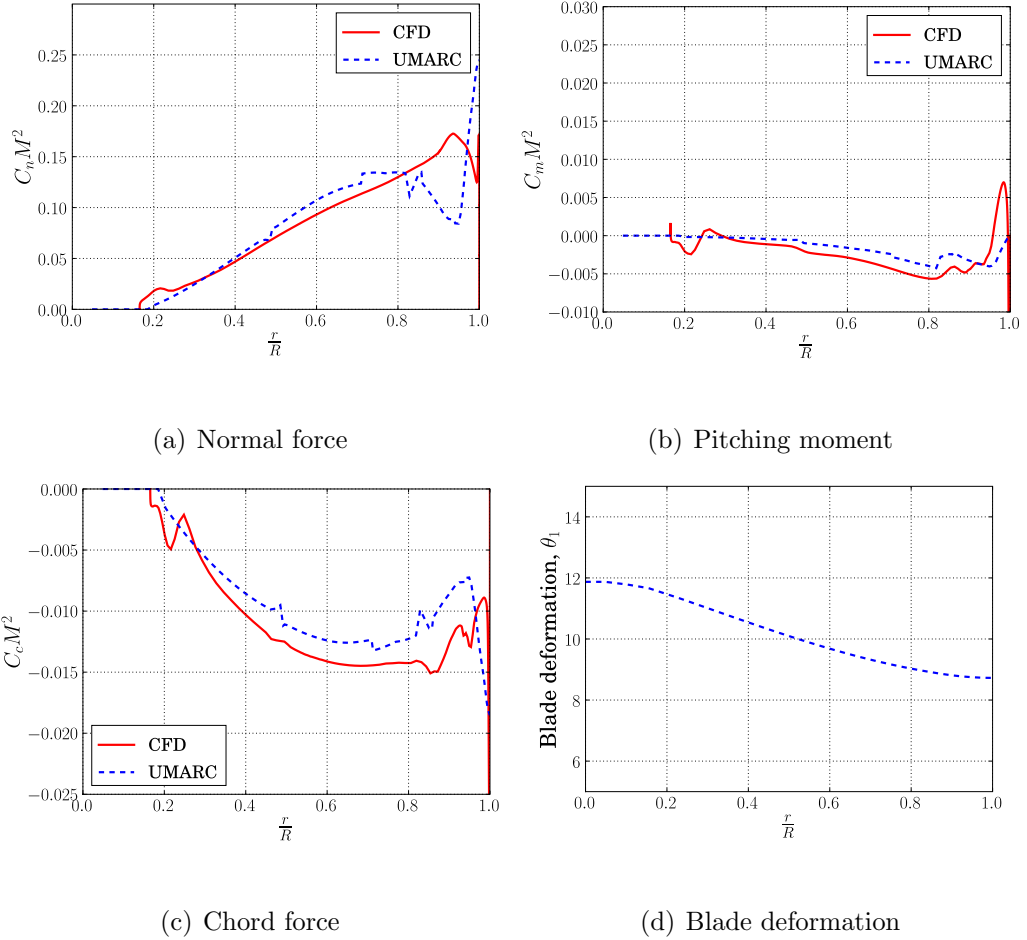
Figure 4.2: Airloads and blade deformation for baseline rotor at $C_T/\sigma = 0.084$ on a fine mesh for prescribed deformations.

tion for a baseline UH-60 rotor at $C_T/\sigma = 0.084$. The CFD results are compared with uniform inflow based UMARC airloads which are used to determine the blade configuration provided to the CFD solver. From the airloads plots, it is seen that UMARC provides reasonable predictions for the lift, except near the blade tip where the differences are more pronounced because of the limiting assumptions (uniform inflow, locally 2D flow, etc.) of the UMARC aerodynamic model. The close proximity of the blade and the first returning vortex also contributes to the differences between UMARC and the CFD predictions. While UMARC captures the general

176
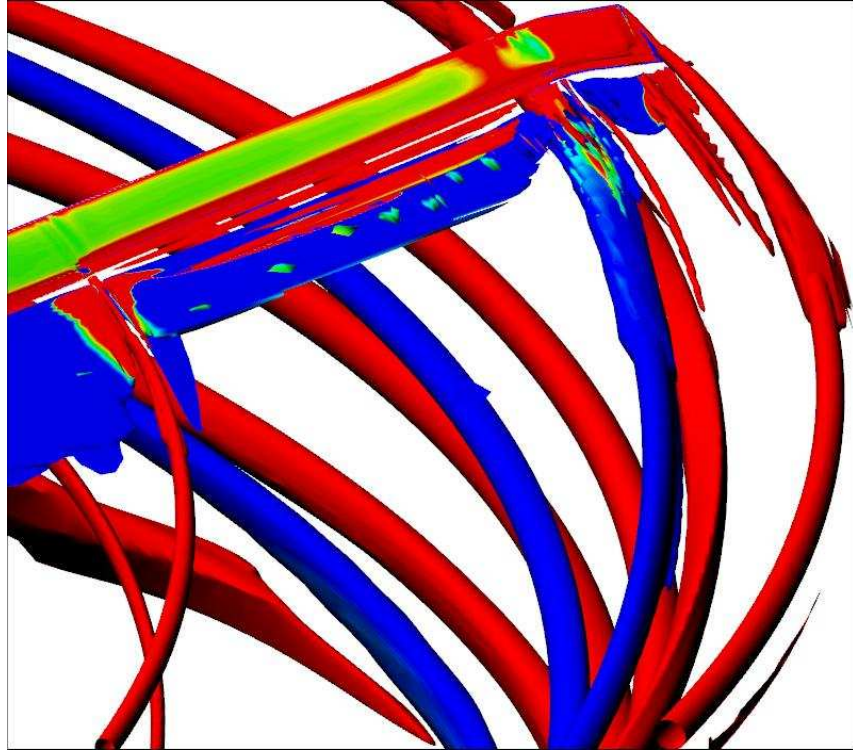
Figure 4.3: Iso-surfaces of q-criterion for swashplateless TEF rotor at $C_T/\sigma = 0.084$ on a fine mesh for prescribed deformations.

trends in drag (which is the negative of the chord force) and pitching moment, it under-predicts the magnitudes of both. The blade deformation, is seen to increase monotonically from the root to the tip (see Fig. 4.2(d)). Note that the blade deformation, as shown, consists of the difference between the local pitch angle and the built-in twist; and thus for the baseline rotor it also includes the collective angle specified to the pitchlink.

Figure 4.3 shows the wake structure for the swashplateless TEF rotor at a $C_T/\sigma = 0.084$. The TEF deflection corresponding to this C_T/σ is about $-6°$ based on the UMARC trim calculations. One important difference in the wake of a swashplateless TEF rotor, is the formation of an inboard trailed vortex at the spanwise

177

(a) Normal force

(b) Pitching moment

(c) Chord force

(d) Blade deformation
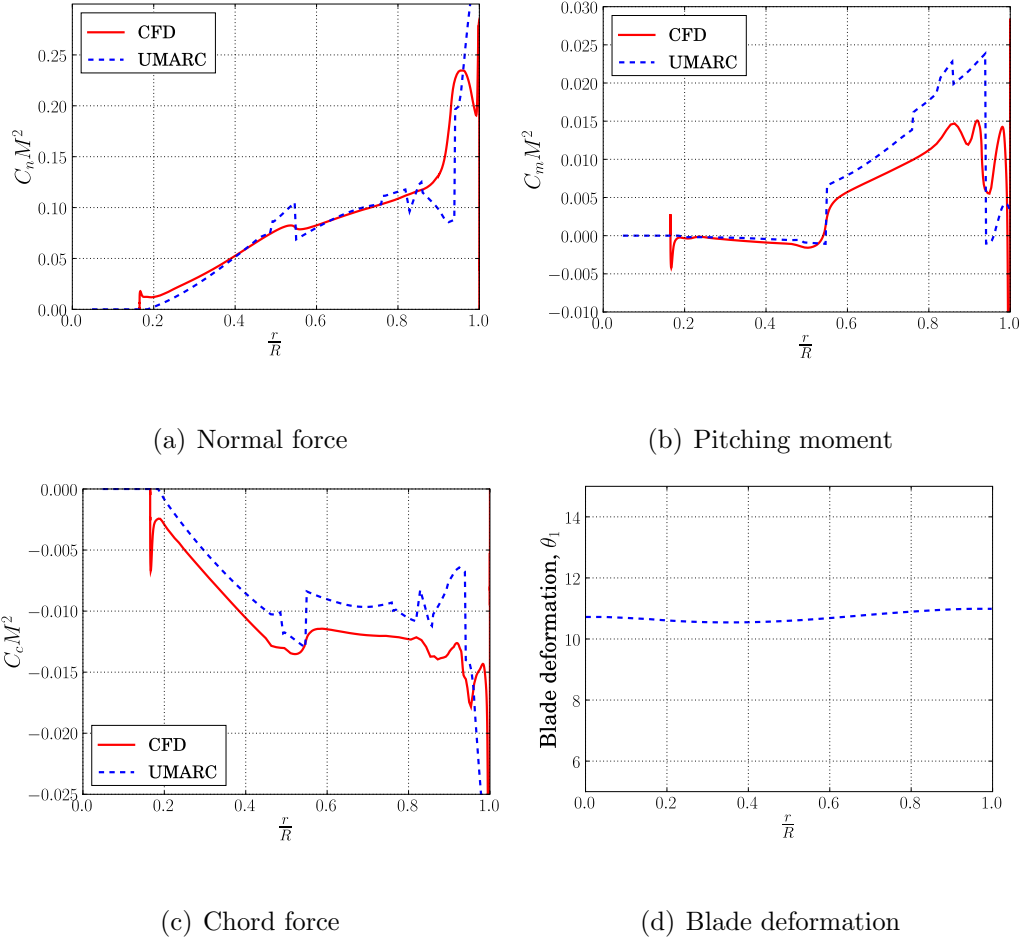
Figure 4.4: Airloads and blade deformations for swashplateless TEF rotor at $C_T/\sigma = 0.084$ on a fine mesh for prescribed deformations.

edge of the TEF (see Fig. 4.3). The inboard vortex is formed due to the discontinuity in the lift/geometry at the TEF juncture. Figure 4.4 shows the airloads and blade deformation for the swashplateless TEF rotor at an index angle of 15°. It is observed that the swashplateless TEF rotor has a steeper increase in lift near the tip than the baseline rotor. Both UMARC and CFD show the same trends in the normal force distribution. The UMARC normal force distribution shows discontinuities at the TEF edges (which are not seen in the CFD airloads) because UMARC does not include radial effects and treats each cross section to be independent of the other.

The lift distribution is less steep in the region spanned by the TEF because the radial increase in lift caused by increasing sectional free-stream velocity is countered by the decrease in lift due to an upward TEF deflection. In the tip region however, the lift is seen to increase much more rapidly than for the baseline rotor because the blade deformations for the swashplateless TEF rotor do not decrease toward the tip as much as in the case of the baseline rotor (see Fig. 4.4(d)).

It is observed that in the spanwise region where the TEF is present, the pitching moments are significantly larger. This is because an upward TEF deflection produces a positive (nose up) pitching moment. It is this capacity of the TEF to produce pitching moments that makes it possible for it to twist the blade elastically and control the rotor to produce the required thrust. UMARC is again seen to underpredict the magnitude of the pitching moments. Note that the elastic deformation, as shown, consists of the difference between the local pitch angle and the built-in twist; and thus for the swashplateless TEF rotor it also includes the index angle specified to the pitchlink. Thus, the pitching moment has significantly changed the pitch angle at the blade root. The chord force (which is the negative of the drag) is seen to be comparable to that of a baseline rotor at the same thrust. The chord force shows a slight decrease in magnitude in the region of the TEF. This is because, the local angle of attack in the TEF region is positive for this case, and deflecting the flap upward decreases the effective angle of attack. Since effective angle of attack is an approximate indicator of the drag (see the section on drag modeling in Chapter 2), it is actually lower in the region of the TEF. Again, as in the case of the baseline rotor, the chord force predictions from the two methods

179

show deviations in the region where the first returning vortex interacts with the blade.

4.1.0.2 Wake Structure

The wake has an important effect on the airloads of the baseline and swashplateless rotors, primarily because it affects the inflow distribution over the blade. The most important components of the wake are the trailed tip vortex and, in the case of the swashplateless rotor, the inboard trailed vortex at the inboard edge of the TEF (see Figs. 4.1 and 4.3). In the present work, the use of highly refined meshes makes it possible to preserve these vortices well below the rotor plane. The first returning vortex typically hits (or passes near) the blade around the 90% span location. The relatively high strength of the tip vortex and its close proximity to the blade at first passage makes the flow field complicated near the tip. The shear layer behind the baseline rotor remains relatively undisturbed. This is indicated by the continuous blue sheet behind the blade. On the other hand, for the swashplateless TEF rotor, the shear layer encounters perturbations from the inboard trailed vortex, the deflected TEF and the discontinuities at the spanwise edges of the TEF. Also, the relatively rapid increase in lift near the tip increases the gradients in the shear layer and makes it less stable in this region.

One byproduct of the close proximity of the first returning vortex with the blade is the "opposite sense vortex" (OSV) which has an opposite sense of rotation to that of the tip vortex. The interaction of the first returning tip vortex with

180
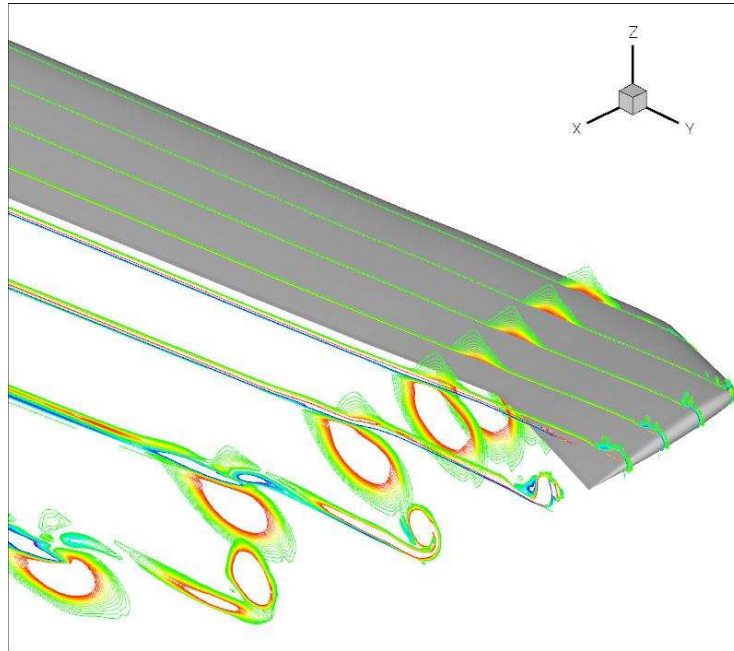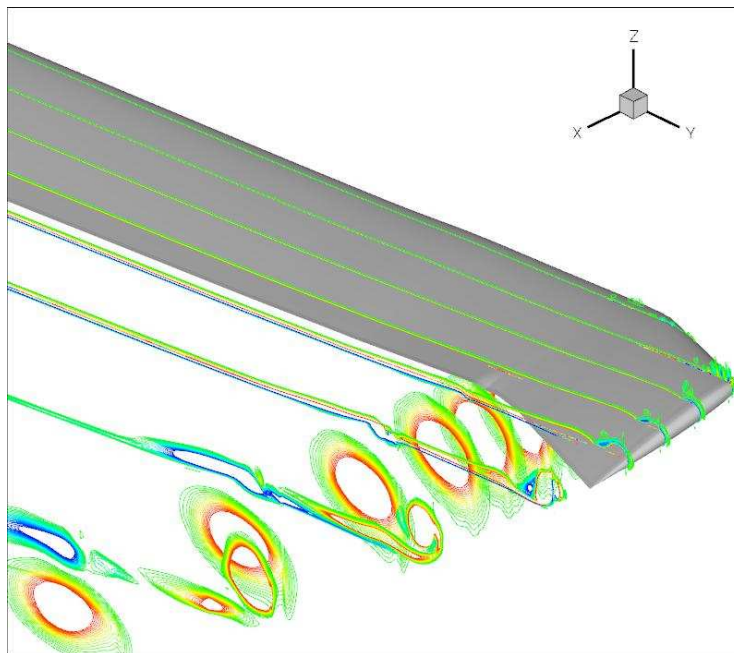
(a) Baseline rotor

(b) Swashplateless TEF rotor

Figure 4.5: Vortex-shear-layer interaction at $C_T/\sigma = 0.084$ on a fine mesh for prescribed deformations.
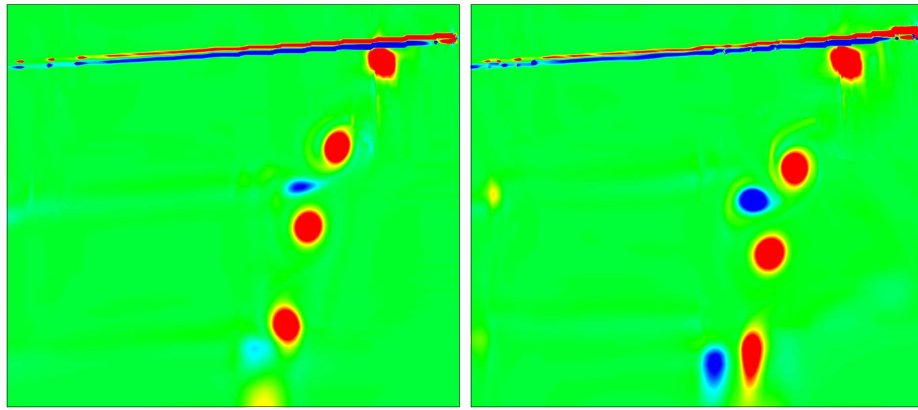
(a) Baseline, 0° wake age

(b) Swashplateless, 0° wake age
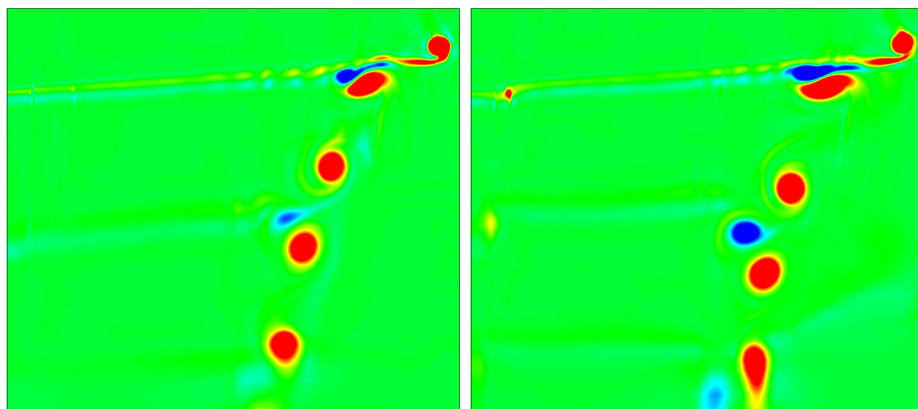
(c) Baseline, 15° wake age

(d) Swashplateless, 15° wake age
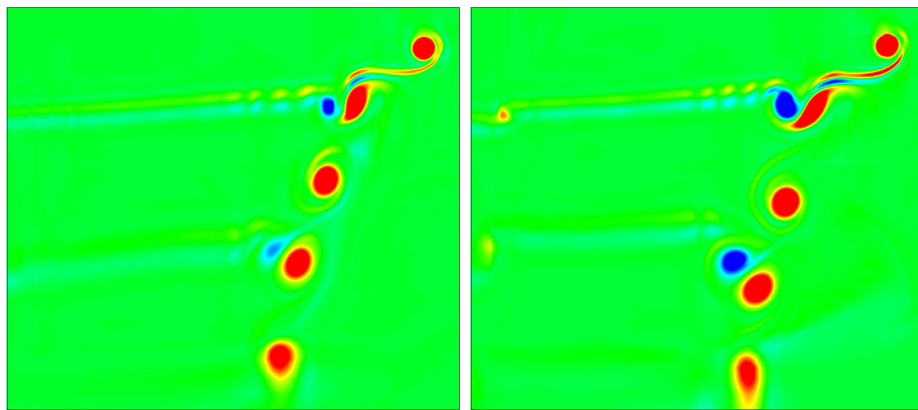
(e) Baseline, 30° wake age

(f) Swashplateless 30° wake age

Figure 4.6: Vorticity contours for the baseline and swashplateless UH-60 rotors at different wake ages for $C_T/\sigma = 0.084$ on a fine mesh for prescribed deformations.

the shear layer induces the shear layer to roll up, leading to the formation of the OSV. The tendency to form an OSV is more pronounced for a swashplateless TEF rotor because of the gradients in the shear layer and the higher lift gradients in the tip region. Figure 4.5 shows the formation of the OSV by the interaction of the first returning vortex with the shear layer for a baseline and swashplateless rotor at the same approximate thrust. It is seen that for the baseline rotor, the first returning vortex touches the blade and interacts strongly with the shear layer. For the swashplateless TEF rotor, the first returning vortex passes slightly beneath the rotor, however the opposite sense vortex formed appears to be stronger for the swashplateless TEF rotor.

Figure 4.6 shows the vorticity contours at different wake ages and shows the development of the wake for the baseline and swashplateless TEF rotors. The close proximity of the returning tip vortex and the formation of the OSV due to the interaction of the returning tip vortex with the shear layer can be clearly seen. The OSV is seen to be stronger for the swashplateless TEF rotor. The tip vortex trailed from the blade tip of a UH-60 rotor is typically observed to convect downward relatively slowly until the first blade passage because it lies in the region where the inflow is less. The OSV convects much faster than the tip vortex because it lies slightly inboard where the inflow is higher. The vortex trailed at the inboard TEF juncture convects downward at a rate comparable to that of the OSV, indicating that the inflow is nearly constant inboard of the tip region (see Fig. 4.15(e)).

The flow features observed in the wake in the present study can affect various aspects of the performance of swashplateless rotors. Besides affecting the pressure

distribution over the blade by changing the inflow, these wake structures (inboard trailed vortex and opposite sense vortex) could affect vibration, noise levels and brownout behavior as well. In forward flight conditions, the inboard trailed vortex can lead to additional blade vortex interactions (BVI) and thereby affect the vibratory loads and noise levels. The effect of the opposite sense of vortex and the inboard trailed vortex on the brownout, could also be important. An understanding of these effects is only possible by performing more detailed simulations in hover and forward flight and is beyond the scope of the present work.

It is seen from these uncoupled simulations that UMARC provides first order estimates of the airloads. Differences are observed between CFD and UMARC predictions in the spanwise distribution of the airloads, particularly in the tip region. While the uncoupled simulations may be adequate for understanding the wake behavior and general trends, the differences in airloads could give rise to errors in structural deformations which in turn would affect the airloads still further. Accurately capturing the structural and aerodynamic coupling is particularly important for swashplateless TEF rotors because they rely on the coupling between the aerodynamic and structural loads to produce the forces required to control the rotor. If greater confidence is to be placed in the airloads and performance estimates of swashplateless TEF rotors, a more sophisticated framework is required to accurately capture the structural and aerodynamic interactions. The following sections describe the results obtained for the baseline and swashplateless rotors using the *coupled* CFD-CSD approach.

4.2 Validation of CFD-CSD code

The coupled CFD-CSD simulations are performed using the loose coupling strategy described in Chapter 2. Unlike the uncoupled simulations which are performed on a fine mesh (computationally expensive), the coupled CFD-CSD simulations are performed mostly on a coarser mesh (computationally less expensive) in order to cover a larger range of thrusts and are used to study performance and airloads behavior. The coarse mesh has about $1/4^{\text{th}}$ the grid points of the fine mesh.

The first step in establishing the reliability of the 3D CFD-CSD code is to validate it against available experimental data. Because relevant experimental data is not available for the swashplateless TEF rotor, the validation is performed for the baseline (conventional) UH-60 rotor. Since the basic code and solution procedure is similar for the baseline and swashplateless simulations, it is reasonable to assume that the baseline validation supports the validity of the swashplateless TEF rotor simulations as well.

4.2.1 Details of Experiment

The baseline UH-60 rotor simulations are validated with experimental data obtained by Lorber, et. al (Ref. 108). This test was conducted using a geometrically and approximately aerodynamically scaled model of the UH-60A main rotor. The primary rotor used in this experiment is a 2.9m (9.4 ft) diameter (1:5.73 scale), 4-bladed rotor. Comprehensive data was obtained for the UH-60A rotor, including: rotor performance (from a balance), blade surface pressures (from 176 miniature
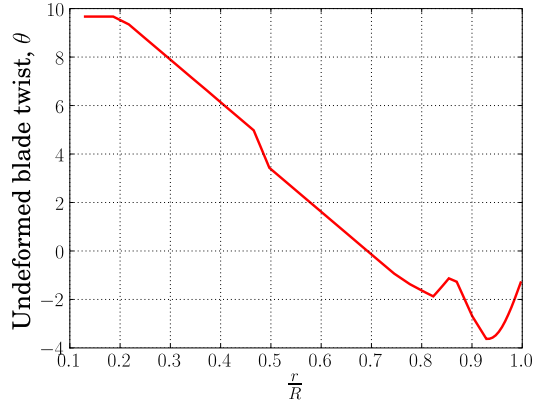
Figure 4.7: Twist distribution for undeformed UH-60 rotor.

pressure transducers), flow field velocities, aeroelastic deflections and wake geometry. Only the performance data is compared with the computational data obtained in the present work.

4.2.2 UH-60 Rotor Specifications

The UH-60 rotor is one of the most widely studied rotors. It has two airfoil sections — SC1095 and its higher lift variant, the SC1095R8. The SC1095 is used in the inboard and tip regions while the SC1095R8 is used in the remaining portion of the blade. The blade has a nonlinear twist distribution (see Fig. 4.7), a tip sweep of about 20°, an aspect ratio of 15.3 and a geometric solidity of 0.0825. Since the UH-60 rotor does not have a simple and typical blade geometry, some of the structural and aerodynamic behavior that it exhibits may not be found in other helicopter rotors. However, the UH-60 rotor is used for most simulations in the present work primarily because it builds on previous work done on the UH-60 rotor at the University of Maryland and also because it is an experimentally well tested rotor.

4.2.3 Grid Convergence Analysis

Before comparing the coupled CFD-CSD results on a coarse mesh with experiment, it would be useful to demonstrate that the coarse mesh solutions do not compromise significantly on the accuracy, particularly with regard to blade configuration. Figure 4.8 shows the airloads and blade deformation for a baseline rotor at low thrust ($C_T/\sigma = 0.04$). The airloads are plotted for coarse and fine mesh cases. The coarse mesh solution is based on 10 coupling cycles. While the fine mesh solution is based on four additional cycles on a mesh initialized by interpolating the final coarse mesh solution. It is seen that the differences in airloads between the coarse and fine meshes is small, and mainly in the tip region. Also, the blade configuration (collective, deformations) is almost identical for the coarse and fine mesh simulations.

The CFD-CSD results are compared with results obtained using UMARC coupled with freewake. It is seen that although the performance predictions using the same UMARC code in Figs. 4.10 and 4.11 give almost the same integrated quantities as CFD, the spanwise loading shows clear differences. The interaction of the returning tip vortex with the blade is seen to have a significant effect on the airloads in the tip region, as shown by the differences in lift, drag and pitching moment in the region of blade-vortex interaction. Figure 4.9 shows a high thrust condition ($C_T/\sigma = 0.09$) for the same rotor. The observations made for the $C_T/\sigma = 0.04$ are seen to be valid for the high thrust case as well.

(a) Normal force

(b) Pitching moment

(c) Chord force

(d) Blade deformation
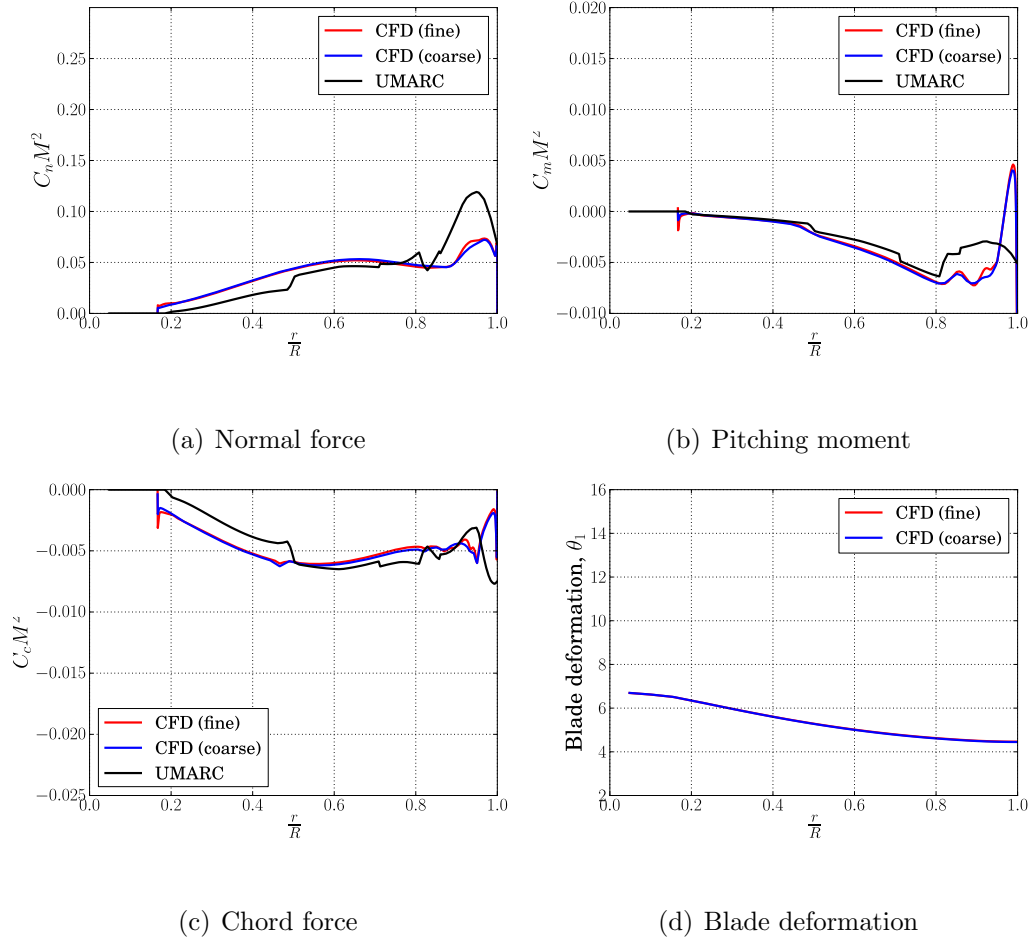
Figure 4.8: CFD-CSD coupled predictions of aerodynamic loads, blade deformation, inflow and structural loads for baseline rotor at $C_T/\sigma = 0.04$.

4.2.4 Details of Validation Runs

In order to compare with the experimental results, a thrust sweep is carried out. CFD-CSD simulations are performed with target thrusts of $C_T/\sigma = 0.02$, 0.04, 0.05, 0.06, 0.08, 0.10. For each target thrust, 10 CFD-CSD coupling cycles are run in order to achieve converged blade deformations and airloads. Typically, the first CFD-CSD coupling cycle consisted of 3 rotor revolutions in order to sufficiently convect the initial starting vortex, while the subsequent cycles consisted of 1.25

(a) Normal force

(b) Pitching moment

(c) Chord force

(d) Blade deformation
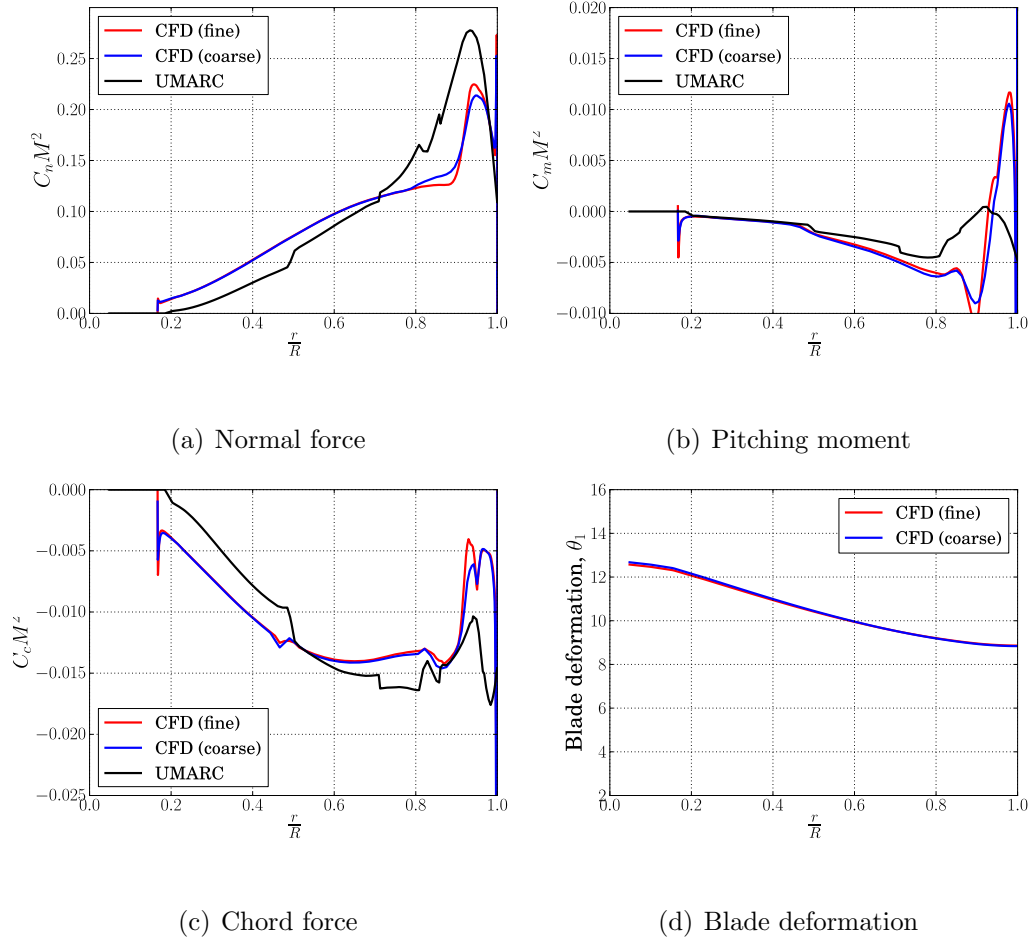
Figure 4.9: CFD-CSD coupled predictions of aerodynamic loads, blade deformation, inflow and structural loads for baseline rotor at $C_T/\sigma = 0.09$.

revolutions. All the coupled CFD-CSD simulations are performed using the Spalart-Allmaras turbulence model.

Figure 4.10 shows C_T/σ vs C_Q/σ for both CFD and experiment. The values obtained using UMARC alone (without coupling with CFD) are also shown. The UMARC results shown in Figs. 4.10 and 4.11 are obtained using Maryland Freewake (MFW) model for the wake rather than the uniform inflow model used in CFD-CSD coupling. It is observed that there is very good agreement between experiment, coupled CFD-CSD and UMARC for all thrusts. Figure 4.11 shows the variation of
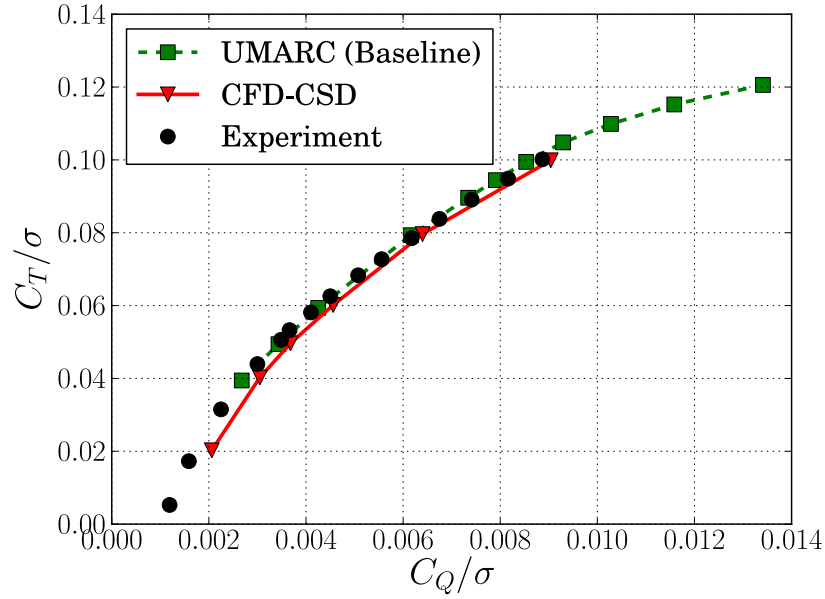
Figure 4.10: Comparison of C_T/σ vs C_Q/σ for baseline UH-60 rotor from CFD-CSD and experiment.

figure of merit (FM) with C_T/σ. The experiment shows that the figure of merit becomes nearly constant beyond a $C_T/\sigma \approx 0.08$. Again, both computational models show good agreement with experiment.

4.3   Full Scale Rotor Simulations

Having validated the code for model UH-60 rotor, simulations are performed for the full-scale rotor. The basic UH-60 blade configuration is retained and appropriate modifications are made so that the rotor corresponds to a typical full scale UH-60 rotor. Modifications included changes in the pitch link stiffness (the model UH-60 rotor had a very high pitch link stiffness), tip Reynolds number (7.4 million instead of 2.75 million for the model rotor), etc. For the swashplateless UH-60 rotor,
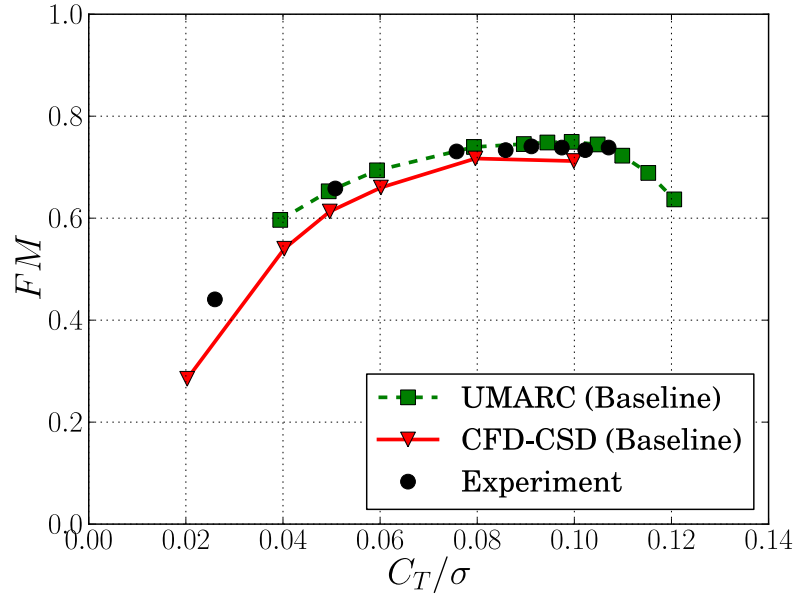
Figure 4.11: Comparison of FM vs C_T/σ for baseline UH-60 rotor from CFD-CSD and experiment.

simulations are performed for index angles of $15°$ and $20°$.

4.3.1 Comparison between Baseline and Swashplateless UH-60 Rotor

For the swashplateless TEF rotor, a thrust sweep similar to that for the baseline rotor simulations is carried out. However, rather than specify a target thrust and determine the TEF deflection corresponding to that thrust, a fixed TEF deflection is used and the blade structural response to the updated airloads is adjusted at the end of each cycle. This was done because steady state CFD-CSD coupling simulations were found to be easier to converge when the TEF deflection is kept constant and the thrust adjusted, rather than vice versa. Flap deflections of $-8°$, $-7°$, $-6°$, $-5°$, $-4°$ are used. Index angles of $15°$ and $20°$ are considered. Figures 4.12
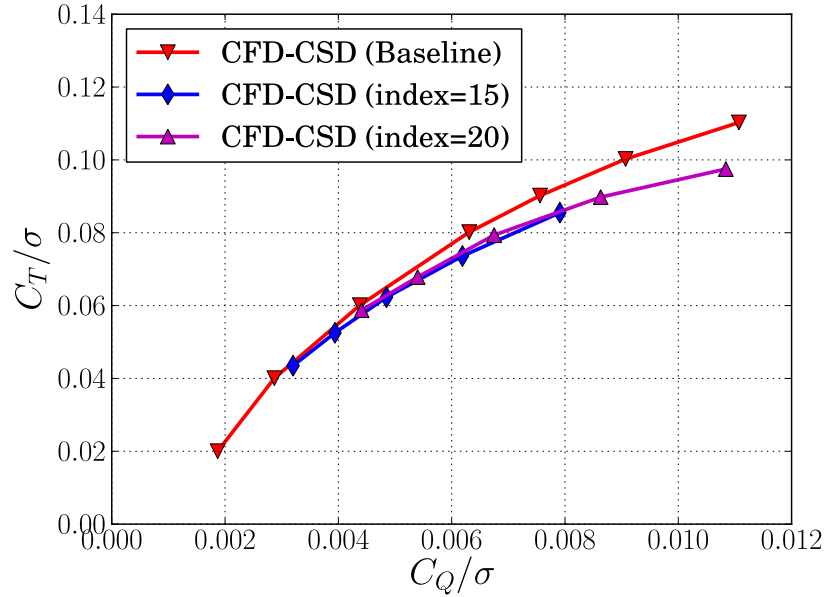
Figure 4.12: Comparison of C_T/σ vs C_Q/σ for baseline and swashplateless UH-60 rotor using coupled CFD-CSD simulations.

and 4.13 compare the performance of the two swashplateless configurations with the baseline UH-60 rotor. It is observed that the swashplateless TEF rotors have a higher power requirement for the same thrust as compared to the baseline rotor. From the figure of merit plot (Fig. 4.13) it is clearly seen that the baseline UH-60 rotor performs much better than the swashplateless configurations, especially at the higher thrusts.

However, although the swashplateless TEF rotor performs slightly worse than the baseline rotor for the cases considered here, it must be noted that only a limited number of rotor configurations and flight conditions are considered here. Also, it must be remembered that design of the UH-60 rotor was optimized as a conventional rotor and not as a swashplateless TEF rotor. Therefore, although the swashplateless
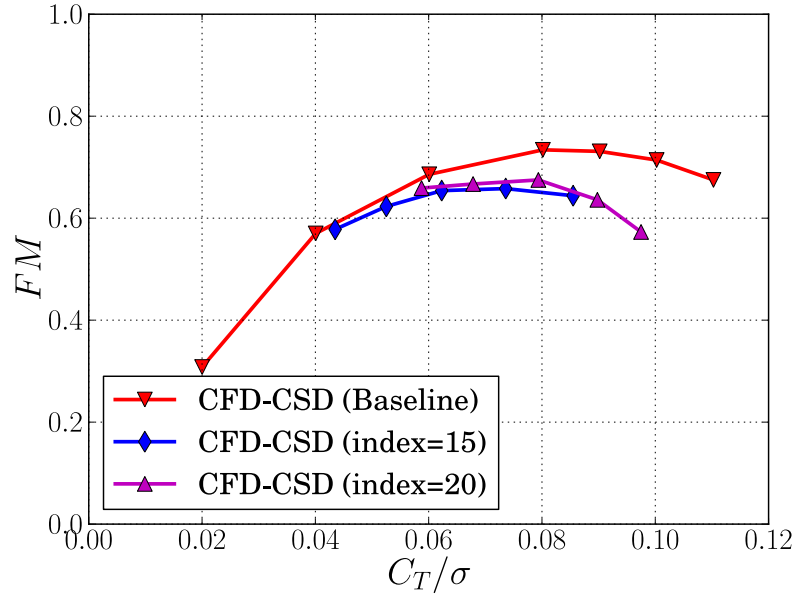
Figure 4.13: Comparison of FM vs C_T/σ for baseline and swashplateless UH-60 rotor using coupled CFD-CSD simulations.

UH-60 rotor performs worse than the conventional UH-60 rotor, designing the rotor specifically for a swashplateless configuration would provide better performance than a modified UH-60 rotor.

4.3.2   Structural and Aerodynamic Loads

Figure 4.14 shows spanwise distributions of several aerodynamic and structural parameters for the baseline UH-60 rotor for all the thrusts considered. In general, it was observed that the UH-60 rotor has a sharp increase in the magnitude of the normal force, pitching moment and chord force beyond $0.9R$. This may be partly attributed to the interaction of the blade with the first returning vortex. Figure 4.14(e) shows the inflow distribution for the various thrusts. The inflow

was obtained by averaging flow-velocity obtained from CFD at z-planes 0.1-chord above and below the rotor throughout the azimuth. It is seen that as the thrust increases, the inflow increases in the outboard region and the point of maximum inflow gradually moves inboard. However, near the tip there is upwash that increases with increasing thrust due to the increasing strength of the tip vortex and this causes the large increase in local loading around $0.95r/R$. The torsion moment is seen to increase monotonically in magnitude from the tip to the root. This explains why the baseline rotor has a significant variation in blade deformation from root to tip (see Fig. 4.14(d)).

Figures 4.15 and 4.16 similarly summarize all the spanwise distributions of airloads and structural behavior of the swashplateless TEF rotor for index angles of $15°$ and $20°$ respectively. The general trends are similar for both index angles. The inflow distribution for the swashplateless TEF rotor shows a small bump in the curve because of the inboard trailed vortex. Unlike the baseline rotor, as we move from tip to root, the torsion moment for the swashplateless TEF rotor first increases, reaches a maximum positive value and then decreases. This is because of the high positive nose up pitching moments generated by the upward deflection of the TEF which ultimately gives rise to a smaller range of spanwise variation for the torsion moment. This explains the relatively uniform blade deformation for the swashplateless TEF rotor (when the TEF is deflected upwards) as compared to the baseline rotor (see Figs. 4.15(d) and 4.16(d)).
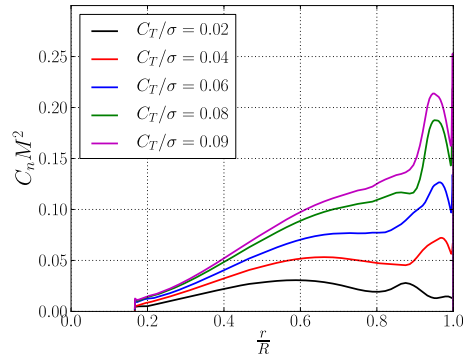
(a) Normal force
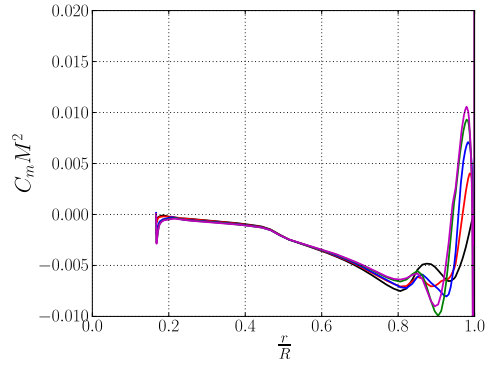
(b) Pitching moment
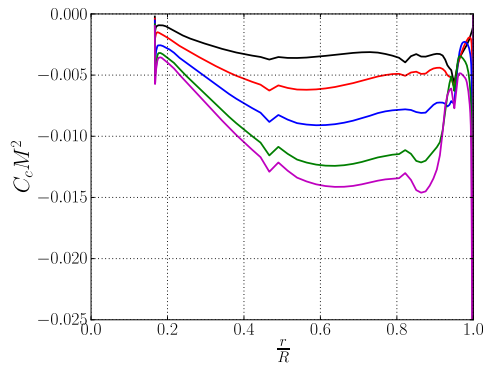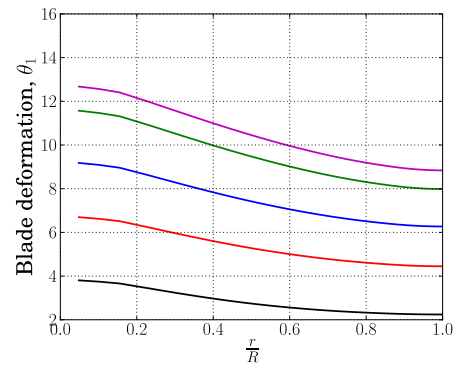
(c) Chord force

(d) Blade deformation
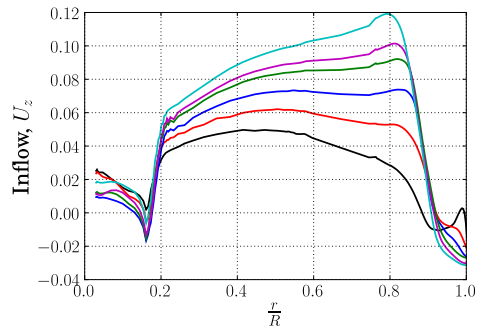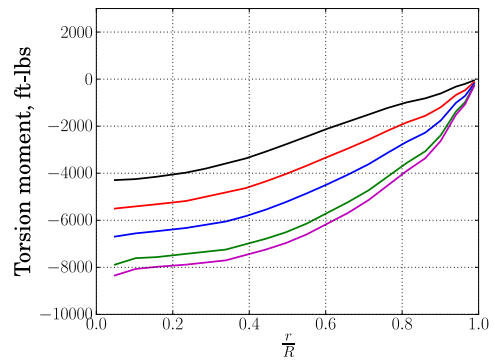
(e) Inflow

(f) Torsion moment

Figure 4.14: CFD-CSD coupled predictions of aerodynamic loads, blade deformation, inflow and structural loads for baseline rotor.
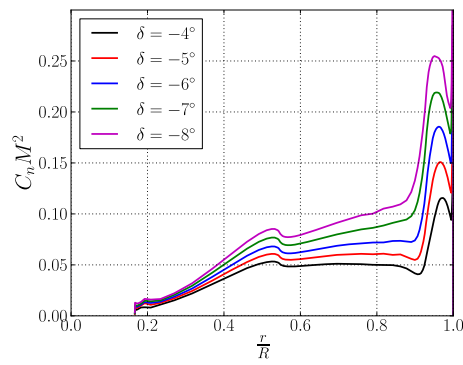
(a) Normal force
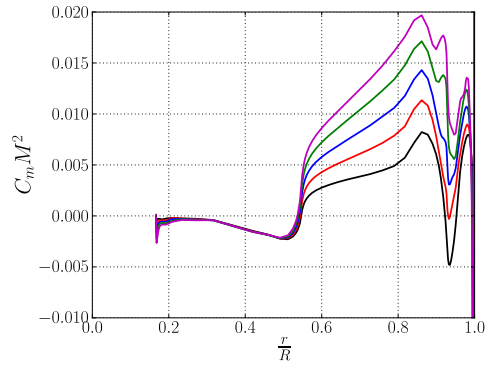
(b) Pitching moment
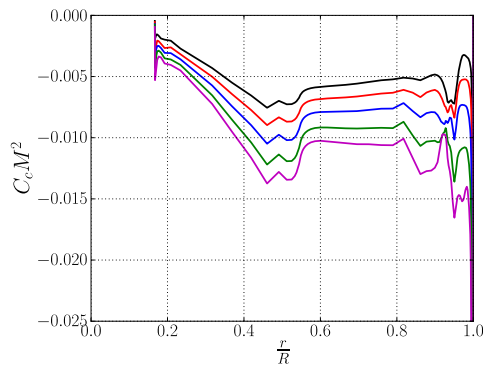
(c) Chord force
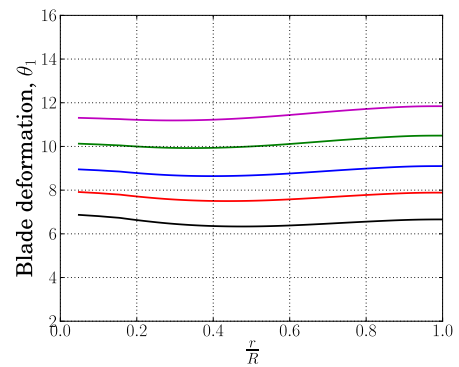
(d) Blade deformation
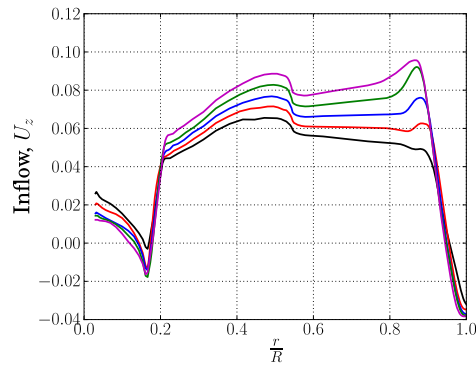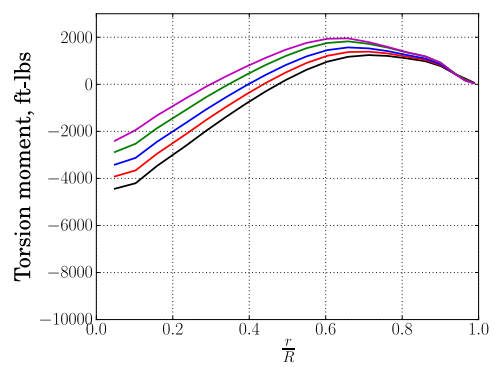
(e) Inflow

(f) Torsion moment

Figure 4.15: CFD-CSD coupled predictions of aerodynamic loads, blade deformation, inflow and structural loads for swashplateless TEF rotor with an index angle of 15°.
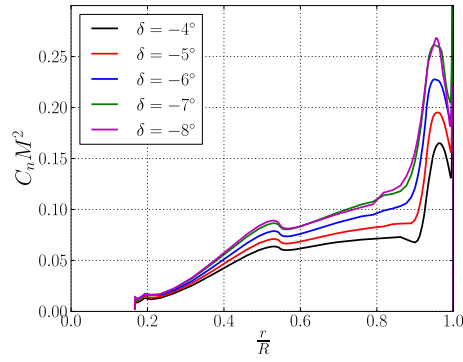
(a) Normal force
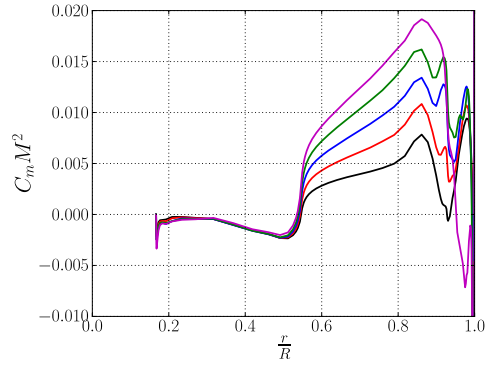
(b) Pitching moment
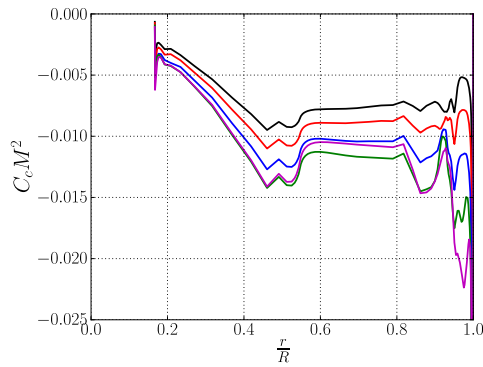
(c) Chord force
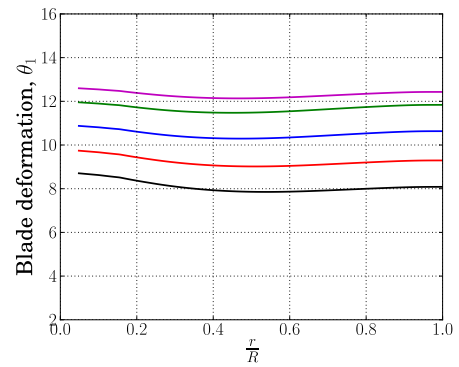
(d) Blade deformation
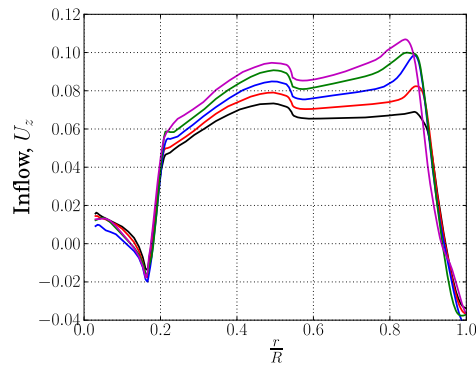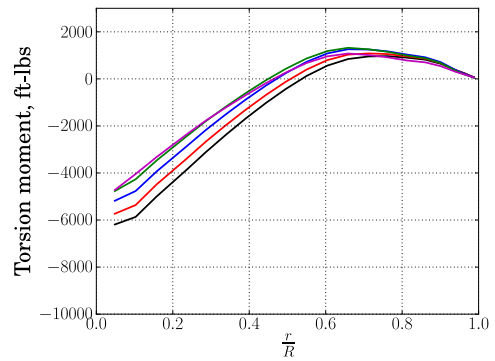
(e) Inflow

(f) Torsion moment

Figure 4.16: CFD-CSD coupled predictions of aerodynamic loads, blade deformation, inflow and structural loads for swashplateless TEF rotor with index angle of 20°.

Overall, the uncoupled and coupled CFD-CSD simulations on the baseline and swashplateless UH-60 rotors provide useful insights on the wake, performance and airloads behavior. However, since the UH-60 rotor, with its sweep and nonlinear twist distribution, is not a simple rotor, it would be useful to study the behavior of the baseline and swashplateless rotors for a simple untwisted, zero sweep rotor. This is considered in the following section.

4.4 Baseline and Swashplateless Simulations for the Simplified (NACA0012 Airfoil Based) Rotor

In order to isolate effects that are specific to the UH-60 rotor from general behavior encountered in rotors, a series of runs were performed for the baseline and swashplateless rotors using a NACA0012 airfoil based rotor with zero twist and no sweep. For ease of description, this rotor will be referred to as the *simplified rotor*. The following changes were incorporated into the rotor as compared to the UH-60 rotor :

1. The NACA0012 airfoil was used throughout the blade span.

2. The twist was set to zero and the sweep was eliminated.

3. The mass and structural properties were made uniform.

4. The offset between the C.G. and elastic axis was set to 0.02 chord.

In order to support the aerodynamic calculations in the CSD code (UMARC), lookup tables were generated, using CFD, for the NACA0012 airfoil by performing

a large number of runs for different AoA (0° to 20° in steps of 2.5°), flap deflections (−10° to 10° in steps of 2.5°) and Mach numbers (M = 0.3, 0.4, 0.5, 0.6, 0.65, 0.7, 0.75, 0.8). The data so obtained was also useful for understanding the aerodynamics of TEF airfoils (as discussed in Chapter 3). It is to be noted that since the NACA0012 airfoil is symmetric, airloads data needs to be obtained only for positive angles of attack. The airloads for negative AoA can be obtained from the data for positive AoA by using the formulas :

$$C_l(-\alpha, \delta) = -C_l(\alpha, -\delta) \qquad (4.1)$$

$$C_d(-\alpha, \delta) = C_d(\alpha, -\delta) \qquad (4.2)$$

$$C_m(-\alpha, \delta) = -C_m(\alpha, -\delta) \qquad (4.3)$$

$$C_h(-\alpha, \delta) = -C_h(\alpha, -\delta) \qquad (4.4)$$

Using the CFD-CSD code, a thrust sweep was performed for the baseline and swashplateless simplified rotor. The baseline rotor was run for C_T/σ = 0.02, 0.04, 0.06 and 0.08 while the corresponding swashplateless TEF rotor was run with an index angle of 15° at TEF deflections of −2.5°, −2°, −1°, 0°, +1° and +2° to produce a comparable thrust range. All the simulations were performed using the Spalart-Allmaras turbulence model.

Figure 4.17 shows the C_T/σ vs C_Q/σ plot for the simplified baseline and swashplateless rotors. Notice that for a similar thrust range, the simplified rotor requires a different range of TEF deflections from those of the UH-60 rotor at the same index angle. It is seen that for the simplified rotor, the baseline and swashplateless configurations have similar performance behavior. This observation is reinforced in

the figure of merit plot (see Fig. 4.18). It was seen that for $C_T/\sigma > 0.08$, the CFD-CSD coupling process for the baseline and swashplateless simulations took longer to converge (or encountered difficulties in convergence). This is possibly because of the untwisted nature of the blade which leads to much of the lift being carried by the outboard region, resulting in earlier occurrence of stall.
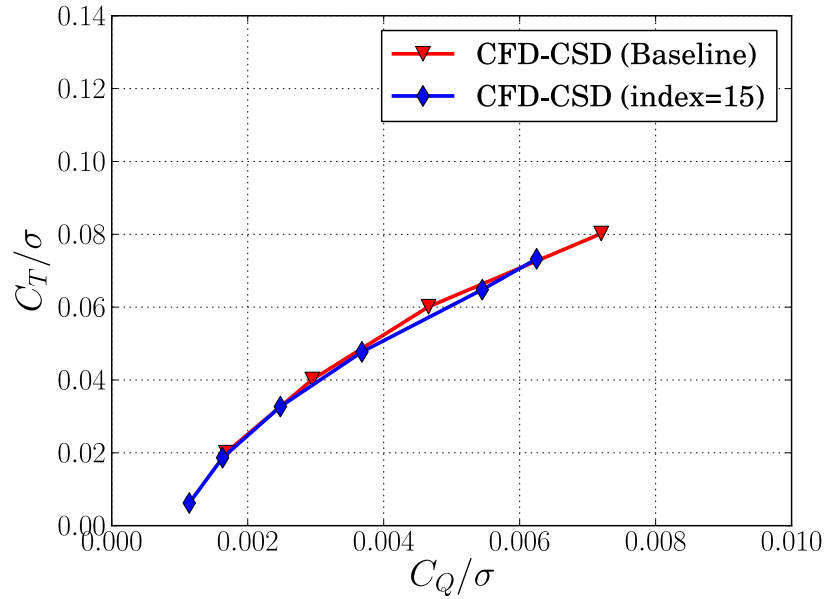
Figure 4.17: Comparison of C_T/σ vs C_Q/σ for baseline and swashplateless rotor with NACA0012 airfoil.

Figure 4.19 shows the spanwise structural and aerodynamic loads for the simplified baseline rotor. It is seen that for the simplified rotor, much of the lift is generated in the outboard region of the blade. This is because the blade has zero twist and is not designed for optimum performance. A comparison with the UH-60 rotor on the other hand (see Fig. 4.14) shows that the UH-60 rotor has a more uniform lift distribution because of its optimized design. This means that the stall limit
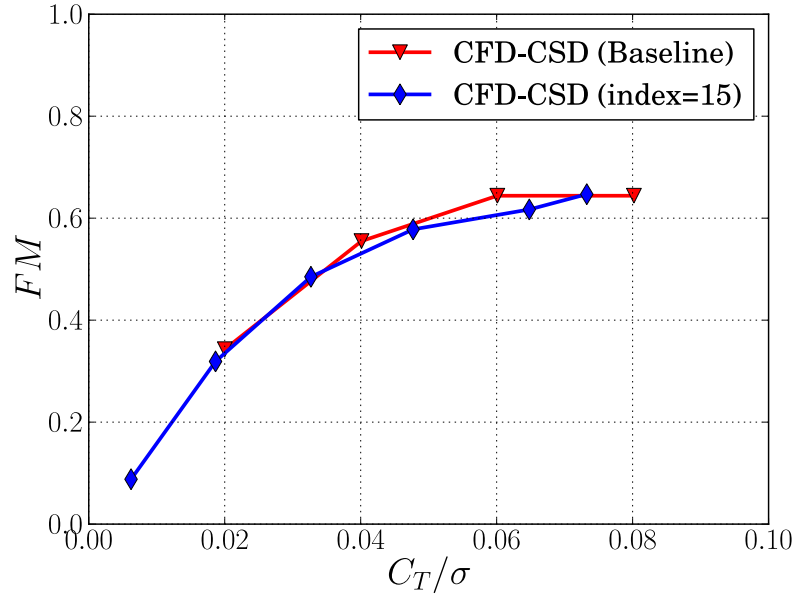
Figure 4.18: Comparison of FM vs C_T/σ for baseline and swashplateless rotor with NACA0012 airfoil.

is reached much later for the UH-60 rotor as compared to the simplified rotor. The simplified rotor has an almost zero pitching moment over most of its span except near the tip, where the presence of the tip vortex and the first returning tip vortex leads to an increase in the pitching moment (see Fig. 4.19(b)). The relatively low pitching moments give rise to a smaller range in the torsion moment (see Fig. 4.19(f)) for the simplified baseline rotor, thereby resulting in smaller blade deformation from root to tip as compared to the baseline UH-60 rotor (see Fig. 4.19(d)). Because there is no twist, the inflow for the simplified rotor is seen to be less uniform than that of the UH-60 rotor.

Figure 4.20 shows the spanwise structural and aerodynamic loads for the simplified swashplateless TEF rotor. Because of the small TEF deflection, the lift and
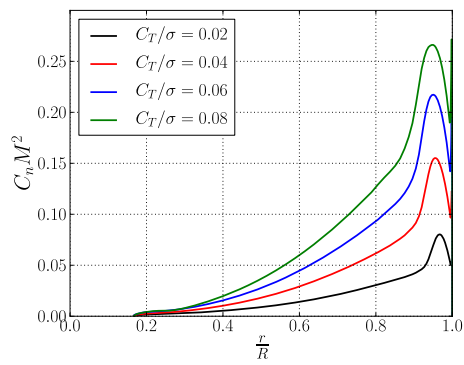
(a) Normal force
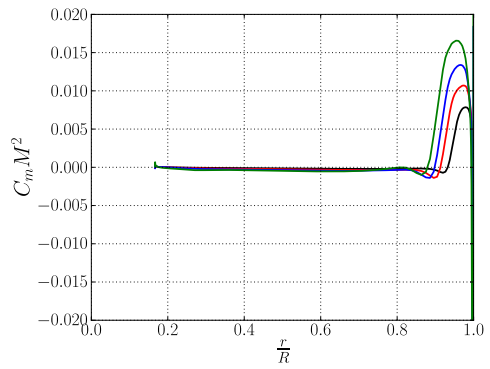
(b) Pitching moment
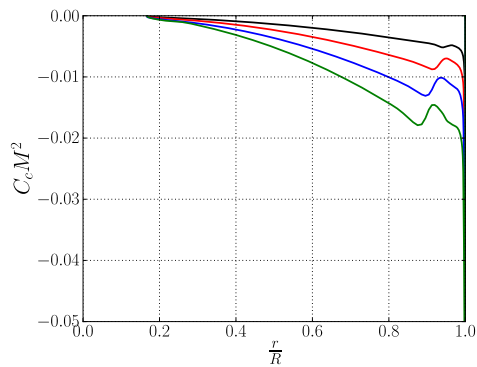
(c) Chord force
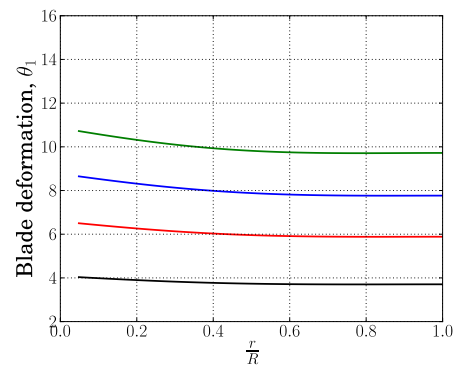
(d) Blade deformation
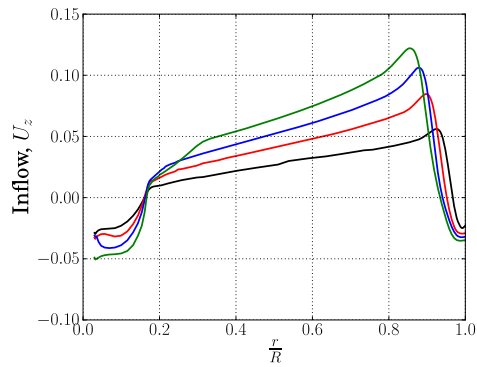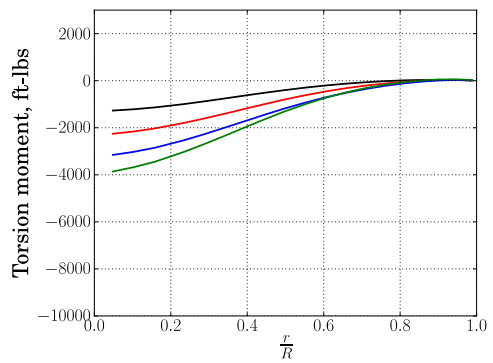
(e) Inflow

(f) Torsion moment

Figure 4.19: CFD-CSD coupled predictions of aerodynamic loads, blade deformation, inflow and structural loads for baseline rotor with NACA0012 airfoil.

drag distribution for the simplified swashplateless TEF rotor is similar to that of the corresponding baseline rotor. The pitching moment on the other hand is clearly affected by TEF deflection. Note that the downward TEF deflection of 2° gives rise to a negative pitching moment (see Fig. 4.20(b)). Therefore, for this case alone, there is a larger variation in the torsion moments (see Fig. 4.20(f)). This in turn results in more blade deformation from root to tip for the case with positive flap deflection (see Fig. 4.20(d)).

Figure 4.21 shows the q-criterion plots for the simplified baseline rotor. All the plots were generated for the same iso-surface specifications so that vortex strengths are not magnified or diminished between the plots. From these plots it is seen that the first returning vortex convects very close to the rotor for the simplified rotor as well. The close proximity of the first returning vortex produces an upwash on the blade that is seen to affect the airloads, particularly the drag, which experiences a small decrease in magnitude in the region of interaction. The pitching moment, which is largely zero over most of the blade, also experiences a sharp increase in magnitude in the tip region.
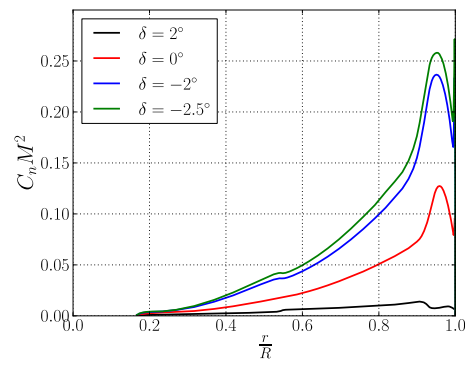
(a) Normal force
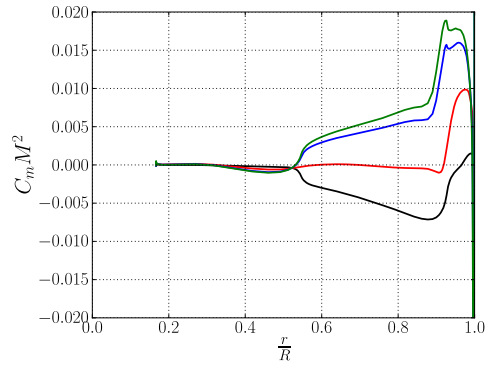
(b) Pitching moment
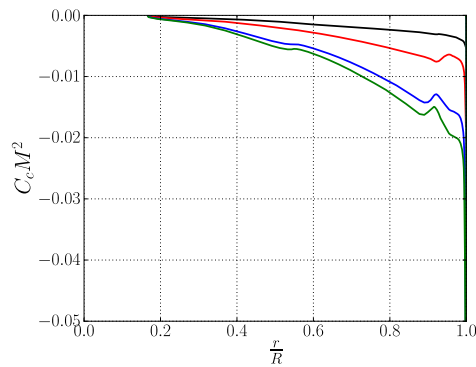
(c) Chord force
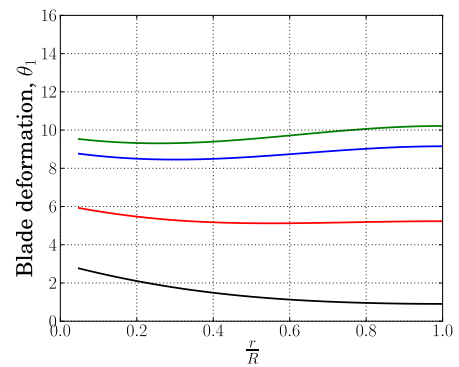
(d) Blade deformation
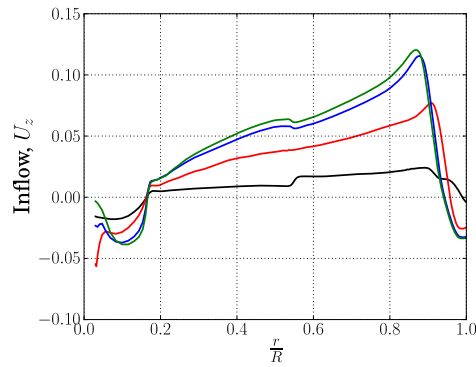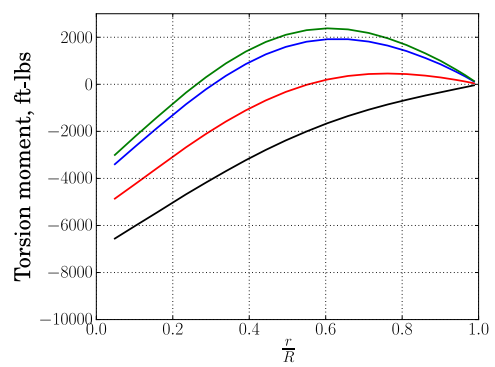
(e) Inflow

(f) Torsion moment

Figure 4.20: CFD-CSD coupled predictions of aerodynamic loads, blade deformation, inflow and structural loads for swashplateless TEF rotor with an index angle of 15°.
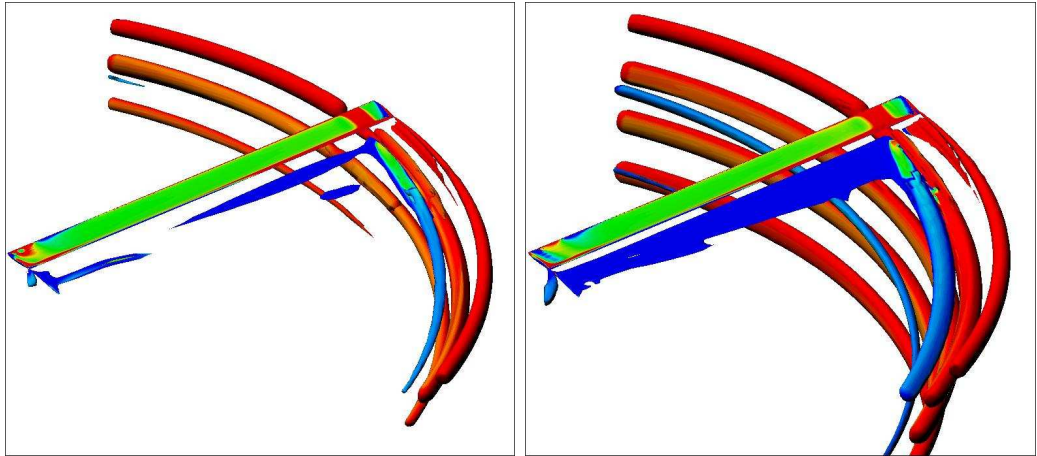
(a) $C_T/\sigma = 0.02$

(b) $C_T/\sigma = 0.04$
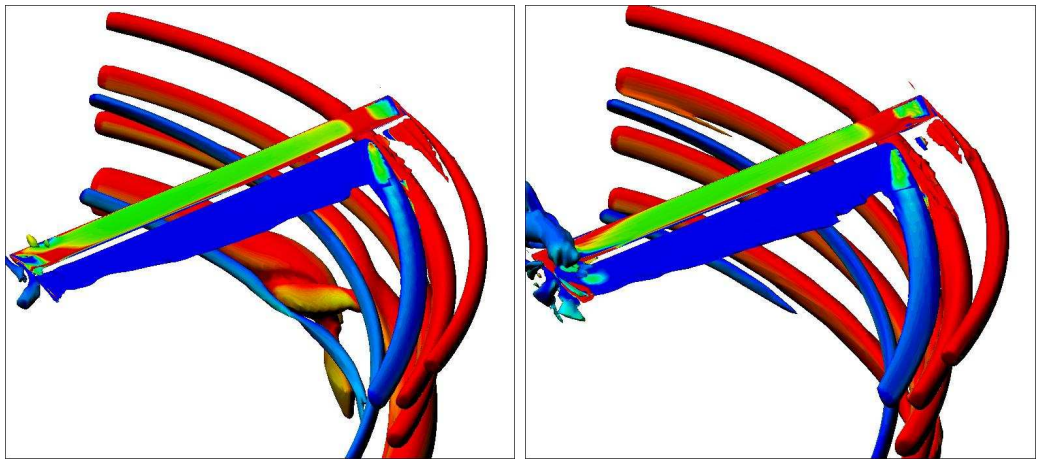
(c) $C_T/\sigma = 0.06$

(d) $C_T/\sigma = 0.08$

Figure 4.21: q-criterion plots for the simplified baseline rotor at different thrusts.

(a) $\delta = -2°$

(b) $\delta = 0°$

(c) $\delta = 2°$

(d) $\delta = 2.5°$
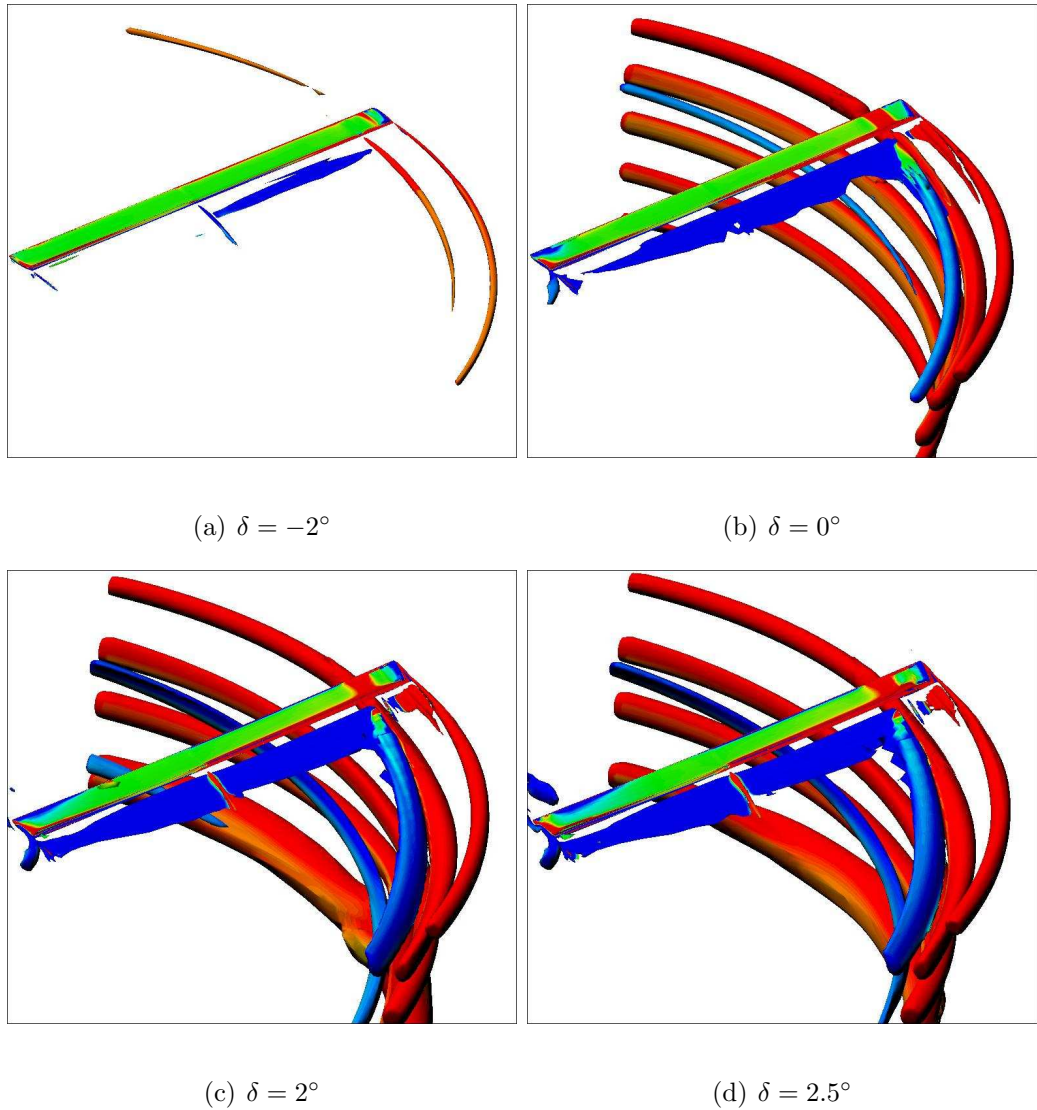
Figure 4.22: q-criterion plots for the simplified swashplateless TEF rotor at different thrusts.

The interaction of the first returning tip vortex with the shear layer behind the blade also leads to the formation of the opposite sense vortex for all the thrusts considered. This confirms that the formation of the opposite sense vortex for the UH-60 rotor is not induced by sweep or twist. Figure 4.22 shows the q-criterion plots for the simplified swashplateless TEF rotor. Because of the small TEF deflections,

the wake structure is similar to the baseline rotor and the shear layer is largely undisturbed, except in the tip region due to the formation of the OSV. For the same reason, the inboard trailed vortex is seen to be weak.

4.5   Effect of Gap

Although, the integrated TEF concept aims at having no gap, the mechanical implementation of the flap mechanism is likely to involve some gaps or leakages at chordwise and spanwise edges of the TEF. The gaps in these cases would be expected to be small. The purpose of using CFD to model these gaps is to determine the extent to which these flow leakages affect the aerodynamics of TEF airfoils for the relatively large flap deflections encountered in swashplateless TEF rotors.

In the present work, the effect of the gaps was modeled using the gap averaging approach described earlier (see Chapters 2 and 3). Although the approach is approximate, it gives a first order estimate of the effect of the gap. Also, since there are no analytical or semi-empirical approaches for modeling the gap, the effect of the gap cannot be modeled using UMARC and requires CFD for capturing the effects. To understand the effect of the gap, results are obtained for two gap configurations:

1. 0.01c chordwise gap and 0.01R side gaps.

2. Only 0.01c chordwise gap.

Simulations are performed for swashplateless UH-60 rotor for TEF deflections of $-8°$, $-6°$ and $-4°$. Figures 4.23 and 4.24 show the performance of the no gap
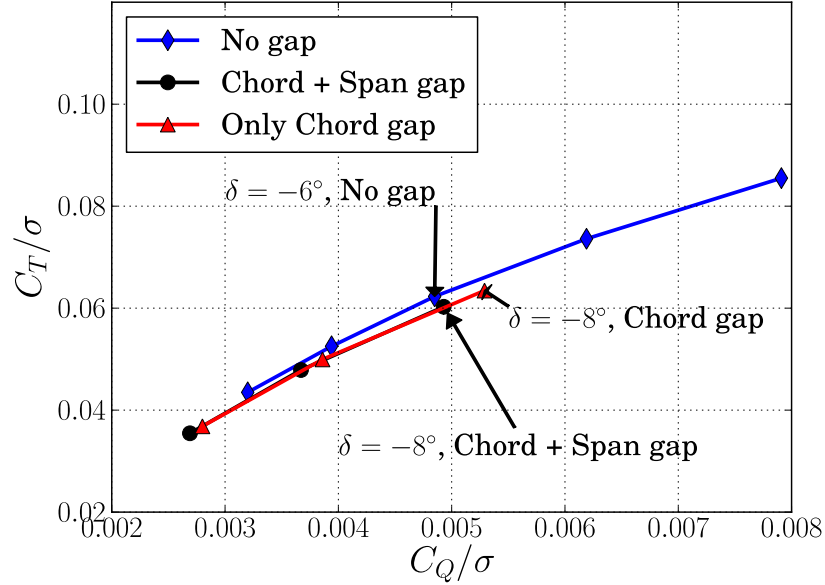
Figure 4.23: Comparison of C_T/σ vs C_Q/σ for swashplateless UH-60 rotor at an index angle of 15° with and without gaps using coupled CFD-CSD simulations.

configuration (for an index angle of 15°) with the gap configurations. The following observations can be made :

- The presence of chordwise gap leads to a loss of flap effectiveness. To produce the same thrust, a TEF rotor with a chordwise gap requires a higher flap deflection than a TEF rotor with no gap. For example, to produce a thrust of $C_T/\sigma \approx 0.061$, the TEF rotor with no gap requires a flap deflection of only $-6°$ whereas a TEF rotor with chordwise gap requires a flap deflection of $-8°$.

- For the same thrust, the power required for a TEF rotor with gaps is comparable with that of a TEF rotor with no gaps. This is indicated by the fact that the C_T/σ vs C_Q/σ curves with and without gaps are similar.
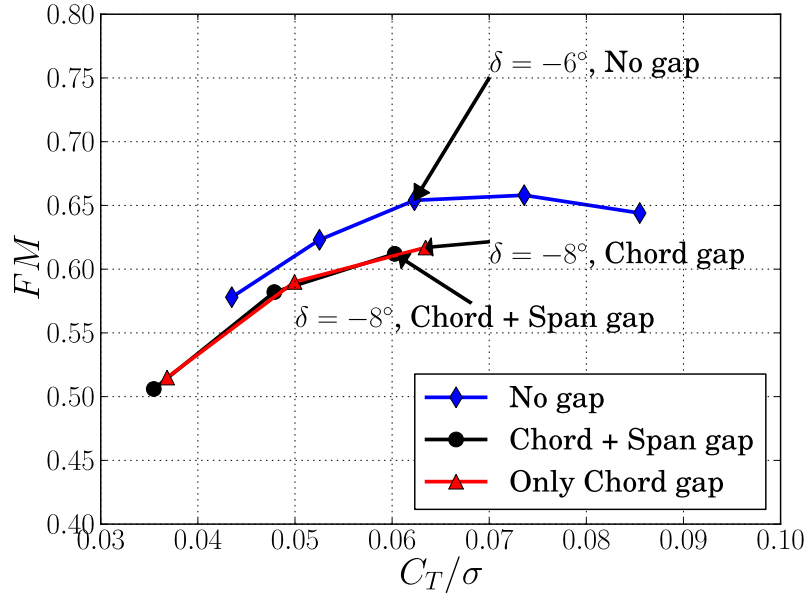
Figure 4.24: Comparison of FM vs C_T/σ for swashplateless UH-60 rotor at an index angle of 15° with and without gaps using coupled CFD-CSD simulations.

- The presence of chordwise gaps leads to a significant loss of rotor efficiency ($\approx 4\%$ drop in FM for $\delta = -8°$), as indicated by the reduction in figure of merit (see Fig. 4.24). The loss of efficiency because of gaps decreases as the magnitude of flap deflection decreases.

- The presence of spanwise gaps leads to a small loss of the flap effectiveness, as indicated by the slightly higher flap deflection required to produce the same thrust, with the addition of spanwise gaps.

- There is almost no loss of flap efficiency because of spanwise gaps, as indicated by the fact that the C_T/σ vs C_Q/σ as well as FM vs C_T/σ curves do not change after the addition of the spanwise gaps.

In order to understand the behavior described, the sectional loads need to be studied. Figure 4.25 shows the spanwise variation of airloads and structural properties for different gap configurations for $\delta = -8°$. It is observed that there is a drop in the sectional lift distribution when the chord gap is present. Normally, the lift would be expected to increase when the gap is present because the presence of the chordwise gap decreases the flap effectiveness. Since deflecting the flap upwards decreases the lift, the loss of flap effectiveness due to the gap would be expected to increase the overall lift. This would indeed be the case if there was no coupling between the aerodynamic and the structural components of the system.

However, in a swashplateless TEF rotor, there is strong coupling between the aerodynamic and structural loads. The drop is thrust due to the gap arises because of this coupling and is described in Fig. 4.26.

1. When the chordwise gap is introduced at a negative flap deflection, there is an increase in upward lift and a decrease in nose up pitching moment in the blade sections spanned by the TEF (see Chapter 3 for effect of gap on lift and pitching moment). This is because deflecting a TEF upward corresponds to a decrease in lift and an increase in nose-up pitching moment. Consequently, a loss of flap effectiveness due to the gap would result in an increase in lift and a decrease in nose-up pitching moment (see first step in Fig. 4.26).

2. Change in lift does not change the blade response significantly but the decrease in pitching moment leads to reduced torsion moments along the blade span. The reduced torsion moment has a significant effect on the blade response

210

because this is a moment flap based swashplateless TEF rotor and therefore, the torsional stiffness is very low. Because of the decrease in nose-up pitching moment, the blade undergoes a decrease in collective (see intermediate step in Fig. 4.26).

3. The decrease in blade collective then gives rise to a decrease in the overall blade lift (see final step in Fig. 4.26).

The presence of spanwise gaps also results in a loss of thrust because of the drop in pitching moment and the resultant decrease in the blade pitch. As seen in Fig. 4.25(b) it is the gap at the outboard edge of the TEF that contributes primarily to the loss in thrust. Since the pitching moments are higher near the outboard edge of the TEF, the loss in flap effectiveness in that region has a greater effect. Interaction with the first returning tip vortex could exacerbate the situation.

Thus, the coupling of the structural and aerodynamic loads plays an important role in the behavior of the swashplateless TEF rotor. This also highlights the need for a CFD-CSD coupling strategy to properly capture the behavior, since an uncoupled CFD simulation (i.e., where the structural loads are provided only at the start of the simulation) would be unable to capture the blade response in the presence of the gap. From a design perspective this means that the presence of chordwise gaps can have a significant effect on the performance of swashplateless TEF rotors and therefore special care should be taken to eliminate flow leakages along the chordwise edges of the TEF.
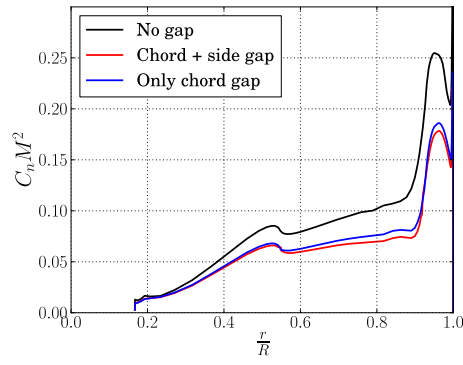
(a) Normal force
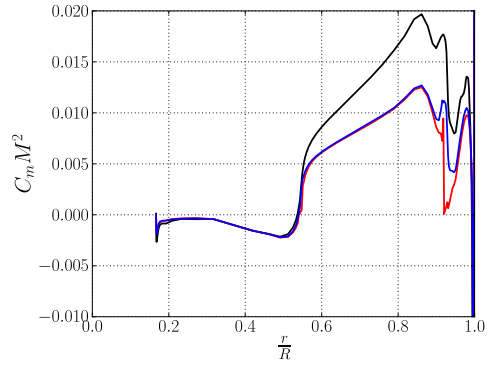
(b) Pitching moment
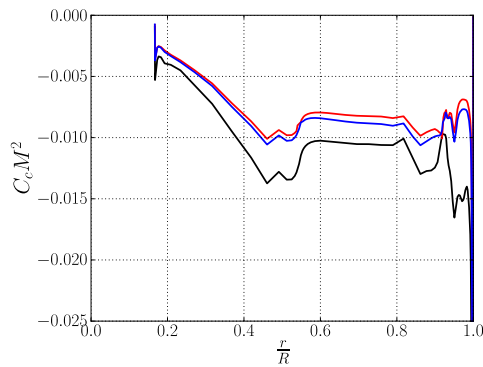
(c) Chord force
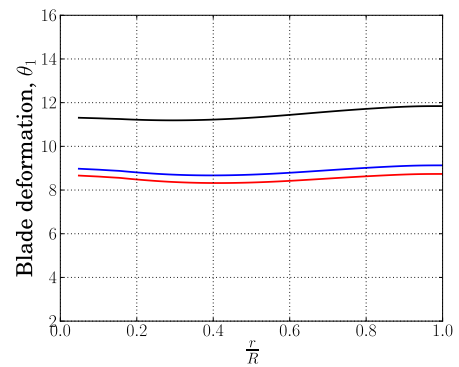
(d) Blade deformation
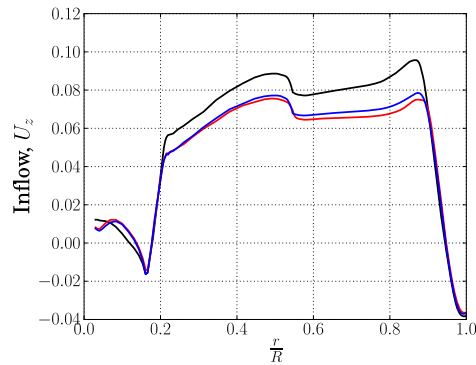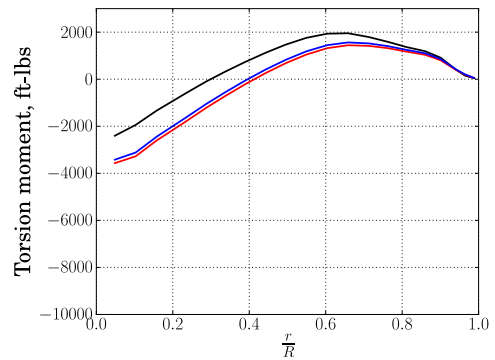
(e) Inflow

(f) Torsion moment

Figure 4.25: CFD-CSD coupled predictions of aerodynamic loads, blade deformation, inflow and structural loads for swashplateless TEF rotor at $\delta = -8°$, index angle of 15°, 1% spanwise gap and 1% chordwise gap.
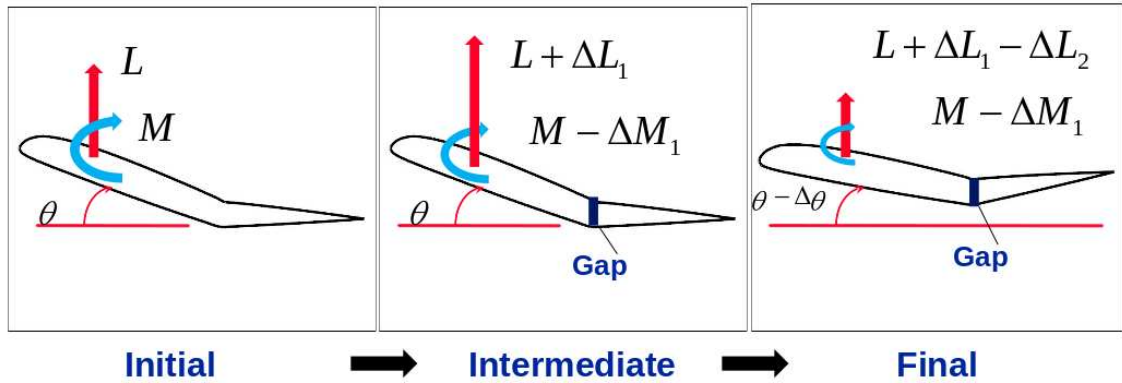
Figure 4.26: Swashplateless TEF rotor response to presence of gap.

One important point to note is that all these conclusions have been made using the gap averaging approach, which is only approximate. Also, the mesh refinement in the region of the gaps is not very high for the simulations shown here. Therefore, some inaccuracies are bound to be present. However, the actual trends may be expected to be similar to those observed here.

4.6   Summary

This chapter looked at various aspects of the aerodynamics of swashplateless TEF rotors in hover using CFD. Simulations were performed for the UH-60 rotor and a simplified rotor based on the NACA0012 airfoil. The uncoupled CFD simulations were used to study the wake structure in hover. The formation of an opposite sense vortex was observed for the baseline and swashplateless simulations for all the rotor configurations considered (baseline/swashplateless, UH-60/simplified). The interaction of the first returning tip vortex with the shear layer of the blade was seen to be the reason behind the formation of the OSV. Full fledged CFD-CSD

coupling cycles were used to study the performance and airloads for the baseline and swashplateless rotors. One important observation was that the swashplateless TEF rotor performs worse than the baseline rotor for the UH-60 rotor cases considered. For the simplified (untwisted NACA0012 airfoil based) rotor, the performance is similar for both the baseline and swashplateless rotor configurations. Lastly, the effect of gaps on the performance of swashplateless TEF rotors was studied. The simulations showed that the presence of gaps does have a significant effect on the behavior of swashplateless TEF rotors and therefore special care must be taken to minimize any flow leakages at the edges of the TEF. This is primarily because of loss of flap effectiveness due to the presence of the chordwise gap, leading to a reduction in pitching moment, which in turn results in decreased blade pitch and rotor thrust. However, while there is a significant reduction in thrust for a given flap deflection, the thrust to power ratio is not too different when the gap is present. A significant drop in figure of merit ($\approx 4\%$ for $\delta = -8°$) is also observed when gaps are present.

Chapter 6

Conclusions and Future Work

Integrated TEF based swashplateless rotors offer the possibility of improved performance and cost benefits for next generation helicopters. However, they have not previously been studied thoroughly. Understanding the aerodynamics and performance of swashplateless TEF rotors is very important in establishing confidence in their use for a wide range of applications. The present work investigated the swashplateless TEF rotor, focusing primarily on its aerodynamics. CFD studies were performed both for 2D TEF airfoils as well as for 3D swashplateless TEF rotors. Various aspects of the aerodynamics of TEF airfoils/rotors were studied in detail. The following sections summarize the present work and list its important conclusions.

6.1   Overall Summary

The present study can been split into parts – 2D TEF airfoil aerodynamics and 3D swashplateless TEF rotor aerodynamics. The 2D analysis investigated various aspects of the aerodynamics of TEF airfoils. Steady and unsteady tools were developed and applied for studying the aerodynamics of TEFs. Firstly, analytical tools for predicting steady and unsteady airloads for TEF airfoils were described. Because there is no purely analytical model to predict drag, an approach for esti-

mating the drag for TEF airfoils was proposed that requires only AoA data (from CFD or experiment) for the given airfoil.

Next, the effect of various airfoil properties on the airloads of a TEF airfoil was discussed. The codes used to perform the simulations were validated against experimental data and good agreement was observed between CFD and experiment. The effect of gaps at the leading edge of the flap is investigated in great detail. Various approaches to model the effect of gaps are considered. Modeling the gap using direct CFD meshes is done using patched and overlapping meshes using the implicit hole cutting (IHC) scheme. The patched mesh approach had problems with convergence, grid quality and robustness. The implicit hole cutting approach, while harder to implement, resolved many of the problems associated with patched meshes. An approximate "gap averaging" technique was also developed which was found to provide reasonable airloads predictions at no additional computational cost.

Next, the TEF airfoil was studied for a wide range of flow conditions by varying flow parameters such as AoA, Mach number and flap deflections for the NACA0012 airfoil and SC1095R8 airfoils. Trends in airloads (C_l, C_m, C_d and C_h) were studied. The use of the effective angle of attack (α_{eff}) concept was seen to provide benefits in representing and modeling lift and drag. Nonlinear flow phenomena such as flow separation, shocks and vortex shedding were studied. Stall boundaries were identified for the airfoils for different Mach numbers. The stall boundary information can prove useful both in design analysis as well as for modeling the airloads. The 2D analysis provided valuable insights and data that can be applied for better design and analysis of 3D TEF rotors.

216

For the 3D rotor analysis, the OVERTURNS code was coupled with UMARC to provide coupled CFD-CSD analysis of conventional (baseline) and swashplateless rotors in hover. The lookup tables required for the comprehensive analysis code were obtained from 2D CFD simulations. The CFD-CSD code was extended for swashplateless TEF rotors and validated via comparison to experimental data available for the baseline model scale UH-60 rotor. Fine mesh simulations were first performed to study the wake structure for the baseline and swashplateless rotors. Performance and airload analyses were performed on the full scale UH-60 and simplified (rectangular NACA0012 airfoil) rotors for a range of thrusts. Analysis was also performed to study the effect of gaps at the leading edge of the TEFs. Because 3D CFD simulations of the swashplateless TEF rotor have not been performed before, the present study provides new insights into the behavior of swashplateless TEF rotors.

6.2   Key Observations and Conclusions

Specific conclusions drawn from the analysis and simulations performed by applying the tools developed in the present work are summarized below.

6.2.1   2D Aerodynamics

Studying the 2D aerodynamics of TEF airfoils is essential for understanding the behavior of TEFs and how they can be effectively employed on helicopter rotors for realizing the swashplateless rotor concept. This includes analytical modeling

as well as steady/unsteady CFD simulations aimed at understanding the effect of airfoil properties (airfoil thickness, overhang and gap), airloads and aerodynamic phenomena associated with TEF airfoils. The following sections outline the important conclusions in each of these areas.

6.2.1.1 Analytical Modeling of Steady and Unsteady Airloads

Analytical and semi-empirical tools are useful for making computationally inexpensive predictions of steady/unsteady airloads as well as for understanding the general behavior of TEF airfoils. Some of the conclusions drawn from a study of the analytical models discussed in the present work are listed below:

1. For unsteady flows with pure flap deflections, analytical lift and pitching moment predictions show excellent agreement with CFD even for flap amplitudes as high as 20° (at zero AoA). Flap hinge moment predictions are also seen to be good.

2. The drag can be modeled for a TEF airfoil (without overhang) by treating the flap deflection in terms of an effective angle of attack. This makes it possible to estimate the drag for a flapped airfoil based on a knowledge of drag data already available for the baseline airfoil without flap (from CFD or experiment) as a function of angle of attack alone. This approach seems to provide reasonable drag estimates for subcritical and unstalled flows.

6.2.1.2 Airfoil Properties

Understanding how different airfoil properties (airfoil thickness, overhang and gap) affect the airloads of TEF airfoils is essential for making good design choices when designing TEF rotors. Some of the important insights obtained from studying the effect of various airfoil properties on the aerodynamics of TEF airfoils are listed below:

1. In unstalled conditions, flap overhang has a relatively small effect on lift and pitching moment. Hinge moment varies linearly with thickness and can be predictably controlled by varying overhang. Flap actuation power can thus be reduced by appropriately adjusting flap overhang.

2. In low lift conditions when there are no nonlinear phenomena, airfoil thickness has only a small effect on lift. Drag increases linearly with airfoil thickness. Pitching moment decreases gradually and linearly in magnitude with increasing airfoil thickness. The effect of airfoil thickness on hinge moment is more pronounced and results in a decrease in the magnitude of the hinge moment (C_h). For small to moderately sized flaps, C_h is seen to decrease linearly in magnitude with airfoil thickness.

3. Results of gap modeling based on gap averaging seems to suggest that for the range of AoA and flap deflections encountered by helicopter rotors, the effect of flow through the gap may not be negligible, especially if the TEF is used as a primary control surface. The overall effect of the gap flow on the flap is to reduce its effectiveness as a moment flap.

219

4. The gap averaging technique provides a good approximation of the airloads and flow field at almost no additional computational cost over a no gap simulation. It was found to be most effective for small gap sizes ($< 2\%$ chord) and zero overhang.

6.2.1.3 Airloads and Flow Phenomena

Extensive 2D simulations were performed on the NACA0012 and SC1095R8 airfoils and the trends in the airloads (lift, drag, pitching moment and hinge moment) and associated aerodynamic phenomena were studied. Some of the important conclusions are given below:

1. For the flap size and Reynolds number considered, the NACA0012 and SC1095R8 airfoils exhibited trailing edge stall. The stall limits for the two airfoils were seen to be largely affected by angle of attack rather than flap deflection.

2. The drag exhibits a parabolic dependence on the effective angle of attack (α_{eff}). Beyond stall, drag varies linearly with α_{eff} with the same slope for all flap deflections.

3. The pitching moment varies linearly with flap deflection for subsonic and even at transonic Mach numbers. However, at higher angles of attack, significant discrepancies were observed between the pitching moment versus flap deflection curves obtained using CFD and theory.

4. The hinge moment varies linearly with flap deflection. Significant differences in

offset and slope were observed between the hinge moment versus flap deflection curves obtained using CFD and theory.

5. The significant differences between CFD and theory in the pitching moment and hinge moment predictions indicate that it is important to use CFD-CSD coupling or atleast a lookup table based aerodynamic models in comprehensive analysis codes for swashplateless TEF rotors.

6.2.2   3D CFD Simulations

The present study involved uncoupled and coupled CFD-CSD simulations that investigated the performance, airloads and wake for baseline (conventional) and swashplateless rotors. The important conclusions derived from the 3D simulations are listed below:

1. The performance of the swashplateless UH-60 rotor is worse than that of the baseline UH-60 rotor, particularly at higher thrusts ($C_T/\sigma > 0.06$). However, for the simplified NACA0012 airfoil based rotor, the baseline and swashplateless rotors have nearly the same performance behavior.

2. The sharp rise and fall in loading near the blade tip and the interaction of the shear layer with the returning tip vortex often leads to the formation of an opposite sense vortex (OSV) that has a sense of rotation opposite to that of the tip vortex. A vortex is trailed at the inboard TEF boundary because of the discontinuities in lift/geometry at the spanwise edge of the TEF.

3. The presence of chordwise gaps degrades the effectiveness of the TEF to produce the forces and moments required to control the rotor. The loss of flap effectiveness occurs because the chordwise gap significantly reduces the pitching moment produced by the flap. In a moment flap based swashplateless TEF rotor, the decrease in pitching moment leads to a decrease in blade pitch and overall lift.

4. Although the presence of gaps significantly reduces the thrust produced by the rotor for a given flap deflection, the thrust to power ratio may not be too different when the gap is present.

5. A significant drop in figure of merit ($\approx 4\%$ for $\delta = -8°$) is also observed when gaps are present. Loss of rotor efficiency (quantified by the reduction in figure of merit) because of gaps decreases as the magnitude of flap deflection decreases.

6. The effect of spanwise gaps is smaller than the effect of the chordwise gaps but is not negligible.

6.3   Future Work

The following possibilities can be considered for future work :

1. The present work considers only briefly the unsteady aerodynamics of TEF airfoils and relies primarily on thin airfoil analysis. Various aspects of the unsteady aerodynamics of TEF airfoils require further investigation:

a) Unsteady airloads of TEF airfoils with time-varying free-stream Mach numbers.

b) Modeling unsteady behavior in nonlinear flow regimes.

c) Modeling dynamic stall for TEF airfoils. This is particularly useful because TEFs can be used to alleviate stall.

2. The present work only considers straight gaps with sharp edges. Because the effect of gaps is significant, investigating other gap configurations could lead to improvements in the performance of swashplateless TEF rotors.

3. Modeling the gaps using actual CFD grids can be done for 3D rotors to validate the results obtained using the gap averaging technique and determine its accuracy and range of validity.

4. The swashplateless hover runs can be extended for forward flight conditions. This would be necessary to determine the feasibility and range of applicability of the swashplateless TEF rotor concept.

5. The rotors considered in the present study were not optimized for swashplateless TEF rotors. Optimizing the blade for swashplateless TEF rotors could make it perform better than the baseline rotor.

Appendix A

Flap Functions

The flap functions — $T_i(x)$ — are defined in Ref. 41 and are reproduced here for reference. The flap (T) functions are a function of the flap location $(\hat{x}_f)$, here denoted by x.

$$T_0(x) = x\sqrt{1-x^2}\cos^{-1}x - (1-x^2) \tag{A.1}$$

$$T_1(x) = -\frac{1}{3}(2+x^2)\sqrt{1-x^2} + x\cos^{-1}x \tag{A.2}$$

$$T_2(x) = x(1-x^2) - (1+x^2)\sqrt{1-x^2}\cos^{-1}x + x(\cos^{-1}x)^2 \tag{A.3}$$

$$T_3(x) = -\frac{1}{8}(1-x^2)(5x^2+4) + \frac{1}{4}x(7+2x^2)\sqrt{1-x^2}\cos^{-1}x -$$

$$= \left(\frac{1}{8}+x^2\right)(\cos^{-1}x)^2 \tag{A.4}$$

$$T_4(x) = x\sqrt{1-x^2} - \cos^{-1}x \tag{A.5}$$

$$T_5(x) = -(1-x^2) + 2x\sqrt{1-x^2}\cos^{-1}x - (\cos^{-1}x)^2 \tag{A.6}$$

$$T_6(x) = T_2 \tag{A.7}$$

$$T_7(x) = -\frac{1}{8}x(7+2x^2)\sqrt{1-x^2} - \left(\frac{1}{8}+x^2\right)\cos^{-1}x \tag{A.8}$$

$$T_8(x) = -\frac{1}{3}(1+2x^2)\sqrt{1-x^2} + x\cos^{-1}x \tag{A.9}$$

$$T_9(x) = \frac{1}{2}\left(\frac{1}{3}(1-x^2)^{3/2} + aT_4\right) \tag{A.10}$$

$$T_{10}(x) = \sqrt{1-x^2} + \cos^{-1}x \tag{A.11}$$

$$T_{11}(x) = (2-x)\sqrt{1-x^2}) + (1-2x)\cos^{-1}x \tag{A.12}$$

$$T_{12}(x) = (2+x)\sqrt{1-x^2}) - (1+2x)\cos^{-1}x \tag{A.13}$$

$$T_{13}(x) = -\frac{1}{2}\left(T_7 + (x-a)T_1\right) \tag{A.14}$$

$$T_{14}(x) = \frac{1}{16} + \frac{1}{2}ac \tag{A.15}$$

$$T_{15}(x) = (1+x)\sqrt{1-x^2} \tag{A.16}$$

$$T_{16}(x) = \frac{2}{3}(1-x^2)^{3/2} - \left(\frac{1}{2}-a\right)T_4 \tag{A.17}$$

$$T_{17}(x) = -\frac{1}{3}(1-x^2)^{3/2} - T_1 - \frac{1}{2}T_4 \tag{A.18}$$

$$T_{18}(x) = T_5 - T_4 T_{10} \tag{A.19}$$

$$T_{19}(x) = -\frac{1}{2}T_4 T_{11} \tag{A.20}$$

$$T_{20}(x) = -\sqrt{1-x^2} + \cos^{-1}x \tag{A.21}$$

$$T_{21}(x) = \sqrt{\frac{1+x}{1-x}} \tag{A.22}$$

$$T_{22}(x) = 2\sqrt{1-x^2} - \sqrt{\frac{1+x}{1-x}} \tag{A.23}$$

$$T_{23}(x) = (-1-2x+2a)\sqrt{1-x^2} \tag{A.24}$$

$$T_{24}(x) = -2T_9 \tag{A.25}$$

$$T_{25}(x) = T_4 - (1-x)\sqrt{1-x^2} \tag{A.26}$$

$$T_{26}(x) = 2\sqrt{1-x^2}T_{20} + T_4\sqrt{\frac{1+x}{1-x}} \tag{A.27}$$

$$T_{27}(x) = T_4 T_{10} - \sqrt{1-x^2}T_{11} \tag{A.28}$$

$$T_{28}(x) = 2(1+x+\log N(x,x')) \tag{A.29}$$

$$T_{29}(x) = 2\sqrt{1-x^2}T_{10} \tag{A.30}$$

The term $T_{28}(x)$ requires special treatment and this is discussed in detail in Ref. 41.

Appendix B

Mach Contours and Pressure Profiles for NACA0012 Airfoil

This section provides 2D Mach contour and presssure coefficient (C_p) plots for combinations of AoA (α) and flap deflection (δ) at several Mach numbers for the NACA0012 airfoil. These results are obtained from CFD simulations on 2D TEF airfoils. The plots are organized in the form of 2D arrays with AoA variation along the x-axis and TEF deflection variation along the y-axis. The shaded area in the plots corresponds to the region of stall. Because the NACA0012 airfoil experiences trailing edge stall, the stall process is gradual and it is not always possible to pinpoint the start of stall. If the point at which stall occurs occurs is not obvious from the Mach contour or C_p plots, it is assumed to be the point where C_l is maximum (Fig. 3.41). Also, where there is some ambiguity because two adjacent α-values in the stall region have nearly the same value of C_l, the lower angle of attack is taken to be the stall point. This ensures a conservative estimate for the stall boundary. Cases which did not run to completion are indicated by the color-inversed in the plots.
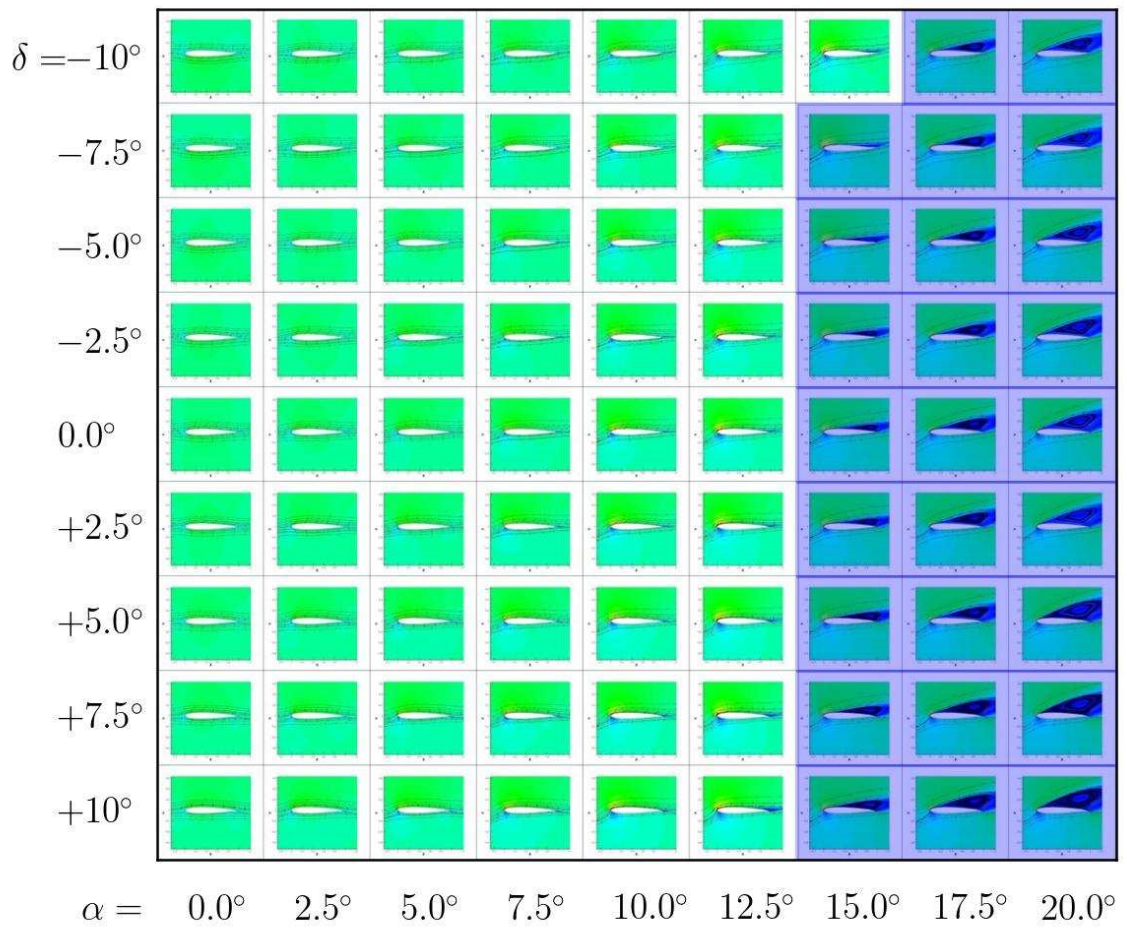
Figure B.1: Mach contours for different α and δ for a NACA0012 airfoil, $M = 0.3$, 15% chord flap, $Re = 4.8$ million.
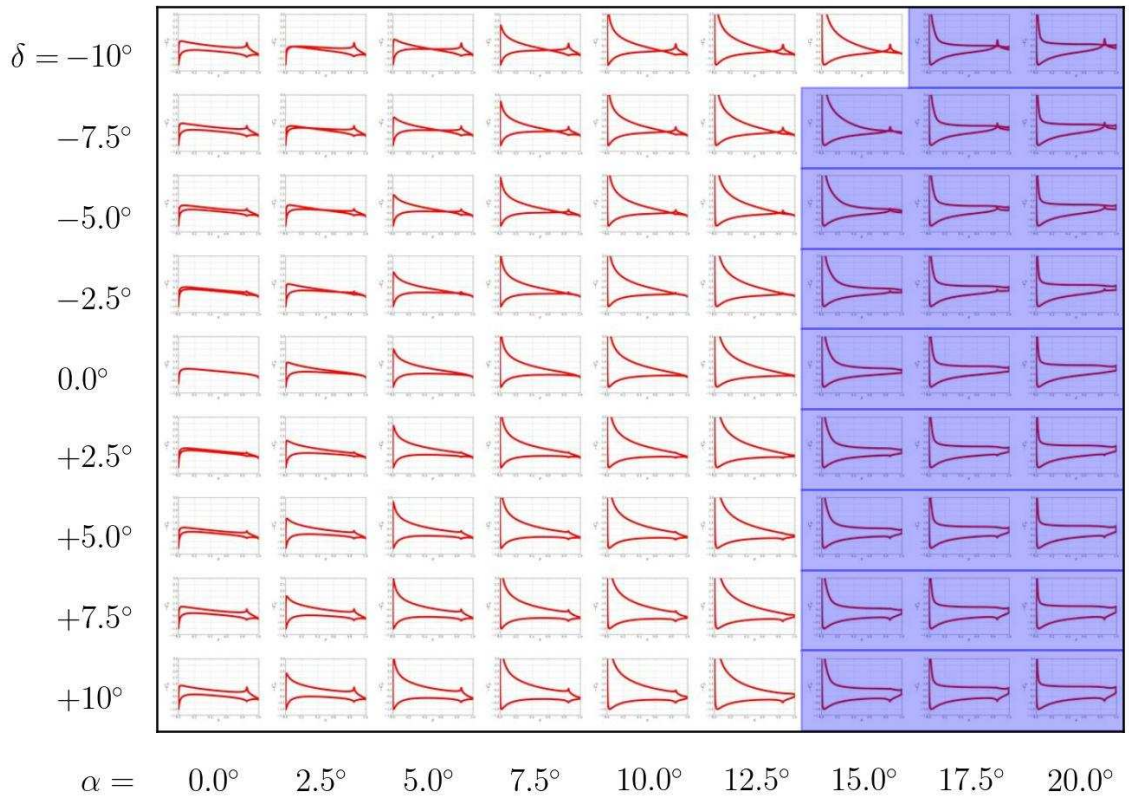
Figure B.2: $-C_p$ vs x for different α and δ for a NACA0012 airfoil, $M = 0.3$, 15% chord flap, $Re = 4.8$ million.
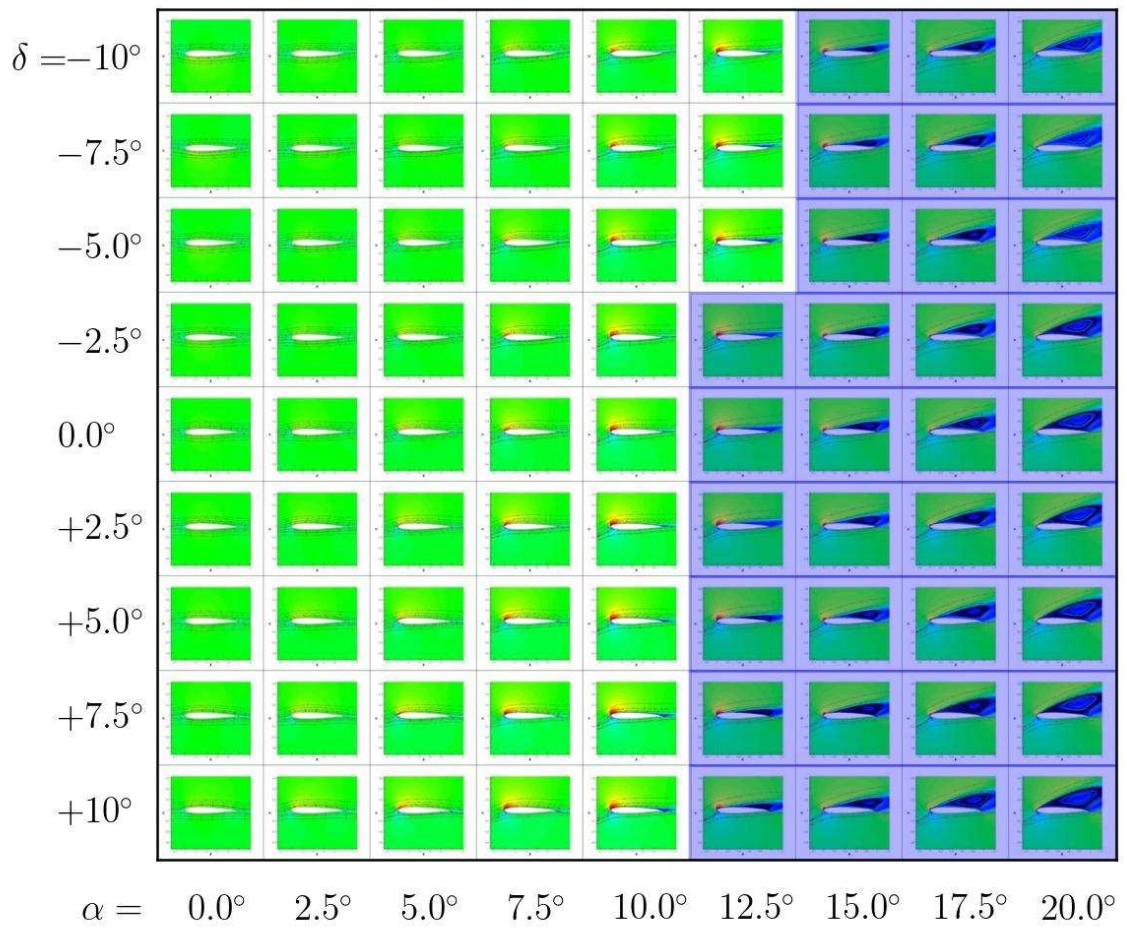
Figure B.3: Mach contours for different α and δ for a NACA0012 airfoil, $M = 0.4$, 15% chord flap, $Re = 4.8$ million.
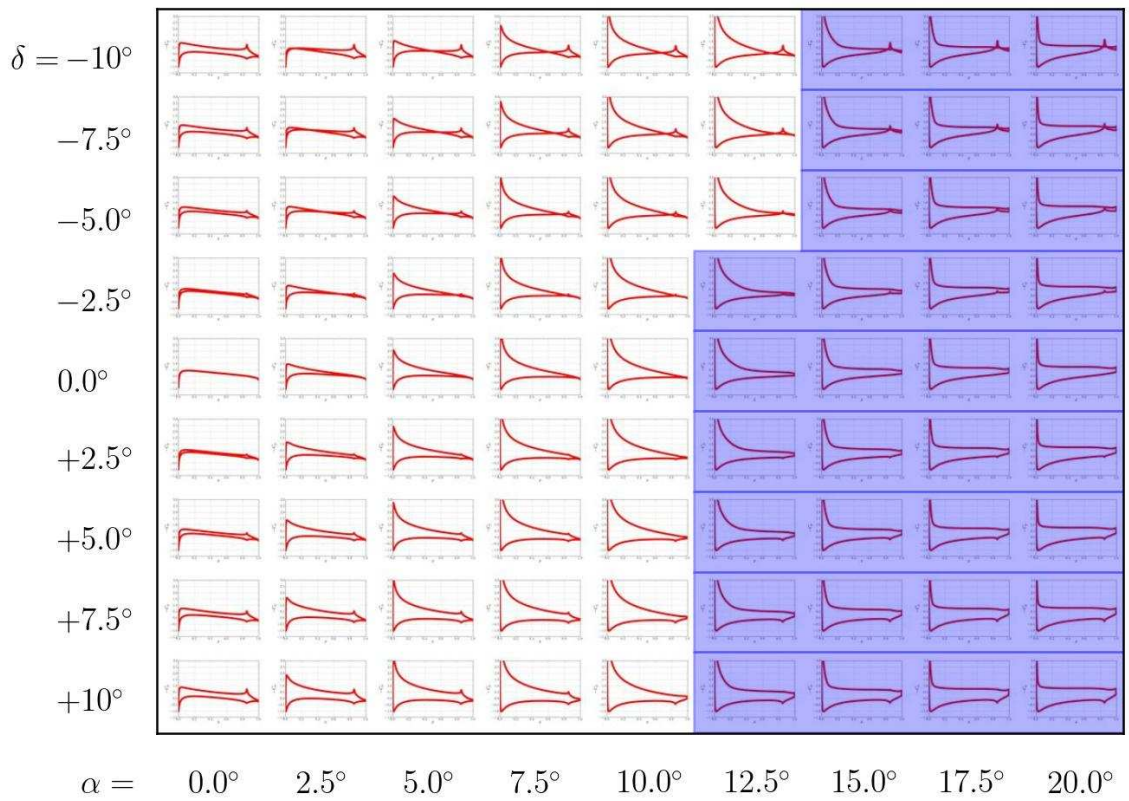
Figure B.4: $-C_p$ vs x for different α and δ for a NACA0012 airfoil, $M = 0.4$, 15% chord flap, $Re = 4.8$ million.
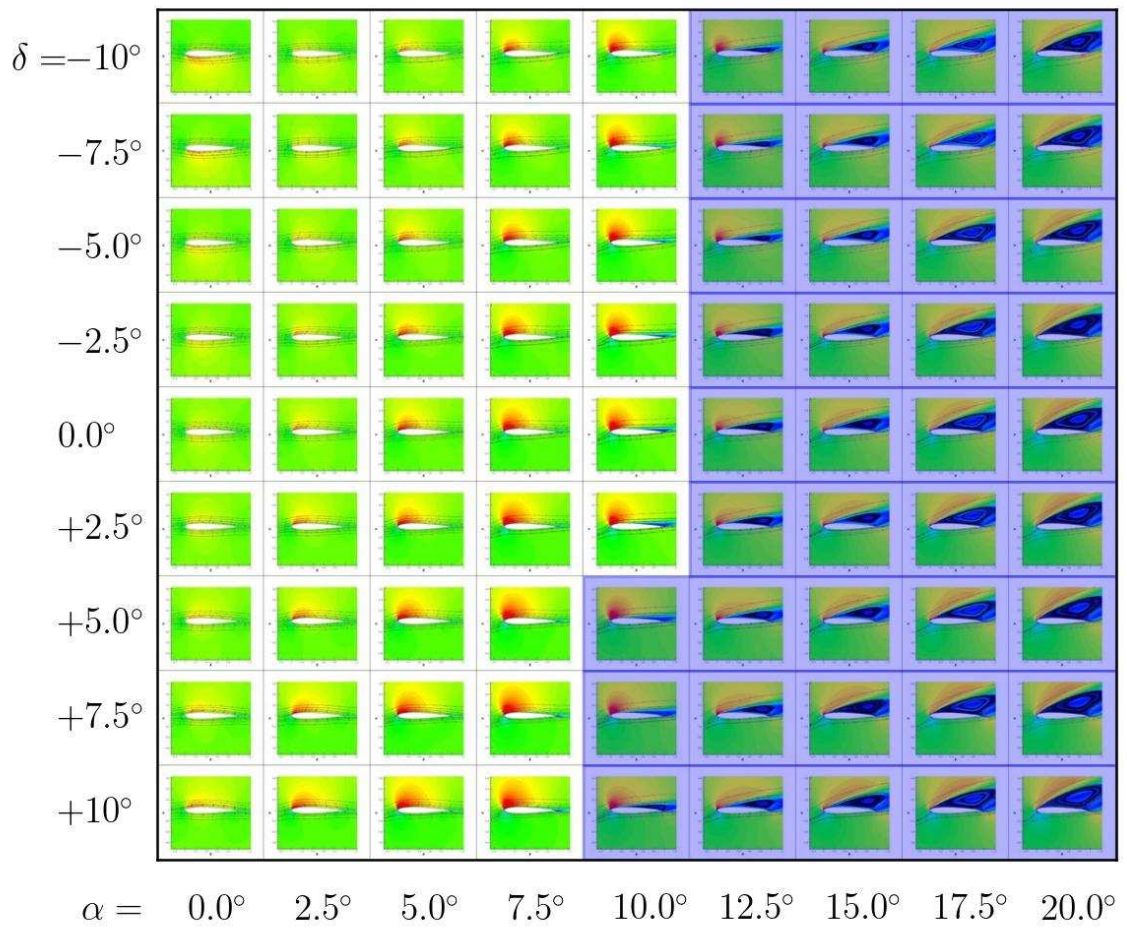
Figure B.5: Mach contours for different α and δ for a NACA0012 airfoil, $M = 0.5$, 15% chord flap, $Re = 4.8$ million.
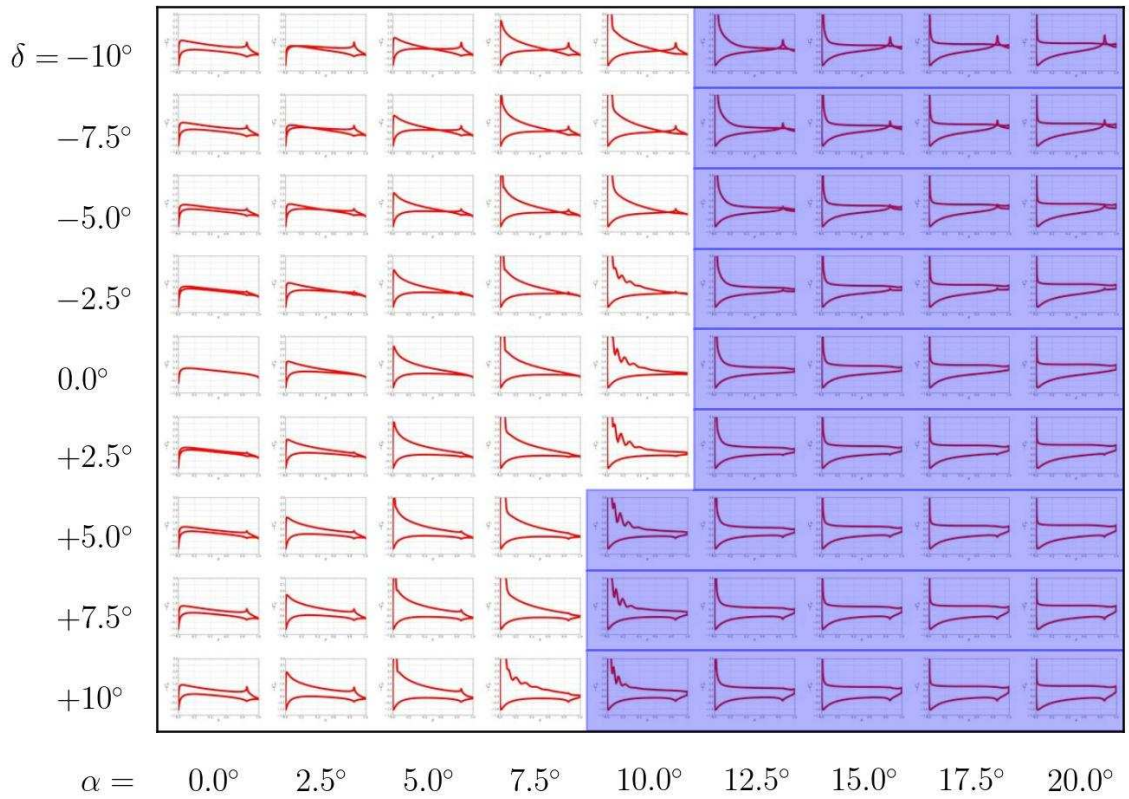
Figure B.6: $-C_p$ vs x for different α and δ for a NACA0012 airfoil, $M = 0.5$, 15% chord flap, $Re = 4.8$ million.
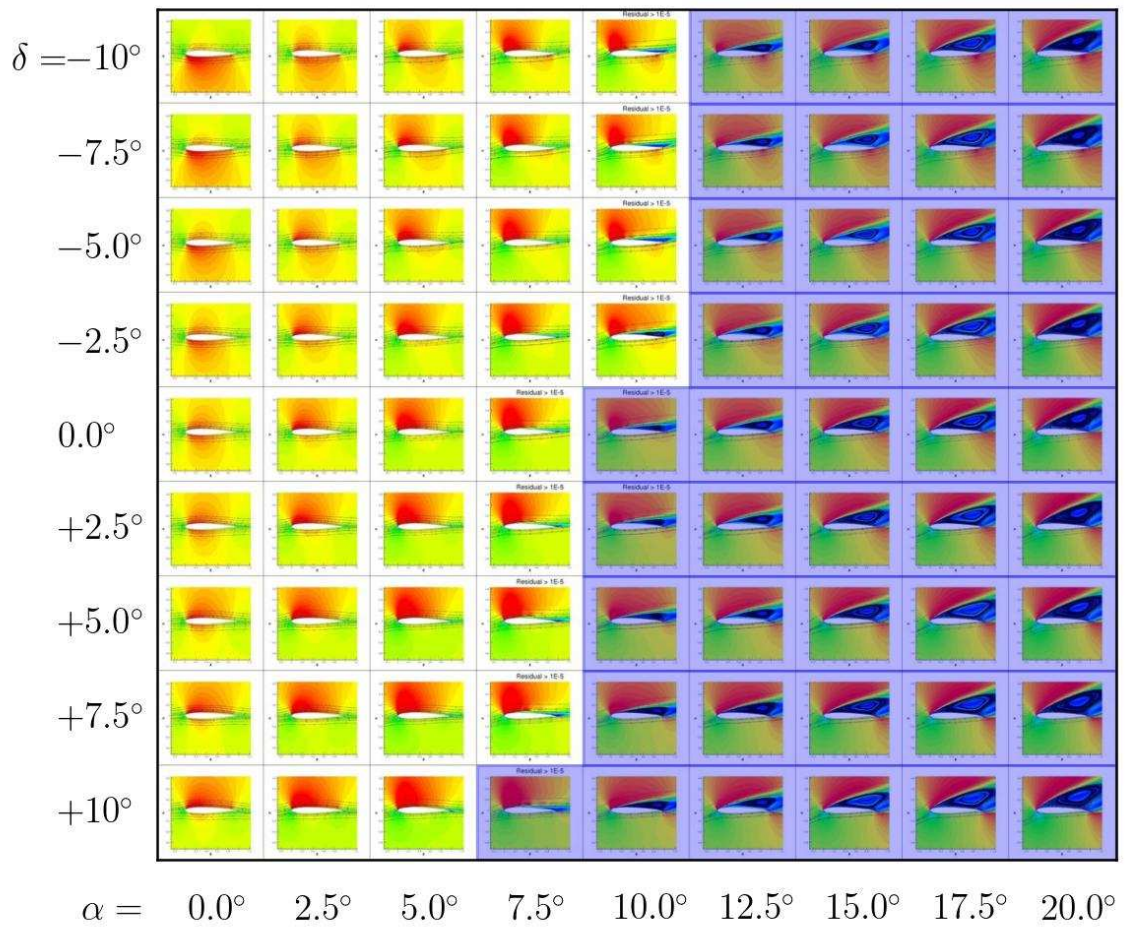
Figure B.7: Mach contours for different α and δ for a NACA0012 airfoil, $M = 0.6$, 15% chord flap, $Re = 4.8$ million.
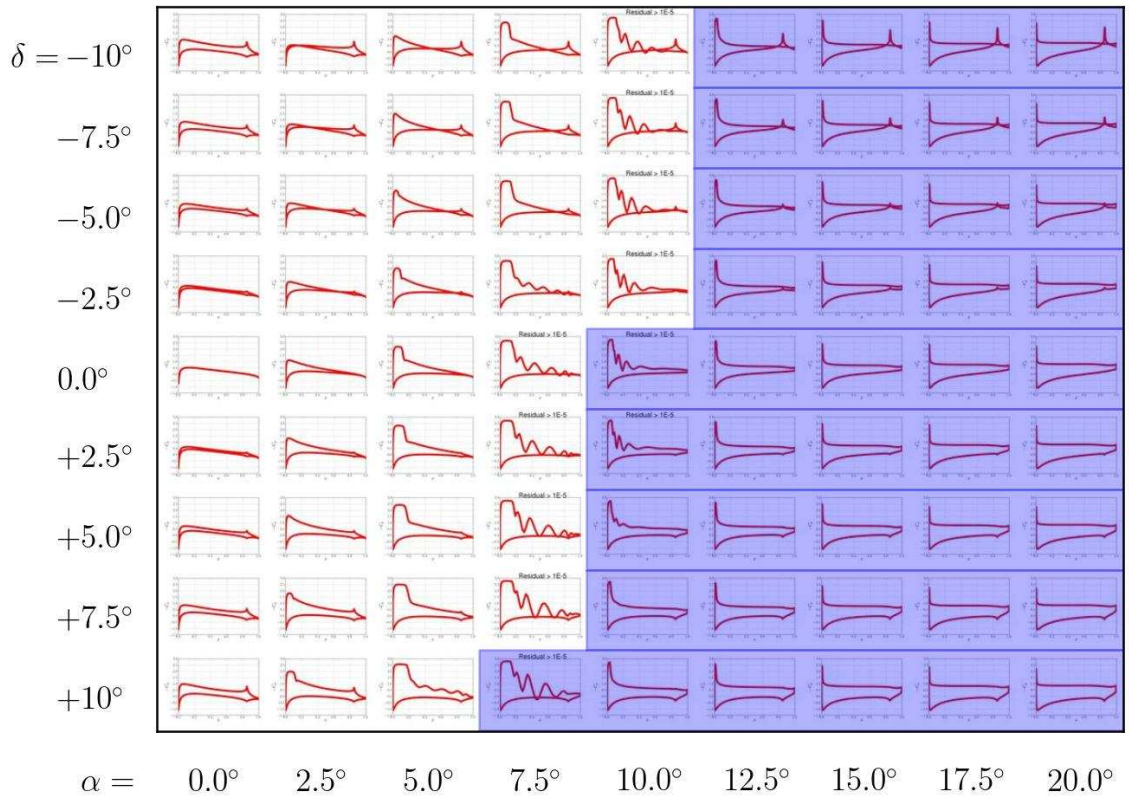
Figure B.8: $-C_p$ vs x for different α and δ for a NACA0012 airfoil, $M = 0.6$, 15% chord flap, $Re = 4.8$ million.
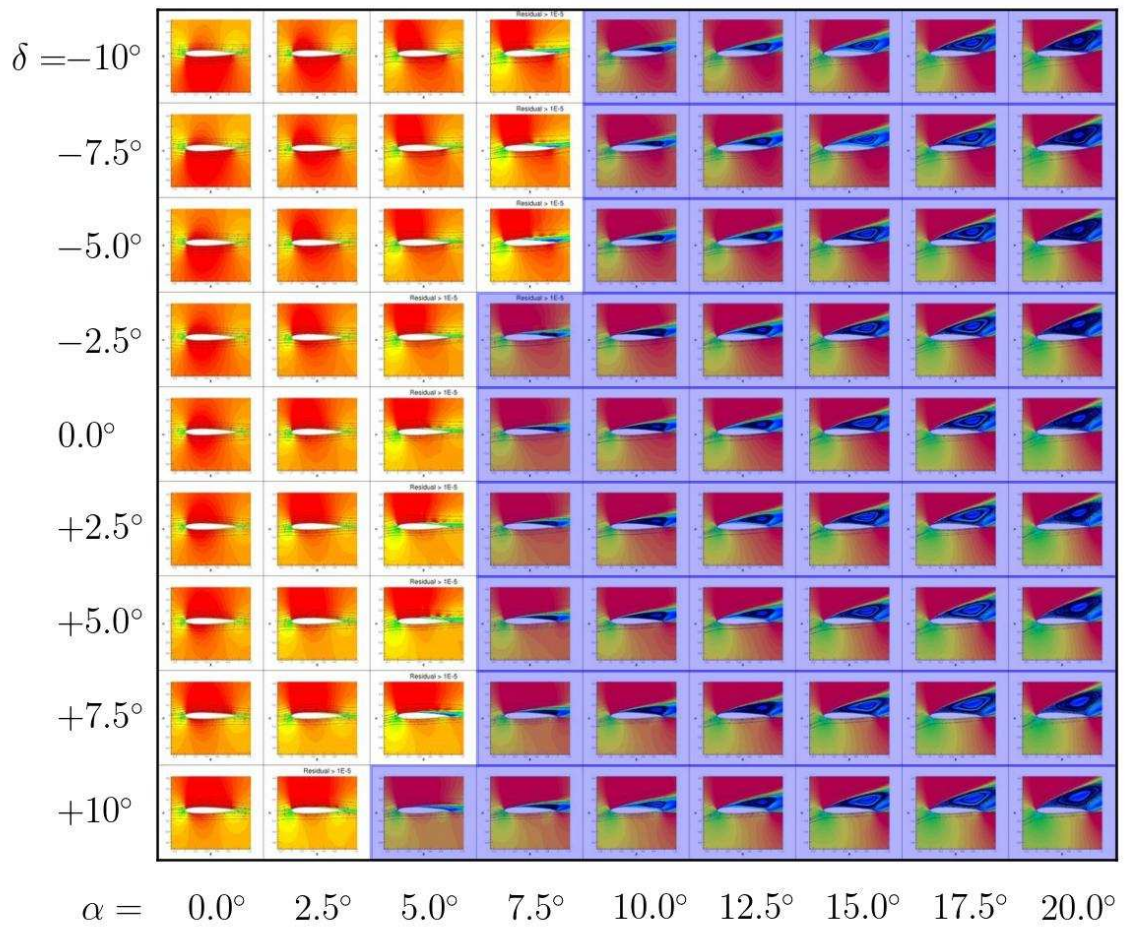
Figure B.9: Mach contours for different α and δ for a NACA0012 airfoil, $M = 0.7$, 15% chord flap, $Re = 4.8$ million.
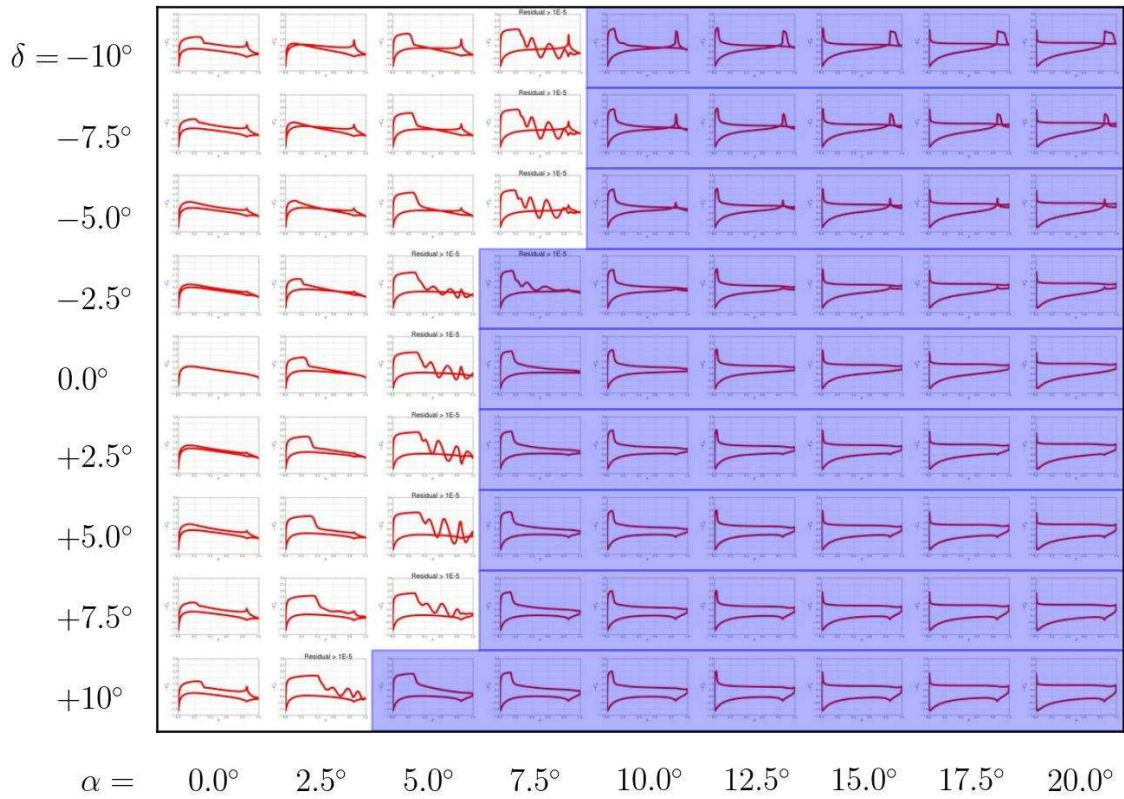
Figure B.10: $-C_p$ vs x for different α and δ for a NACA0012 airfoil, $M = 0.7$, 15% chord flap, $Re = 4.8$ million.
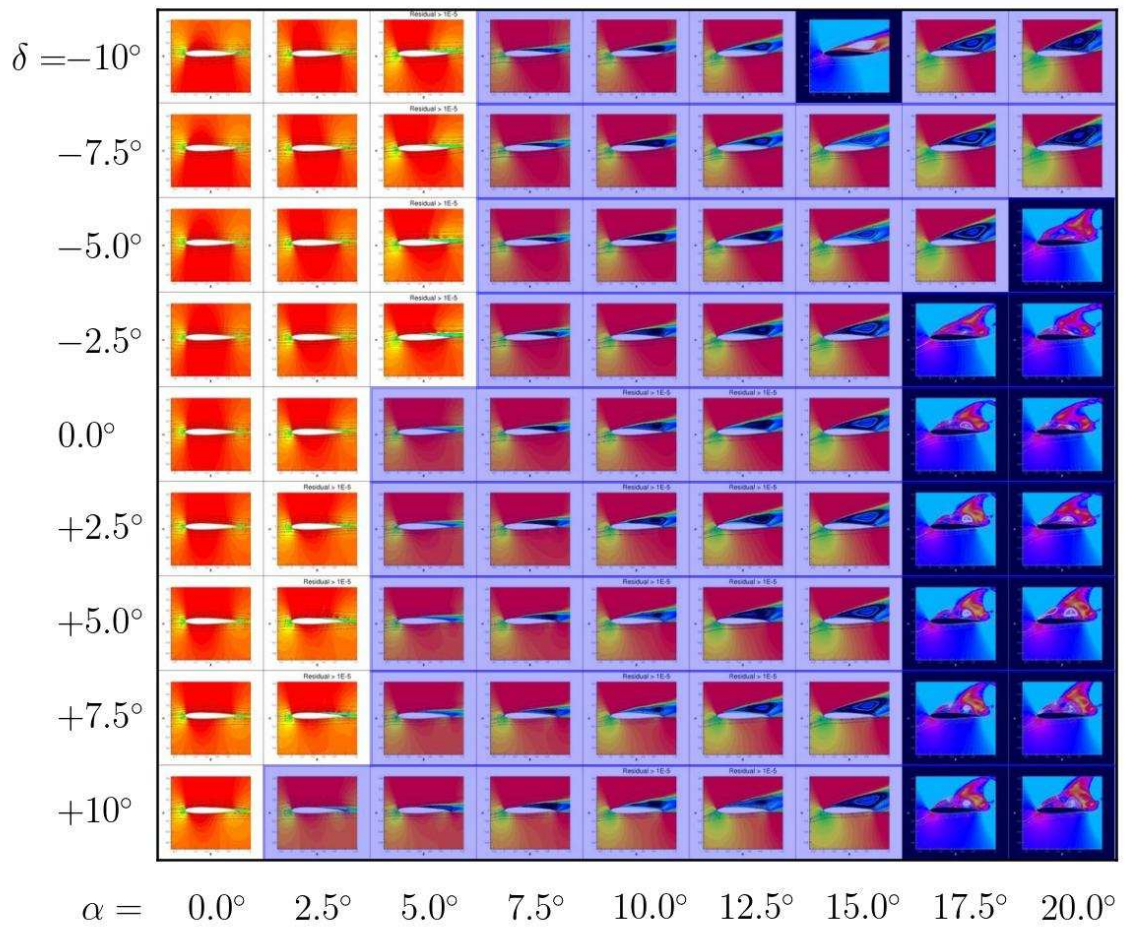
Figure B.11: Mach contours for different α and δ for a NACA0012 airfoil, $M = 0.75$, 15% chord flap, $Re = 4.8$ million.
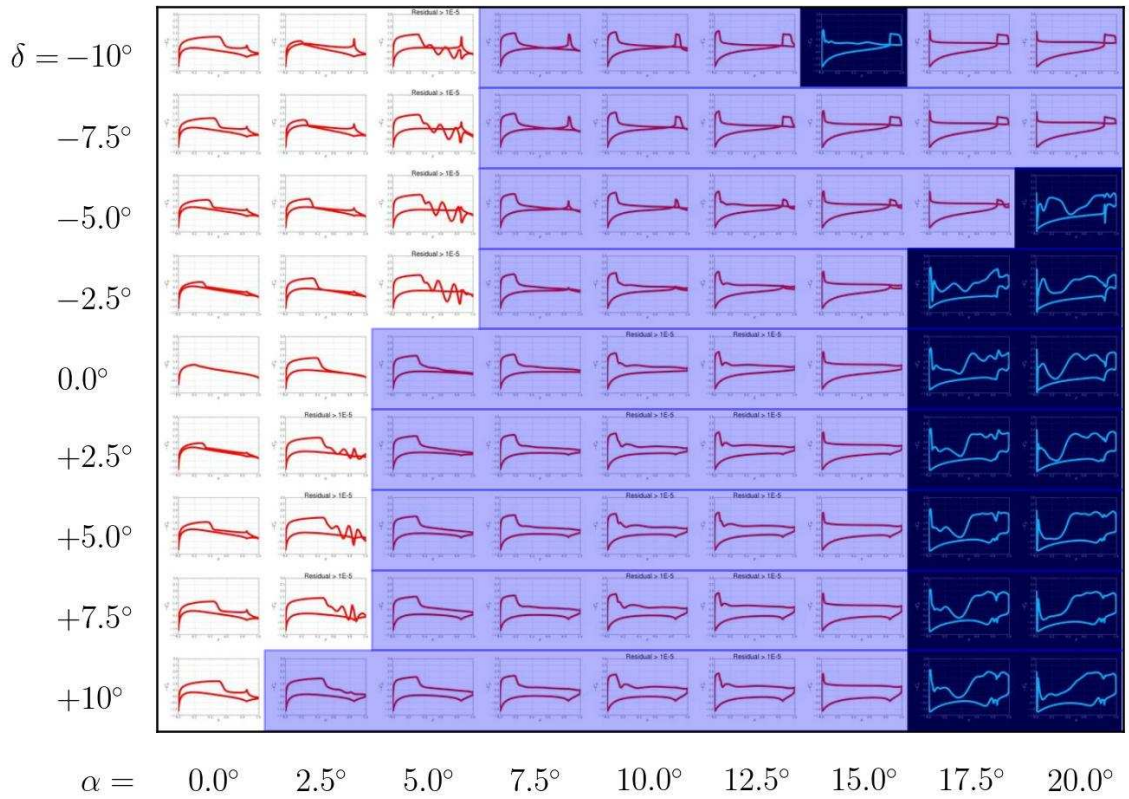
Figure B.12: $-C_p$ vs x for different α and δ for a NACA0012 airfoil, $M = 0.75$, 15% chord flap, $Re = 4.8$ million.

Appendix C

Mach Contours, Pressure Profiles and Airloads for SC1095R8 Airfoil

This section provides 2D Mach contour and presssure coefficient (C_p) plots for combinations of AoA (α) and flap deflection (δ) at several Mach numbers for the SC1095R8 airfoil. These results are obtained from CFD simulations on 2D TEF airfoils. The plots are organized in the form of 2D arrays with AoA variation along the x-axis and TEF deflection variation along the y-axis. The shaded area in the plots corresponds to the region of stall. Because the SC1095R8 airfoil experiences trailing edge stall, the stall process is gradual and it is not always possible to pinpoint the start of stall. If the point at which stall occurs occurs is not obvious from the Mach contour or C_p plots, it is assumed to be the point where C_l is maximum (Fig. C.13). Also, where there is some ambiguity because two adjacent angle of attack values in the stall region have nearly the same value of C_l, the lower angle of attack is taken to be the stall point. This ensures a conservative estimate for the stall boundary. Cases which did not run to completion are indicated by the color-inversed in the plots. Airloads (C_l, C_d, C_m and C_h) plots are also shown for range of Mach numbers.
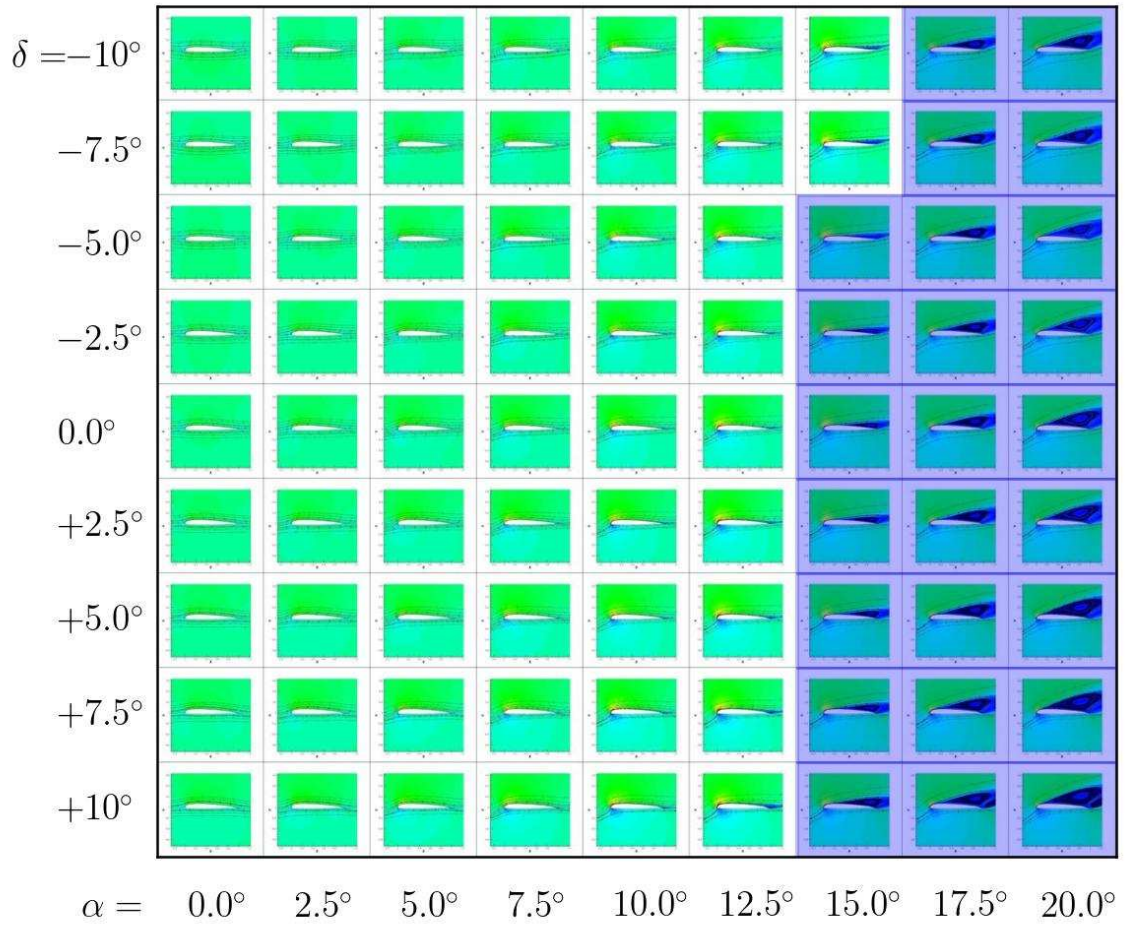
Figure C.1: Mach contours for different α and δ for a SC1095R8 airfoil, $M = 0.3$, 15% chord flap, $Re = 4.8$ million.
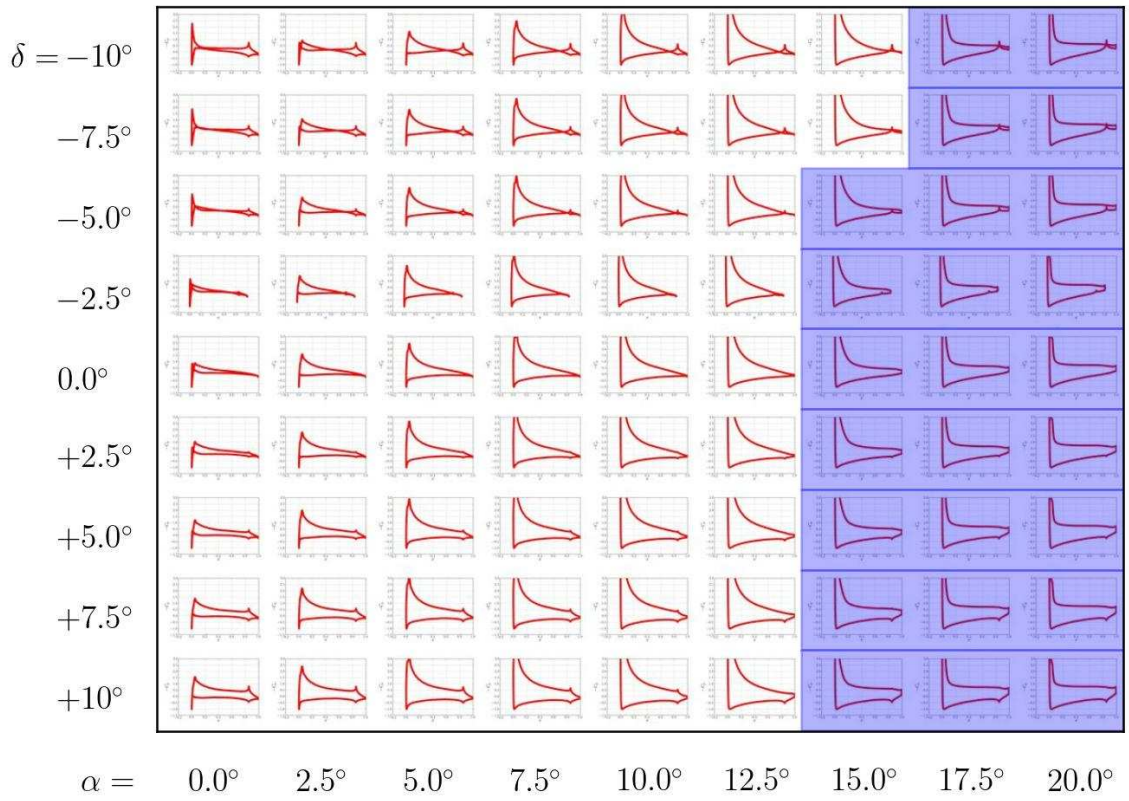
Figure C.2: $-C_p$ vs x for different α and δ for a SC1095R8 airfoil, $M = 0.3$, 15% chord flap, $Re = 4.8$ million.
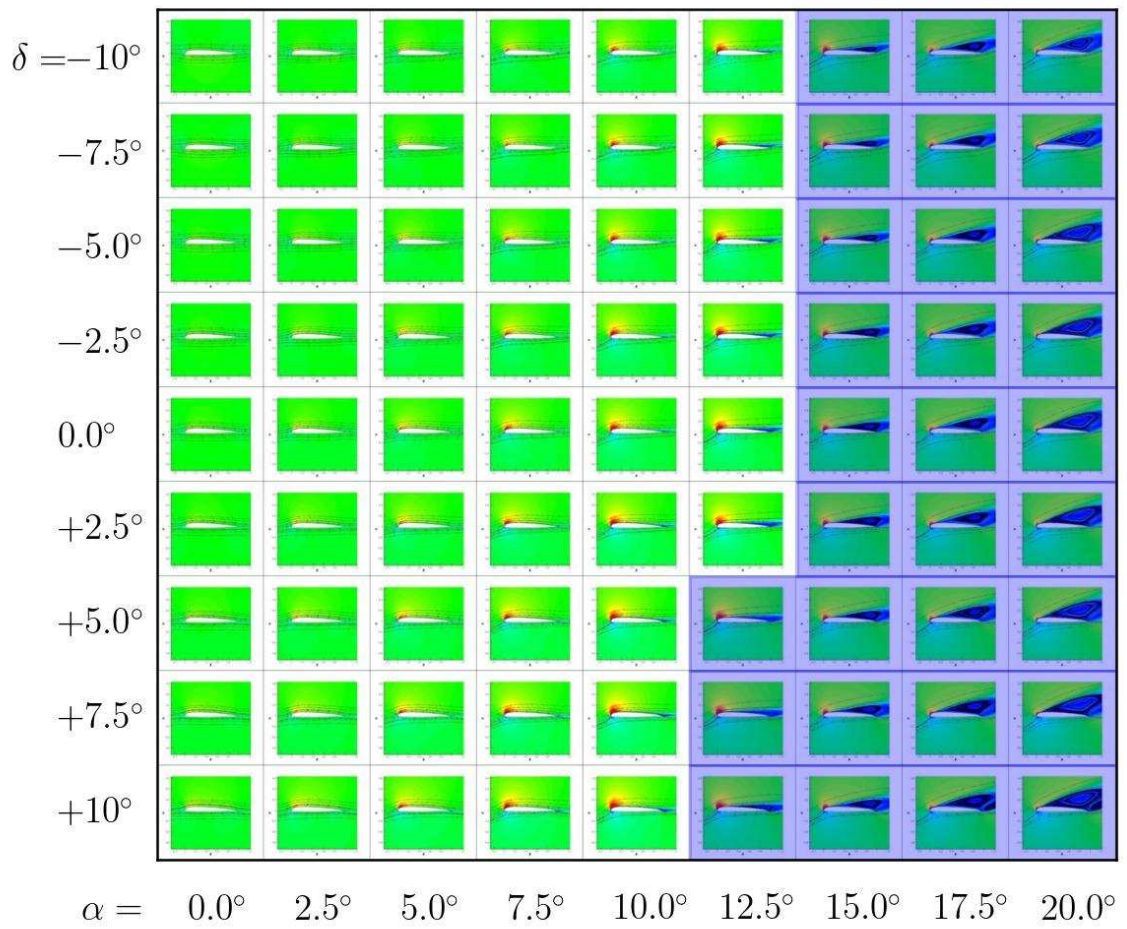
Figure C.3: Mach contours for different α and δ for a SC1095R8 airfoil, $M = 0.4$, 15% chord flap, $Re = 4.8$ million.
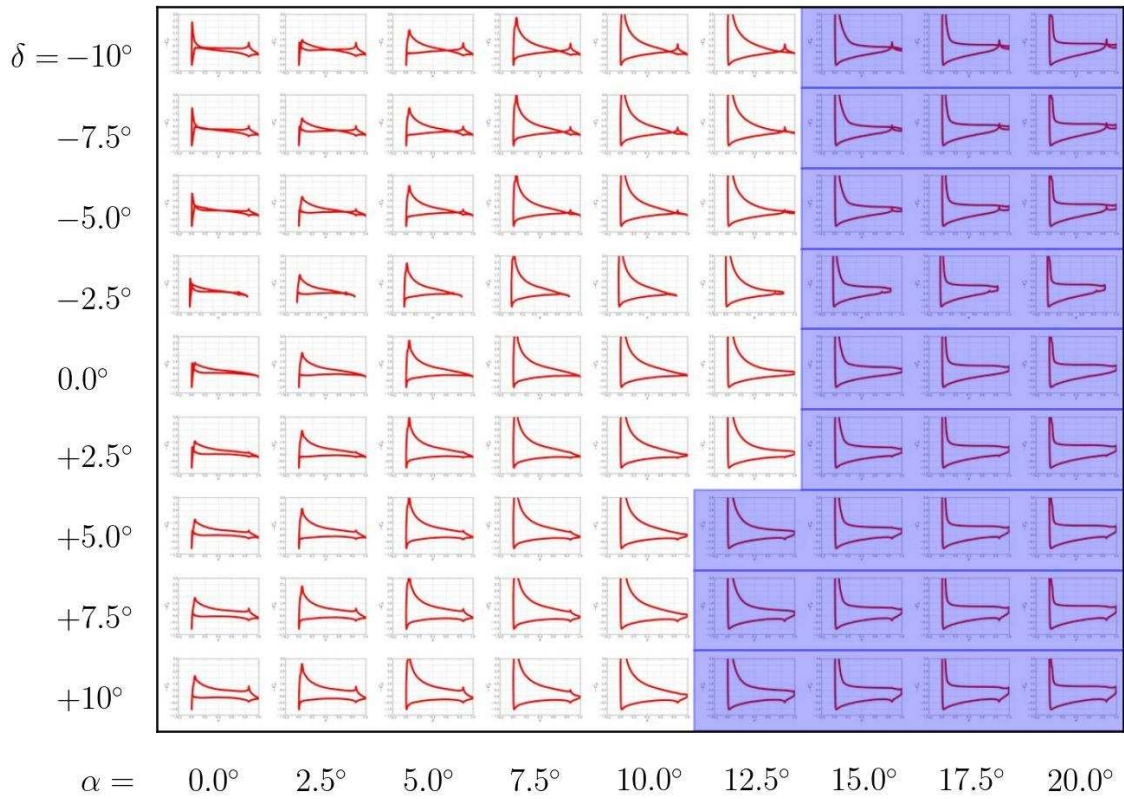
Figure C.4: $-C_p$ vs x for different α and δ for a SC1095R8 airfoil, $M = 0.4$, 15% chord flap, $Re = 4.8$ million.
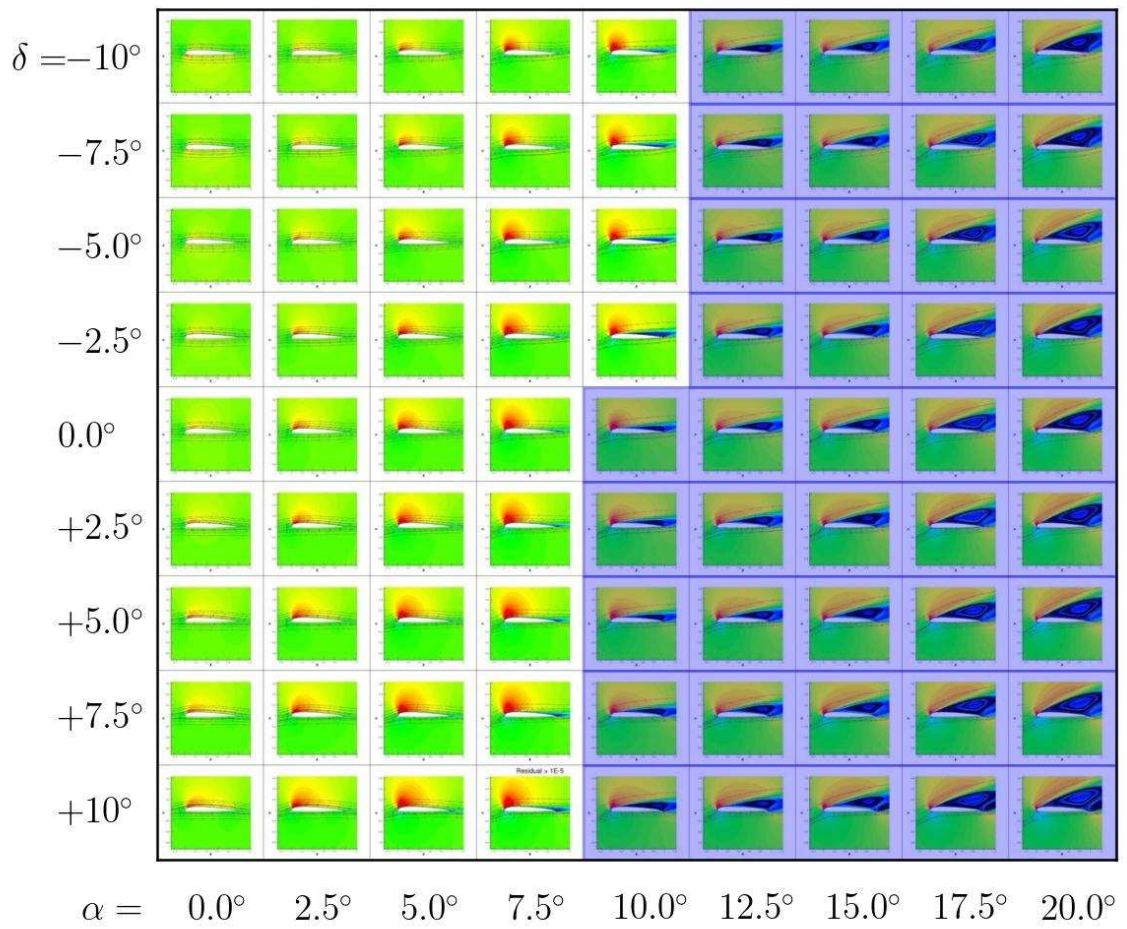
Figure C.5: Mach contours for different α and δ for a SC1095R8 airfoil, $M = 0.5$, 15% chord flap, $Re = 4.8$ million.
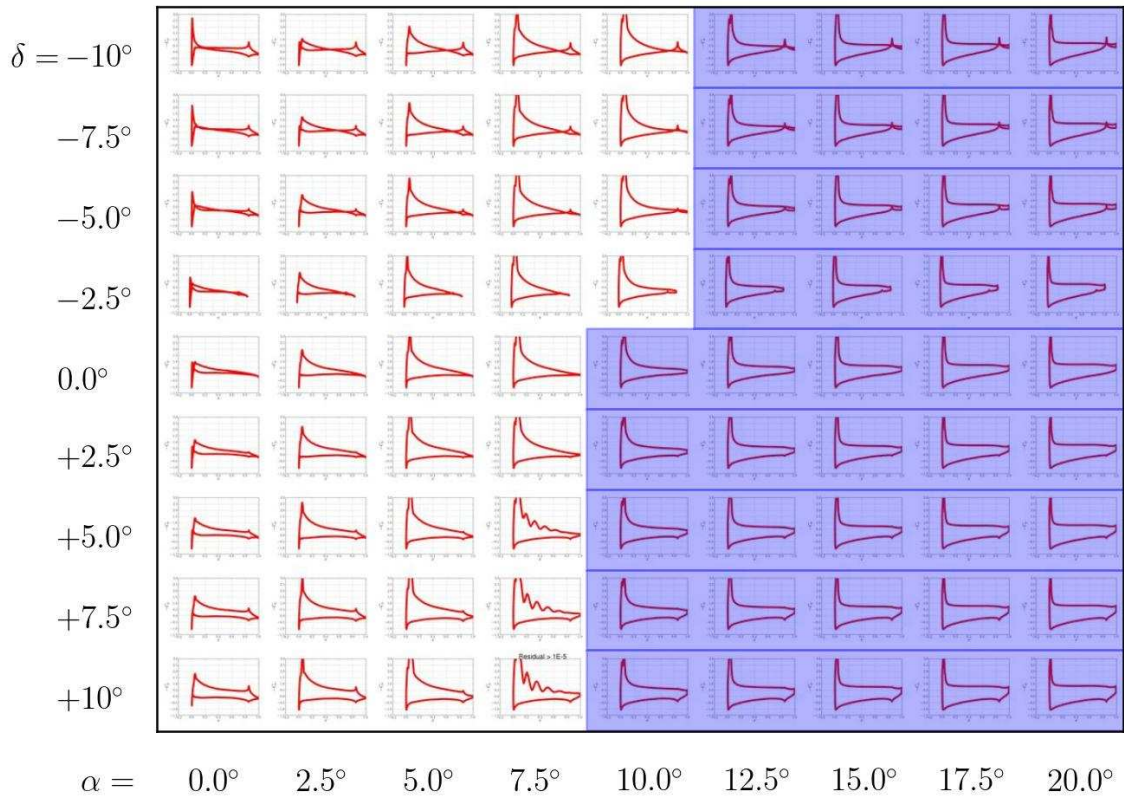
Figure C.6: $-C_p$ vs x for different α and δ for a SC1095R8 airfoil, $M = 0.5$, 15% chord flap, $Re = 4.8$ million.
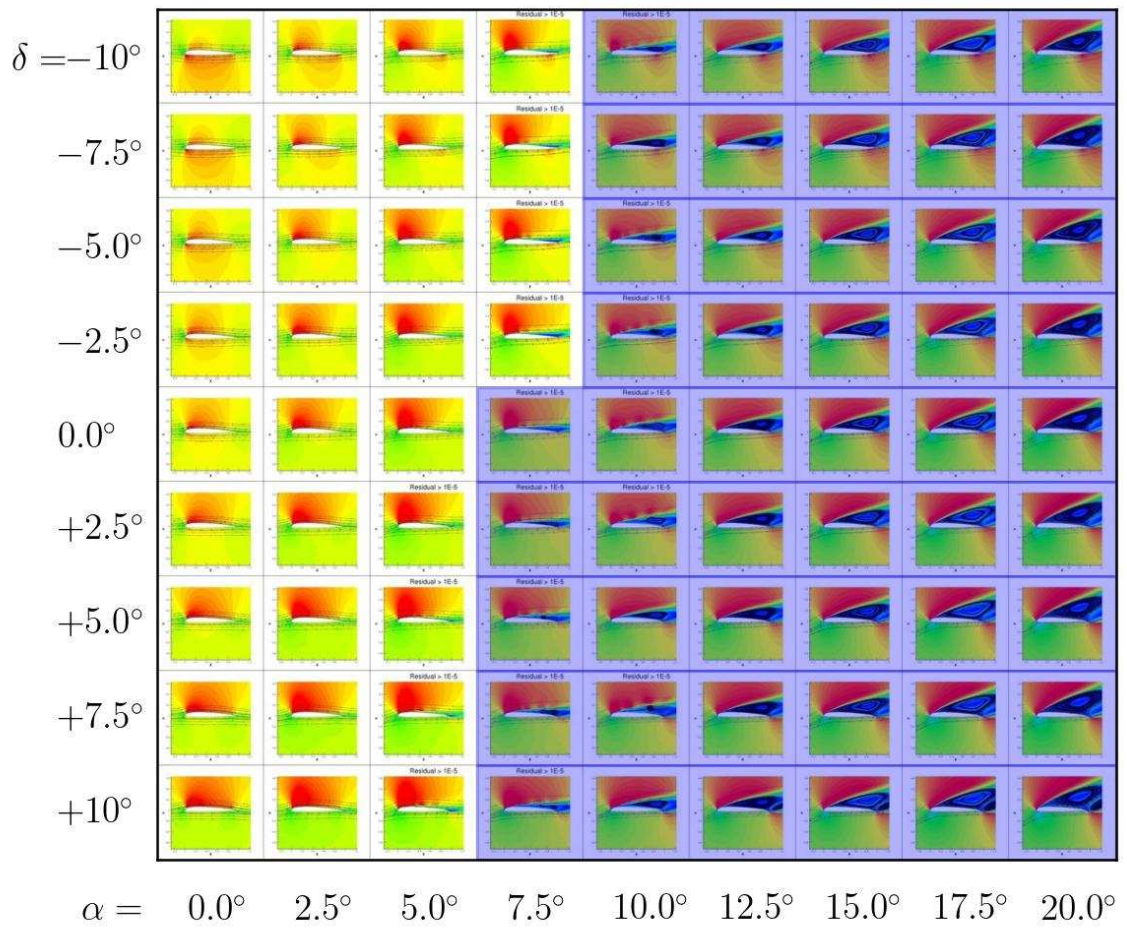
Figure C.7: Mach contours for different α and δ for a SC1095R8 airfoil, $M = 0.6$, 15% chord flap, $Re = 4.8$ million.
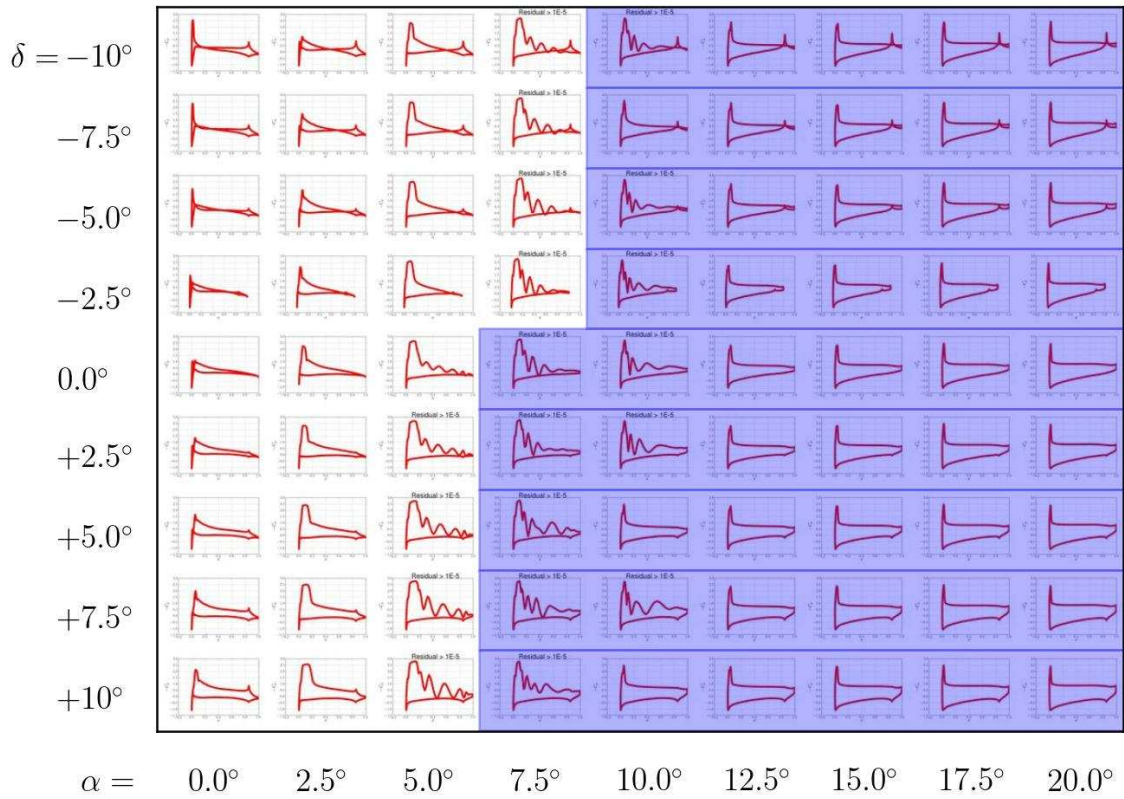
Figure C.8: $-C_p$ vs x for different α and δ for a SC1095R8 airfoil, $M = 0.6$, 15% chord flap, $Re = 4.8$ million.
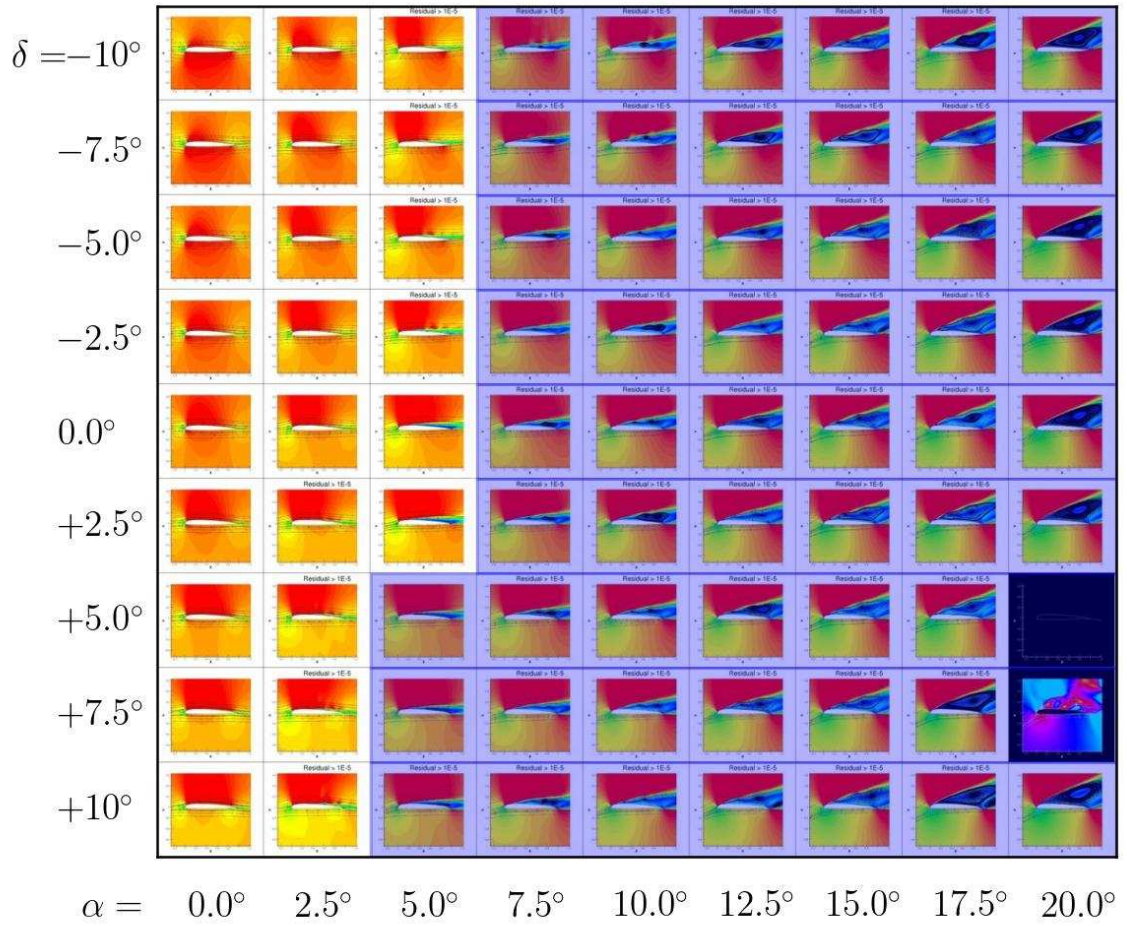
Figure C.9: Mach contours for different α and δ for a SC1095R8 airfoil, $M = 0.7$, 15% chord flap, $Re = 4.8$ million.
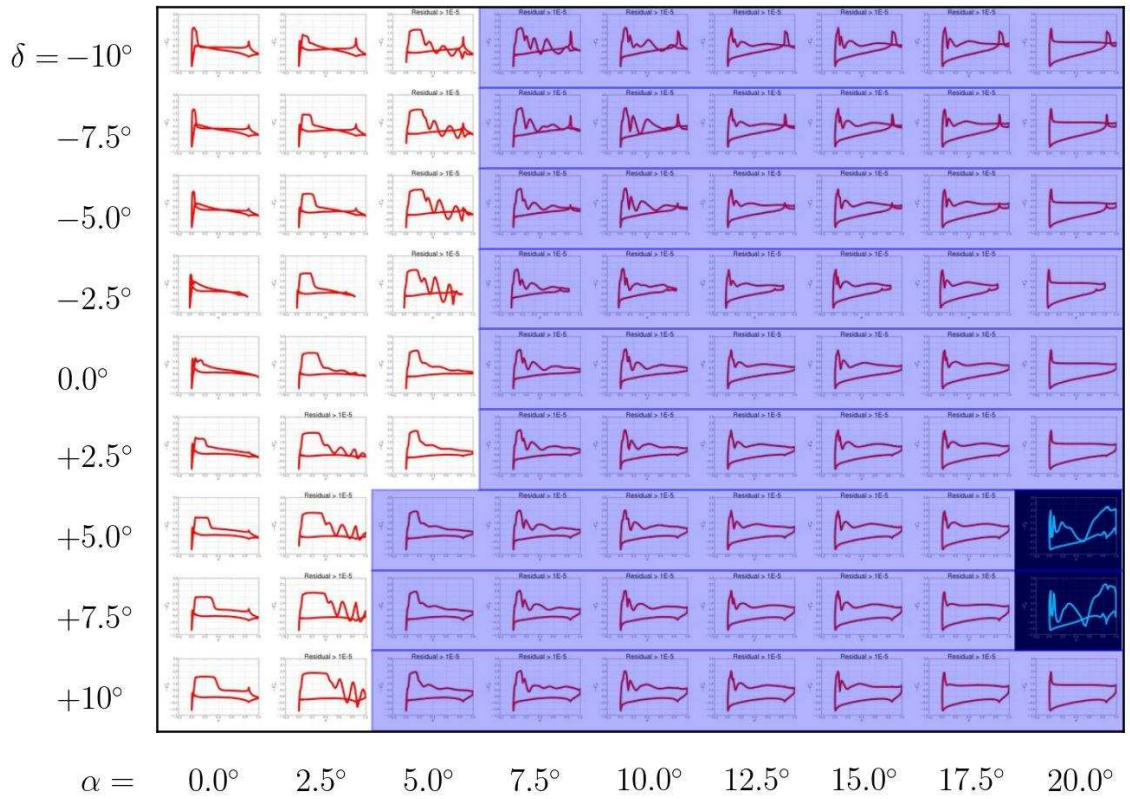
Figure C.10: $-C_p$ vs x for different α and δ for a SC1095R8 airfoil, $M = 0.7$, 15% chord flap, $Re = 4.8$ million.
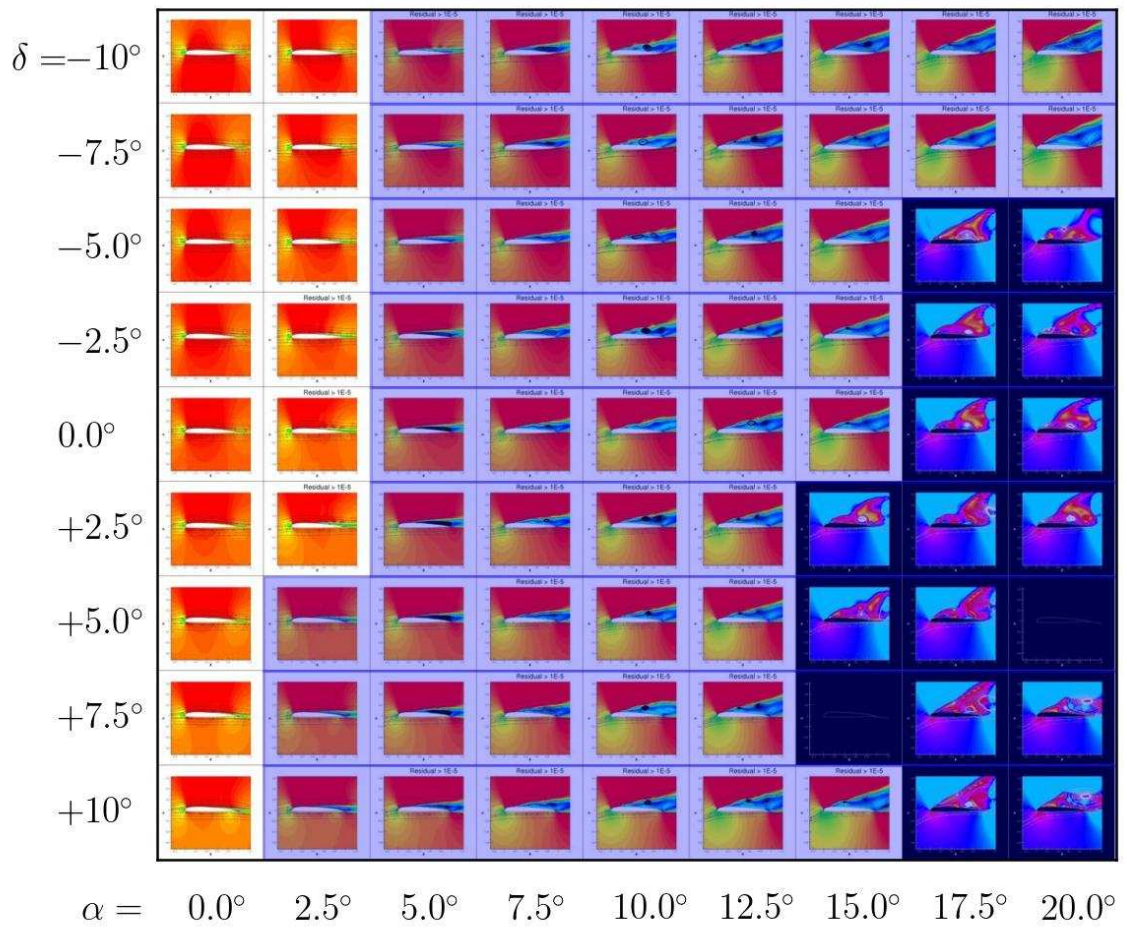
Figure C.11: Mach contours for different α and δ for a SC1095R8 airfoil, $M = 0.75$, 15% chord flap, $Re = 4.8$ million.
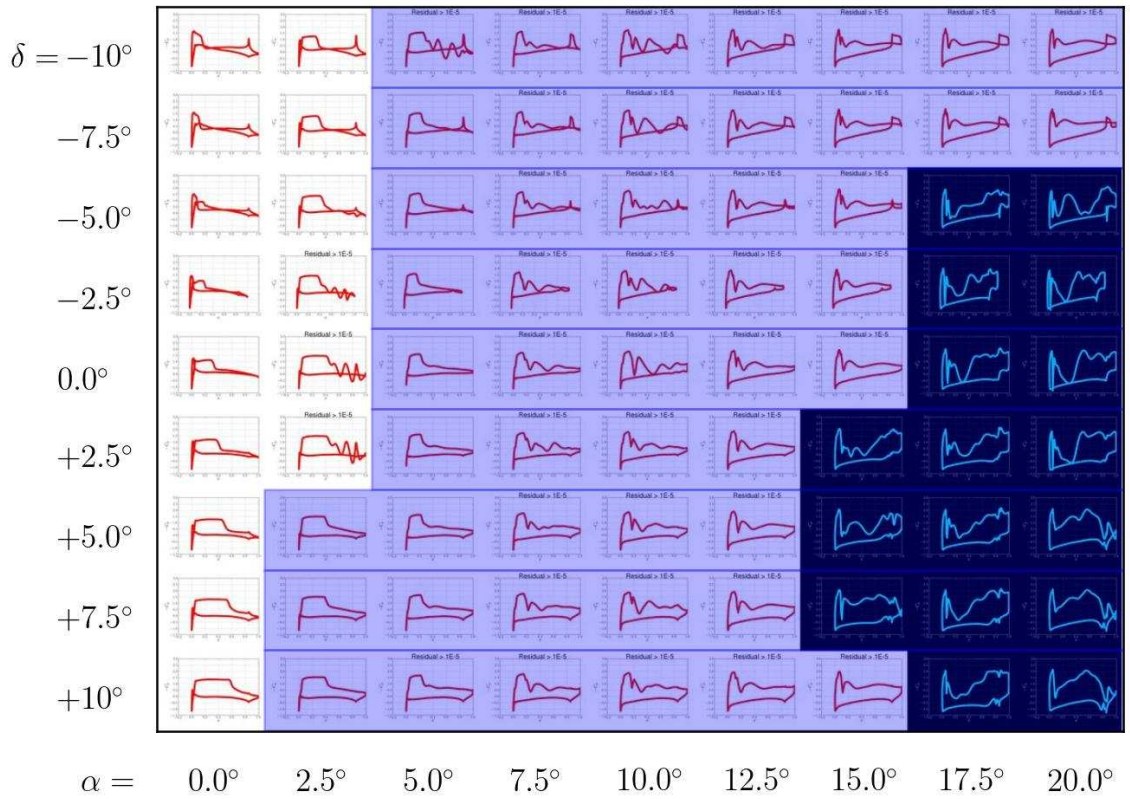
Figure C.12: $-C_p$ vs x for different α and δ for a SC1095R8 airfoil, $M = 0.75$, 15% chord flap, $Re = 4.8$ million.
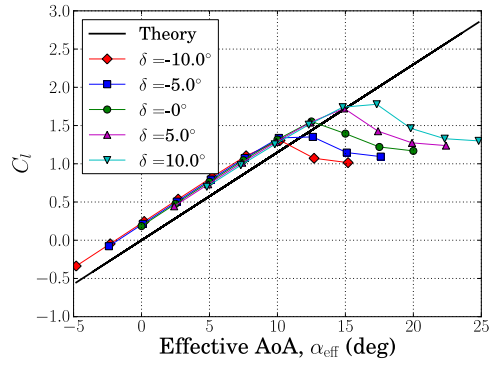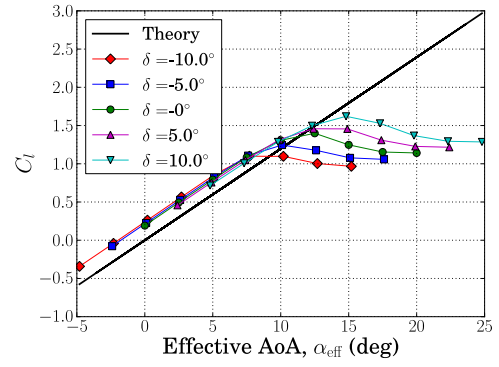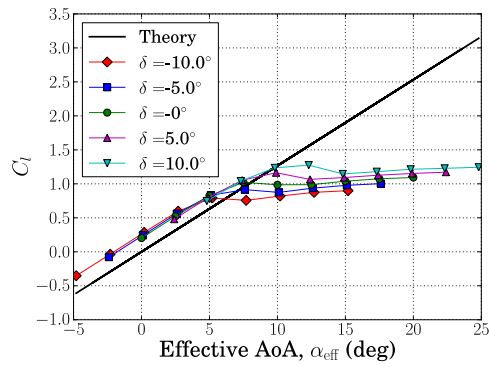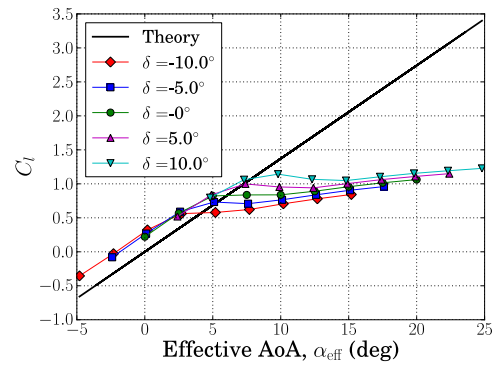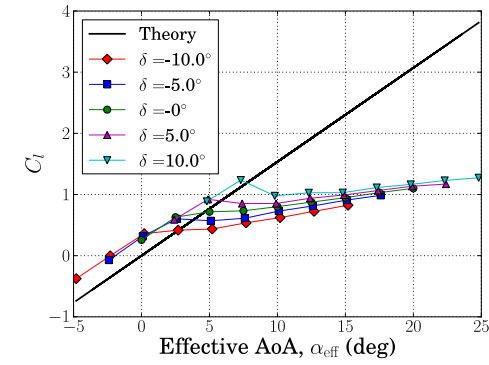
(a) $M = 0.3$
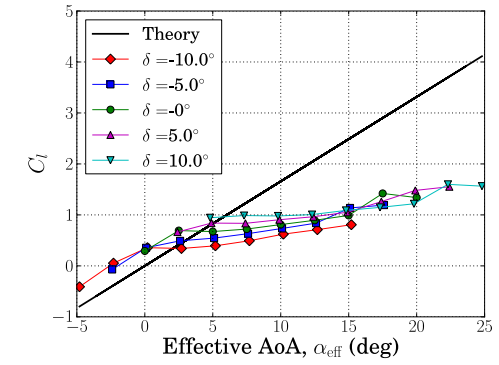
(b) $M = 0.4$

(c) $M = 0.5$

(d) $M = 0.6$

(e) $M = 0.7$

(f) $M = 0.75$

Figure C.13: C_l vs α_{eff} for different Mach numbers for a SC1095R8 airfoil, 15% chord flap, $Re = 4.8$ million.
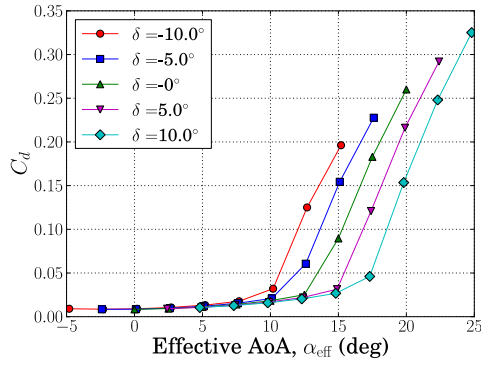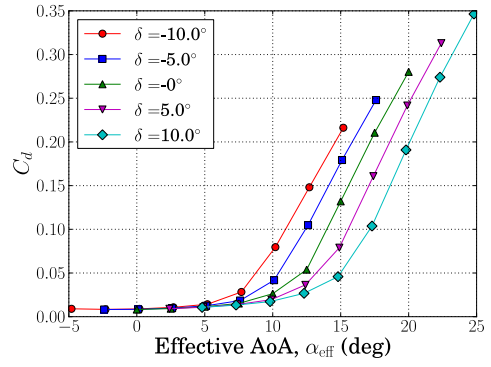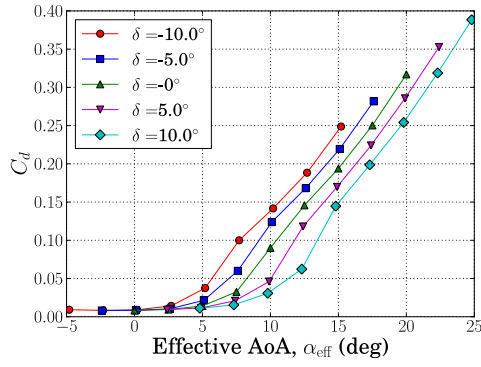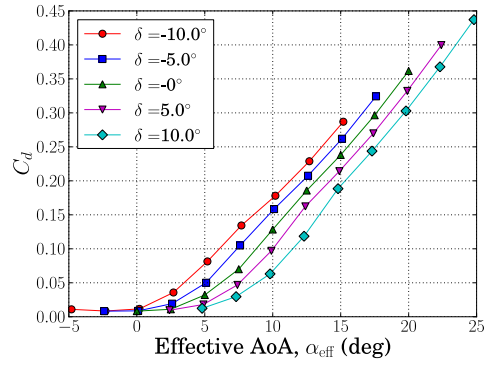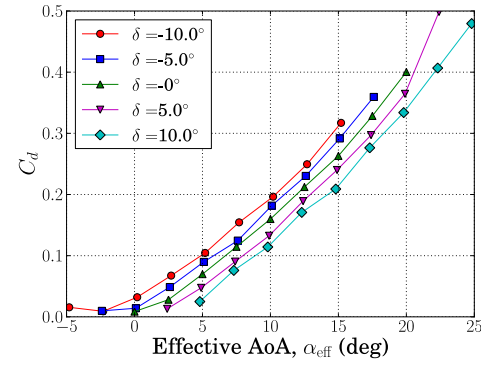
(a) $M = 0.3$
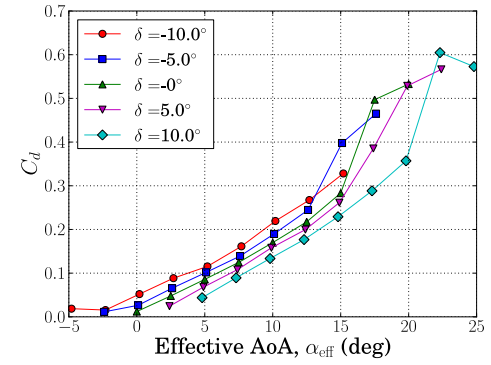
(b) $M = 0.4$

(c) $M = 0.5$

(d) $M = 0.6$

(e) $M = 0.7$

(f) $M = 0.75$

Figure C.14: C_l vs α_{eff} for different Mach numbers for a SC1095R8 airfoil, 15% chord flap, $Re = 4.8$ million.
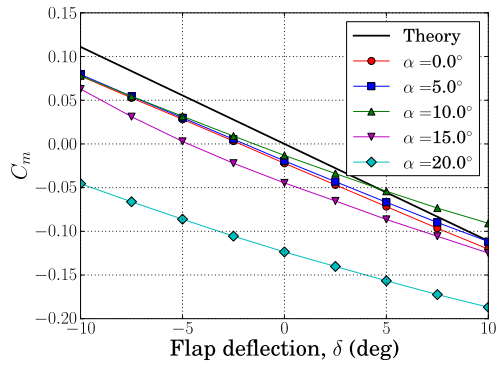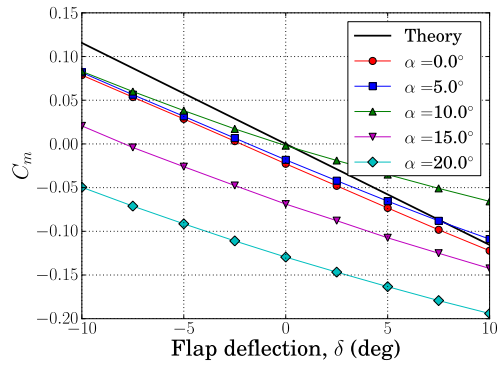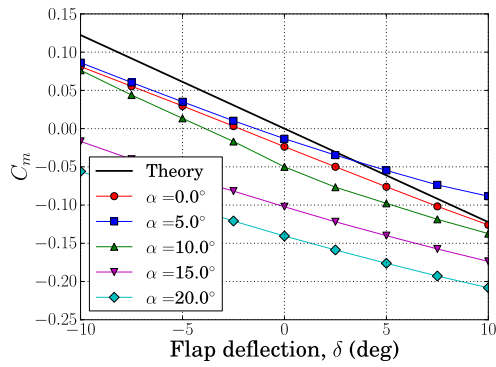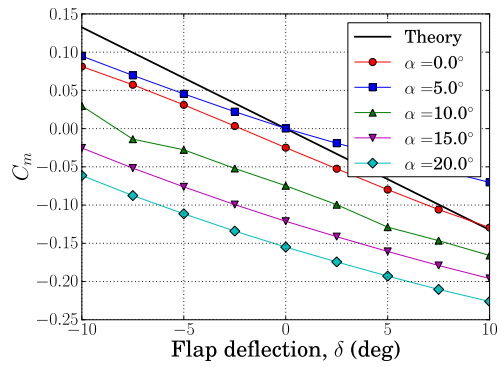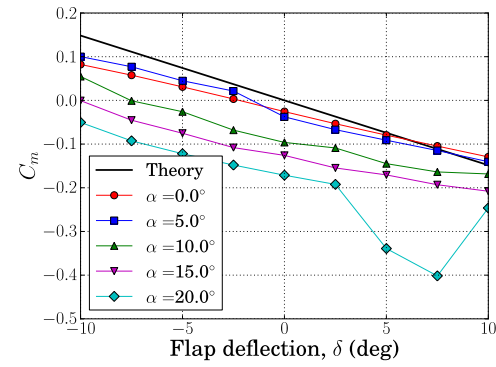
(a) $M = 0.3$ (b) $M = 0.4$
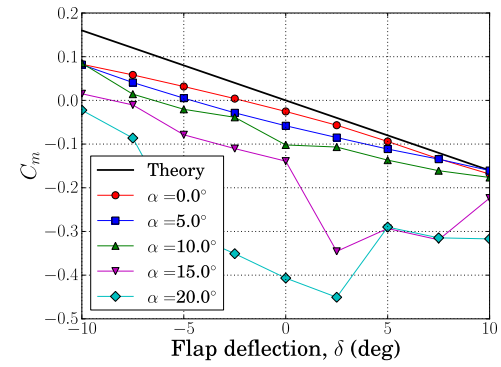
(c) $M = 0.5$ (d) $M = 0.6$

(e) $M = 0.7$ (f) $M = 0.75$

Figure C.15: C_m vs δ at different Mach numbers for the SC1095R8 airfoil, 15% chord flap, $Re = 4.8$ million.
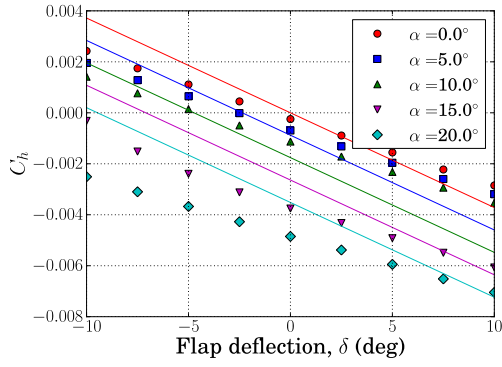
(a) $M = 0.3$
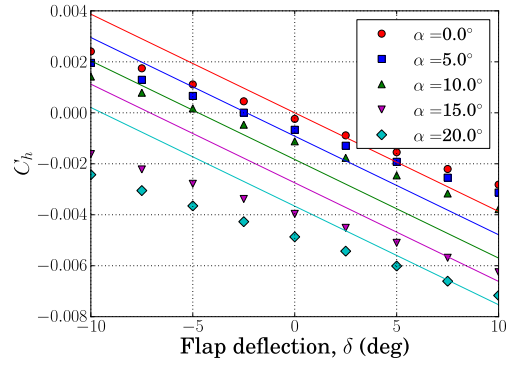
(b) $M = 0.4$
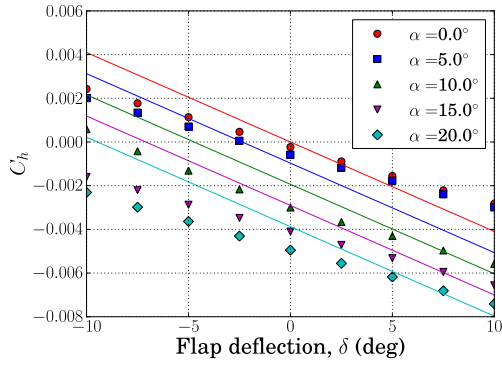
(c) $M = 0.5$
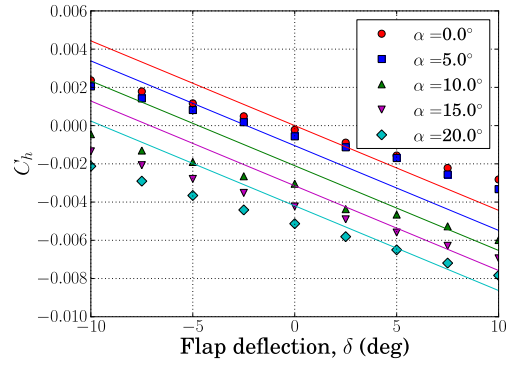
(d) $M = 0.6$
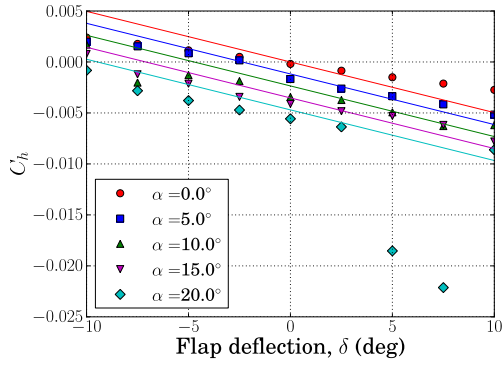
(e) $M = 0.7$
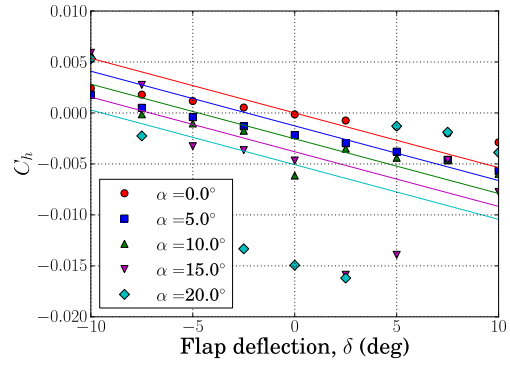
(f) $M = 0.75$

Figure C.16: C_h vs δ at different Mach numbers for the SC1095R8 airfoil, 15% chord flap, $Re = 4.8$ million.

Bibliography

[1] Hobbs, J., "Bristol Helicopters: A Tribute to Raoul Hafner", *Frenchay Publications,* Bristol, UK, 1st Edition, 1984.

[2] Sheehy, T. W., and Clark, D. R., "Rotorcraft Parasitic Drag", 31st *Annual Forum of the American Helicopter Society,* Washington DC, May, 1975.

[3] Sheehy, T. W., "A General Review of Helicopter Rotor Hub Drag Data", *Journal of the American Helicopter Society,* Vol. 22, No. 2, pp. 2–10, 1977.

[4] Leishman, J. G., "Principles of Helicopter Aerodynamics," *Cambridge University Press,* UK, 1st Edition, 2000.

[5] Nguyen, K., and Chopra, I., "Application of Higher Harmonic Control to Rotors Operating at High Speed and Thrust", *Journal of the American Helicopter Society,* Vol. 35, No. 3, pp. 78–79, July 1990.

[6] Nguyen, K., "Active Control of Helicopter Blade Stall", *Journal of Aircraft,* Vol. 35, No. 1, pp. 91–98, January-February, 1998.

[7] Nguyen, K., "Active Suppression of Stall on Helicopter Rotors", 25th *European Rotor Craft Forum,* Rome, Italy 1999.

[8] Wachspress, D., Quackenbush, T., and Solomon, C., "On Minimum Induced Power of the Helicopter Rotor", *American Helicopter Society* 61st *Annual Forum,* Grapevine, TX, June 2005.

[9] Lemnios, A., Z. and Smith, A., F., "An Analytical Evaluation of the Controllable Twist Rotor Performnce and Dynamic Behavior", *Technical Report TR 72–16, USAAMRDL,* May 1972.

[10] Lemnios, A., Z., and Dunn, F., K., "Theoretical Study of Multicyclic Control of a Controllable Twist Rotor", *Technical Report NASA-CR-151959, NASA,* May 1976.

[11] McCloud, J., L., "An Analytical Study of a Multicyclic Controllable Twist Rotor," *American Helicopter Society* 31st *Annual National Forum,* Washington, D.C., May 1975, AHS.

[12] McCloud, J., L., and Weisbrich, A. L., "Wind-tunnel Test Results of a Full-scale Multicyclic Controllable Twist Rotor," *American Helicopter Society* 34th *Annual National Forum,* Washington, D.C., May 1978.

[13] Straub, F., and Hassan, A., "Aeromechanic Considerations in the Design of a Rotor with Smart Material Actuated Trailing Edge Flaps", *American Helicopter Society* 52nd *Annual Forum Proceedings,* Washington, D.C, June 1996.

[14] Straub, F., Kennedy, D., Domzalski, D., Hassan, A., Ngo, H., Anand, V., and Birchette, T., "Smart Material-Actuated Rotor Technology – SMART," *Journal of Intelligent Material Systems and Structures,* 15:249–260, April 2004.

[15] Hassan, A. A., Straub, F. K., and Noonan, K. W., "Experimental/Numerical Evaluation of Integral Trailing Edge Flaps for Helicopter Rotor Applications," *Journal of the American Helicopter Society,* Vol. 50, No. 1, January 2005, pp. 3–17.

[16] Feszty, D., Gillies, E. A., and Vezza, M., "Alleviation of Airfoil Dynamic Stall Moments via Trailing-Edge-Flap Flow Control," *AIAA Journal,* Vol. 42, No. 1, 2004, pp. 17–25.

[17] Ormiston, R. A., "Aeroelastic Considerations for Rotorcraft Primary Control with On-Blade Elevons ", 57th *Annual Forum of the American Helicopter Society International,* Washington, DC, May 2001.

[18] Shen, J., "Comprehensive Aeroelastic Analysis of Helicopter Rotor With Trailing-Edge Flap For Primary Control and Vibration Control," *Doctoral Thesis,* University of Maryland College Park, 2003.

[19] Falls, J., "Design and Performance Prediction of Swashplateless Helicopter Rotor With Trailing Edge Flaps and Tabs," *Doctoral Thesis,* University of Maryland College Park, 2010.

[20] Mishra, A., and Baeder, J. D., "Computational Investigation of Trailing Edge Flap For Control of Vibration," AIAA 2007-4290, 25th *Applied Aerodynamics Conference,* Miami, FL, June 25–28, 2007.

[21] Ananthan, S., and Baeder, J. D., "Prediction and Validation of Loads on Bearingless Rotors Using a Coupled CFD-CSD Methodology," *Proceedings of the 64th Annual Forum and Technology Display of the American Helicopter Society International,* Montréal, Canada, May 2008.

[22] Theodorsen, T., "General Theory of Aerodynamic Instability and Mechanism of Flutter," *NACA Report 496,* 1935, pp. 413–433.

[23] Wagner, H., "Über die Entstehung des dynamischen Auftriebs von Tragflügeln," *Zeitschrift für angewandte Mathematik und Mechanik,* Band 5, 1925, pp. 17–35.

[24] Greenberg, J. M., "Airfoil in Sinusoidal Motion in a Pulsating Stream," *NACA TN No. 1326,* 1946.

[25] Kottapalli, S. B. R., "Drag on an Oscillating Airfoil in Fluctuating Free Stream," *Doctoral Thesis,* Georgia Institute of Technology, 1977.

[26] Isaacs, R. , "Airfoil Theory for Flows of Variable Velocity," *Journal Aeronautical Sciences,* Vol. 12, No. 1, Month 1945, pp. 113–117.

[27] Van der Wall, B. and Leishman, J. G., "On the Influence of Time-Varying Flow Velocity on Unsteady Aerodynamics," *Journal of the American Helicopter Society,* Vol. 39, No. 4, October 1994, pp. 25–36.

[28] Beddoes, T. S., "Practical Computation of Unsteady Lift," *Vertica*, Vol. 8, No. 1, 1984, pp. 55–71.

[29] Mazelsky, B., "Determination of Indicial Lift and Moment of a Two-Dimensional Pitching Airfoil at Subsonic Mach Numbers from Oscillatory Co-efficients with Numerical Calculations for a Mach Number of 0.7," *NACA TN2613,* 1952.

[30] Mazelsky, B. and Drischler, J. A., "Numerical Determination of Indicial Lift and Moment Functions of a Two-Dimensional Sinking and Pitching Airfoil at Mach Numbers 0.5 and 0.6," NACA TN2739, 1952.

[31] Mazelsky, B., "On the Noncirculatory Flow about a Two-Dimensional Airfoil at Subsonic Speeds," *Journal of the Aeronautical Sciences*, Vol. 19, No. 12, pp. 848—849, 1952.

[32] Bisplinghoff, R. L., Ashley H., and Halfman, R. L., *Aeroelasticity*, Addison-Wesley, 1955.

[33] Lomax, H., "Indicial Aerodynamics," *AGARD Manual of Aeroelasticity*, Part II, Chapter 6, Nov. 1960.

[34] Tyler, J. C., and Leishman, J. G., "An Analysis of Pitch and Plunge Effects on Unsteady Airfoil Behavior," *Journal of the American Helicopter Society*, Vol. 37, No. 3, July 1992, pp. 69–82.

[35] Leishman, J. G., "Unsteady Lift of an Airfoil with a Trailing-Edge Flap Based on Indicial Concepts," *Journal of Aircraft*, Vol. 31, No, 2, March-April, 1994, pp. 288–297.

[36] Hariharan, N., and Leishman, J. G., "Unsteady Aerodynamics of a Flapped Airfoil in Subsonic Flow by Indicial Concepts," *Journal of Aircraft*, Vol. 33, No. 5, Sept./Oct. 1996, pp. 855–868.

[37] Leishman, J. G., "Subsonic Unsteady Aerodynamics Caused by Gusts and Vortices Using the Indicial Method," *Journal of Aircraft*, Vol. 33, No. 5, Sept./Oct. 1996, pp. 869–879.

[38] Leishman, J. G., "Unsteady Aerodynamics of Airfoils Encountering Traveling Gusts and Vortices," *Journal of Aircraft*, Vol. 34, No. 6, Nov.-Dec. 1997, pp. 719–729.

[39] Lee, D., Leishman, J. G., and Baeder, J. D., "A Nonlinear Indicial Method For the Calculation of Unsteady Airloads," 59th *Forum of the American Helicopter Society*, Phoenix, Arizona, May, 2003.

[40] Jose, A. I., Leishman, J. G. and Baeder, J. D,"Unsteady Aerodynamic Modeling With Time-Varying Free-Stream Mach Numbers," *Journal of the American Helicopter Society,* Vol. 51, No. 4, October 2006.

[41] Theodorsen, T. and Garrick, I. E., "Nonstationary Flow About a Wing-Aileron-Tab Combination Including Aerodynamic Balance," *NACA Report 736*, 1942, pp. 129–138.

[42] Ames, M. B., and Sears, R. I., "Determination of Control-Surface Characteristics From NACA Plain-Flap and Tab Data," *NACA Report 721*, 1941, pp. 295–311.

[43] Street, W. G. and Ames, M. B., "Pressure Distribution of An N.A.C.A. 0009 Airfoil with a 50-percent-chord Flap and Three Tabs," *National Advisory Committe For Aeronautics,* Technical Notes No. 734, November 1939.

[44] Milgram, J. and Chopra, I., "A Parametric Design Study for Actively Controlled Trailing Edge Flaps," *Journal of the American Helicopter Society*, Vol. 43, No. 2, pp. 110-119, 1998.

[45] Milgram, J., Chopra, I., and Straub, F., "Rotors with Trailing Edge Flaps: Analysis and Comparison with Experimental Data," *Journal of the American Helicopter Society,* Vol. 43, No. 4, pp. 319–332, 1998.

[46] Roget, B. and Chopra, I., "Robust Individual Blade Control Algorithm for a Dissimilar Rotor," *Journal of Guidance, Control and Dynamics*, Vol. 25, No. 5, Sept-Oct 2002, pp. 915-923.

[47] Roget, B. and Chopra, I., "Closed-Loop Test of a Rotor with Individually Controlled Trailing-Edge Flaps for Vibration Reduction," *Proceedings of 61st Annual Forum of the American Helicopter Society,* Grapevine, TX June 2005.

[48] Liu, L., Friedmann, P., P., and Padthe, A. K., "Comparison of Approximate Time Domain Aerodynamics for Flapped Airfoils with CFD Based Results with Applications," *Presented at the AHS Specialist's Conference on Aeromechanics,* San Francisco, CA, Jan. 23-25, 2008.

[49] Falls, J., Datta, A., and Chopra, I., "Design and Analysis of Trailing-Edge Flaps and Servotabs for Primary Control", *63rd Annual Forum of the American Helicopter Society International*, Virginia Beach, VA, May 1–3, 2007.

[50] Falls, J., Datta, A., and Chopra, I., "Performance Analysis of Trailing-Edge Flaps in Helicopter Primary Control", *AHS Specialists Conference on Aeromechanics,* San Francisco, CA, January, 2008.

[51] Sekula, M. K., and Wilbur, M. L., "Analysis of a Multi-Flap Control System for a Swashplateless Rotor", *67th Annual Forum of the American Helicopter Society International*, VA, May 2011.

[52] Shen, J., and Chopra, I., "Actuation Requirements for a Swashplateless Helicopter Control System With Trailing-Edge Flaps," *AIAA-2002-1444*, 2002.

[53] Fulton, M. V., and Ormiston, R. A., "Hover Testing of a Small Scale Rotor with On-Blade Elevons", 53$^{\text{rd}}$ *Annual Forum of the American Helicopter Society International*, Virginia Beach, VA, May 1997.

[54] Duling, C., Gandhi, F., and Straub, F., "On Power and Actuation Requirement in Swashplateless Primary Control Using Trailing-Edge Flaps", 66$^{\text{th}}$ *Annual Forum Proceedings - AHS International*, May, 2010.

[55] Walz, C., and Chopra, I., "Design and Testing of a Helicopter Rotor Model with Smart Trailing Edge Flaps," 35$^{\text{th}}$ *AIAA/ASME/ASCE/AHS/ASC Structures, Structural Dynamics and Materials Conference and Adaptive Structures Conference,* Hilton Head, SC, April 1994.

[56] Ben-Zeev, O., and Chopra, I., "Development of an Improved Helicopter Rotor Model with Smart Trailing Edge Flaps for Vibration Suppression," *1995 North American Conference on Smart Structures and Materials,* San Diego, Calif., February 1995.

[57] Bernhard, A. and Chopra, I., "Hover Testing of a Smart Flap Activated by Bending-Torsion Coupled Beam," 37$^{\text{th}}$ *AIAA/ASME/ASCE/AHS/ASC Structures, Structural Dynamics and Materials Conference and Adaptive Structures Forum,* Salt Lake City, Utah, April 1996.

[58] Koratkar, N., and Chopra, I., "Analysis and Testing of a Froude Scaled Helicopter Rotor with Piezoelectric Bender Actuated Trailing Edge Flaps," *Journal of Intelligent Material Systems and Structures,*, Vol. 8, No. 7, July 1997.

[59] Falls, J., and Chopra, I. "Piezobimorph Actuated Servotab For Controlling a Trailing Edge Flap," 46$^{\text{th}}$ *AIAA/ASME/ASCE/AHS/ASC Structures, Structural Dynamics and Materials Conference*, Austin, Texas, April 2005.

[60] Saxena, A., and Chopra, I., "Development and Testing of a Swasplateless Rotor with Compact Brushless Motor Actuated Flaps for Primary Control", 67$^{\text{th}}$ *Annual Forum of the American Helicopter Society International*, VA, May 2011.

[61] John, S., Sirohi, J., and Werely, N. M., "Development of a Piezo-hydraulic Active Pitch Link for a Swashplateless Rotor", 48$^{\text{th}}$ *AIAA/ASME/ASCE/AHS/ASC Structures, Structural Dynamics and Materials Conference*, HI, April 2007.

[62] Furst, D., Hausberg, A., and Neuheuser, T., "Experimental Verification of an Electro-Mechanical-Actuator for a Swashplateless Primary and Individual Helicopter Blade Control System", 64$^{\text{th}}$ *Annual Forum of the American Helicopter Society International*, Montreal, April 2008.

[63] Arnold, U. T. P., Furst, D., Neuheuser, T. and Bartels, R., "Development of an Integrated Electrical Swashplateless Primary and Individual Blade Control System", 63$^{\rm rd}$ *Annual Forum of the American Helicopter Society International*, VA, May 2007.

[64] Altmikus, A. R. M., Wagner, S., Beaumier, P., and Servera, G., "A Comparison: Weak versus Strong Modular Coupling for Trimmed Aeroelastic Rotor Simulations," 58$^{\rm th}$ *Annual Forum of the American Helicopter Society,* Montreal, Quebec, June 2002.

[65] Tung, C., Caradonna, F. X. and Johnson, W., "Conservative Full Potential Model for Unsteady Transonic Rotor Flows," *AIAA Journal,* Vol. 25, No. 2, 1987, pp. 193–198.

[66] Servera, G., Beaumier, P., and Costes, M., "A Weak Coupling Method between the Dynamics Code Host and the 3D Unsteady Euler Code Waves," 26$^{\rm th}$ *European Rotorcraft Forum*, The Hague, The Netherlands, September 2000.

[67] Pahlke, K., and Van Der Wall, B., "Calculation of Multibladed Rotors in High-Speed Forward Flight with Weak Fluid-Structure-Coupling," 27$^{\rm th}$ *European Rotorcraft Forum,* Moscow, September 2001.

[68] Datta, A., Sitaraman, J., Chopra, I. and Baeder, J. D., "CFD/CSD Prediction of Rotor Vibratory Loads in High-Speed Flight," *Journal of Aircraft*, Vol. 43, No. 6, pp. 1698–1709, November-December, 2006.

[69] Potsdam, M., Yeo, H., and Johnson, W., "Rotor Airloads Prediction Using Loose Aerodynamic/Structural Coupling", *Journal of Aircraft,* Vol. 43, No. 3, pp. 732–742, May/June 2006.

[70] Yeo, H., Potsdam, M. and Ormiston, R. A., "Rotor Aeroelastic Stability Analysis Using Coupled Computational Fluid Dynamics/Computational Structural Dynamics", *Journal of the American Helicopter Society*, Vol. 56, No. 4, pp. 1–16, October 2011.

[71] Silbaugh, B., and Baeder, J. D., "Coupled CFD/CSD Analysis of a Maneuvering Rotor Using Staggered & Time-Accurate Coupling Schemes", *AHS Specialist's Conference on Aeromechanics*, San Francisco, CA, January 23–25, 2008.

[72] Abhishek, A., Ananthan, S., Baeder, J. D., and Chopra, I., "Prediction and Fundamental Understanding of Stall Loads in UH-60A Pull-Up Maneuver", 66$^{\rm th}$ *Annual Forum of the American Helicopter Society*, Phoenix, AZ, May 11–13, 2010.

[73] Steger, J. L., Dougherty, F. C., and Benek, J. A., "A Chimera Grid Scheme," *Advances in Grid Generation,* American Society of Mechanical Engineers, Fluids Engineering Division (Publication) FED, Vol. 5, 1983, pp. 59–69.

[74] Meakin, R., "Composite Overset Structured Grids," *Handbook of Grid Generation*, CRC Press, 1999, Chapter 11.

[75] Meakin, R., "Object X-Rays for Cutting Holes in Composite Overset Structured Grids," 15th *AIAA Computational Fluid Dynamics Conference*, AIAA Paper 20012537, Anaheim CA, June, 2001.

[76] Brown, D. L., Henshaw, W. D., and Quinlan, D. J., "Overture : Object Oriented Tools for Overset Grid Applications," 15th *AIAA Applied Aerodynamics Conference*, AIAA Paper 99-3130, June 1999.

[77] Chesshire, G., and Henshaw, W. D., "Composite Overlapping Meshes for the Solution of Partial Differential Equations," *Journal of Computational Physics*, Vol. 90, 1990, pp. 1–64.

[78] Suhs, N. E., Rogers, S. E., and Dietz, W. E., "PEGASUS 5: An Automated Pre-Processor for Overset Grid CFD," 32nd *AIAA Fluid Dynamics Conference*, AIAA Paper 2002-3186, St. Louis, MO, June, 2002.

[79] Prewitt, N. C., Belk, D. M., and Shyy, W., "Parallel Computing of Overset Grids for Aerodynamic Problems with Moving Objects," *Progress in Aerospace Sciences*, Vol. 36, 2000, pp. 117–172.

[80] Petersson, N. A., "An Algorithm for Assembling Overlapping Grid Systems," *SIAM Jouranl of Scientific Computing*, Vol. 20, No. 6, 1999, pp. 1995–2022.

[81] Petersson, N. A., "Hole-Cutting for Three-Dimensional Overlapping Grids," *SIAM Journal of Scientific Computing*, Vol. 21, No. 2, 1999, pp. 646–665.

[82] Noack, R., "DiRTlib: A Library to Add an Overset Capability to your Flow Solver," 17th *AIAA Computational Fluid Dynamics Conference*, AIAA Paper 2005-5116, Toronto Canada, June 6–9, 2005.

[83] Noack, R., "SUGGAR: A General Capability for Moving Body Overset Grid Assembly," 17th *AIAA Computational Fluid Dynamics Conference*, AIAA Paper 2005-5117, Toronto, Canada, June 6–9, 2005.

[84] Wang, Z. J. and Parthasarathy, V., "A Fully Automated Chimera Methodology for Multiple Moving Body Problems," *International Journal for Numerical Methods in Fluids*, Vol. 33, 2000, pp. 919–938.

[85] Lee, Y., "On Overset Grid Connectivity and Automated Vortex Tracking in Rotorcraft," *Doctoral thesis*, Department of Aerospace Engineering, University of Maryland College Park, 2008.

[86] Lakshminarayan, V. K., "Computational Investigation of Micro-Scale Coaxial Rotor Aerodynamics in Hover," *Doctoral thesis*, Department of Aerospace Engineering, University of Maryland College Park, 2009.

[87] Sitaraman, J., Floros, M., Wissink, A. M., and Potsdam, M., "Parallel Unsteady Overset Mesh Methodology for a Multi-Solver Paradigm with Adaptive Cartesian Grids", 26th *AIAA Applied Aerodynamics Conference*, Honululu, HI, August, 2008.

[88] Liao, W., Cai, J., and Tsai, H. M., "A Multigrid Overset Grid Flow Solver With Implicit Hole Cutting Method", *Computer Methods in Applied Mechanics and Engineering*, Vol. 196, No. 9–12, pp. 1701–1715, February 1, 2007.

[89] Leishman, J. G., "A Two-Dimensional Model for Airfoil Unsteady Drag below Stall," *Journal of Aircraft,* , Vol. 25, No. 7, 1987, pp. 665-666.

[90] Leishman, J. G., "Principles of Helicopter Aerodynamics," *Cambridge University Press,* New York, 2002, Chapter 8.

[91] Jones, R. T., "Operational Treatment of the Non-Uniform Lift Theory in Airplane Dynamics," *NACA Technical Note 667*, 1938.

[92] Lomax, H., "Lift Developed on Unrestrained Rectangular Wings Entering Gusts at Subsonic and Supersonic Speeds," *NACA Technical Note 2925*, 1954.

[93] Hariharan, N., "Unsteady Aerodynamics of a Flapped Airfoil in Subsonic Flow Using Indicial Concepts," *M.S. Thesis,* Department of Aerospace Engineering, University of Maryland, College Park, MD, 1995.

[94] Heaslet, M. A., and Sprieter, J. R., "Reciprocity Relations in Aerodynamics," *NACA Report 1119*, 1952.

[95] Srinivasan, G. R., Baeder, J. D., Obayashi, S., and McCroskey., W. J., "Flowfield of a Lifting Rotor in Hover: A Navier-Stokes Simulation," *AIAA Journal*, Vol. 30, No. 10, Oct. 1992, pp. 2371–2378.

[96] Gumerov, N. A., and Duraiswami, R., "Fast Multipole Methods for the Helmholtz Equation in Three Dimensions," *Elsevier Science,* 1st Edition, 2005, Chapter 5, pp. 207–222.

[97] Gumerov, N. A., Duraiswami, R., and Borovikov, E. A., "Data Structures, Optimal Choice of Parameters, and Complexity Results for Generalized Multilevel Fast Multipole Methods in d Dimensions," *UMIACS TR 2003-28,* University of Maryland, College Park, 2003.

[98] Duraisamy, K., "Studies in Tip Vortex Formation, Evolution and Control," *Doctoral Thesis,* Department of Aerospace Engineering, University of Maryland College Park, 2005.

[99] Buelow P. E. O., Schwer D. A., Feng J. and Merkle C. L. "A Preconditioned Dual-Time, Diagonalized ADI scheme for Unsteady Computations," 13th *AIAA Computational Fluid Dynamics Conference, AIAA paper 97-2101*, Snowmass Village, CO, July 1997.

[100] Pandya, S. A., Venkateswaran, S. and Pulliam, T. H. "Implementation of Preconditioned Dual-Time Procedures in OVERFLOW," 41st *AIAA Aerospace Sciences Meeting and Exhibit,* AIAA paper 2003-0072, Reno, NV, January 2003.

[101] Pulliam, T. H. and Chaussee, D. S., "A Diagonal Form of an Implicit Approximate Factorization Algorithm," *Journal of Computational Physics*, Vol. 39, 1981.

[102] Chopra, I. and Bir, G., "University of Maryland Advanced Rotor Code: UMARC," *American Helicopter Society Aeromechanics Specialists Conference,* San Francisco, CA, January 1994.

[103] Weissinger, J., "The Lift Distribution of Swept-Back Wings," *NACA Technical Report TM 1120,* 1947.

[104] Leishman, J. G. and Beddoes, T. S., "A Semi-Empirical Model for Dynamic Stall," *Journal of the American Helicopter Society,* Vol. 34, No. 3, July 1989, pp. 3–17.

[105] Bhagwat, M. J., Ormiston, R. A., Saberi, H. A., and Xin, H., "Application of CFD/CSD Coupling for Analysis of Rotorcraft Airloads and Blade Loads in Maneuvering Flight", *63*rd *Annual Forum of the American Helicopter Society International*, Virginia Beach, VA, May 1–3, 2007.

[106] Datta, A., Nixon, M. and Chopra, I., "Review of Rotorcraft Loads Prediction With the Emergence of Rotorcraft CFD," 31st *European Rotorcraft Forum,* Florence, Italy, September, 2005.

[107] Leishman, J. G., "Principles of Helicopter Aerodynamics," *Cambridge University Press,*, New York, 2002, Chapter 7.

[108] Lorber, P. F., Stauter, R. C., and Landgrebe, A. J., "Comprehensive Hover Test of the Airloads and Airflow of an Extensively Instrumented Model Helicopter Rotor," *Proceedings of the* 45th *Annual American Helicopter Society Forum,* Boston, MA, May 1989.